Development and Application of a Novel Approach to Sand Production Prediction

Mustapha Halilu Lamorde B.Sc., M.Sc.

Thesis presented for the degree of Doctor of Philosophy

Heriot-Watt University
Institute of Petroleum Engineering
School of Energy, Geoscience, Infrastructure and Society

October 2015

Abstract

Sand production is a complex problem that has plagued the oil and gas industry for decades, leading to reduced productivity, wellbore instability, equipment failure and expensive sand control and management techniques. Therefore, a reliable prediction of the potential of a formation to produce sand as well as the mass and volume of the sand produced is required for an appropriate and economically effective sand management.

In this thesis a novel approach (yield energy model) to predict the potential of formation to produce sand and to quantify the mass of sand produced around yielded wellbore region based on energy dissipation is presented. During drilling and hydrocarbon production, yield and fragmentation of rock around a wellbore may occur when the rock is exposed to stresses which exceed its failure criterion, creating yield zone and hence the potential for instability and sand production. Generally, in brittle rocks, grains are deformed elastically with increasing stress, storing strain energy in the process. The stored strain energy is dissipated during failure, some of which is available for the fragmentation of the rock along failure surfaces. It is argued that the major source of sand production in competent rock is associated with the debris created by slippage along shear fractures in the yielded zone along perforation wall. The potential for sand production and the mass or volume of the sand created around the yield zone is predicted by quantifying the reduction in strain energy stored in the rock as its yields around a completion on removal of completion fluid and the imposition of drawdown. The resultant sand then becomes available as a source for sand production.

The yield energy model has been applied to assess the potential of several reservoir samples to produce sand and also quantify the mass of the sand produced as a result of formation instability caused by drilling and hydrocarbon production in a field specific manner. Results from laboratory testing of representative samples and field data has been utilised as input parameters. The extent of the failed zone, the sand production potential and the mass of debris have been analysed as a function of mud weights, drawdown pressures and production rates. The impact of unique production performance of different horizons on formation stability has been accounted for by employing deliverability expressions. The results have been assessed with regards to field observations and were found to be consistent.

Dedication

This thesis is dedicated to
My Parents Dr Hajo Sani and Alhaji Halilu Lamorde

and to

Late Hajiya Aisha Addah Mashi Lamorde and
Late Alhaji Ahmadu Mashi Lamorde

Acknowledgement

All praise and glory is due to Allah (S.W.T) for giving me the strength and perseverance to complete this challenging and yet fulfilling journey.

First and foremost, I would like to express my deepest gratitude to my supervisor, Dr. Jim Somerville of the Institute of Petroleum Engineering for his immense technical and moral support, guidance, mentorship and friendship throughout my PhD study without which this project would not have been completed.

I would like to specially thank my office colleagues: Sally Hamilton for allowing me to tab into her wealth of laboratory experience and for her 'hands on' assistance, the input from her expertise improved my project immensely; Peter Olden, for offering exceptional guidance and direction to me most especially at the start of the project and Min Jin, for the late evening discussions on the technical issues that gave me clarity and vision to put things together. I would like to thank Dennis McLaughlin, for his valuable assistance with my laboratory work. I would also like to extend my appreciation to all the staff of the Institute of Petroleum Engineering for their support at various phases of my program. I would like to appreciate my fellow PhD colleagues for their encouragement, support and comradeship. I wish everyone all the best.

I remain eternally grateful to my wonderful, loving, caring and inspiring mother, Dr. Hajo Sani and my father, Alhaji Halilu Lamorde for their continuous support, love and guidance throughout my life. I deeply appreciate all the inspiring and encouraging words from my friends, brothers, sisters, cousins, aunties, uncles, nephews, nieces and my entire extended family. I thank all my friends and colleagues at Shell for their continuous support. I would like to thank my lovely wife, Maryam and our little angel, Zaynab for their love, support, patience and encouragement during the course of this program and especially at the writing up phase when they spent most time without me. Umar Farouk was born towards the end of this research; the anticipation of your arrival was a source of inspiration in completing this thesis.

Finally, I would like to recognise and appreciate the Petroleum Technology Development Fund (PTDF), Nigeria for generously funding my PhD program.

Declaration Statement

ACADEMIC REGISTRY
Research Thesis Submission

Name*:*	Mustapha Lamorde		
School/PGI:	EGIS/Institute of Petroleum Engineering		
Version: *(i.e. First, Resubmission, Final)*	Final	Degree Sought: *(Award and subject area)*	PhD Petroleum Engineering

Declaration

In accordance with the appropriate regulations I hereby submit my thesis and I declare that:

1) the thesis embodies the results of my own work and has been composed by myself
2) where appropriate, I have made acknowledgement of the work of others and have made reference to work carried out in collaboration with other persons
3) the thesis is the correct version of the thesis for submission and is the same version as any electronic versions submitted*.
4) my thesis for the award referred to, deposited in the Heriot-Watt University Library, should be made available for loan or photocopying and be available via the Institutional Repository, subject to such conditions as the Librarian may require
5) I understand that as a student of the University I am required to abide by the Regulations of the University and to conform to its discipline.

* *Please note that it is the responsibility of the candidate to ensure that the correct version of the thesis is submitted.*

Signature of Candidate:		Date:	

Submission

Submitted by (name in capitals):		
Signature of Individual submitting:		
Date Submitted:		

For Completion in Student Service Centre

Received in the SSC by *(name in capitals):*			
Method of Submission *(Handed in to SSC; posted through internal/external mail):*			
E-thesis submitted ***(mandatory for final theses)***			
Signature:		Date:	

Table of Contents

List of Tables

List of Figures

Nomenclature

a	semi major axis
b	semi minor axis
E'	energy expended
E	Young's modulus
E_A	energy per unit area of slip
C_L	closure
D_F	fractal dimension
G	Shear modulus
G_{IIC}	fracture surface energy
k	triaxial stress factor
p	pressure on borehole wall
P_p	pore pressure
P_{wf}	flowing bottom hole pressure
p'	augmentation to strength due friction
P''	reservoir static pressure
P_m	restraint due to mud weight
Δp	pressure drawdown
q	redistributed effective stress around well
S_W	surface area per gram
r	radius of point of interest
R_w	wellbore radius
R_{ye}	yield zone radius
S_W	surface area per gram of powder
V	volume
W_A	energy density
W_0	strain energy per unit volume of rock

Greek Letter

α	biot's constant,
ρ	density
γ	specific surface energy
γ_{xy}	shear strain in x-y plain
γ_{yz}	shear strain in y-z plain
ε	strain
ε_x	normal strain in x direction
ε_y	normal strain in y direction
ε_a	axial strain
ε_r	radial strain
θ	angle
μ	viscosity
σ_θ	tangential stress
σ_r	radial stress
σ_1	maximum principal stress
σ_2	intermediate principal stress
σ_1	maximum principal stress
σ_h	minimum horizontal stress
σ_H	maximum horizontal stress
σ_0	unconfined compressive stress
σ_n	normal stress
σ_{Rye}	radial stress yield/elastic boundary
$\sigma_{\theta y}$	tangential stress on the yield side boundary
$\sigma_{\theta e}$	tangential stress on the elastic side boundary
σ_0^*	unconfined compressive strength broken material
σ_1^*	maximum principal stress broken material
$\hat{\sigma}_r$	effective radial stress
$\hat{\sigma}_{Rye}$	effective tangential stress on the yield side boundary
$\hat{\sigma}_{\theta y}$	effective tangential stress on the yield side boundary
υ	Poisson's ratio
$\Delta\sigma_a$	change in axial stress

$\Delta\varepsilon_a$	change in axial strain
$\Delta\varepsilon_r$	change in radial strain
τ	shear stress
τ_{xy}	shear stress in x-y plane
τ_{xz}	shear stress in x-z plane
τ_{yz}	shear stress in y-z plane
τ^p	peak shear strength
τ^f	residual frictional strength
δ_s	nominal slip
δ_s^*	critical slip
δ	shear slip
ΔL_s	change in displacement

Abbreviation

CEF	Comminution Efficiency Factor
IPR	Inflow Performance Relationship
ISRM	International Society for Rock Mechanics
LVDT	linear variable displacement transducers
SED	Strain Energy Function (elastic)
SEY	Strain Energy Function (yield)
UCS	Unconfined Compressive Strength

1 Introduction

1.1 Problem Statement

A significant proportion of the world's oil and gas wells are drilled and produced from sandstone formations (Walton et al., 2002). The mechanical stability and strength of these sandstone formations are controlled by the original *in situ* stress and subsequent changes due to petroleum related operations such as drilling and hydrocarbon production. When the mechanical strength is exceeded, the resulting formation failure or breakdown may lead to wellbore instability and consequently sand production.

Several attempts have been proposed to predict sand production by applying a failure criterion. However, these approaches only predict catastrophic sand failure neglecting the continuous changes and post-failure characterisation of the formation and the volume of the produced sand. In particular, a link between altered stress changes in the formation and resulting energy changes to determine whether a rock will fail or remain is missing.

Generally, existing sand failure models are commonly associated with unconsolidated and poorly cemented sandstones, however, formation considered to be moderately consolidated and competent have also been found to fail and produce sand. It has even been the case that no sand control measures were considered for such formations at the conceptual design phase. These formations were later found to produce sand, resulting in equipment damage, reduced production, costly remedial workovers and even loss of the wellbore. Sand failure models predicted for unconsolidated sandstone formations may not be applicable to moderately consolidated and competent sandstone formations since the failure mechanism in more competent sandstones is different from the sand arch mechanism (Hall and Harrisberger, 1970, Risnes et al., 1982a, Arii et al., 2005) which prevails in unconsolidated sandstones. Several workers report the occurrence of shear fractures in moderately consolidated and competent sandstone formations (e.g. Al-Awad and Desouky, 1997) similar to that observed in triaxial tests.

1.2 Objectives of the Research

The following are the objectives of this research:

1. Develop a new sand production prediction model (yield energy model) that can be applicable to moderately consolidated and competent sandstones to predict both the potential and the mass of sand produced.
2. Determine rock mechanic properties and comminution data for both reservoir and analogue sandstones thus generating the input data required for the application of the yield energy model.
3. Apply the yield energy model to predict the sand production potential and mass of produced sand as a function of production behaviour of reservoir formation.

1.3 Organisation of the Thesis

This thesis is presented in eight chapters, starting with the current introductory chapter which gives problem statement and objectives of the thesis.

- Chapter 2 defines basic theory and concepts in rock mechanics. It also provides a literature review of previous studies on stress sensitivity in sandstones.
- Chapter 3 presents a description of the material tested and sample preparation techniques. This is followed by an overview of the laboratory equipment, experimental set-ups and procedures.
- Chapter 4 presents results and analysis obtained from the experimental work.
- Chapter 5 presents the development of the strain energy approach to sand prediction and the application of this technique to the rock mechanical data generated.
- Chapter 6 present the development of the yield energy model and the application of this approach to quantify the amount of failed sand in the yielded zone as a function of production behaviour of reservoir formation.
- Chapter 7 summarises the main conclusions from this work and recommends further areas of research.

2 Definitions, Basic Concepts and Review of Past Studies

2.1 Basic Characteristics of Sandstones

Sandstones consist of a framework of grains and pores (Figure 2.1). The pores may be filled by a combination of finer-grained primary or secondary clastic matrix, cement (typically calcite, quartz, chert, or hematite) and/or fluids such as gas, air, oil, and formation water. The grains may be held together by the cement matrix thereby inhibiting continuous framework. The rock in this case is described as matrix-supported since the matrix contributes to the load bearing capacity of the rock. In the absence of a matrix though, the load bearing capabilities of the assemblage is contained only in the framework; this is called a grain supported rock. Thus the knowledge of sandstones is centred on the framework, composition, and on the nature and volume of pores and the pore fluids.

Sandstones are formed by a complex process which involves the deposition and lithification (bonding individual grains to form aggregate mass results) of quartz-rich sediments as a result of weathering (chemical or physical breakdown of minerals), transportation (wind, water, or ice) and deposition of pre-existing rocks. Lithification is the process where freshly deposited sediments are converted to rock while diagenesis refer to chemical and physical changes which occur in the character and composition of the mineral grains during burial, including cementation and compaction. Quartz and feldspars (K-feldspar and plagioclase) are the major components of the framework in most sandstones due to their resistance to weathering, stability and hardness. Both quartz and feldspar are quite common and abundant in the earth's crust. Accessory minerals such as calcite, Fe-Oxide, mica, glauconite and heavy minerals (e.g. magnetite, zircon, ilmenite, garnet and pyrite) may be present in sandstones.

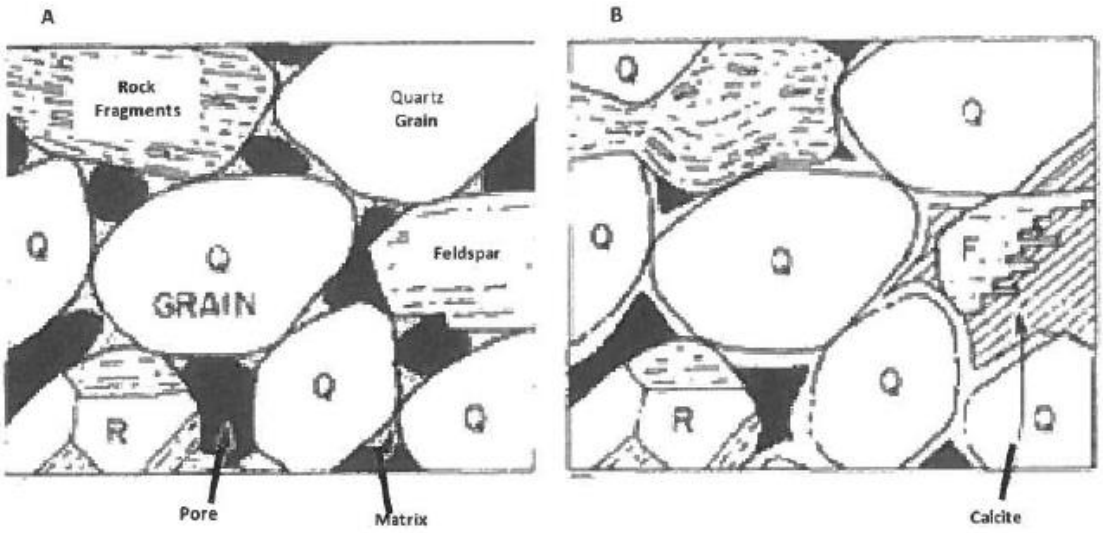

Figure 2.1: Morphology of sandstone showing (a) detrital grains, pores and matrix; (b) altered grains and matrix and cement (quartz overgrowth and calcite) shortly after deposition (Berg, 1986).

2.1.1 Physical Properties of Reservoir Sandstones

Physical description of the properties of reservoir sandstones is usually required to quantify the amount of fluids present and also to understand how the fluids will flow through the reservoir. These parameters include the capacity of the rock to store fluid, called porosity and the connectivity of pore spaces allowing fluid flow through the rock, the permeability.

2.1.1.1 *Porosity*

Porosity, ϕ of a rock is defined as the ratio of void space to total volume of rock, usually expressed as the percentage of the pore spaces in the total volume of rock. Porosity can be determined by the following equation:

$$\phi = \frac{V_p \times 100}{V_b} \qquad (2.1)$$

where V_p is the pore volume and V_b is the bulk volume.

However, in practice the grain volume of sandstone is easier to determine than the pore volume, thus porosity is often expressed as:

$$\phi = \frac{V_b - V_g}{V_b} \times 100 \qquad (2.2)$$

where V_g is the grain volume.

The pore space is the area of interest as it is a potentially hydrocarbon-bearing. Total porosity refers to the total amount of pore space in a rock, regardless of whether or not the

space is accessible to free fluid penetration as contrasted with effective or available pore space. Effective porosity is the amount of interconnected pore space available to free fluid penetration. Porosity can be considered as primary (initial) or secondary (usually diagenetic). Primary porosity refers to intergranular spaces between grains formed during deposition and lithification processes while secondary porosity occur after burial due to diagenetic process e.g. leaching of cement, fracturing and dissolution of soluble grains especially feldspar.

2.1.1.2 *Permeability*

Permeability is a measure of the ease with which a fluid can flow through a rock. To make fluid flow through a porous rock sample, a pressure differential is required across the sample. The resulting flowrate through the sample depends on the sample dimensions, the fluid viscosity and the internal pore geometry of the sample and is given as:

$$Q = \frac{kA\Delta P}{\mu L} \tag{2.3}$$

where A is the area of the rock (m^2), L is the length of the rock sample (m), ΔP is the pressure differential across the sample (Pa), μ is the viscosity of the fluid (Pa.sec), Q is the flowrate (m^3/sec), and k is the permeability (m^2).

2.1.1.3 *Primary Controls on Properties of Sandstones*

Porosity and permeability are controlled by the primary textural parameters of a rock, i.e. grain size, sorting, shape, roundness, packing and orientation as well as diagenetic alterations such as cementation and/or clay content. Permeability and to a lesser extent porosity, are also influenced by sedimentary structures and bioturbation on a large scale. Texture concepts of sandstone grain include all the descriptor of the geometry, size and shape of the particle and pores that form the sandstone and the relationship of these components.

2.1.1.3.1 Grain Size and Grain Size Distribution

Sandstones are composed of grains of different sizes. Grain size enables the sandstone to be categorised as fine, medium or coarse grained sandstone. Several grain size classifications have been suggested but the Udden-Wentworth scale is widely accepted (Table 2.1). Grain size is measured in millimetres, or phi (ϕ) unit, where phi is the logarithm transformation of the Udden-Wenworth scale.

$$\phi = -\log_2 d \tag{2.4}$$

where d is grain size in millimetres.

The range of grain sizes of sandstones, if arranged statistically, has been found to differ from one another. This size distribution of grain size may be presented graphically as histograms or frequency curves. When the distribution of grain size has been obtained, sediments can be characterised by several parameters: mean grain size, mode, median grain size, sorting and skewness (Tucker, 2009).

Rock Type	Wentworth Class	Sub-class	Length	
			mm	Phi (ϕ)
Conglomerate/Gravel	boulder	very coarse	4096	-12
		coarse	2048	-11
		medium	1024	-10
		fine	512	-9
	cobble	coarse	256	-8
		fine	128	-7
	pebble	very coarse	64	-6
		coarse	32	-5
		medium	16	-4
		fine	8	-3
	granule		4	-2
Sandstone/Sand	sand	very coarse	1	0
	sand	coarse	0.5	1
	sand	medium	0.25	2
	sand	fine	0.125	3
	sand	very fine	0.063	4
Siltstone/Silt	silt	coarse	0.031	5
		medium	0.015	6
		fine	0.008	7
		very fine	0.004	8
Calystone/Mud	clay	fine	0.006	14

Table 2.1: Wentworth grain size scale (after Pettijohn, 1987).

From the reservoir point of view, sorting is the most important parameter for grain size distribution, which describes the spread in the grain size classes or grain size distribution. The terms used to describe sorting are illustrated in Figure 2.2. In well-sorted sandstone most of the grains are close to the mean grain size, whereas in poorly sorted sediments there is a wide spread of grain sizes about the mean. Good sorting is achieved either when grains have undergone transport for long periods of time, or when the transporting medium is selective with respect to the grain size it can move, for example wind transport. Poorly sorted sandstones are produced when a mass of material is transported and deposited fairly rapidly without being reworked, for example deposition by glaciers. Well sorted sediments have higher porosity and permeability than poorly sorted ones,

knowledge of the nature of the depositional environment may be used to predict the location of the best quality reservoir units.

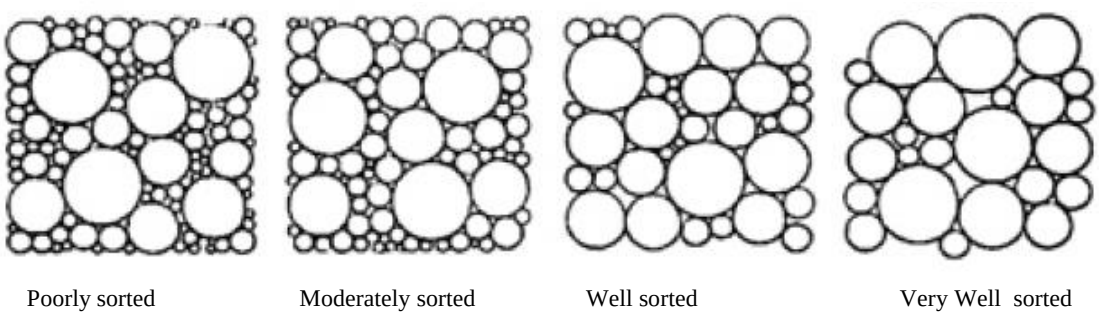

Figure 2.2: Term used to describe grain sorting (after Pettijohn, 1987).

2.1.1.3.2 Grain Shape

The grain shape of a sandstone particle or grain is essentially its geometric form. The quantification of shape is more difficult and is normally expressed in terms of two separate parameters, sphericity and roundness. Sphericity of the grains is ideally defined as the ratio of the surface area of a sphere (with the same volume as the given particle) to the surface area of the particle. It describes how closely a rock particle resembles a sphere while roundness is a measure of how much the angular corners and edges have been worn away. The sphericity of a particle influences erosion, transportation, and deposition patterns. The roundness on the other hand is a direct measure of the distance that particle travelled during transportation. Naturally occurring grains are never truly spherical. The terms used to describe roundness shown in Figure 2.3 are purely descriptive; varying between very angular and well rounded (Pettijohn, 1987).

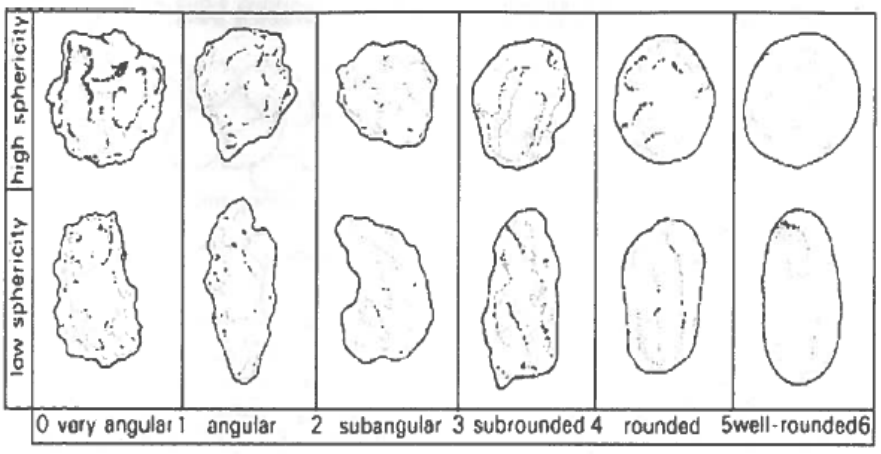

Figure 2.3: Categories of roundness of grains for each category a grain of low and high sphericity is shown (after Pettijohn, 1987).

Sediments that have been transported far enough for the grains to become well rounded and efficiently separated so that they are well sorted are called 'texturally mature'. Conversely sediments that are poorly sorted with angular fragments are said to be texturally immature. Texturally mature deposits constitute the best reservoirs, provided their porosity is not altered during burial.

2.1.1.3.3 Grain Fabric and Packing

The fabric of a sandstone is the way and manner in which the individual grains are put together to make up the assemblage. Basically, this term refers to the orientation, packing and to the nature of boundaries between the individual grains (Tucker, 2009). The fabric of sandstone is largely dependent on the means of deposition of the diverse size, shape and roundness and also on how the aggregate is later compacted by physical and chemical processes. When a significant number of the grains have assumed a certain orientation or orientations in preference to all other, these grains are said to show preferred orientation, or to have an anisotropic fabric pattern.

Packing is the spacing or density of mineral grains in a rock (Graton and Fraser, 1935). Grain packing is considered as the most significant textural parameter controlling the permeability and porosity of sandstones. There are several ways in which grains can be arranged or packed (even in uniformly sized spherical grains). Experimental studies of uniform spheres by Graton and Fraser (1935) established some basic relationships between the arrangement (packing) of the spheres (grains) and porosity where six 'cases' were identified. The most 'open' and hence porous of these was cubic packing and the 'closest' was rhombohedral packing. This packing arrangement is illustrated in Table 2.2.

Graphic Representation	Pore (void) Shape between Grains	Grain Arrangement
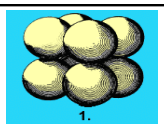	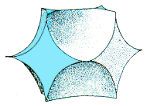	**Cubic packing** [Square layer arrangement vertically and horizontally].
	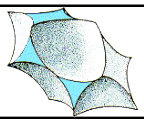	**Orthorhombic packing** [Square layer arrangement but at angles of 60° to one another].
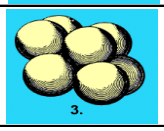	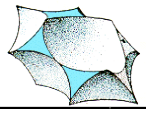	**Rhombohehral packing** [Square layer arrangement corresponding to the three diagonal planes of a regular octahedron].
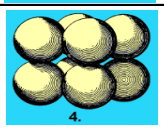	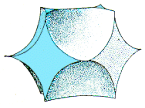	**Orthorhombic packing** [Square layers rotated 90° about the edge formed by the junction of the basal square layer with the simple rhombic layer].
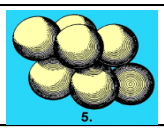	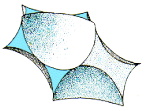	**Tetragonal-spheroidal packing** [Simple rhombic packing in two planes at right angles].
	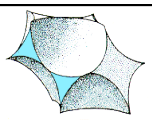	Rhomboidal packing [As 3., square layer rotated $109^{0}28'$ about the edge of basal square arrives at the same packing].

Table 2.2: Sphere packing 'cases' of (Graton and Fraser, 1935) showing the six possible packing arrangement.

Grain orientation is the alignment of the particles with regards to a characteristic dimension and is found to influence permeability. Grain orientation has a significant effect in which contact type arises; if ellipsoidal grains are oriented with their long axis parallel to each other then it is more likely there will be a high occurrence of long contacts.

One important feature of rock fabric is the relationship between the grains, which make up the coarser components of the sediment, and the finer grained matrix, which occupies the inter-grain spaces. As earlier discussed in section 2.1, if the grains form a self-supporting framework, the fabric is described as grain supported. However, if larger grains are separated from each other by the finer matrix with little or no inter-grain contact, the rock fabric is said to show matrix support. Matrix supported rocks have lower porosity and permeability than grain supported ones.

2.2 Mechanical Properties of Reservoir Sandstones

2.2.1 Concept of Stress

Stress is a combination of body forces, which act on each individual component of material e.g. gravity, inertia, magnetic attraction and surface forces e.g. fluid pressure wedging opens a hydraulically induced fracture, which act on the bounding surface of a body. Body forces are vectorial quantities, i.e. they are characterised by both direction and magnitude. Also, body forces generate surface forces. In general rock in the subsurface does not move, meaning that the forces acting on elements and surfaces are in equilibrium. Consider a body in equilibrium due to the action of surface and body force as shown in Figure 2.4.

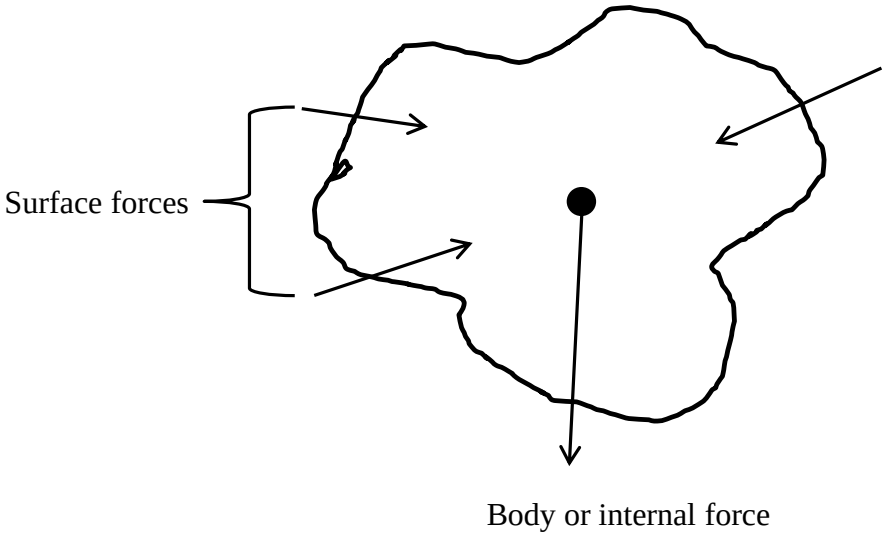

Figure 2.4: An irregular-shaped body at equilibrium due to action of surface and body forces.

The intensity of these forces, F as they are distributed through the body, i.e. the force per unit area is known as stress, σ. The stress in direction 'a' on a plane with a normal in direction 'n' (Figure 2.5) is given by:

$$\sigma_{na} = \lim_{\Delta A \to 0} \frac{\Delta F}{\Delta A} \qquad (2.5)$$

In the context of a reservoir rock, a stress state exists in a particular portion of the reservoir that in itself is related to the adjacent rock masses. Therefore, vertical stresses in a reservoir are related to the overburden and horizontal stresses to the confinement by laterally adjacent rock masses. This shows that stress not only varies with the force and the surface area but also depends on the orientation of the surface element. For this reason, stress is considered a tensor quantity rather than a vector.

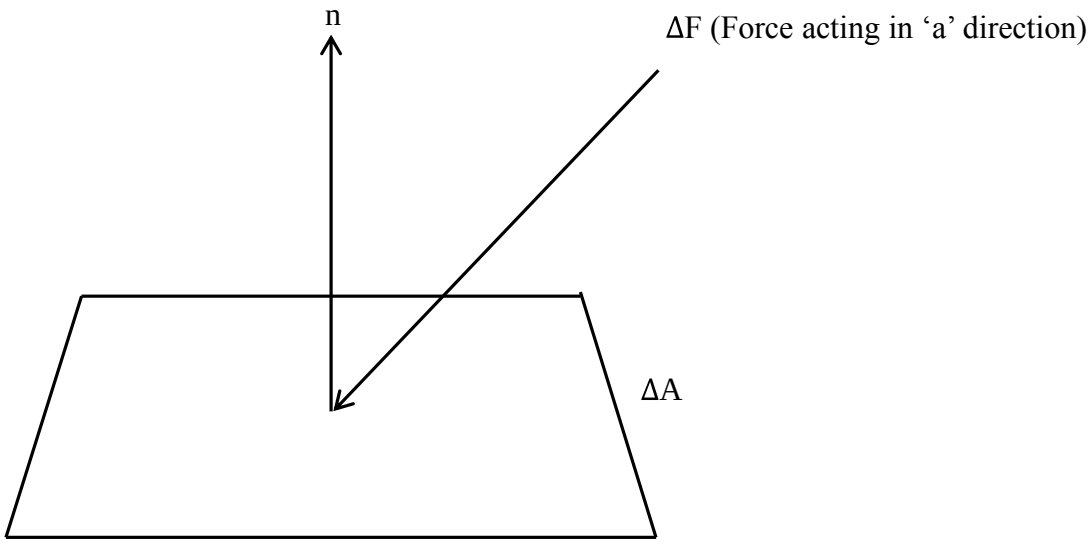

Figure 2.5: Local stress at a point

As shown in equation (2.5), stress is defined by the force and cross sectional area on which the force is acting (surface area). In reality, we may have a number of stresses acting on a surface and the magnitude of each will depend on the orientation of the force relative to the surface area. Consider a forces, ΔF acting on a body with a cross sectional area, A as illustrated in Figure 2.6. The force can be resolved into x, y and z directions such that:

$$\Delta F = \Delta F_x + \Delta F_y + \Delta F_z \tag{2.6}$$

If θ_x, θ_y and θ_z are the angles between ΔF and x, y and z respectively, applying results in equation (2.5) we have:

$$\sigma_{nx} = \lim_{\Delta A \to 0} \frac{\Delta F \cos \theta_x}{\Delta A} \tag{2.7}$$

$$\sigma_{ny} = \lim_{\Delta A \to 0} \frac{\Delta F \cos \theta_y}{\Delta A} \tag{2.8}$$

$$\sigma_{nz} = \lim_{\Delta A \to 0} \frac{\Delta F \cos \theta_z}{\Delta A} \tag{2.9}$$

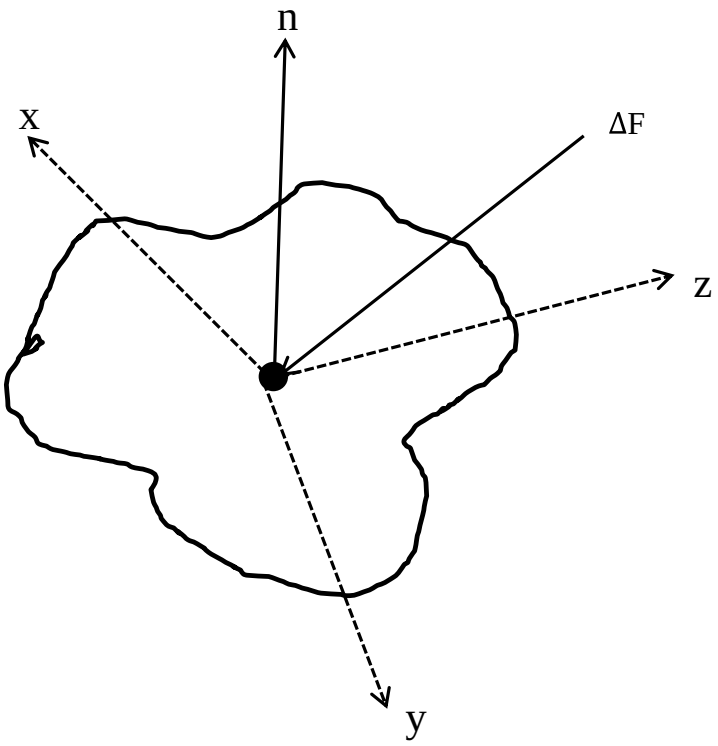

Figure 2.6: Illustration of decomposition of stress in x,y and z directions.

A special case may arise when ΔF is resolved parallel and perpendicular to the plane as shown in Figure 2.7. The resultant stresses are

$$\sigma_{xx} = \lim_{\Delta A \to 0} \frac{\Delta F \cos \theta_x}{\Delta A} = \sigma_x \tag{2.10}$$

$$\sigma_{xy} = \lim_{\Delta A \to 0} \frac{\Delta F \cos \theta_y}{\Delta A} = \tau_{xy} \tag{2.11}$$

$$\sigma_{xz} = \lim_{\Delta A \to 0} \frac{\Delta F \cos \theta_z}{\Delta A} = \tau_{xz} \tag{2.12}$$

τ_{xy} and τ_{xy} are called the shear stresses.

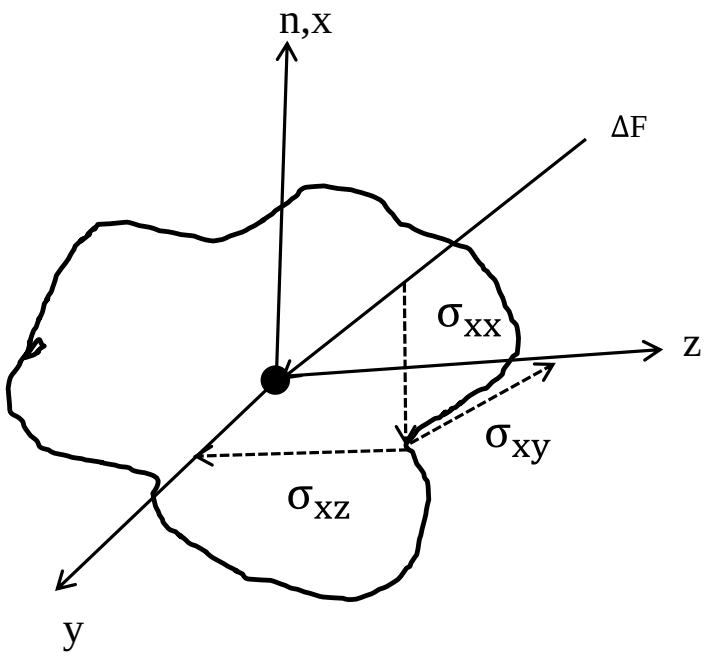

Figure 2.7: Illustration of decomposition of stress parallel and perpendicular to the plane.

2.2.1.1 *Stress Analysis in Two Dimensions*

Many design problems of practical interest encountered in rock mechanics can be treated satisfactorily in two dimensions in which only the stresses or strains in a single plane need to be considered. The two dimensional state of stress is illustrated in Figure 2.8, where σ_x and σ_y are normal stresses and τ_{xy} and τ_{yx} are the shear stresses.

One derives $\tau_{xy} = \tau_{yx}$ by imposing force equilibrium on the square surface (any other solution would cause rotation of the block). Thus in two dimensions, the stress state at a point can fully be defined by these three independent stress components. The normal and shear stress components σ and τ acting on any plane defined by the orientation θ can be calculated by adding the contributions of the various stress components. This gives:

$$\sigma'_x = \left[\frac{(\sigma_x + \sigma_y)}{2}\right] + \left[\frac{(\sigma_x - \sigma_y)}{2}\right] \times \cos 2\theta + \tau_{xy} \sin 2\theta \qquad (2.13)$$

$$\sigma'_y = \left[\frac{(\sigma_x + \sigma_y)}{2}\right] - \left[\frac{(\sigma_x - \sigma_y)}{2}\right] \times \cos 2\theta - \tau_{xy} \sin 2\theta \qquad (2.14)$$

and

$$\tau = -\left[\frac{(\sigma_x - \sigma_y)}{2}\right] \times \sin 2\theta + \tau_{xy} \cos 2\theta \qquad (2.15)$$

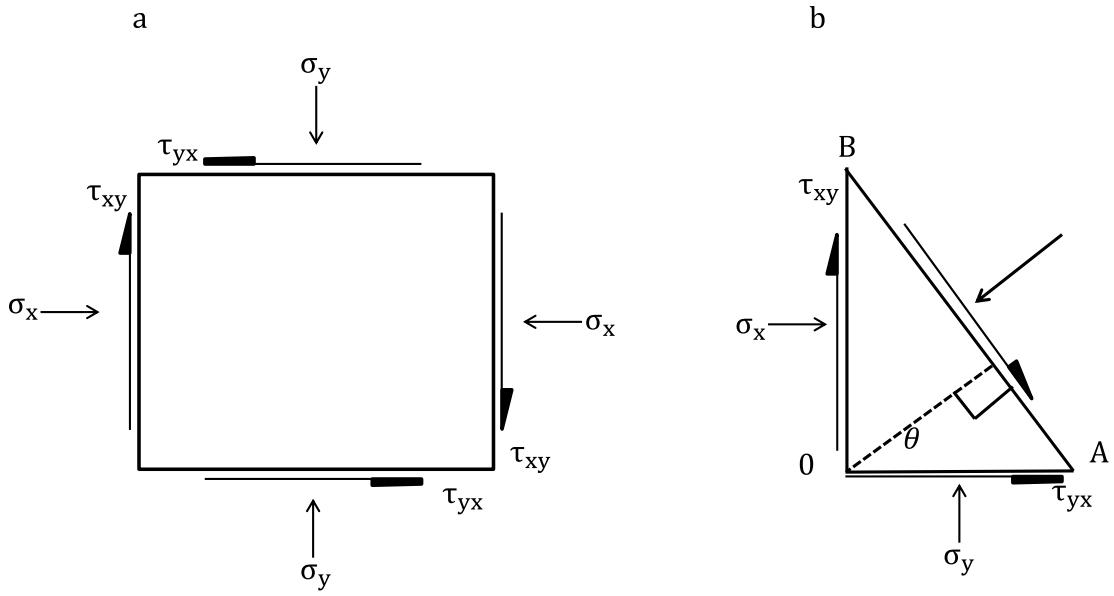

Figure 2.8 Representation of stress in two dimensions.

Equation (2.13) to equation (2.15) enable the stresses acting on any axis of a given orientation through a point to be solved (Figure 2.9). This is known as a Mohr circle. The position on the circle depends on the angle of rotation θ i.e. on the orientation of the surface element: the circle is transcribed at an angle 2θ in clockwise direction.

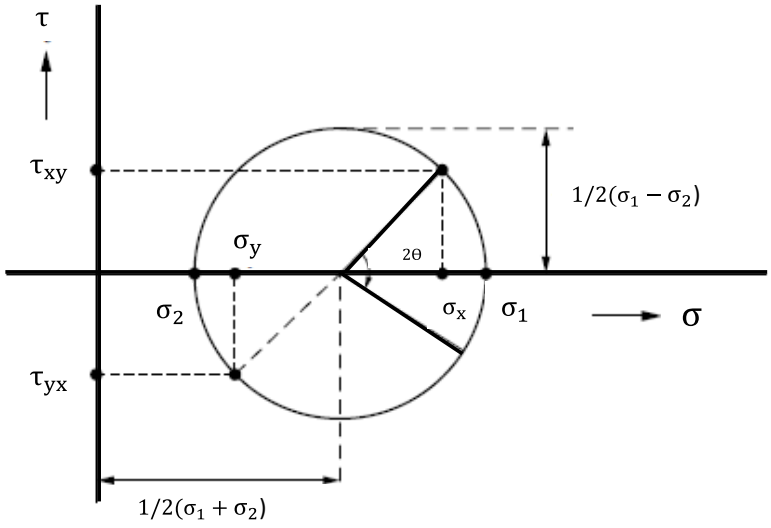

Figure 2.9: Representation of stress in Mohr circle.

There are two points where the shear stresses are zero solutions based on the orientation angle. The corresponding normal stresses are called the principal stresses as indicated in Figure 2.8b. From these stresses the maximum and minimum principal stresses, are denoted σ_1 and σ_2 ($\sigma_1 > \sigma_2$) which is given by the expression:

$$\sigma_{1,2} = \frac{1}{2}(\sigma_x + \sigma_y) \pm \sqrt{\tau_{xy}{}^2 + \frac{1}{4}(\sigma_x - \sigma_y)^2} \qquad (2.16)$$

and the principal angle is:

$$\tan 2\theta = \frac{2\tau_{xy}}{(\sigma_x - \sigma_y)} \qquad (2.17)$$

2.2.1.2 *Stress Analysis in Three Dimensions*

For the three dimensional case, the complete state of stress requires the normal and shear stress components described on three mutually perpendicular surface elements as illustrated in Figure 2.10.

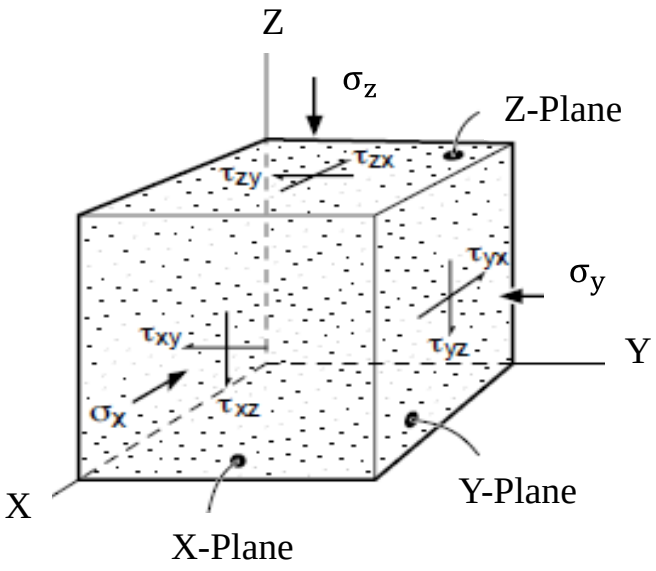

Figure 2.10: Representation of stress in three dimensions.

The stress state at a point is represented by nine components which constitute the so-called stress tensor. This is generally represented as σ_{ij} where i represents x, y and z planes and j represents the three stress directions. The normal stresses are σ_x, σ_y and σ_z, while the shear stresses are $\tau_{xy}, \tau_{xz}, \tau_{yx}, \tau_{yz}, \tau_{zx}$ and τ_{zy} (see Figure 2.10). The normal and shear stress components form the stress tensor and are often presented in matrix form as follows:

$$\sigma_{ij} = \begin{bmatrix} \sigma_x & \tau_{xy} & \tau_{xz} \\ \tau_{yx} & \sigma_y & \tau_{yz} \\ \tau_{zx} & \tau_{zy} & \sigma_z \end{bmatrix} \qquad (2.18)$$

The stresses shown in Figure 2.10 are the result of forces acting on the cube. The cube will be stationary only if the stresses are in equilibrium. If we consider the stresses acting

in the x direction they must add up to zero, otherwise the cube would start to move off in the x direction etc. In this manner one derives: $\tau_{xy} = \tau_{yx}, \tau_{xz} = \tau_{zx}$ and $\tau_{yz} = \tau_{zy}$. Thus, the stress state in three dimensions is fully described by six independent stress components: three normal and three shear stresses.

The cube of Figure 2.10 can be rotated such that the shear stresses acting on its surfaces vanish. The normal stresses at this orientation are the principal stresses denoted by σ_1, σ_2 & σ_3. In the general case these principal stresses will not be equal; one can distinguish a maximum, an intermediate and a minimum principal stress. Knowing the magnitude and orientation of the three principal stresses allows one to calculate the normal and shear stress for any surface orientation.

2.2.1.3 *Stress Invariants*

Whenever the coordinate axes change, the six stress components change too. However, there are specific combinations of the stress components independent of the coordinate axes. These are referred to as stress invariants. The three common stress invariants are:

$$I_1 = \sigma_M = (\sigma_x + \sigma_y + \sigma_z)/3 \quad (2.19)$$

$$I_2 = \sigma_M = (\sigma_x + \sigma_y + \sigma_z)/3 \quad (2.20)$$

$$I_3 = \sigma_x\sigma_y\sigma_z + 2\tau_{xy}\tau_{xz}\tau_{yz} - (\sigma_x{\tau^2}_{yz} + \sigma_x{\tau^2}_{yz} + \sigma_y{\tau^2}_{yz}) \quad (2.21)$$

2.2.2 Strain

The mechanical response of a body of rock to a change in loading conditions from an initial state to a final state is characterised by displacements which results in change in size and shape at each location called strain. The displacement can be composed of changes in length, volume and angle between different sections of the rock. Thus, strain is the deformation of a rock as a result of applied stress.

2.2.2.1 *Strain Analysis in Two Dimension*

Figure 2.11 illustrates changes in shape of an element acted upon by stress in two dimensions. The shape changes are described by two types of strain. These are called normal and shear strain, corresponding to changes of length and orientation respectively. The displacement component in the x direction is denoted by u and displacement component in the y direction denoted by v. For the normal strain, given displacement components u and v in the x- and y-direction, one derives:

$$\varepsilon_x = -\frac{\partial u}{\partial x} \quad (2.22)$$

$$\varepsilon_y = -\frac{\partial v}{\partial y} \qquad (2.23)$$

The sign convention is that a positive normal strain corresponds to shortening (contraction) and a negative normal strain reflects stretching (extension).

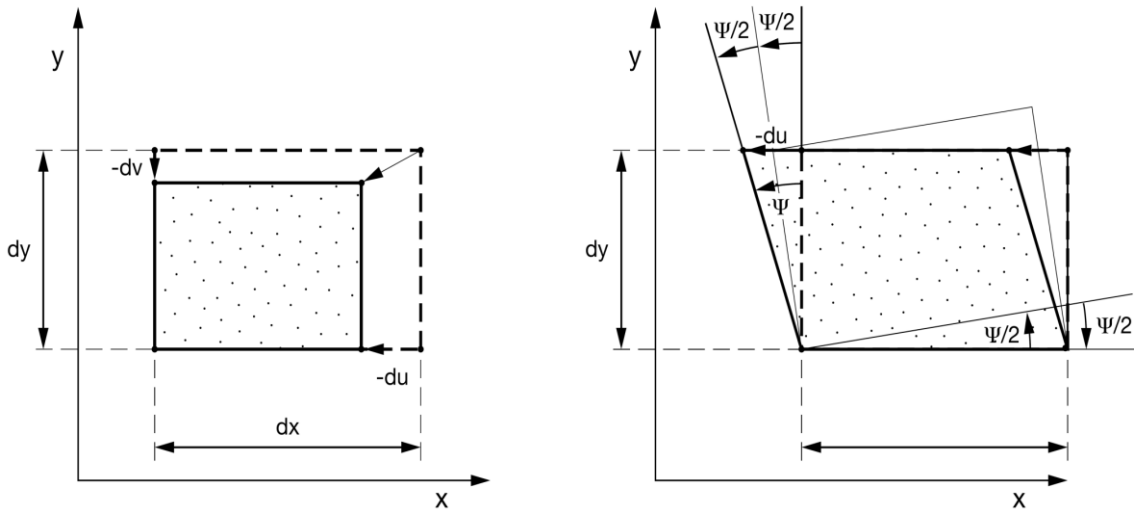

a) Normal strain b) Shear strain

Figure 2.11: Representation of normal and shear strain in two dimensions.

The other strain is the shear strain which describes the shape change associated with the relative rotation of two initially perpendicular line elements. The shear strain is described by rotation over an angle $\psi/2$ as:

$$\Gamma_{xy} = \Gamma_{yx} = \frac{1}{2}\tan\psi \qquad (2.24)$$

where Γ_{xy} characterises the relative rotation of the x-element and Γ_{yx} characterises the relative rotation of the y-element. A positive shear strain indicates an increase of the angle between the x- and y-elements.

$$\Gamma_{xy} = -\frac{1}{2}\left(\frac{\partial u}{\partial x} + \frac{\partial v}{\partial y}\right) \qquad (2.25)$$

Strain is a tensor which, in two dimensions, is fully defined by three independent strain components: ε_x, ε_y and Γ_{xy}. The strain components depend on the orientation of the line elements just like the stress components depend on the orientation of the surface elements. There exist two perpendicular axes that are characterised by zero shear strain. The normal strains along the axes are called principal strains denoted ε_1 and ε_2 with $\varepsilon_1 > \varepsilon_2$. The change of strain components with rotation of the axes can be expressed in a

similar manner as the change of stress components (equations (2.13), (2.14), (2.15) and (2.16)). The maximum shear strain occurs for two elements oriented 45° with respect to the maximum and minimum principal strain directions.

2.2.2.2 *Strain Analysis in Three Dimension*

Generally, as in the case with stress in three dimensions, nine components of strain exist at a point. However, since it possible to show that the strain matrix is symmetric: $\Gamma_{xy} = \Gamma_{yx}$, $\Gamma_{xz} = \Gamma_{zx}$ and $\Gamma_{yz} = \Gamma_{zy}$, the state of strain can be fully defined by six strain components: ε_x, ε_y, ε_z, Γ_{xy}, Γ_{xz} and Γ_{yz}. The corresponding strain tensor is represented in a matrix form as:

$$\begin{bmatrix} \varepsilon_x & \Gamma_{xy} & \Gamma_{xz} \\ \Gamma_{yx} & \varepsilon_y & \Gamma_{yz} \\ \Gamma_{zx} & \Gamma_{zy} & \varepsilon_z \end{bmatrix} \tag{2.26}$$

The axes can be rotated such that the shear strains vanish i.e. the relative rotation of the axes during deformation is zero. The corresponding normal strains are the principal strains denoted as ε_1, ε_2 and ε_3 where $\varepsilon_1 > \varepsilon_2 > \varepsilon_3$. Knowing the magnitude and orientation of the principal strains allows one to calculate the normal and shear strain for any orientation of axes. The change in volume of element is described by the volumetric strain, ε_v. Assuming small strains one calculates:

$$\varepsilon_v = \varepsilon_x + \varepsilon_y + \varepsilon_z = \varepsilon_1 + \varepsilon_2 + \varepsilon_3 \tag{2.27}$$

A positive volumetric strain indicates volume reduction.

The volumetric strain does not change with change in the coordinate axes, making it an invariant of strain. Similar to the stress invariants of equations (2.19) - (2.21), other strain invariants are derived as:

$$J_2 = -\left(\varepsilon_x\varepsilon_y + \varepsilon_y\varepsilon_z + \varepsilon_z\varepsilon_x\right) + \Gamma^2{}_{xy} + \Gamma^2{}_{yz} + \Gamma^2{}_{xz} \tag{2.28}$$

$$J_3 = \varepsilon_x\varepsilon_y\varepsilon_z + 2\Gamma_{xy}\Gamma_{yz}\Gamma_{xz} - \varepsilon_x\Gamma^2{}_{yz} + \varepsilon_y\Gamma^2{}_{xz} + \varepsilon_z\Gamma^2{}_{xy} \tag{2.29}$$

2.2.3 Composite Stress-Strain Curve

The stress-strain curve is commonly used to show the relationship between stress and strain. Figure 2.12 displays a typical stress-strain behaviour observed during confined compression testing. The graph shows the axial stress, σ_a the radial stress, σ_r versus the axial strain, ε_a. At low axial stress deformation is more or less elastic and characterised by a constant or increasing slope of the axial stress versus axial strain curve. During the initial stage of loading, the rock "stiffens up". This is a non-linear regime due to closure of pre-existing pores. This part of the curve is more important in very porous rocks than

crystalline or low porosity rocks. Upon increased loading, elastic compression of constituent grains and fragments will dominate the stress-strain behaviour. The coefficient of proportionality, E is the elastic modulus also known as the Young's modulus. This represents a linear relationship where if the load is removed the rock will return to its original shape. Therefore, elastic modulus can be interpreted as the measure of the rock "stiffness' or a parameter expressing the resistance of the rock to deform under a given loading condition.

Towards the end of the elastic curve, most rock will become damaged with potential grain cracking and limited opening of void space. The rock enters the region of strain hardening accompanied by dilatancy. Crack growth is approximately stable, i.e. keeping pace with the increased load. The onset of this type of deformation is called the elastic limit or yield stress, σ_y. Where this point occurs, expressed as percentage of the maximum load, depends on rock type but also on loading rate. The yield stress is best identified from the reduction of the slope of the axial stress versus axial strain curve. Deformation of the rock after yield stress is permanent. Even after unloading some deformation will be retained and the sample will not regain its original shape.

As compression continues, the axial stress typically reaches a maximum or failure stress, σ_f. This is known as the peak stress or compressive strength. A further increase of axial strain leads to a reduction in axial stress as the sample loses its load bearing capacity. After peak stress the deformation is characterised by strain softening. Due to the propagation and linkage of microcracks, arrays of larger cracks and ultimately fractures will form. Further deformation of the sample becomes a balance between the load applied and the frictional resistance of the fractures in the rock. When load is continually being applied, potentially large displacement along coalescing cracks can be accommodated. The stress-strain curve flattens to a horizontal constant slope, which is called the residual strength.

The stress-strain response between yield and failure is denoted as plastic-hardening since plastic strain increases the load bearing capacity. The post-peak behaviour is referred to as plastic-softening since the sustainable stress level decreases as plastic strain progresses.

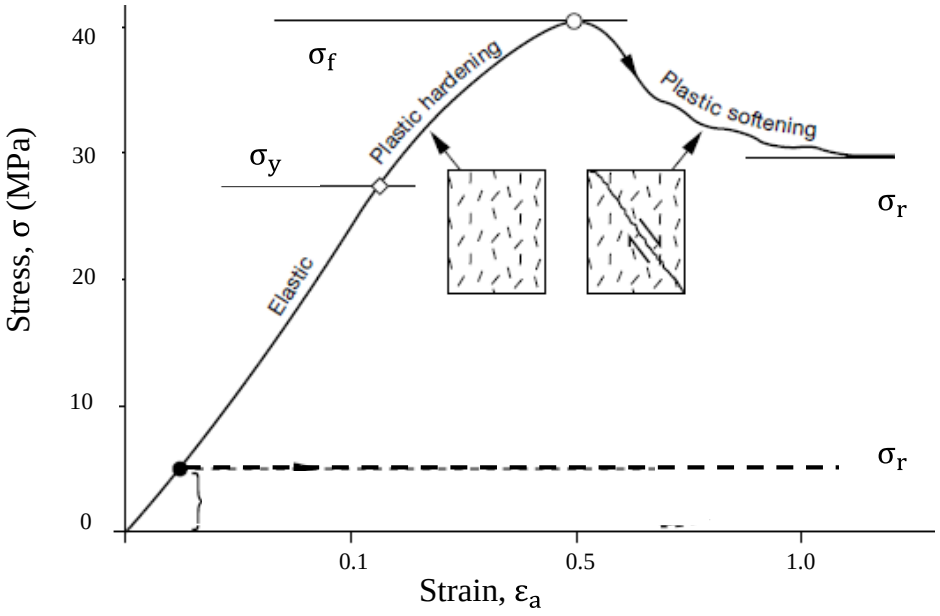

Figure 2.12: Composite stress - strain curve showing basic terminology.

2.2.4 Linear Elastic Deformation and Elastic Parameters

The elastic path of the stress-strain curve discussed above can be considered to be approximately linear. This relation is known as Hooke's Law. The slope of the stress-strain curves is used to calculate the elastic modulus, E and Poisson's ratio, ν:

$$E = \frac{d\sigma_a}{d\varepsilon_a} \tag{2.30}$$

$$\nu = -\frac{d\varepsilon_r}{d\varepsilon_a} \tag{2.31}$$

In materials that obey Hooke's Law, deformation is linearly proportional to the stress. The generalised Hooke's Law for a three dimensional state of stress and strain in a homogeneous and isotropic material can be shown to be:

$$\varepsilon_x = \frac{1}{E}\left[\sigma_x - \nu(\sigma_y + \sigma_z)\right], \qquad \gamma_{xy} = \frac{\tau_{xy}}{2G} \tag{2.32}$$

$$\varepsilon_y = \frac{1}{E}\left[\sigma_y - \nu(\sigma_x + \sigma_z)\right], \qquad \gamma_{xz} = \frac{\tau_{xz}}{2G} \tag{2.33}$$

$$\varepsilon_z = \frac{1}{E}\left[\sigma_z - \nu(\sigma_x + \sigma_y)\right], \qquad \gamma_{yz} = \frac{\tau_{yz}}{2G} \tag{2.34}$$

where E, ν and G are the elastic modulus, Poisson's ratio, and shear modulus respectively.

In case of loading in one direction, the elastic modulus characterises the rock shortening in the direction of load, while Poisson's ratio describes the expansion in lateral direction. Linear-elastic deformation is fully described by any combination of two independent parameters as G is related to E and ν via:

$$G = \frac{E}{2(1+\nu)} \tag{2.35}$$

Summation of equations (2.32) - (2.34) shows that volumetric strain, ε_v only depends on the mean stress, $\sigma_m = (\sigma_x + \sigma_y + \sigma_z)/3$:

$$\varepsilon_v = \frac{\sigma_m}{K} \tag{2.36}$$

where K is the bulk stiffness which is related to E and ν via:

$$K = \frac{E}{3(1-2\nu)} \tag{2.37}$$

The inverse of K is the bulk compressibility, $C_b = 1/K$.

Therefore bulk compressibility from elastic constants is given as:

$$C_b = \frac{1}{E} \times 3(1-2\nu) \tag{2.38}$$

The six stress-strain relations in equation (2.32) to equation (2.34), can be rewritten and express in terms of the strain. Thus:

$$\sigma_x = \frac{\nu E}{(1+\nu)+(1-2\nu)}\varepsilon_v + \frac{E}{1+\nu}\varepsilon_x \tag{2.39}$$

$$\sigma_y = \frac{\nu E}{(1+\nu)+(1-2\nu)}\varepsilon_v + \frac{E}{1+\nu}\varepsilon_y \tag{2.40}$$

$$\sigma_z = \frac{\nu E}{(1+\nu)+(1-2\nu)}\varepsilon_v + \frac{E}{1+\nu}\varepsilon_z \tag{2.41}$$

$$\tau_{xy} = \frac{E}{2(1+\nu)}\gamma_{xy}, \quad \tau_{yz} = \frac{E}{2(1+\nu)}\gamma_{yz}, \quad \tau_{zx} = \frac{E}{2(1+\nu)}\gamma_{zx} \tag{2.42}$$

The quantity $\nu E/(1+\nu)+(1-2\nu)$ is known as Lame's constant and is denoted by λ. Equation (2.39) through equation (2.42) can be rewritten, using λ and G as:

$$\sigma_x = \lambda\varepsilon_v + 2G\varepsilon_x, \quad \tau_{xy} = G\gamma_{xy} \tag{2.43}$$

$$\sigma_y = \lambda\varepsilon_v + 2G\varepsilon_y, \quad \tau_{yz} = G\gamma_{yz} \tag{2.44}$$

$$\sigma_z = \lambda\varepsilon_v + 2G\varepsilon_z, \quad \tau_{zx} = G\gamma_{zx} \tag{2.45}$$

2.2.5 Dynamic Equivalents of Elastic Parameters

The linear-elastic relationship discussed in section 2.2.4 refers to static rock deformation. On the other hand, because the dynamic response of rock materials to time harmonic loading is closely related to and controls the propagation of acoustic waves, a fundamental connection between rock acoustics and rock mechanics exists (Fjaer et al., 2008). In an ideal elastic medium, these two methods should yield the same result. However, rock are not ideal elastic materials, their stress-strain curves show non-linearity, hysteresis, and sometimes permanent deformation. The presence of porosity cause strain amplitude and frequency dependency on the elastic coefficient. A detailed overview and literature review can be found in Fjaer et al. (2008) and Cheng et al. (1992).

The propagation of compressional acoustic waves occurs at a velocity V_p or, equivalent, a transit time (slowness) $\Delta t_p (= \frac{1}{V_p}$, p stands for primary referring to first arrival). Likewise shear wave propagation is expressed in terms of velocity V_s or transit time (slowness) $\Delta t_s (= \frac{1}{V_s}$, s stands for secondary referring to second arrival). The compressional and shear wave velocities are related to the dynamic elastic modulus, E_d Poisson's ratio, ν_d and shear modulus, G_d as:

$$E_d = \frac{\rho_b V_p^2 (3{V_p}^2 - 4{V_s}^2)}{({V_p}^2 - {V_s}^2)} \tag{2.46}$$

$$\nu_d = \frac{({V_p}^2 - 2{V_s}^2)}{2({V_p}^2 - {V_s}^2)} \tag{2.47}$$

$$G_d = \rho_b V_s^2 \tag{2.48}$$

where ρ_b is the bulk density and the subscript d indicates the dynamic equivalent of E and ν.

The bulk compressibility is given as:

$$C_b = \frac{1}{\rho_b V_p^2 - \frac{4}{3}\rho_b V_s^2} \tag{2.49}$$

2.2.6 Total and Effective Stress

Sandstones in nature generally exist in a multiphase system comprising of a skeletal framework and pore spaces which may be filled with gas, water or oil. The presence of fluids in the system will present a mechanical impact. In the subsurface, a portion of the total stress acting on rock is supported by the pressure of the fluid contained in the pores.

The remainder is carried by the rock matrix and is called the effective stress. The concept of effective stress is illustrated in Figure 2.13 and can be expressed as:

$$\sigma' = \sigma - p \tag{2.50}$$

where σ' is the effective stress, σ is the overburden stress and p denotes the pore pressure.

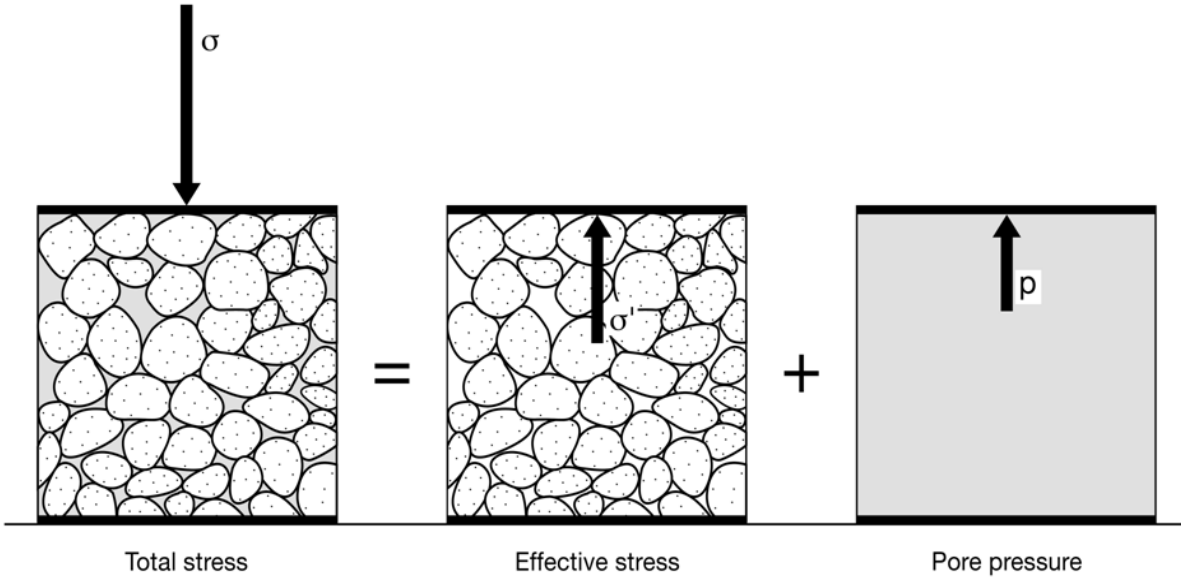

Figure 2.13: Concept of effective stress.

Equation (2.50) is called Terzaghi's effective stress law and was originally designed for saturated soil materials (Terzaghi, 1923). The relationship has been verified for a wide variety of porous rock by Skempton (1961) from which he concluded that effective stress is independent of granular contact. Terzaghi (1923) observed that a change in pore pressure produces practically no volume change and has practically no influence on the stress condition for failure in porous rocks, and concluded that deformation and failure are controlled exclusively by effective stresses.

The deformation of rock material is largely due to the effective stress as defined above. However, the fluid pressure contributes to the deformation as well since the hydrostatic pressure slightly compresses the grain material. This contribution is very small and is usually neglected. However, in petroleum engineering, this contribution has been incorporated in the effective stress formulation via Biot's coefficient (Biot, 1941) as follows:

$$\sigma' = \sigma - \alpha p \tag{2.51}$$

where α is Biot's constant.

This implies that the rock skeleton carries the part σ' of the total external stress σ, while the remaining part, αp is carried by the fluid in the porous medium. The Biot's coefficient is given by the ratio between the bulk rock stiffness (K) and the grain bulk stiffness (K_s).

$$\alpha = 1 - \frac{K}{K_s} \tag{2.52}$$

2.2.7 Reservoir *In Situ* Stress

Reservoir rocks at depth are subjected to the effect of *in situ* stresses. The *in situ* stresses are generally described in terms of the magnitude and direction of the three principal stresses (Hudson and Cooling, 1988). For most sandstone reservoirs, the three principal stresses will be different, with the vertical principal stress, σ_v which equals the weight of the overburden, being the largest, and the two unequal horizontal stresses, σ_H being the maximum horizontal stress, and σ_h being the minimum horizontal stress.

The vertical stress is largely determined by gravitational loading and is adequately described by the weight of the overburden. Hence, overburden stress, σ_v at depth, h is simply the integral of the rock density over the burial depth and is given as:

$$\sigma_v = \int_0^h \rho g h \tag{2.53}$$

where h is the burial depth, g is the acceleration due to gravity and ρ is the formation density variation with depth. Equation (2.53) is a simplification since other factors such as mountains and salt domes may cause slight deviations from the gravitational trend. However, this assumption is considered acceptable for most petroleum engineering applications.

The horizontal *in situ* stresses in the subsurface are influenced by a combination of processes. The most significant ones are: burial or uplift, tectonics or stress relaxation, pressure inflation or depletion, and heating or cooling. The magnitude and orientation of the *in situ* horizontal stresses are determined from field techniques e.g. micro/minifrac and formation strength test and laboratory techniques e.g. anelastic strain recovery.

2.3 Failure Criteria

The fundamental principle of any laboratory experiment on the mechanical strength of rock is that applied stresses to the rock sample should be able to simulate the *in situ* stresses (Brady and Brown, 1985). The combination of the applied stresses in relation to the rock failure limit, determines the extent to which the rock will deform or fail. The

standard way of estimating the strength of rocks under various loading conditions is using a failure criterion. A failure criterion is a mathematical equation used to check whether failure will occur under combinations of stresses predicted at a particular location. Generally, the word "failure" is defined as the breakage/fracturing that occurs when rock is stressed beyond its limit of strength.

Numerous rock failure criteria have been proposed including Mohr-Coulomb criterion (Lambe and Whitman, 1969, Jaeger et al., 2007), Hoek-Brown criterion (Hoek and Brown, 1980), Griffith criterion (Lambe and Whitman, 1969, Griffith, 1924), Drucker - Prager criterion (Drucker et al., 1951) and Mogi criterion (Mogi, 1971). The Griffith, Mohr-Coulomb and Hoek-Brown failure criteria are the most popular and commonly used criteria and have been adopted for use in this thesis since their parameters correspond to standard laboratory testing technique.

2.3.1 Griffith Criterion

Griffith (1924) postulated that failure of a brittle material is initiated due to tensile stress concentration at the tip of minute thin microcracks abundant in most rocks due state of impurities. The criterion is based on mechanics of brittle fracture, using elastic strain energy concept. A balance exists between strain energy and the surface energy within microcracks and the material structure. For a crack to propagate, sufficient energy must be released to provide the necessary new surface energy. The rate of strain energy release must be equal to or greater than the required surface energy increase. According to Griffith, failure would occur when the local stress at the most critical or most optimally oriented flaw reached a critical value that is characteristic for the material.

Under compression, elliptical crack will propagate from the point of maximum tensile stress concentration. Griffith obtained the following criterion for crack extension in plane compression as:

$$(\sigma_1 - \sigma_2)^2 - 8\sigma_t(\sigma_1 + \sigma_2) = 0 \qquad \text{if } \sigma_1 + 3\sigma_2 > 0 \tag{2.54}$$

and

$$\sigma_2 + \sigma_t = 0 \qquad \text{if } \sigma_1 + 3\sigma_2 < 0 \tag{2.55}$$

where σ_t is the uniaxial tensile strength of the uncracked material.

Murrell (1958) expressed this criterion in terms of the shear stress (τ) and normal stress (σ_n) acting on the plane containing the major axis of the crack (Figure 2.14) as:

$$\tau^2 = 4\sigma_t(\sigma_n + \sigma_t) \tag{2.56}$$

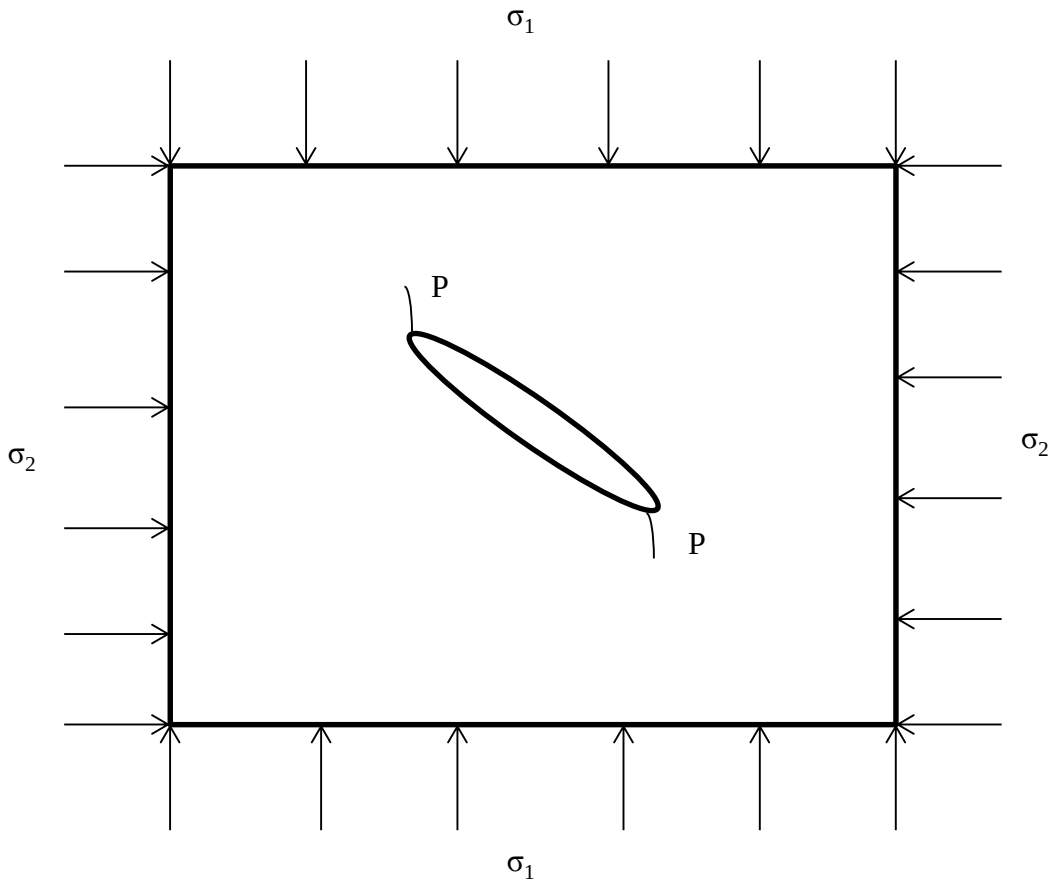

Figure 2.14: Griffith Crack model for plane compression (after Brady and Brown, 1985).

The failure envelopes given by equation (2.54) to equation (2.56) are shown in (Figure 2.15). This criterion predicts that the uniaxial compressive strength value, $\sigma_0 = 8\sigma_t$ from equation (2.56) by setting $\sigma_2 = 0$ (Brady and Brown, 1985).

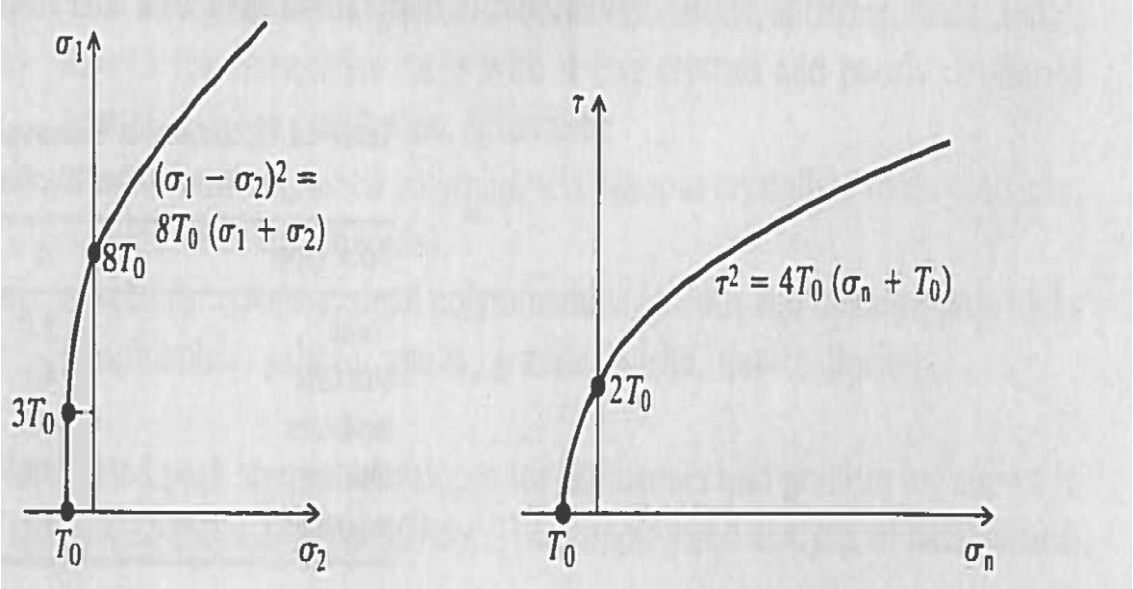

Figure 2.15: Griffith envelopes for crack extension in plane compression (after Brady and Brown, 1985).

2.3.2 Mohr-Coulomb Criterion

The Mohr-Coulomb failure criterion is one of the most commonly used strength criterion due to its simple mathematical expression and physical meaning of the material parameters. The Mohr-Coulomb criterion assumes that shear failure occurs when the shear stress along a plane exceeds the friction strength. According to the Mohr-Coulomb criterion the maximum shear stress that can be sustained on a plane is the sum of a constant cohesion component and a frictional component proportional to the normal stress acting on that plane:

$$\tau = c + \mu * \sigma \tag{2.57}$$

The failure envelope corresponding to the Mohr-Coulomb criterion in the (τ, σ) plane is illustrated in Figure 2.16 where the angle of internal friction, ϕ relates to the coefficient of friction, μ as:

$$\tan\phi = \mu \tag{2.58}$$

The position where the failure line coincides with the Mohr's circle is characterised by the angle 2β as shown in Figure 2.16 and the shear stress at this point is given as:

$$|\tau| = \frac{1}{2}(\sigma_1 - \sigma_3)\sin 2\beta \tag{2.59}$$

and the normal stress is expressed as:

$$\sigma = \frac{1}{2}(\sigma_1 + \sigma_3) + \frac{1}{2}(\sigma_1 - \sigma_3)\cos 2\beta \tag{2.60}$$

and that β and ϕ are related by:

$$\phi + \frac{\pi}{2} = 2\beta \tag{2.61}$$

One derives:

$$\beta = \frac{1}{4}\pi + \frac{1}{2}\phi \tag{2.62}$$

However, strength test data are usually presented in the (τ, σ) plane. The corresponding stress states are highlighted on the Mohr circles in Figure 2.16.

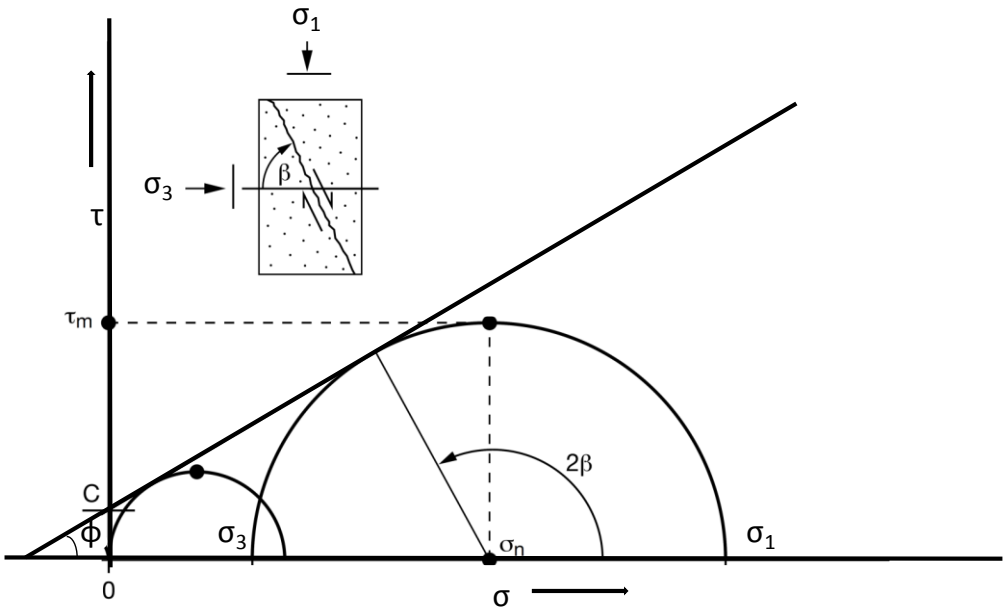

Figure 2.16: Illustration of Mohr-Coulomb criterion in the (τ, σ) plane (after Fjær et al., 2008).

The Mohr-Coulomb criteria can also be expressed in principal stresses as:

$$\sigma_1 = 2C\frac{\cos\phi}{(1-\sin\phi)} + \sigma_3\frac{(1+\sin\phi)}{(1-\sin\phi)} \tag{2.63}$$

where uniaxial compressive strength is the term:

$$\sigma_0 = 2C\frac{\cos\phi}{(1-\sin\phi)} \tag{2.64}$$

the cohesion, C can be obtained from:

$$C = \sigma_0\frac{(1-\sin\phi)}{2\cos\phi} \tag{2.65}$$

In this case one can plot directly the principal stresses (e.g. Figure 2.17) which also fall on a linear trend.

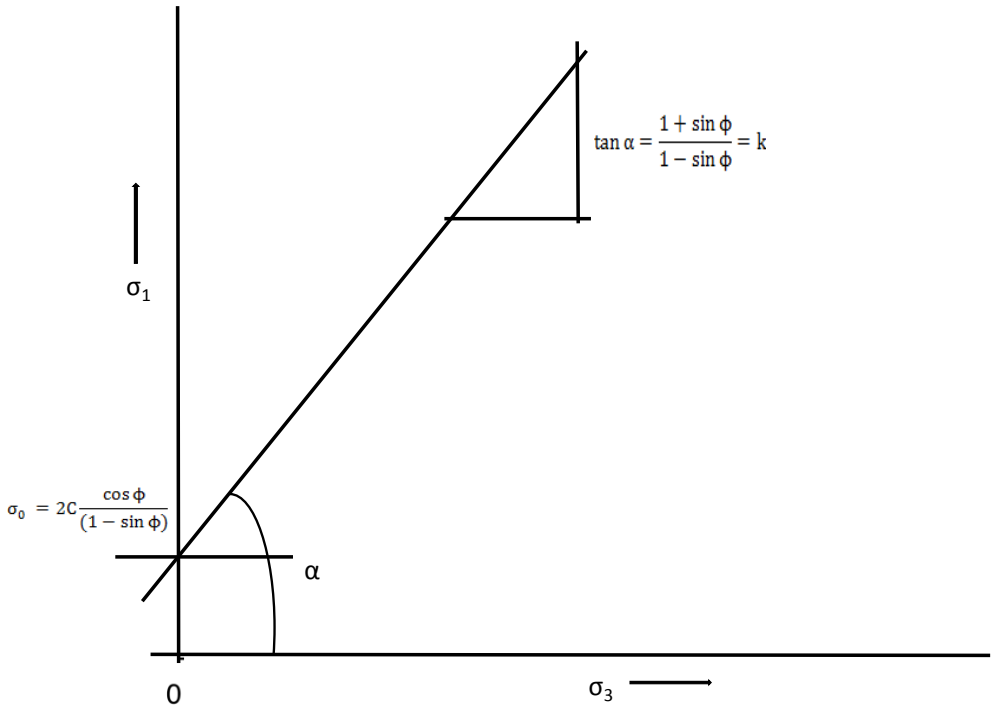

Figure 2.17: Illustration of Mohr-Coulomb criterion in the (σ_1, σ_3) plane (after Fjær et al., 2008).

σ_0 is the uniaxial compressive strength and k is the slope of line, where

$$\tan\alpha = \frac{1+\sin\phi}{1-\sin\phi} = k \tag{2.66}$$

where $\tan\alpha$ is the triaxial stress factor usually denoted as k.

$$\sin\phi = \frac{k-1}{k+1} \tag{2.67}$$

and ϕ can be obtained as:

$$\phi = \sin^{-1}\frac{k-1}{k+1} \tag{2.68}$$

Thus equation (2.63) can be written as:

$$\sigma_1 = \sigma_0 + k\sigma_3 \tag{2.69}$$

2.3.3 Hoek-Brown Empirical Failure Criterion

The Hoek-Brown criterion is an empirical relationship, which represents the response of fractured rock to stress. Laboratory results of triaxial tests on rocks often show a curved strength envelope (Hoek and Brown, 1980). The Hoek-Brown criterion is a non-linear, empirical relationship which accounts for the curvilinear form observed in the development of strength with increasing confinement in many types of rocks. Hoek and

Brown (1980) found that the peak triaxial strength of a wide range of rock materials could be reasonably represented by the expression:

$$\sigma_1 = \sigma_3 + (m\sigma_0\sigma_3 + s\sigma_0^2)^{1/2} \quad (2.70)$$

Where σ_1 and σ_3 are the major and minor principal stresses respectively, σ_0 the uniaxial compressive strength and m and s are empirical constants, dependant on the characteristics of the rock and the extent to which the rock is broken prior to testing.

Equation (2.70) can be rewritten in the form:

$$y = m\sigma_0 x + \sigma_0 \quad (2.71)$$

where

$x = \sigma_3$, and $y = (\sigma_1 - \sigma_3)$.

2.4 Fracture Mechanics

Fracture mechanics is the study of stress concentration caused by sharp-tipped cracks and the conditions governing the propagation of these cracks. Fracture mechanics theory is used to analyse the relationship among stresses, cracks, and fracture toughness (the resistance of a material to fracturing). The work of Griffith (1921) and Irwin (1958) present a major contribution to fracture mechanics in which the importance of crack as stress concentrator was recognised as being fundamental in controlling brittle fracture. Griffith (1921) suggested a fracture criterion based on energy balance where he assumes that the growth of a crack requires creation of surface energy. Failure occurs when the loss of strain energy is sufficient to provide increase in the surface energy. Due to the difficulty involved in the experimental estimation of the fracture energy, Griffith's work was modified by Irwin (1958) who introduced stress intensity factor, K and fracture toughness, K_{IC} to replace strain energy release rate and surface energy respectively. A brief summary of the major aspects of fracture mechanics is presented in this section which is largely drawn in part from Atkinson (1987).

2.4.1 Fracture Mode

In fracture mechanics, cracks or fractures are usually subdivided into three basic types to explain the different modes of propagation. These are designated as modes I, II and III with respect to reference plane that is normal to a straight-line crack edge as illustrated in Figure 2.18. Cracks that dilate or move perpendicular to the crack plane (symmetric with respect to the x-y and x-z planes) are called Mode I or opening mode. Mode II is term the sliding mode and represents shear displacement in the crack plane in the direction of smallest dimension. Mode III is called the anti-plane shear mode which is

the equivalent of the Mode II shear displacements but now in the direction of the largest crack dimension.

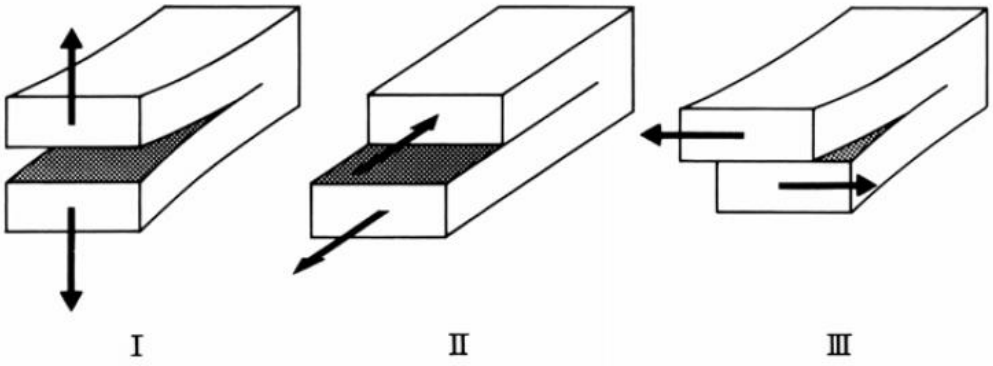

Figure 2.18: Modes of fracture propagation (Atkinson, 1987).

2.4.2 Stress Intensity Analysis and Fracture Toughness

Stress intensity analysis is used to determine the magnitude of applied force to the crack tip and to measure whether the crack will propagate or remain stable as a result of applied force. Although it is clearly acknowledged that non-elastic effects are involved at crack tips in most materials, and that even the elastic behaviour in the most highly stressed regions may be non-linear, the practical analysis of the stress distribution in the neighbourhood of the crack tip is usually done on the basis of the classical linear theory of elasticity. Provided that the region of non-linear elastic behaviour is negligibly small compared to the length of the crack, linear theory of elasticity can be applied to analyse the stress distribution in the crack tip region (Atkinson, 1987). The stress intensity analysis comprises of two stages: an initial analysis of the stress distribution around the crack tip region alone followed by the influence of external applied force and its geometry on the crack tip region. In the case of a homogeneous, linear elastic medium, the stress surrounding the crack tip is proportional to one over the square root of the distance from the crack tip, r. The tensile strength indicates the tensile stress necessary to induce a tensile fracture in intact rock. The tensile stress required to propagate a pre-existing crack may be much smaller than the tensile strength. The reason is the stress concentration at the crack tip. Figure 2.19 shows the situation of a rock sample containing an initial circular crack with radius, r and subject to a far field tensile stress.

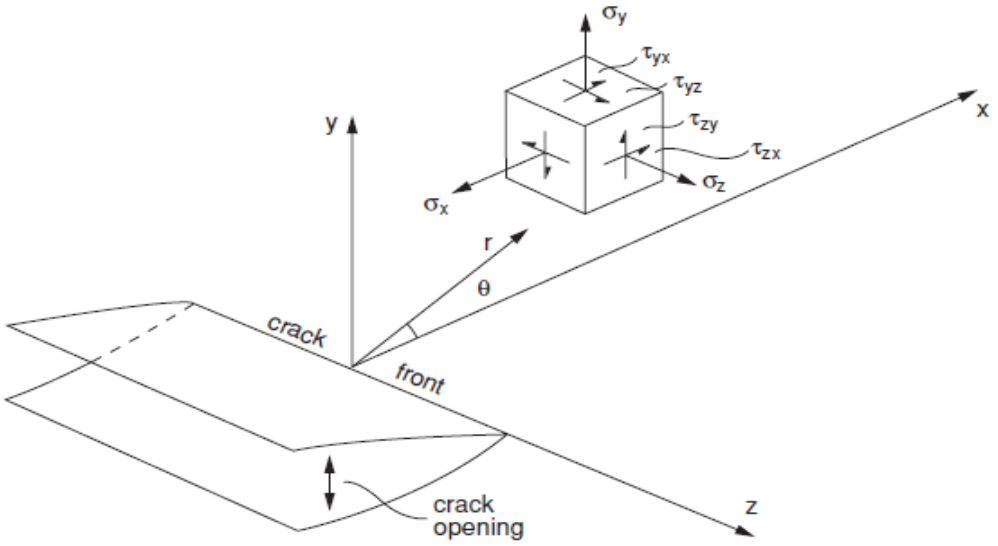

Figure 2.19: The stress field surrounding a crack tip (Atkinson, 1987).

In a homogenous linear elastic material, the stress intensity factor, K is the magnitude of the crack tip stress field for a particular failure mode. The solutions for a mode I loading in a cylindrical coordinates are given by Atkinson (1987) as:

$$\begin{Bmatrix}\sigma_{xx}\\ \sigma_{yy}\\ \sigma_{xy}\end{Bmatrix} = \frac{K_I}{(2\pi)^{1/2}} \begin{Bmatrix}\cos(\theta/2)[1-\sin(\theta/2)\sin(3\theta/2)]\\ \cos(\theta/2)[1-\sin(\theta/2)\sin(3\theta/2)]\\ \sin(\theta/2)\cos(\theta/2)\cos(3\theta/2)\end{Bmatrix} \qquad (2.72)$$

The stress intensity factor is usually given as a subscript depending on the mode of the crack: K_I, K_{II} or K_{III} and is viewed as a material property. Experience has shown that crack propagates when the stress intensity exceeds a critical value called the critical stress intensity factor, also referred to as fracture toughness. Lawn (1993) provided a general expression for crack-tip stress and displacement fields for any mode as:

$$\sigma_{ij} = \frac{K_L}{\sqrt{2\pi r}} f_{ij}(\theta) \qquad (2.73)$$

where K_L is the stress intensity factor (subscript L denote loading mode L = I, II, or III), r is the distance from the crack tip and $f_{ij}(\theta)$ is the bounded function on the angle θ measured from the crack plane (Figure 2.19).

2.4.3 Strain Energy Release Rate

While the crack tip stresses provides a great deal of insight to the fracture process, an alternative method is the "crack extension force" or "strain energy release rate", G which is the loss of energy per unit of new crack separation area formed during an increment of crack extension. Note that the use of the word ‘rate’ here is in reference to the crack

length, not time. So, it is the change of the fracture energy with respect to the crack length, and is independent of time. Interior and surface flaws are found in all rocks. These act as stress magnifiers, raising the effective stress normal to the crack plane. In order for the crack to propagate spontaneously, following Griffith's concept the elastic strain energy must exceed the surface energy of the new crack surfaces. When there is plastic deformation at the crack tip the energy available to propagate the crack may increase by several orders of magnitude. This total energy release rate is given by the symbol, G where the Roman number I, II or III, indicates the way the crack opens. The crack will only propagate when G_I exceeds some critical value G_{IC} i.e. the surface energy where C denotes criticality. For fracture in the three mode of displacement, the crack extension for plane strain and assuming linear elasticity is given by Atkinson (1987) as:

$$G_I = \frac{K_{I^2}(1-\upsilon^2)}{E} \tag{2.74}$$

$$G_{II} = \frac{K_{II^2}(1-\upsilon^2)}{E} \tag{2.75}$$

$$G_{III} = \frac{K_{III^2}}{2\mu} = \frac{K_{III^2}(1-\upsilon^2)}{E} \tag{2.76}$$

where υ is the Poisson's ratio, E the elastic modulus and the μ shear modulus. For plane stress, the factor $(1-\upsilon^2)$ in equations (2.74) and (2.75) is replaced by unity.

2.5 Acquisition of Rock Mechanical Parameters

The rock mechanical parameters presented in sections 2.2 form the basis for majority of rock mechanics applications in petroleum engineering. The method of acquisition of these parameters is of extreme importance as the quality of any rock mechanics analysis cannot exceed the reliability of its input data. Rock deformation shows more variability and heterogeneity than rock stress. Therefore, assessing parameters such as rock strength is more difficult than determining in situ stress. For example, one can estimate the horizontal *in situ* stresses at a certain depth within a factor of two without even drilling a hole given knowledge of the tectonic regime. The unconfined compressive strength at the same depth will not be accurately known within the same factor of two until core material has been tested in the laboratory. The underlying reason is that the *in situ* stress regime is mainly controlled by global processes such as burial, uplift and tectonics, and not by formation lithology. The mechanical behaviour of rock on the other hand is completely governed by its local architecture and mineral composition and therefore changes as its

lithology changes. Thus, rock deformation reflects all the variability and heterogeneity inherent to sedimentary structures.

2.5.1 Core Damage and Representation

Laboratory testing on core samples is the most important source of data for mechanical characterisation of rocks. However, careful planning and quality control during all stages of coring, core handling and storage is considered to be essential in ensuring that recovered core is and remains of good quality. The failure to meet these criteria may result in changes of the rock properties by introducing damage to the core sample.

Core damage is particularly a problem in unconsolidated reservoirs but its effects are also seen in consolidated and poorly consolidated reservoirs. Core damage includes any interaction between the formations which results in changes in the original rock integrity of the core retrieved from the cored interval. This includes coring procedure (associated with factors such as core bit and sleeve design and handling at surface), retrieval and handling techniques due to transport and storage of the core material. Core damage as a result of these factors could ideally be minimised by optimising the coring procedure, through careful planning and quality control during all stages of coring, core handling and storage.

Core damage associated with the reduction of the effective stress or matrix stress as the core is drilled and brought to surface cannot be avoided. Drilling of the core introduces a drastic change of loading conditions within the core material itself, resulting in permanent deformation in as grains and bonds roll, slip, and break (Holt et al., 2000). For example, cracks may close but do not heal. Therefore rock properties such as strength, elastic constants, porosity, resistivity, acoustic velocity and permeability are measured under loading conditions representative of the *in situ* situation. This is achieved by re-applying the *in situ* stresses to the core material. However, the rock stiffness after reloading is typically less than the stiffness *in situ* due to permanent core damage. The core material may appear intact on a macroscopic scale, but could be severely damaged on a microscopic scale due to the stress relief experienced during coring. Microcracks affect rock deformation; this can lead to a discrepancy between laboratory measured and *in situ* properties (Holt and Kenter, 1992). The largest difference is expected at low confining stress; the difference should become negligible at high confining stress since microcracks close at high stress levels.

Although direct laboratory testing of core material provides relevant mechanical data, , the acquisition of core samples from whole reservoir interval is prohibitively expensive

(Ameen et al., 2009). Consequently, most cases the number of representative cores are insufficient for a complete mechanical characterisation across relevant intervals of the reservoir (Holt et al., 2005). A core used for mechanical testing only has a diameter of 1.5''. This means that core tested may not capture all the heterogeneities present in reservoir. Both core damage and representation create difficulties in valid sampling of the rock (e.g. for petrophysical and mechanical measurements) and thus, their effects should consequently be recognised and taken into consideration.

2.6 Stresses around a Wellbore

2.6.1 Drilling Process

The *in situ* principal compressive stresses in an intact formation can be resolved into vertical or overburden stress, σ_v and the two unequal horizontal stresses; the maximum horizontal stress, σ_H and the minimum horizontal stress, σ_h. The process of drilling a hole by removal of the original rock creates a cylindrical cavity (with radius, $r = R_w$) and consequently alters the *in situ* stress state of the formation which leads to redistribution and reorientation of the stresses around the wellbore. In such cases, the stresses around the wellbore is conveniently defined with respect to a cylindrical coordinates, r, θ and z. These stresses are denoted as radial stress σ_r (radial to borehole wall), tangential or hoop stress, σ_θ (circumferential along borehole wall), axial stress, σ_z (along borehole axis), shear stress, $\tau_{\theta z}$ (parallel to borehole wall), shear stress, $\tau_{r\theta}$ and shear stress, τ_{rz}. These stresses are related to the Cartesian coordinate's stresses as:

$$\sigma_r = \frac{1}{2}(\sigma_x + \sigma_y) + \frac{1}{2}(\sigma_x - \sigma_y)\cos 2\theta + \tau_{xy}\sin 2\theta \quad (2.77)$$

$$\sigma_\theta = \frac{1}{2}(\sigma_x + \sigma_y) - \frac{1}{2}(\sigma_x - \sigma_y)\cos 2\theta - \tau_{xy}\sin 2\theta \quad (2.78)$$

$$\sigma_z = \sigma_z \quad (2.79)$$

$$\tau_{r\theta} = \tfrac{1}{2}(\sigma_y - \sigma_x)\sin 2\theta + \tau_{xy}\cos 2\theta \quad (2.80)$$

$$\tau_{rz} = \tau_{xz}\cos\theta + \tau_{yz}\sin\theta \quad (2.81)$$

$$\tau_{\theta z} = \tau_{yz}\cos\theta - \tau_{xz}\sin\theta \quad (2.82)$$

2.6.2 Stresses on the Wellbore Wall

The largest stress concentration for a linear elastic material occurs at the wall of the wellbore wall. Therefore to assess the stress required to induce failure, the stress at the wellbore wall are usually compared against a failure criterion during wellbore stability analysis. For an inclined borehole, the normal and shear stresses that act on the wellbore

wall ($r = R_w$) are functions of inclination and azimuth, besides the far field stresses, pore pressure and hydraulic pressure inside the wellbore. Including the effect of wellbore pressure, and considering compressive stresses and fluid pressure as positive, the effective stresses acting on the wall of wellbore are given as follows:

$$\sigma_r = P_w \tag{2.83}$$

$$\sigma_\theta = \left(\sigma_x^0 + \sigma_y^0\right) - 2\left(\sigma_x^0 - \sigma_y^0\right)\cos 2\theta - 4\tau_{xy}^0 \sin 2\theta - P_w \tag{2.84}$$

$$\sigma_z = \sigma_z^0 - 2\upsilon\left(\sigma_x^0 - \sigma_y^0\right)\cos 2\theta - 4\tau_{xy}^0 \sin 2\theta \tag{2.85}$$

$$\tau_{\theta z} = 2\left(\tau_{yz}^0 \cos\theta - \tau_{zx}^0 \sin\theta\right) \tag{2.86}$$

$$\tau_{rz} = \tau_{r\theta} = 0 \tag{2.87}$$

where σ_y^0 and σ_x^0 are the maximum and minimum *in situ* stress components acting normally to the axis of the wellbore and θ is the angular position around the wall of the wellbore.

2.6.3 Transformation of the Stresses around a Wellbore

In an inclined wellbore or wellbore not aligned with the principal *in situ* stresses, besides the far field stresses, it is necessary to transform the principal stresses into the coordinate frame of the wellbore to obtain *in situ* stress components. This is usually accomplished by mathematically rotating the principal stresses by the use of direction cosines where α is rotated around the z-axis, and i rotated around the y′-axis as shown in Figure 2.20. If the *in situ* stresses are associated with the co-ordinate system x', y', z', it is possible to determine the stresses acting on any other wellbore passing through the same origin but with different orientation (x, y, z).

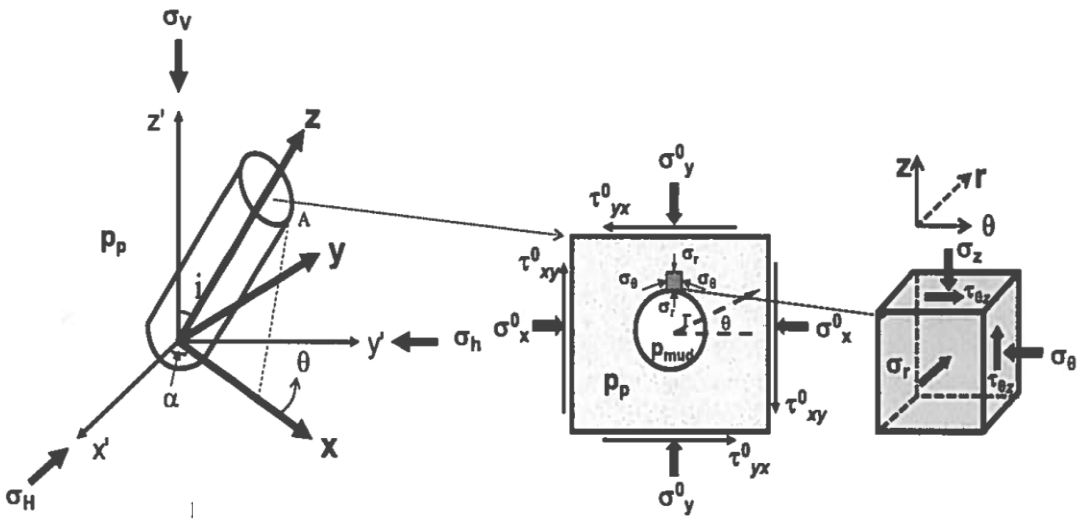

Figure 2.20: Wellbore orientation with respect to far field *in situ* stresses (after Zhang, 2013).

The angles between the rotated wellbore axis and the x, y, z axes are called the 'direction angles' and their cosines are termed the 'direction cosines'. Therefore the transformation can be described mathematically by the direction cosines, where $l_{ij'}$ is the cosine of the angle between i-axis and j′-axis and is given as (Fjaer et al., 2008):

$$\begin{array}{lll} l_{xx'} = \cos\alpha\cos i & l_{xy'} = \sin\alpha\cos i & l_{xz'} = -\sin i \\ l_{yx'} = -\sin\alpha & l_{yy'} = \cos\alpha & l_{yz'} = 0 \\ l_{zx'} = \cos\alpha\sin i & l_{zy'} = \sin\alpha\sin i & l_{zz'} = \cos i \end{array} \quad (2.88)$$

The full set of the direction cosines are then applied to the following set of equations to obtain the transformed rectangular coordinates as:

$$\sigma_x^0 = \sigma_H l^2_{xx'} + \sigma_h l^2_{xy'} + \sigma_v l^2_{xz'} \quad (2.89)$$

$$\sigma_y^0 = \sigma_H l^2_{yx'} + \sigma_h l^2_{yy'} + \sigma_v l^2_{yz'} \quad (2.90)$$

$$\sigma_z^0 = \sigma_H l^2_{z} + \sigma_h l^2_{zy'} + \sigma_v l^2_{zz'} \quad (2.91)$$

$$\tau_{xy}^0 = \sigma_H l_{xx'} l_{yx'} + \sigma_h l_{xy'} l_{yy'} + \sigma_v l_{xz'} l_{yz'} \quad (2.92)$$

$$\tau_{yz}^0 = \sigma_H l_{yx'} l_{zx'} + \sigma_h l_{yy'} l_{zy'} + \sigma_v l_{yz'} l_{zz'} \quad (2.93)$$

$$\tau_{zx}^0 = \sigma_H l_{zx'} l_{xx'} + \sigma_h l_{zy'} l_{xy'} + \sigma_v l_{zz'} l_{xz'} \quad (2.94)$$

The wellbore orientation is characterised by a deviation angle, i relative to the vertical direction ($i = 0°$ for vertical and $i = 90°$ for horizontal hole) and an azimuth angle, α relative to the minimum horizontal direction ($\alpha = 0°$ for hole in σ_v, σ_h-plane and $\alpha = 90°$ for hole in σ_v, σ_H-plane). σ_x^0, σ_y^0, σ_z^0, τ_{yx}^0, τ_{yz}^0 and τ_{xz}^0 are the original *in situ* stresses. The rotated *in situ* coordinates are then inserted into equations (2.83) to (2.87).

Therefore, the state of stress acting on the wellbore wall can be determined for any combination of wellbore inclination and azimuth from the above theory.

2.7 Stress Sensitivity in Sandstones

The state of stress in hydrocarbon reservoirs is in a continuous dynamic state due to generation and/or migration of hydrocarbons, production and injection processes. These processes will either elevate or lower the pore pressure and as such decrease or increase the effective stress on the framework of the reservoir sandstone. This mechanism is known as stress-sensitivity and can alter some key mechanical properties of the sandstones. Numerous researches on the development and evolution of stress with reservoir parameters have been performed since the early 1940's. This section reviews some the previous experimental research conducted on the stress sensitivity of sandstone.

2.7.1 Elastic Constants Stress Sensitivity

Numerous experimental studies have shown non-linear elasticity for porous sandstones (Teeuw, 1971, Yale and Crawford, 1998, Santarelli et al., 1986, Franquet and Economides, 1999, Yi et al., 2005). Cleary (1959) conducted laboratory studies using sandstones of varying porosities to determine the influence of mean effective stress on elastic properties. They observed that the elastic modulus of sandstones follow a non-linear trend with applied stresses. The degree of non-linearity was found to be small for the lower porosity sandstones than for higher porosity sandstones. However, when small changes in stress and strain are observed in porous rock the changes appear to be linear and follow Hooke's law. The value of Poisson's ratio does not appear to change a great deal from one sample to another nor does it vary a great deal with different stress conditions.

Similar observation by Evans (1973) confirmed that the modulus of elasticity increases with applied stress, and that Poisson's ratio changed only slightly with increasing stress. Higher porosity sandstones tended to have higher values of Poisson's ratio. Senseny (1983a) reported experiments on samples of sandstones, shales, siltstones and mudstones from different horizons. The test data show that elastic modulus increase linearly with increasing confining pressure while that of shale decrease slightly. Poisson's ratio for both materials, however, shows no trend with changes in confining pressure. They also observed that the stress-strain curves for the sandstones are non-linear at both low and high stress difference, and the volumetric strain curve shows substantial dilation of the sample before peak strength.

Elastic modulus typically increases with confining stress as shown in Figure 2.11 (Kooijman et al., 1991). This is attributed to microcrack closure and a tighter packing of grains (increasing contact area). The variations have been described by various empirical expressions. One type of expression is (Warpinski and Smith, 1989):

$$E = A + B\sigma_r^n \qquad (2.95)$$

where E, B and n are constants.

Equation (2.95) is illustrated by the example in Figure 2.21a (Kooijman et al., 1991), which shows n=0.57. Alternative expressions are used e.g. by Brown et al. (1989). Poisson's ratio may increase or decrease depending on the material and the stress range considered (decrease in Figure 2.21b); the direction and magnitude of the Poisson's ratio change is difficult to predict. In principle, elastic parameters are determined at a stress level most representative of specific *in situ* stress conditions.

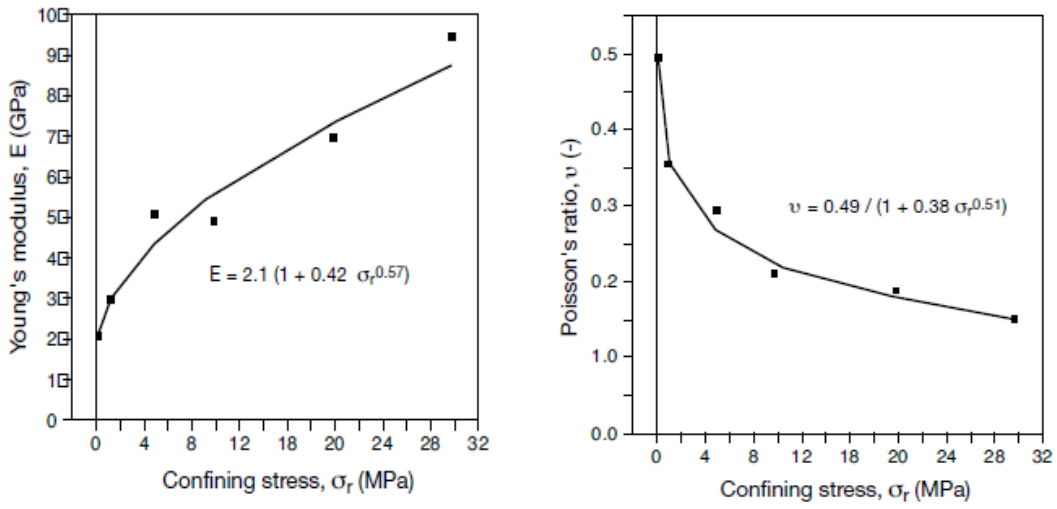

a) Young's modulus vs confining pressure b) Poisson's ratio vs confining pressure

Figure 2.21: Variation of Young's modulus and Poisson's ratio with confining stress - Castlegate sandstone (Kooijman et al., 1991).

Warpinski and Smith (1989) presented a range of values for B and n assuming A=0. The exponent n typically ranges between 0.01 and 0.3. For comparison, n=0.33 is theoretically derived for a cubic pack of spherical grains (this is referred to as the Hertz-Mindlin theory (Fjaer et al., 2008)).

Triaxial testing of reservoir sandstones have shown a strong non-linear correlation between elastic modulus, Poisson's ratio and the magnitude of the applied stress (Franquet and Economides, 1999) and stress paths (Yale, 1984, Santarelli et al., 1986, Franquet and Economides, 1999). At a constant confining pressure, elastic modulus decreased substantially with increasing differential stress. With lower effective confining

stress the decrease in the elastic modulus is more abrupt and the steep decline happens at lower differential stresses.

2.7.2 Strength Stress Sensitivity

The mechanical properties of sandstones, in particular their strength and deformation characteristics can vary appreciably. The stress-strain relationship of Berea sandstone loaded to failure for a series of tests under different confining pressure conducted by Morita et al. (1992) are presented in Figure 2.23. It can be seen that as confining pressure increases the failure strength increases. This result has been observed by many authors for sandstones and shales. The stress required for failure has been found to be a function of effective confining stress (Handin et al., 1963a, Paterson and Wong, 2005) and in general, strength and ductility increase with increasing effective stress. An excellent overview of the changes that occur in rock with increasing confining stress can be found in Jaeger et al. (2007). In some rock types, notably carbonates, ductility increases such that the material can sustain large strains without loss of strength at high confining stresses. At higher confining pressure the applied axial load can increase steadily with increasing stress after the yield point has been exceeded. This process is termed work hardening and associated with pore collapse and compaction (Jones, 1987).

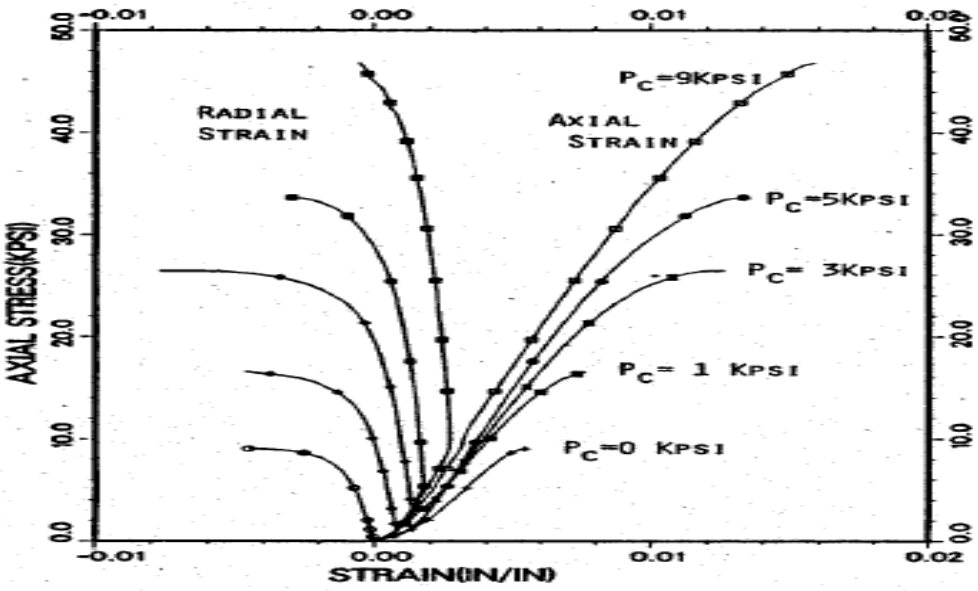

Figure 2.22: Stress-strain curve for triaxial tests on Berea sandstones (Morita et al., 1992).

Senseny (1983a) found that compressive strength increase linearly with increasing confining pressure. Morita et al. (1992) however, found strength to increase more rapidly at high confining stress than was observed at lower confining stresses, which implies non-

linearity. Holt et al. (1989) produced results which tend to support this since they found that neither a linear Mohr-Coulomb nor Griffith failure criteria will adequately fit their data. Shale and mudstone/siltstone exhibits a slower increase in strength at higher confining pressures. Morita et al. (1992) also observed that the shape of the stress-strain curve becomes more linear for failure test as confining pressure is increased. Holt (1990) noted at low confining pressures failure is predominantly brittle in nature but becomes more ductile at higher confining pressures, in agreement with ideas of other authors (Terzaghi 1936).

Senseny (1983a) found that strength of sandstones and shales did not appear to be correlated to either lithology or depth. Several authors have published correlations between strength and porosity of sandstones (Dunn et al., 1973, Hoshino and Chosajo, 1972). Dunn et al. (1973) noted that as confining pressure increased, the strength at zero porosity predicted by extrapolation of their data approached that of a single quartz crystal. Correlation between strength and elastic moduli have been found by several workers (Deere and Miller, 1966, Holt et al., 1989) which are used to predict strength from mechanical properties logs.

3 Determination of Rock Mechanical Properties: Test Materials, Equipment and Procedures

3.1 Introduction

Rock mechanical parameters derived from laboratory experiment on core samples are usually required as input parameters to validate newly developed techniques, models or theories in petroleum engineering applications such as sand prediction, wellbore stability studies, hydraulic fracturing, reservoir stress management etc. Thus the objective of the rock mechanical experiment is to generate the input data required for application of newly developed techniques for predicting sand production potential and assessing wellbore stability of sandstone formation.

In any experimental study, the choice of test materials and careful preparation are critical in ensuring that correct and accurate sample specifications are obtained with a view of minimising errors that would be associated with the experiment. As such, a consistent and standard method of sample preparation was adopted. Equally important and critical is the design of experiment. Therefore, standard experimental set-ups and procedures are adopted for this thesis. Careful adherence to these predetermined set of conditions were upheld in order to obtain representative results.

The rock mechanical experiment is presented in two chapters; this chapter and the following chapter. The test materials, techniques employed to prepare the material for testing and description of the various experimental equipment and set-ups/procedures are described in this chapter. Experimental results and analysis are presented in the following chapter.

3.2 Description and Preparation of Test Materials

Reservoir samples from six wells and five outcrop sandstones samples were used. The outcrop sandstones will be referred to as analogue sandstones for the remainder of this thesis. Analogue sandstones have been utilised due to their physical similarities with reservoir sandstones as they provide an economic alternative to the costly retrieval of deep reservoir core samples. This section describes the basic properties of each of these materials. A complete sedimentological and petrophysical data set of each material is presented in **Error! Reference source not found.**.

3.2.1 Reservoir Sample

Reservoir core samples from two fields in the North Sea and one field in the Columbus basin, Trinidad were provided by oil companies for mechanical testing over a period of time. Information and data concerning the reservoir samples are classified as confidential, and therefore only basic and general information are presented in this thesis. The three fields are designated as Field A, Field B and Field C. In total thirty six (36) reservoir samples were subjected to various petrophysical and mechanical testing.

3.2.1.1 *Field A*

Field A is located in the Central North Sea in water depth of 300 ft and comprises two gas-condensate horizons (Famgee and Deekay). The Famgee horizon belongs to Paleocene origin while the Deekay is of Upper Jurassic origin. Core data from three exploration and appraisal wells (AFA, AFB and AFC) were available from Field A. Wells AFA and AFB found hydrocarbons in both Famgee and Deekay horizons while well AFC only penetrated the Deekay horizon.

3.2.1.1.1 Famgee Horizon

The Famgee horizon consists of turbidite sand which lies about 9,000 ft below mean sea level. This horizon consists of well sorted and sub-rounded fine to medium grained, moderately to poorly-sorted homogeneous sandstones with average porosity of 25% and permeability of 380 mD.

3.2.1.1.2 Deekay Horizon

The Deekay horizon comprises mainly fine-grained sandstones of shallow marine shore face sediments. A distinctive feature of this sand was a continuous and apparently uniform graduation in lithological and reservoir properties from top to the bottom. The sand is well sorted with a course to medium grain size, demonstrating porosities of over 26% and permeability 430 mD.

3.2.1.2 *Field B*

Field B encountered gas in the Rotliegendes Formation (Lower Permian) in the Southern North Sea. The Rotliegendes sandstone is subdivided into three reservoir horizons, X, Y and Z. Core samples recovered from three wells (BFA, BFB and BFC) which have been under production were available from Field B.

3.2.1.2.1 X Horizon

X horizon consists predominantly of well-developed reworked aeolian dune and inter dune sand, together with fluvial sand deposit. Permeability in the fluvial deposits is generally lower than those in the aeolian sand where permeabilities of 100 mD are common. With the general predominance of aeolian facies in X horizon, the porosity and permeability is around 14% and 200 mD respectively.

3.2.1.2.2 Y Horizon

Y horizon is dominated by fluvial facies with aeolian sand being absent. This horizon is characterised by the occurrence of very coarse sandy conglomerates and medium to coarse sandstone. The upper and lower parts consist mostly of conglomerate, while the middle part is dominated by medium to coarse pebbly sand with lesser amounts of conglomerate with porosities of 11% and permeability of 70 mD. Consequently the average reservoir parameters here are slightly lower than for X horizon.

3.2.1.2.3 Z Horizon

As in X horizon, the depositional process of Z horizon was controlled by aeolian and fluvial processes. In general, Z horizon consists of lower interval of fluvial facies and an upper one containing aeolian sands interbedded with certain amount of fluvial sand. This horizon has similar reservoir qualities to the X horizon.

3.2.1.3 *Field C*

Field C is located in the Columbus basin, Trinidad. Sand was encountered in the Kay reservoir which comprises more than 8,500 ft of Pleistocene-aged clastic marine sediment. The Kay reservoir sands are predominantly massive, very fine grain quartz arenite sand with occasional laminated or cross-bedded intervals. Overall, the sands are moderately to well sorted, containing mainly quartz and between 2% and 7% by weight of subordinate minerals. Porosities in the Kay sand averaged around 15% with corresponding permeability of 35 mD. Core data from well CFA were available from Field C.

3.2.1.4 *Preparation of Reservoir Sample*

The reservoir samples were delivered either as pre-plugged cores of 1.5" diameter cylindrical plugs of variable length or as preserved whole cores. A sample diameter to length (D/L) ratio of 0.5 is required to ensure uniform stress distribution in the sample during mechanical properties testing (ISRM,1983). Whereas most of the pre-plugged 1.5"

diameter samples were found on arrival to be within the optimal D/L ratio, the pre-plugged samples particularly from well AFA were found to be roughly 2” long which is shorter than the desired D/L. Large halite crystals were also observed to have formed on the outer surface of most of the pre-plugged samples from well AFA although they were sealed in paraffin wax. The occurrence of these crystals on the surfaces of plugs indicates that they are not part of the formation mineralogy. The crystals appeared to occlude the surface pores and possibly originated from the drilling or formation fluids and poor sample preparation technique. The reduction of porosity by such pore filling mineralisation could result in the acquisition of formation strength data which is not representative of *in situ* stress. Therefore the samples were cleaned using a Soxhlet Reflux cleaning technique. Toluene was refluxed initially to remove any hydrocarbon remaining from the formation fluids and drilling mud filtrate contamination. When the effluent was observed to be clear, the toluene was replaced with methanol to remove the salt crystals. When samples were judged to be clean, they were oven dried, weighed, dimensioned and stored in a desiccator until required for testing.

For the preserved whole core, test samples were cored to a nominal diameter of 1.5" using a diamond tipped core barrel. The cores are cut to approximately 3” and both ends trimmed to ensure they are smooth and free of any abrupt irregularities and parallel to an accuracy of ±0.02 mm, preventing an uneven distribution of stress on the sample during testing (Hawkes and Mellor, 1970). The samples were then dried, weighed, dimensioned and stored in a desiccator just like the pre-plugged samples.

3.2.2 Analogue Sandstones

Five quarried sandstones including Clashach, Doddington, Fife Silica, Lochaline and Locharbriggs were mechanically tested. Previous laboratory studies have been conducted on the Clashach (Hutcheon et al., 2001, Al-Hinai et al., 2008), Lochaline (Crawford et al., 2004) and Locharbriggs (Mair K. et al., 2002, Mair et al., 2000) sandstones. Clashach and Locharbriggs sandstones have been used in investigating the effect of stress loading rate on permeability progression (Crawford, 1998, Mair K. et al., 2002, Ngwenya et al., 2003, Ojala et al., 2004).

3.2.2.1 *Clashach Sandstone*

The Clashach sandstone was sourced from the Clashach Quarry, near Hopeman Village in the Elgin area of North-Eastern Scotland. This sandstone is part of the Permo-Triassic Aeolian sandstone which is exposed as outcrop on the southern shores of the

Moray Firth basin (Lovell, 1983). The sandstone is pale-fawn, sub rounded, well sorted, medium to coarse grained subarkosic arenitic. It is composed predominantly of quartz (90 - 96%) with a mean size of 335 μm, fresh to altered potassium feldspar make up the remaining constituent (Ngwenya et al., 1993). Detrital grains appear hardly affected by digenetic changes, except for the presence of well-developed secondary quartz overgrowths (Crawford, 1998).

3.2.2.1 *Doddington Sandstone*

The Doddington sandstone was obtained from the Doddington quarry Wools, Northumberland, UK. The sandstone belongs to the Fell sandstone group of Carboniferous period (Taylor et al., 1971). The Doddington sandstone is non-fossiliferous, arenaceous, quartzitic fine-grained sandstone with occasional red veins (Santarelli and Brown, 1989). The sandstone predominantly consists of quartz (96%) with mica and feldspar making up the remaining constituent.

3.2.2.2 *Fife Silica Sandstone*

The host block from which samples of the Fife Silica sandstones were cored was obtained from an outcrop in Burrowine Moor Quarry Fife, Scotland. The Fife Silica is a loosely consolidated to weakly cemented Carboniferous sandstone. The results of XRD analysis of Fife Silica sandstone samples shows that quartz is the dominant framework grain (97% to 100%) with microline varying between <1% to 3%. The Fife Silica sandstone appears brilliantly white and is commonly used for manufacturing of glass. In outcrop the surface appears to be very friable, grains being dislodged by fingers.

3.2.2.3 *Lochaline Sandstone*

The Lochaline sandstone was sourced from the Lochaline silica mine, Morvern Peninsula, West Scotland, where this extensive and best known Cretaceous shallow marine sandstone is exposed as outcrop and preserved *in situ*. The Lochaline sandstone is loosely consolidated, very well sorted, with roundness varying from angular to rounded centred around 200-250 μm (Lowden et al., 1992). XRD analysis shows that the sandstone is exceptionally clean containing 97-99% quartz.

Scanning Electron Micrograph (SEM) on thin sections of the Lochaline sandstones shows partial absence of clay and cementation (Figure 3.1). This loosely consolidated sandstone is held together by pressure dissolution suture at grain to grain contacts. This unique characteristic of the Lochaline sandstone allows manual disaggregation of the

sandstones into purely unconsolidated sand without altering the main physical features of the intact grains.

Silification is the only diagenetic feature of the Lochaline sandstones. This resulted in the formation of two hard lenses of rock with different petrophysical properties from an identical depositional process within this Lochaline sandstone. In these lenses, the sandstone is well cemented with a porosity of 5%, due to concentrated post-depositional silica cementation (Lowden et al., 1992). This zone is equally well sorted quartz arenite consisting of subangular to subrounded quartz grains with an average size of about 200 μm. SEM analysis of the grain fabric from these hard lenses revealed interlocking grains produced by coated quartz overgrowth. In contrast, the high porosity and permeability unconsolidated Lochaline sandstones are held together by the original packing strength which cause the samples to be friable and easily dislodge by hand.

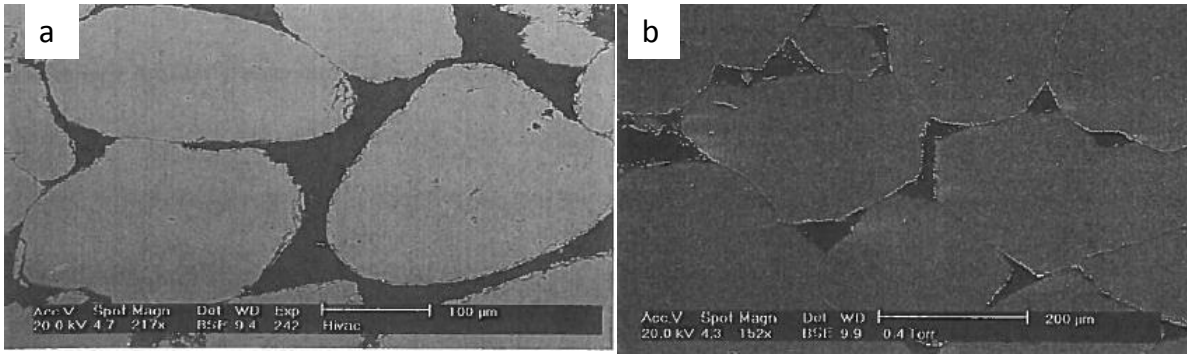

Figure 3.1: SEM photographs on thin section of Lochaline sandstone showing a) loosely consolidated sandstone illustrating grain to grain contact and b) well-cemented section showing pressure dissolution and quartz overgrowth features.

3.2.2.4 *Locharbriggs Sandstone*

The Locharbriggs sandstone is a Permian Aeolian sandstone found from a quarry in Dumfries, South West Scotland. It is rounded to well-rounded medium grained sandstone with a mean diameter of about 200 μm. XRD analysis of the Locharbriggs sandstone samples show it consist of 83% to 88% quartz and subsidiary feldspar (6%), with significant hematite grain-coating as cement (Mair et al., 2000). Planar bedding and the hematite cement produce a characteristic red banded appearance to this Aeolian sandstone.

3.2.2.5 *Preparation of the Analogue Samples*

Core samples were cut from the quarried block using a diamond tipped core barrel with tap water as a flushing and cooling agent to produce 1.5" diameter plugs. The

analogue sandstone samples were all cored from the same block and as such no heterogeneity or anisotropy was detected within each block. The samples were therefore considered to be homogeneous and isotropic. Plugs were cut perpendicular to the apparent bedding plane. The plugs were trimmed using a trimsaw core holder and surface grinder to produce 3" long samples resulting in optimal diameter to length ratio of 0.5. The ends were cut parallel and normal to an accuracy of 0.02 mm (Hawkes and Mellor (1970). Samples tested dry were oven dried at 100℃ for 24 hours. Prior to testing, all samples were weighed and dimensioned.

3.3 Petrophysical Characterisation

In the evaluation of a petroleum reservoir and sandstone, it is necessary to accurately determine the basic petrophysical properties such as porosity and permeability of the sample since these properties can be related to mechanical properties. Additionally, it is important to determine the suitability of the analogue sandstones as representative reservoir analogues from petrophysical point of view. The ambient porosity and permeability data are summarised in Appendix A.

3.3.1 Density and Ambient Porosity Measurements

Bulk volume and dry weight are needed to obtain porosity and grain density. The weight of each sample was taken as an average of six values measured using an electronic weight balance. Both the length and diameter of each sample were measured using a digital calliper in three different locations distributed down the length and about the circumference of the sample from which an average value was taken. This ensures that accurate measurement of the dimensions of each sample was achieved. Thus the bulk volume is calculated from:

$$V_b = \frac{\pi d^2 L}{4} \qquad (3.1)$$

A Boyle's law porosimeter is used to determine the grain volume, V_g based on the principal of gas expansion. A dried sample is placed in a chamber of known volume and the pressure is measured with and without the sample, keeping the volume of gas constant. The difference in pressure indicates the pore volume. Boyle's Law states that for a constant mass of ideal gas, at constant temperature, the product of pressure and volume are constant. Helium gas, at typically 0.69 MPa was introduced into matrix chamber and allowed to expand, the volume of which had been determined by reference to pressure/volume curves calibration. The final equilibrium pressured of gas was

subsequently measured and Boyle's Law used to calculate the grain volume or the pore volume of a sample. Sufficient time was allowed for the pressure to reach equilibrium otherwise porosity and grain density can be underestimated particularly for low permeability samples.

Porosity is then calculated using the following expression:

$$\phi = \frac{V_b - V_g}{V_b} * 100 \qquad (3.2)$$

The bulk and grain density of the samples were determined by dividing the weight of the samples by their bulk and grain volumes respectively.

3.3.2 Ambient Permeability Measurement

Permeability is important rock property as it relates the rate at which hydrocarbons can be recovered. The nitrogen steady state permeameter allow gas permeability to be measured using theory derived from Darcy's Law for laminar flow of gas under steady state isothermal conditions. This can be expressed as follows:

$$k_{gas} = \frac{2\mu\,\overline{ZT}\,P_b L Q_b}{A T_b\,(P_1^2 - P_2^2)} \qquad (3.3)$$

where k_{gas} is the gas permeability (D), μ the gas viscosity (cp), $\bar{Z}$ the mean gas compressibility factor, $\overline{T}$ the mean temperature of flowing gas (℃), T_b the base temperature (℃), P_b the atmospheric pressure (atm), P_1 & P_2 the upstream and downstream pressures respectively (atm), L the sample length (cm) and A the sample cross sectional area (cm^2).

Ambient condition permeability measurements were conducted by encasing the sample of known length and diameter in a Hassler Sleeve. The sample was first radially confined to 3.45 MPa and Nitrogen gas injected with the sample mounted in a horizontal position. The pressure drop across the sample and the flow rate were measured and permeability calculated using Darcy's equation. Differential pressure was calculated by subtracting the upstream pressure from the atmospheric pressure, measured using Torricelli barometer.

Gas permeability was measured over a range of mean gas flowing pressure. Readings were taken when steady-state flow has been established. After sufficient readings and any repeat measurement, the sample was loaded to the next stage in the loading cycle and the measurement process repeated. Between five and six gas permeability measurements were taken at increasing mean flowing gas pressures.

3.3.2.1.1 Klinkenberg correction

Using gas at low pressure leads to an apparent permeability which is too high because the mean free path of the gas is no longer negligible compared to a typical pore size. Corrected permeability values were obtained by measuring the permeability at a series of different mean pressures base on the following equation:

$$K_{air} = K_{\infty}(1 + (b/P)) \quad (3.4)$$

where K_{air} is the apparent gas permeability (mD), K_{∞} the absolute Klinkenberg permeability (mD), P the mean absolute pressure (bar) and b the Klinkenberg gas slippage factor.

Apparent permeability values vary in general, linearly with reciprocal mean pressure. Extrapolation to infinite mean pressure determines the theoretical liquid, or Klinkenberg, permeability, k, and the slope is the Klinkenberg gas slippage factor, b.

3.4 Triaxial Compression System

The mechanical strength of sandstones are usually determined in the laboratory by applying and simulating *in situ* stresses on core sample using compression testing equipment. Generally, the failure pattern can be divided into pre-peak and post-peak regions which are associated with the failure process. It has long been recognised that such failure is influenced by the stiffness of the loading machine relative to that of the sample especially when analysing the post-peak region (Harrison and Hudson, 2000). In this thesis, the post-failure behaviour of the sample is very important in obtaining the relevant parameters for the application of the sand prediction and wellbore failure studies.

When a sample of rock is loaded in a testing machine, a large amount of elastic energy is stored in the machine-sample system. Uncontrolled destruction of the sample would occur if the stiffness of the machine is not high, thus preventing the load bearing of the sample to be readily assessed as a function of deformation. The uncontrolled destruction of the sample is attributed to sudden release of the stored energy from the machine as the load decreases. Rock failure in nature is rarely that catastrophic. The development of stiff and servo-controlled testing machines have now provided a powerful tool for studying the post-peak response of rocks (Hudson et al., 1971), allowing the complete stress-strain curve of the loaded sample to be established.

Mechanical testing of samples was performed using a RDP Howden servo-controlled testing system. This formed the 'backbone' of the testing equipment. Basically, the testing system consists of a servo-controlled stiff testing machine, a Hoek cell, pressure

intensifier (for confining pressure), pore fluid system, strain gauge electronics and a data logging system as shown in Figure 3.2.

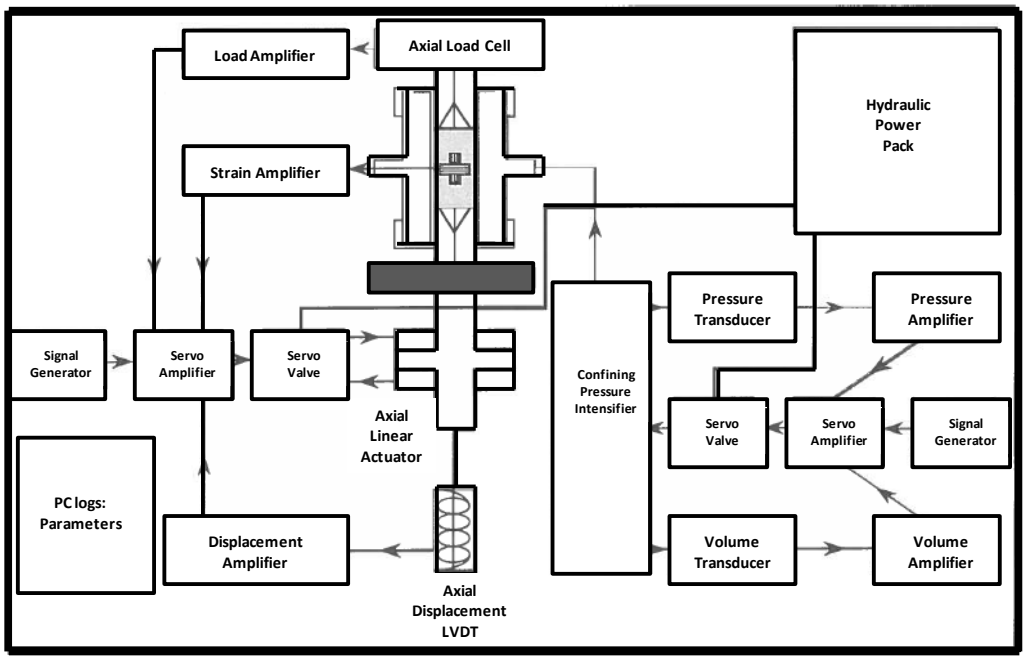

Figure 3.2: Schematic of the triaxial testing machine showing different components and basics of the electro-hydraulic servo system.

3.4.1 Servo-controlled Stiff Testing Machine

A servo-controlled stiff compression machine (>2500 kN/mm) is used for applying axial loads up to 1000 kN over the prepared flat and parallel core plug ends. The compression machine is composed of a four-column, fixed-crosshead straining frame, incorporating a double-acting, and unequal area actuator with an integral displacement transducer. The actuator piston is reciprocated by pressurised fluid controlled by a servo-valve. The integral displacement transducer incorporated in the actuator provides an electrical signal proportional to the piston rod displacement. Samples are tested between the piston rod and a strain gauged load cell attached to the crosshead of the straining frame. The ultra-high mechanical stiffness of the loading machine ensures that minimum strain energy is stored in the frame during loading, allowing a high degree of control of post-failure studies such as required in the current application. The ram operates vertically with the load cell located in the cross head of the straining frame. The position of the ram is monitored by an electronic LVDT and this position signal together with that from the load cell allows the flow of hydraulic oil to the ram to be controlled. Thus the load and rate of loading are controlled.

The "stiff tester" is controlled by a closed loop electro-hydraulic servo system (as shown in Figure 3.3) achieved by obtaining an electrical feedback signal from a transducer tightly coupled to mechanical parameters being controlled. The signal is compared with the command signal, and the error signal, is then amplified to "drive" the mechanical system towards the command signal. The hydraulic power pack provide a supply of pressurised oil which is fed via an electro-hydraulic servovalve to double acting linear actuator causing movement of the system resulting in the sample being loaded. Load, displacement and strain transducers may be used in the system with their respective amplifiers producing a voltage signal proportional to the individual parameters. These are connected via a controlled console to the servo amplifier. The servo amplifier constantly compares the 'command' from signal generator with the selected control parameter and drives the servovalve with the amplified error signal. This results in any difference between the 'commands' and 'actual' signals being corrected.

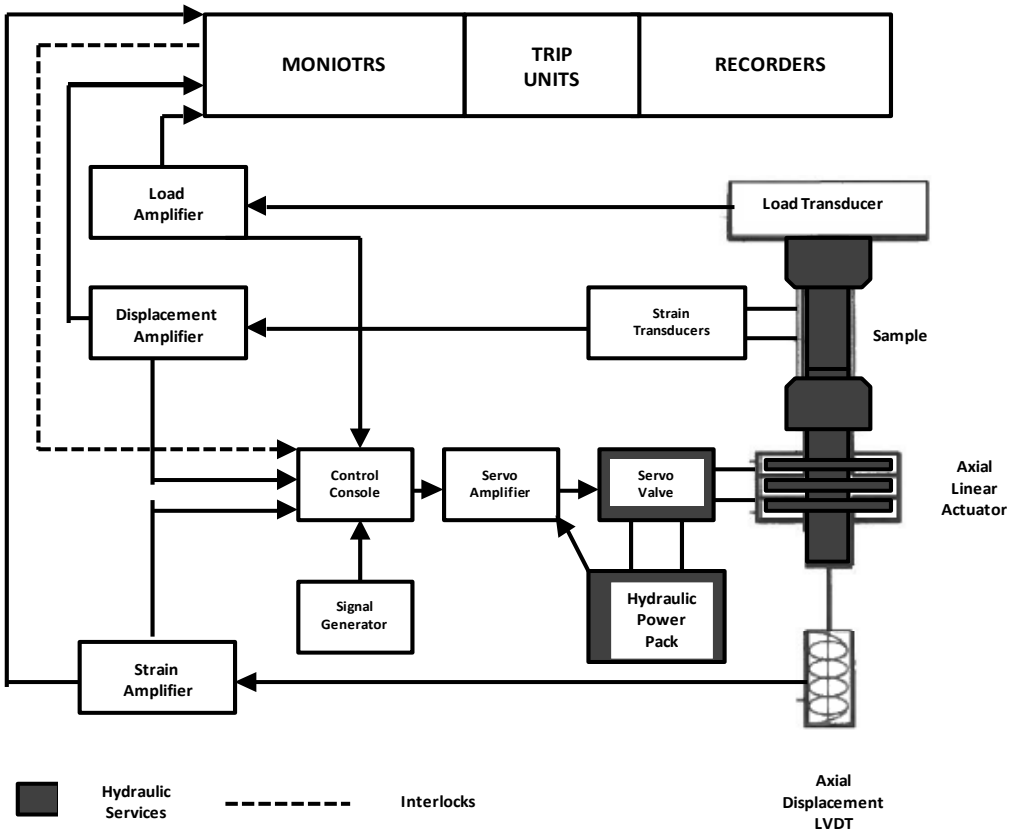

Figure 3.3: Principles of operation of the basic closed loop servo system.

3.4.2 Servo-controlled Pressure Intensifier

Associated with the stiff testing machine is a pressure intensifier which uses a similar servo-hydraulic circuit to control the confining pressure in the Hoek cell. Application of

radial confining pressure developed in the annular space is also achieved by RDP-Howden servo-hydraulic pressure intensifier and the pressure vessel system. The intensifier operates at pressure up to 110 MPa over an 80 cc volume change from a 30 MPa external hydraulic power supply controlled by an electric-hydraulic servo-valve operating under closed loop control with pressure or volume as the feedback parameters. This type of system offers a high degree of control in setting loading parameters and is further characterised by efficient and stable pressure maintenance. A strain gauge pressure transducer measured the output pressure whilst an internal transducer sensed the change in volume over the entire operating range. Volume change measurement is accomplished by a displacement transducer connected to the intensifier piston.

3.4.3 Hoek Cell

The Hoek cell provides a means of applying confining pressure to the sample. It consists of a steel body rated to 68.9 MPa into which the sample may be placed in order to apply the confining pressure. It has threaded end-caps to facilitate easy removal of the deformed sample from the cell and a flexible jacket (usually synthetic rubber) to prevent hydraulic fluid from entering the sample. Confining pressure is transmitted to the radial surface of the sample via hydraulic oil contained within the annulus between the synthetic rubber sleeve surrounding the sample and the outer wall of the cell body. The sample is placed within the sleeve and the hydraulic oil pressurised by the connection to the pressure intensifier. Integral U-shaped seals are pushed against the cell inner wall and the screw on end caps when the oil is pressurised to prevent any leakage or loss of pressure. The pressure and volume of oil introduced or removed from the cell during testing is monitored electronically and the signal is used to control the confining pressure. The Hoek cell is suitable for a 1.5" diameter samples.

3.4.4 Strain Measuring Equipment

The strain measuring equipment comprises of a series of Wheatstone bridges and amplifiers. Each sample is strain gauged with diametrically opposed pairs of active vertical and horizontal strain gauges. The two vertical gauges on the sample serve as the active arm of a Wheatstone bridge. The other two arms of the bridge are formed on external dummy passive gauge bonded to a lithologically similar sandstone core which is not loaded. This completes the Wheatstone bridge (in effect a half bridge is formed) for the vertical strain. An identical bridge measure the horizontal strain. The output from the

bridge is conditioned with a strain gauge amplifier and recorded. The amplified signals are fed to LED meters. Thus the strain can be plotted along with the axial load.

3.4.5 Data Logging

The data logging equipment consists of a computer with data logging hardware and software. The parameters of interest during the tests (axial load, axial deformation, confining pressure, cell hydraulic oil volume and radial deformation) are recorded at appropriate time intervals.

3.5 Experimental Set-up and Procedure

3.5.1 Triaxial Compression Testing

The most conventional procedure for carrying out a 'triaxial' test is by placing a cylindrical core sample in a Hoek cell and applying confining pressure radially. This is commonly referred to as a triaxial test, to distinguish it from a 'uniaxial' stress state where there is no confining pressure. Although the name 'triaxial' test suggests that the stresses would be different in three directions, this is not the case here. However, this method is generally accepted as special case of triaxial stress and best describe as an axisymmetric triaxial test (a two dimensional stress state where the intermediate stress is always equal to one or other of principal stress). In reality, a three dimensional stress state exist which better represents the *in situ* condition known as a 'true' triaxial test. A true triaxial stress mode is the stress state in which the three principal stresses are independent, such that $\sigma_1 \neq \sigma_2 \neq \sigma_3$. Whilst it has been shown that the intermediate principal stress cannot always be ignored (Haimson and Chang, 2000, Haimson and Rudnicki, 2010), carrying out a true triaxial test is experimentally complex and, as a result, this has yet to become a conventional arrangement for compressional testing. Triaxial testing is preferred because of its near approximation to field conditions and simplicity of operation (Skopec, 1991). Adopting the convention that compressive stress is positive, and designated the greatest, intermediate and least principal stresses by σ_1, σ_2 and σ_3 respectively. For a conventional triaxial test, two of the principal stresses are equal to the superposed hydrostatic pressure ($P_c = \sigma_2 = \sigma_3$), whilst the maximum principal stress σ_1, departs from it. This arrangement is conventionally written as $\sigma_1 > \sigma_2 = \sigma_3$. The superposed hydrostatic pressure is known as the confining pressure as shown in Figure 3.4.

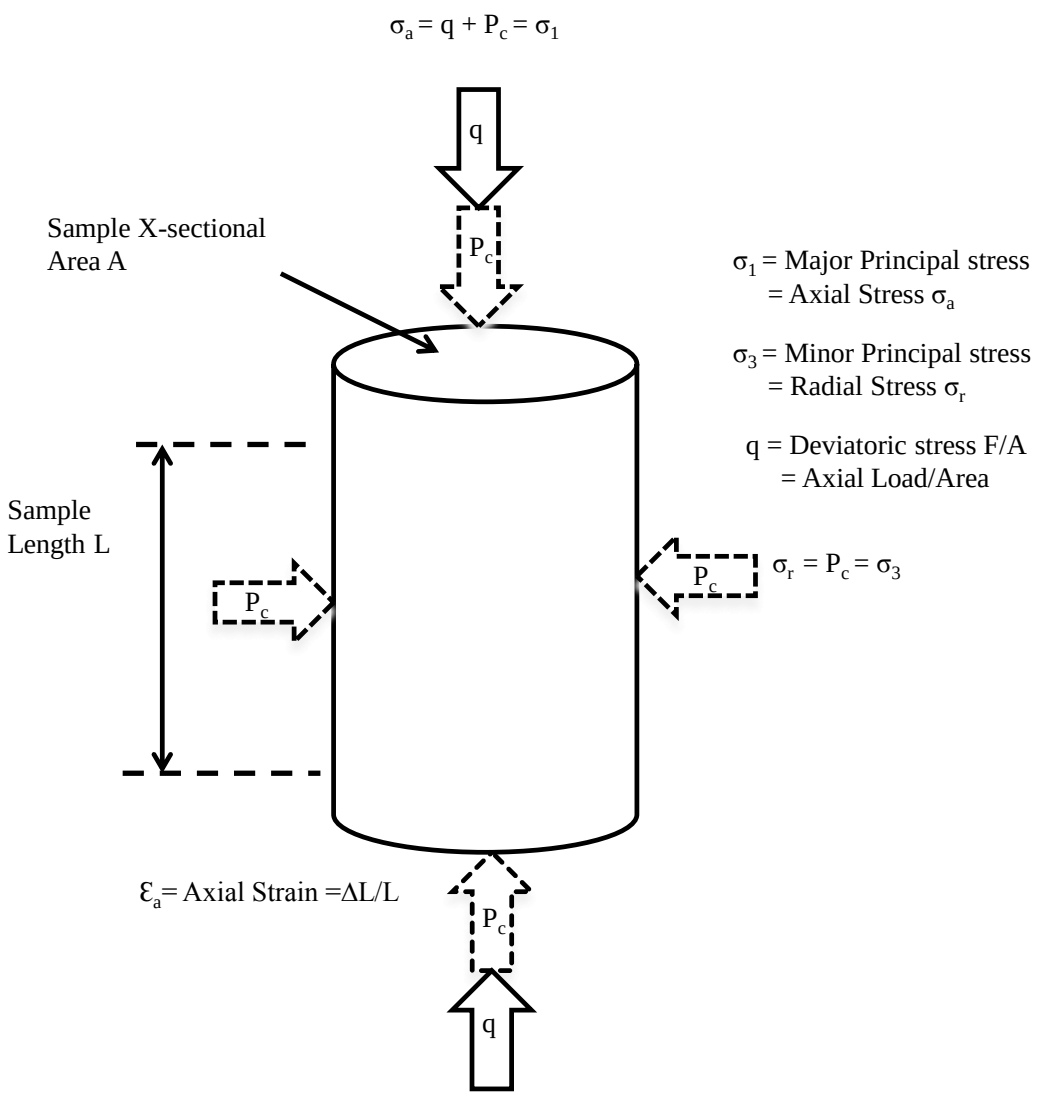

Figure 3.4: Applied stress arrangement in a conventional triaxial compression test.

Generally, there are two techniques used for triaxial compression testing. This includes the conventional single stage tests here in referred to as discrete test and continuous failure test referred to as multi-failure state test.

The discrete test method requires testing of multiple samples from the same formation to define the strength envelope. In the best conservative case, at least two independent tests are required to complete a failure envelope at different confining pressures for a discrete test. Discrete tests were conducted by loading samples hydrostatically to a predetermined confining pressure and maintaining the pressure constant at a selected level. Axial load was then further increased until the sample fails at a specific point known as the 'peak stress', defined as the maximum axial stress which the sample can sustain at a given confining pressure.

Multi-failure state testing presents an attractive and viable means of development of rock strength with increasing confining pressure. Multi-failure state testing can generate a full failure envelope using a single core sample compared with multiple core samples in the case of the discrete test (Harouaka et al., 1995). Since the technique was first introduced in the mid-1970s (Kovari and Tisa, 1975), it has been validated against discrete test results and adopted as a suggested method of testing rock specimen (ISRM, 1983). Thus, the aim of the multi-failure state test is to obtain several stress points on the failure envelope from a single core sample.

Multi-failure test was performed by proportional application of the axial load and confining pressure until the later reaches a pre-selected level. The axial load was then allowed to increase until the peak strength was reached. At this stage, axial load was held constant, and the confining pressure increased rapidly to a higher predetermined value. This was followed by the application of the axial load until the second failure peak point is attained. In a similar manner, several peak strength values were thus obtained. After the ultimate failure of the rock the test was continued in a similar fashion to obtained residual stress points for the rock sample. Increasing the confining pressure at each stage had the effect of returning the sample to within the stable region of the failure envelope and thus maintaining its load bearing capabilities. Experimental work has shown that in general, results from the two techniques yield comparable results (Somerville and Smart, 1991, Holt and Fjaer, 1991).

3.5.2 Elastic Constants Stress Sensitivity Measurement

The elastic properties of the sandstones were determined on separate and dedicated loading cycles using strain gauge measurement technique. Although this may have induced hysteresis associated with the initial loading of these samples up to 34.5 MPa, it was assumed that the differential stress would not be sufficient to induce yield and thus the stress-strain path would remain in the elastic region and within the yield and failure envelop. At the first stress level the axial load was varied by approximately 3 kN to produce a response in the vertical and horizontal gauges. The confining pressure was kept constant during this variation in load. This procedure was repeated at each of the stress levels and the elastic properties are calculated from the stress-strain curve as the ratio of the change in axial stress σ_a, to change in axial strain ε_a, which occurs:

$$E = \frac{\Delta\sigma_a}{\Delta\varepsilon_a} \qquad (3.5)$$

Poisson's ratio ν, is calculated as the ratio of the accompanying change in radial strain ε_r, to the change in axial strain ε_r:

$$\nu = -\frac{\Delta\varepsilon_r}{\Delta\epsilon_a} \tag{3.6}$$

3.5.3 Accuracy of Strain Gauge Measurement Technique

Strain gauge is the most common method of measuring strain of a rock. A strain gauge is made of a continuous electrical conductor (bonded metallic or foil) called the grid, deposited on a very thin flexible insulating material carrier. The strain gauge is attached directly to the rock sample using adhesive. It is very important that the strain gauge be properly mounted onto the rock sample so that the strain is accurately transferred from the rock sample and consequently the change in the strain gauge's electrical resistance can be observed and recorded. The bonding agent itself as well as its careful and skilled use also contributes to the accuracy of the measurement. The application of adhesive particularly in porous sandstone may results in the glue penetrating the surface and influencing the properties of material locally. Therefore the adhesive is only thinly applied over the surface of the sample. Prior to testing, the sample is gently squeezed to observe the response of the strain gauge and to confirm that the strain gauge is properly bonded to the sample. Strain gauges have a characteristic gauge factor, defined as the fractional change in resistance divided by the strain.

Strain is measured by equipping the samples with diametrically opposed pair of bonded 120 Ω active, vertical and horizontal electrical resistance foil strain (Tokyo Sokki TML FCA) arranged in a 90° rosette (Figure 3.5). The very small changes in resistance (typically 0.2 Ωm in 120 Ω per microstrain) are measured using Wheatstone bridge arrangement. Thermal effect are compensated by completing the bridge with a ''dummy'' gauge attached to an unstrained identical sample. A Wheatstone bridge circuit, as a strain indicator, measures an unknown electrical resistance (the resistance of the strain gauge) by balancing two legs of a bridge circuit.

Optimal strain gauge is made out of a material with high resistance. High impedance materials show higher changes in resistance and larger domains for strain changes, due to stretching or compression, in comparison with a material with lower impedance. Strain gauges should have a high elastic limit and their physical and electrical properties both should be insensitive to the temperature changes and they must have a constant gauge factor.

(a) Strain gauge rosette (b) Wheatstone bridge arrangement

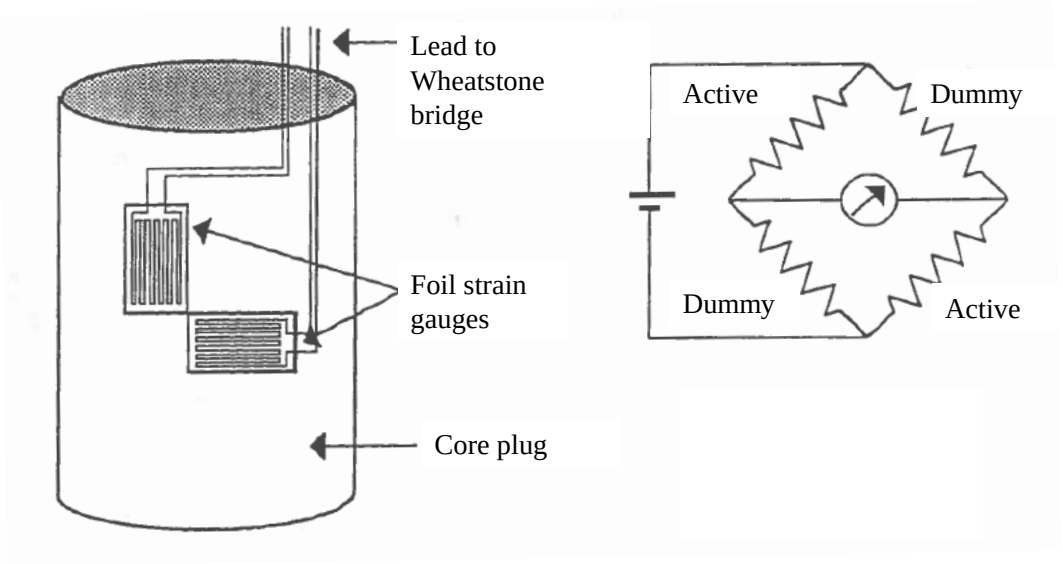

Figure 3.5: Strain gauged sample and circuit diagram of the Wheatstone resistance bridge

Major disadvantage of the strain gauge measuring techniques is the difficulty in having a good contact bond between strain gauge and the rock. Basically, only the area covered by the strain gauge is being monitored and not all of the sample (Brady and Brown 2004). This can especially cause inaccuracies in the strain measurement of coarse grained samples. In the coarse grained samples, if the relative size of the strain gauge is small compared to the grain sizes, the measured strain by the strain gauge can be the combination of the local displacements and slipping of the grains and the total deformation of the sample, rather than be due to the pure global deformation of the sample. Therefore strain gauges should be at least five times longer than the largest grains to ensure that average strain is measured, rather than local fluctuations between the individual particles. This could arise due to small-scale inhomegeneities and strain localisation within the sample particularly after yield.

For measuring displacements in a test, extensometers or linear variable displacement transducers (LVDTs) can also be used. LVDTs consist of a main core that is surrounded by three equally spaced coils and then encased in an insulating container. The movement of the main core, which has a magnet placed in it, inside the coils, produces an electrical output that is proportionate to the displacement of the main core. When the main core is in the central position the output is zero and when it moves to either side, the voltage induced in the coil which the core is moving toward, increases with the proper sign. The

induced voltage can be calibrated to the actual displacement and be used for measuring displacements in a test. LVDTs strain measuring technique has the advantage of measuring strain rate over larger area and, therefore, may give more representative results. However, LVDT has the disadvantage of being bulky in their construction and also requires proper calibration. Fortin et al. (2006) estimated uncertainty from strain measurement to be 10^5 when measured directly by the strain gauges and 5×10^4 when calculated from an LVDT signal.

3.5.4 Determination of Particle Size Analysis

Particle size distribution of the reservoir and analogue samples was determined using a combination of sieve analysis and laser diffraction techniques. Standard sieve shaker were used for the sieving analysis and the laser a high-resolution "Matersizer" laser analyser (from Malvern Instruments Ltd) was utilised for the laser diffraction technique. Both techniques rely upon the preparation of a disaggregated sample. Basically intact samples were gently disaggregated into their component particles using a mortar and pestle. The resultant product was then used for grain size analysis. Care was taken to avoid breaking or grinding of the grains. Sieve sizes used for the sieving ranged from 800 μm to 90 μm. Laser particle analysis was used for particle sizes less than 90 μm. A Malvern "Matersizer" laser light scattering particle size analyser was used for the laser particle size analysis (volume percent). Particle size distribution determined by combination of these techniques has led to the characterisation of the particle size distributions across a broad range of sizes. The results for the particle size analysis are presented as plots of grain size (μm) versus cumulative percentage undersize and frequency plots. These plots were constructed using the combined data set obtained from sieve analysis and the laser particle size experiments.

3.5.4.1 *Sieving*

Sieving analysis was performed by passing a known weight of sample material successively through stack of sieves with known size of mesh and weighing the material retained on each sieve to determine the percentage weight within each sieve size opening. The sieves are nested in order of decreasing size from the top to the bottom (direction of the gravitation gradient) and the sample or a portion of the sample is placed on the top sieve.

Sample of known weight (usually 100 g to an accuracy of 0.1 g) was placed on the top sieve of a nest of successively finer sieves. It should be noted that the minimum sieve size

used for dry sieving in this thesis is 90 μm and the maximum is 850 μm. The sieves are mechanically vibrated for 10 minutes. The weight of sediment retained on each sieve is measured and converted into a weight percentage of the total sediment weight. Sequential calculations are then performed to determine the cumulative mass retained on each sieve, the cumulative percent retained on each sieve, and the percent passing each sieve.

3.5.4.2 *Laser Particle Size Analysis*

Laser particle size analysis was performed using a 'Malvern' Mastersizer which incorporates an optical measurement unit that forms the basic particle size sensor, sample dispersion unit and a computer that manages the measurement results (Figure 3.6). The sample dispersion unit provide continuous flow of dispersed particles into a flow cell, while the computer system manages the calculations of field detection of scattered light to produce particle size distribution. The system utilises composite laser light diffraction patterns produced by the disperse particle to compute size distributions.

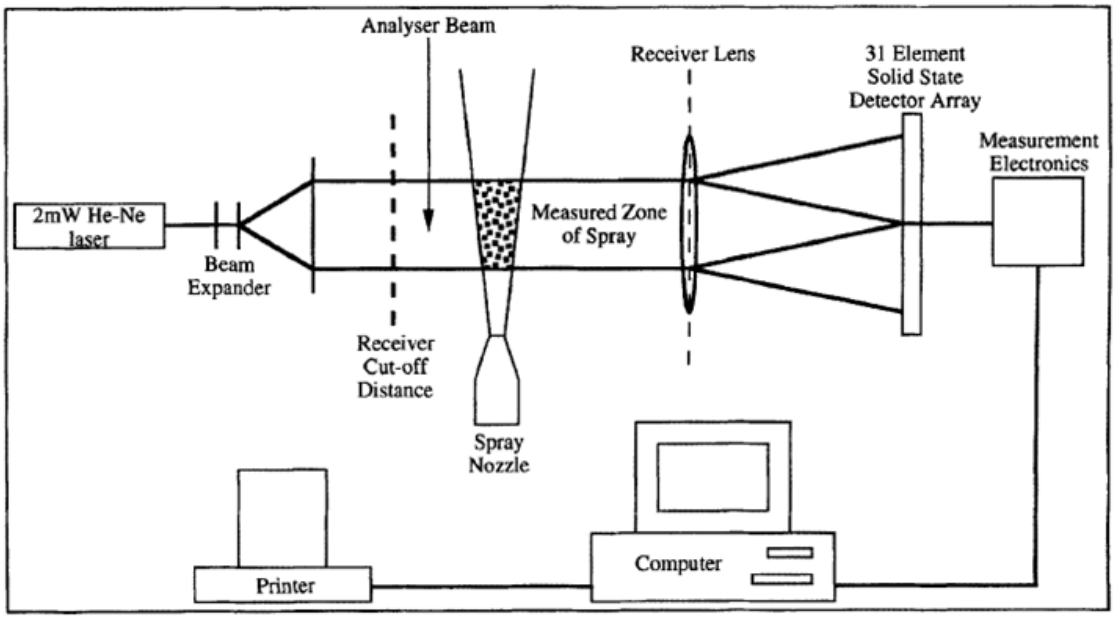

Figure 3.6: Schematic of the laser diffraction unit.

The Mastersizer has three standard user-defined size ranges: 600-1.2, 180-0.5 and 80-0.l μm. It cannot simultaneously cover the complete dynamic range in a single measurement, so the total span is usually broken down into the above size ranges, each selected by fitting the appropriate range lens of focal length 300 mm, 100 mm and 45 mm respectively. When a particle scatters light (sourced from a low power Helium-Neon laser) it produces a unique light intensity characteristic with angle of observation. This light is scattered so that the measured energy on a detector has a peak at a favoured

scattering angle which is related to the particle diameter. Large particles have peak energies in small angles of scatter and vice versa. Over the size range of 2 μm and upwards, the scattering with angle is effectively independent of the optical properties of the material or supporting medium, resulting primarily from diffraction of light around the particle. However at the 0.1 μm size range, interaction of light with the particle is complex and strongly influenced by the optical properties of the particle, necessitating full "Mie" theory modelling of the scattering (Mie theory uses the solution of the electromagnetic wave equations for a spherical particle of specific optical properties). Two optical constants are required to determine the scattering behaviour, the differential refractive index between the dispersant and the particle, and the particle absorption, both of which are user selectable.

Thus it is possible for the computer to predict the scattering signal that would be received from a wide range of materials at a given size. It formulates a table that characterises how a unit volume material of a range of sizes throughout the working range scatters light. Using this theoretical data the computer deduces the volume size distribution that gives raise to the observed scattering characteristics by a process of constrained least squares fitting of the theoretical scattering characteristic to the observed data. The best fit result can either be obtained with no assumed form of size distribution (model independent) allowing the characterisation of multi-modal distribution with high resolution, or else the analysis can be constrained to three known forms of volume distribution, the normal, log-normal or Rosin-Rammler, in which volume distribution is constrained to have single peak which can be completely specified by two parameters of characterising equation, describing the position of the peak on the size scale and width of the distribution. The derivation of the result, the size distribution, V_i can be related to the data, D_j using the matrix equation to describe how a known distribution will scatter light below:

$$D_j = U_{i,j}\, V_i \qquad (3.7)$$

where i is the index of size bands, j is the index of the detector elements and $U_{i,j}$ describes how particles in size band i scatter light to detector element j.

For the model independent mode where no assumption on the form of size distribution is made, volume distribution is estimated based on the measured light energy data and a new light energy distribution is calculated using is equation (3.7). The residual difference is calculated as:

$$\text{Res} = 100\frac{\sum\left(D_j - L_j\right)^2}{\sum D_j} \tag{3.8}$$

where D_j is the measured data and L_j is the data calculated from the estimated volume distribution. The difference between L_i and D_j is used to correct for the initial solution and a new set of value for L_i are calculated. The iterative process is continued until the residual reaches a minimum. The only restriction placed on the volume distribution is that the solution should always be positive.

The two parameter analysis models use a similar analysis technique as the model independent option, however, the volume distribution is constrain to have single peak which can be completely specified by two parameters of characterising equation. The first parameter, X describes the position of the peak on the size scale and the second parameter, N describes the width of the distribution. The natural result of the Malvern laser particle size analyser is a volume distribution. In this thesis, the volume weighted distribution is used since it is closer to sieve size distribution which is based on mass distribution. The volume size distribution can be converted to surface area, length or number distribution using the following formula:

$$X_i = V_i . d_i^{T-3} \tag{3.9}$$

where X_i is the transformed distribution, V_i is the volume is size band i, d_i is the mean diameter of the size band i, and $T = 3$ for volume, 2 for surface, 1 for length and 0 for number.

3.6 Error Analysis

Measurements of physical quantities and result from experimental equipment are usually subjected to errors or uncertainties. In order to obtain representative and accurate experimental results, it is critical to minimise these measurement errors, and to be able to assess their effect on the results obtained. The procedure for estimation of errors due to equipment in this thesis is adopted from Farquhar (1993), since the same equipment is used in those experiments. Thus errors were calculated at the 95% confidence limit using the "method of equal effects" (Doebelin, 1990). The basic procedure is given in Appendix C. The magnitudes of errors due to mechanical measurement are generally dependent on the magnitude of the stress and strain changes with increasing confining pressure. A summary for the error from equipment is presented in Table 3.1.

Paremeter	Error Range (±%)	Comments
Permeability	0.69 - 0.33	0-2000 cc/sec flowtube
	1.43 - 0.05	0-200 cc/sec flowtube
	0.53 - 0.31	0-20 cc/sec flowtube
Porosity	2.31- 1.14	
Elastic Modulus	3.47 - 1.51	6.89 MPa - Confining pressure
	1.69 - 1.17	34.50 MPa - Confining pressure
Poisson's Ratio	50.35 - 7.89	6.89 MPa - Confining pressure
	12.51 - 5.87	34.50 MPa - Confining pressure
Axial Stress at Failure	0.17 - 0.31	6.89 MPa - Confining pressure
	0.15 - 0.25	34.50 MPa - Confining pressure
Confining Pressure	0.15	6.89 MPa - Confining pressure
	0.25	34.50 MPa - Confining pressure

Table 3.1: Summary of measurement errors from equipment.

The errors in the elastic deformation properties are dependent on the magnitude of the component input parameters. Since the magnitude of the stresses and strains change with increasing pressure, the magnitude of the error in the elastic deformation also changes with increasing stress. The error of associated with elastic modulus measurement is obtained by summing the experimental equipment, dimensioning, strain gauge and calculation errors. It is estimated that the elastic modulus has a percentage error ranging from 3.5% to 1.5% at 6.89 MPa confining pressure and from 1.7% to 1.2% at 34.50 MPa confining pressure. Poisson's ratio is subjected to the same errors as the elastic modulus with regards to the equipment, dimension and strain gauge errors. It was estimated that the error in Poisson's ratio to 5.0% to 3.0% at confining pressure of 6.89 MPa and from 3.0% to 2.0% at confining pressure of 34.50 MPa.

In general the errors calculated elastic constants are not significant enough to invalidate the observed trends. In the case of Poisson's ratio, the errors, at the lowest confining pressure are higher which reduces significantly as to permit reasonable qualitative interpretation of the results.

The same procedure was used to evaluate the error in measurement of the axial stress at failure. The error for the axial stress at failure is 0.15% and 0.25% at 6.89 MPa and 34.50 MPa confining pressures respectively. In the multi-failure state test failure is the commutation of many microscopic failure events making identification of the loss in load bearing capacity quite difficult. The error form this source is not quantifiable. Examination of the load displacement curves shows that in general the failure process was halted at the onset of microscopic failure. The error in measuring the confining pressure is

1.50% at 6.89 MPa and reduces to 0.20% at 34.50 MPa. Thus the error transmitted to the calculation of the differential stress at failure will be dominated by the error in confining pressure if the axial stress is judge to be reliable (Farquhar,1993).

3.7 Summary

This chapter described the test materials, testing equipment, procedures and set-ups followed in the experimental part of this thesis. Standard tests according to International Society for Rock Mechanics (ISRM) recommendations were followed in measuring the mechanical properties of the sandstones. The procedures followed in multi-failure state tests, discrete tests, stress sensitivity tests and analysis of errors associated with measurement parameters were also presented. The test results, analysis and their general comparisons will be presented in the next chapter.

4 Determination of Rock Mechanical Properties: Experimental Results

4.1 Introduction

The results of rock mechanical experiment conducted on reservoir and analogue sandstones using equipment and procedures described in chapter 3 are presented in this chapter. The mechanical characterisation of the reservoir sandstones including elastic modulus, Poisson's ratio, failure criteria, strength, rupture mode and granulometric characteristics are first presented. The stress sensitivity of elastic constants and strength of the sandstones have also been characterised to ensure representative data are used.

In the second part of this chapter, a thorough geomechanical appraisal of the analogue sandstones was undertaken to investigate their suitability as rock mechanical analogue for the Famgee reservoir sandstones. Therefore the range of the properties measured on the analogue sandstones are compared with the equivalent range determined for the reservoir sandstones.

4.2 Geomechanical Characterisation of Reservoir Sandstones

A series of tests were conducted on representative samples from seven wells obtained from three fields to determine the evolution of mechanical properties with increasing stress. Elastic constants and strength deformation properties of the samples were evaluated over a range of confining pressures which are thought to reflect the effective reservoir stresses likely to be experienced by the rock *in situ*. The laboratory experiments were specifically designed to obtain the relevant parameters for sand production prediction and wellbore stability analysis. Available well data like reservoir pressures (revealed from repeated formation testing (RFT) and well logs) and drawdown pressure experience during well testing and production were all taken into account in designing the experiment. The range of effective stresses were subsequently calculated, specific to each well and producing horizon (see Table 4.1). This enables stress sensitivity of the mechanical properties of the rock to be taken into consideration in predicting the sand production potential of the wells. Samples were first loaded hydrostatically (principal stresses maintained equal) over the range of values. At each loading stage the axial load was increased by 3 kN and the axial and radial strain measured for the elastic constants to be evaluated. However, mechanical rupture properties from multi-failure state testing were determined on a separate loading cycle due to the irreversible and catastrophic nature of such test.

Stress sensitivity ratio reported in this thesis is defined as the ratio of the measured parameter at near reservoir stress (final confining pressure) relative to the measured data at the initial confining pressure (see Table 4.1). In general, the choice of stress interval to determine stress sensitivity is arbitrary. Samples have been observed to undergo a range of changes in their properties from the initial loading to the final loading conditions. Therefore, the stress sensitivity range adopted here covers the full range of available data and thus errors which could arise from extrapolation are avoided.

The greater stiffness of the compression machine (see section 3.4) compared to the sample enables the post-peak strength behaviour of the sample to be examined. Each rupture test was continued after peak strength has been attained to allow shear displacement of the sample in order to create comminution debris at the final confining pressure. The shearing action between the faces of the shear fractures which form in the sample results in comminution of the sand grains adjacent to the shear surfaces. It is postulated that such debris is a potential source of producible sand. Each sample was sheared for an additional displacement of 0.2 mm after the peak stress. The sample was then unloaded and carefully removed from the Hoek cell for further analysis.

Sample I.D.	Well I.D	Field I.D	Reservoir Horizion	Confining Pressure (MPa)				
				σ_{c1}	σ_{c2}	σ_{c3}	σ_{c4}	σ_{c5}
AFA-1, AFA-2, AFA-3, AFA-4	AFA	Field A	Famgee	10.30	20.70	27.60	31.00	34.50
AFA-5, AFA-6, AFA-7, AFA-8	AFA	Field A	Deekay	10.30	20.70	27.60	34.50	36.50
AFB-1	AFB	Field A	Famgee	10.30	20.70	27.60	32.40	33.10
AFB-2	AFB	Field A	Deekay	10.30	20.70	27.60	34.50	35.10
All	AFC	Field A	Deekay	6.90	13.80	20.70	27.60	34.50
BFA-1, BFA-2, BFA-3, BFA-4	BFA	Field B	Rotliegendes	27.60	34.50	41.28	44.72	48.27
BFB-1, BFB-2, BFB-3, BFB-4	BFB	Field B	Rotliegendes	27.60	34.50	41.28	44.72	48.28
BFC-1, BFC-2, BFC-3	BFC	Field B	Rotliegendes	27.60	34.50	41.28	44.72	48.27
CFA-1	CFA	Field C	Kay	6.90	10.30	20.70	22.90	34.50
CFA-2	CFA	Field C	Kay	6.90	10.30	20.70	23.00	34.50
CFA-3	CFA	Field C	Kay	6.90	10.30	20.70	25.50	34.50
CFA-4	CFA	Field C	Kay	6.90	10.30	20.70	25.60	34.50
CFA-5	CFA	Field C	Kay	6.90	10.30	20.70	26.20	35.20
CFA-6	CFA	Field C	Kay	6.90	10.30	20.70	26.40	35.20
CFA-7	CFA	Field C	Kay	6.90	10.30	20.70	27.30	35.20
CFA-8	CFA	Field C	Kay	6.90	10.30	20.70	31.00	40.30
CFA-9	CFA	Field C	Kay	6.90	10.30	20.70	31.00	41.60

Table 4.1: Confining pressures applied to reservoir samples during the geomechanical appraisal.

4.2.1 Elastic Constants Stress Sensitivity

Elastic modulus (Young's modulus), E and Poisson's ratio, υ as a function of increasing confining pressure are calculated from equation (3.5) and equation (3.6) respectively.

Field A: The relationship between the elastic constants with increasing confining pressure for samples from wells AFA, AFB and AFC are summarised in Table 4.2. The effect of increasing confining pressure on elastic modulus and Poisson's ratio for the Famgee and Deekay samples from wells AFA and AFB are plotted in Figure 4.1 and Figure 4.2 respectively. The figures show that the value of elastic modulus measured at initial confining pressure (approximately 10.34 MPa) ranged from 8.28 to 21.28 GPa with the Poisson's ratio varying from 0.09 to 0.18. Whereas values of elastic modulus measured at near reservoir pressure (approximately 34.5 MPa) ranged from 13.70 to 29.78 GPa and Poisson's ratio from 0.14 to 0.22. These are fairly typical values for sandstones. On the whole the Deekay samples are stiffer than the Famgee samples with the exception of a few low porosity Famgee samples which exhibit high stiffness. The elastic modulus increased in all cases with increasing confining pressure although the Famgee samples tend to be the most stress sensitive. As the confining pressure is increased, the grains become closer to each other and further deformation is reduced. The stress sensitivity ratio shows that elastic modulus measured at the initial confining pressure to the final confining pressure increased by 27% to 88%. This corresponds to the least stress sensitive sample having a stress ratio of 1.27 and the most stress sensitive sample a stress ratio of 1.88. As is typical in sandstones, changes in Poisson's ratio with increasing confining pressure have shown to be unpredictable. In general, the values are either increasing in an erratic path or are fairly constant over the range of pressure. However, at near reservoir stresses values of Poisson's ratio for the Famgee samples are spread over a broader range than the Deekay samples.

Figure 4.3 and Figure 4.4 present plots of the elastic constants versus increasing confining pressure for samples from well AFC with the exception of sample AFC-4. The elastic modulus in all of the samples increased with increasing confining pressure. Samples from well AFC also displayed a wide range of elastic modulus. These values ranged from 5.90 to 15.30 GPa at the initial confining pressure of 10.34 MPa and from 15.60 to 29.50 GPa at the final confining pressure of 34.5 MPa. Sample AFC-4 shows a much higher value of elastic modulus (53.30 and 91.40 GPa at the initial and final confining pressures respectively) than the other samples in this well. Physical observation of this sample did not show any apparent change in structure, however, after failure, it

was noticed that one end of the sample had disintegrated leaving the rest of the core intact. It is thought that there might have been a difference in the structural lithology within the sample resulting in an apparently high stiffness at the centre where the strain gauges are located. The range of elastic modulus stress sensitivity ratio is 1.53 to 2.64 (53% to 164% increment). Poisson's ratio for the samples from well AFC ranged from 0.15 to 0.25 at the final confining pressure of 34.50 MPa. Similar to what was observed in wells AFA and AFB, Poison's ratio were found to increase with increasing confining pressure but could follow an erratic path in some cases.

Field B: Samples from wells BFA, BFB and BFC (Field B) were tested at a higher confining pressure (27.58 to 48.27 MPa). This range of pressure is designed to cover the reservoir depletion stresses in this particular field. Figure 4.5 and Figure 4.6 show the results from all the three wells. The elastic modulus measured on samples from these wells at the initial confining pressure of 27.58 MPa varied from 13.01 to 28.54 GPa with Poisson's ratio varying between 0.02 to 0.22. The average value of the elastic modulus increased with increasing confining pressure from 20.59 GPa at the initial confining pressure of 27.58 MPa to 35.90 GPa at the final confining pressure of 48.27 MPa, representing a range of stress sensitivity ratio from 1.26 to 1.70. It should be noted that strain gauges on four of the samples from these wells malfunctioned during testing which prevented their values of elastic constants to be derived.

Field C: The elastic constants measured on samples from well CFA are graphically shown in Figure 4.7 and Figure 4.8. The elastic modulus measured on samples from this well at the initial confining pressure of 6.90 MPa varied between 2.09 to 5.32 GPa and the Poisson's ratio ranged from 0.07 to 0.19. The four sand samples (CFA-1, CFA-2, CFA-8 and CFA-9) were all found to be stiffer than the shale sample (CFA-6). Elastic modulus trends upward in all cases with increasing confining pressure with the shale sample being the most stress sensitive. The stress sensitivity ratio shows that elastic modulus increased from 32% to 46% over the range of applied confining pressure. In comparison with samples from Field A and Field B, sample tested from these well are generally less stiffer having the lowest values of elastic modulus.

Sample I.D.	Depth (m)	Reservoir Horizion	Confining Pressure (MPa)					Stress Ratio	Confining Pressure (MPa)					Stress Ratio
			σ_{c1}	σ_{c2}	σ_{c3}	σ_{c4}	σ_{c5}		σ_{c1}	σ_{c2}	σ_{c3}	σ_{c4}	σ_{c5}	
			Young's Modulus (GPa)						Poisson's Ratio					
AFA-1	2787.15	Famgee		13.38	15.03	16.40	17.18				0.15	0.17	0.18	
AFA-2	2791.66	Famgee	11.98	14.98	17.12	21.14	21.14	1.76	0.17	0.17	0.19	0.20	0.20	1.18
AFA-3	2796.84	Famgee	17.02	23.83	26.47	27.49	29.78	1.75	0.09	0.20	0.18	0.19	0.20	2.22
AFA-4	2818.18	Famgee	8.28	11.13	12.72	13.19	13.70	1.65	0.14	0.12	0.14	0.11		
AFA-5	3709.11	Deekay	13.50	15.96	20.65	21.28	21.94	1.63	0.09	0.12	0.12	0.12	0.19	2.11
AFA-6	3722.83	Deekay	15.41	19.16	20.85	23.62	25.31	1.64	0.12	0.13	0.14	0.13	0.17	1.42
AFA-7	3724.32	Deekay	14.81	17.78	18.72	20.91	22.22	1.50	0.16	0.12	0.12	0.17	0.20	1.25
AFA-8	3727.52	Deekay	16.10	20.83	22.14	23.61	25.30	1.57	0.14	0.15	0.12	0.13	0.14	1.00
AFB-1	2750.30	Famgee	12.20	14.09	16.65	19.32	22.90	1.88	0.18	0.18	0.19	0.20	0.22	1.22
AFB-2	3427.81	Deekay	21.28	23.41	25.08	25.08	27.02	1.27	0.10	0.12	0.13	0.14	0.14	1.40
AFC-1	5494.05	Deekay	5.90	9.10	11.50	12.90	15.60	2.64	0.07	0.17	0.18	0.19	0.20	2.86
AFC-2	5498.59	Deekay	15.24	18.97	21.90	27.89	29.50	1.94	0.08	0.17	0.15	0.16	0.16	2.00
AFC-3	5509.41	Deekay	9.00	13.90	16.90	20.40	22.70	2.52	0.05	0.09	0.12	0.13	0.15	3.00
AFC-4	5520.93	Deekay	53.30	61.80	73.30	82.00	91.40	1.71	0.15	0.18	0.17	0.23	0.25	1.67
AFC-5	5561.32	Deekay	9.20	13.30	17.40	20.50	22.60	2.46	0.12	0.13	0.15	0.14	0.15	1.25
AFC-6	5572.05	Deekay	9.00	12.50	14.80	16.80	18.30	2.03	0.19	0.19	0.18	0.18	0.17	0.89
AFC-7	5573.48	Deekay	12.00	14.90	16.90	19.20	19.80	1.65	0.04	0.11	0.19	0.20	0.20	5.00
AFC-8	5585.95	Deekay	8.80	12.10	16.40	19.10	21.70	2.47	0.14	0.14	0.16	0.16	0.16	1.14
AFC-9	5601.77	Deekay	15.30	17.70	20.20	22.10	23.40	1.53	0.16	0.18	0.18	0.17	0.23	1.44
AFC-10	5692.23	Deekay	10.90	15.60	20.40	23.10	26.50	2.43	0.13	0.14	0.15	0.17	0.21	1.62

Table 4.2: Elastic constants stress sensitivity data for samples from wells AFA, AFB and AFC.

Sample I.D.	Depth (m)	Reservoir Horizion	Confining Pressure (MPa)					Stress Ratio	Confining Pressure (MPa)					Stress Ratio
			σ_{c1}	σ_{c2}	σ_{c3}	σ_{c4}	σ_{c5}		σ_{c1}	σ_{c2}	σ_{c3}	σ_{c4}	σ_{c5}	
			Young's Modulus (GPa)						Poisson's Ratio					
BFA-1	3020.27	Rotliegendes	20.50	23.40	25.80		26.50	1.29						
BFA-2	3033.45	Rotliegendes	21.37	22.30	29.51	29.06	29.98	1.40	0.10	0.12	0.12	0.13	0.14	
BFA-3	3036.14	Rotliegendes	24.50						0.02	0.04	0.04	0.09	0.12	5.04
BFA-4	3041.90	Rotliegendes	27.54	29.55	33.01	33.85	34.97	1.27	0.16	0.19	0.20	0.21	0.22	
BFB-1	3282.15	Rotliegendes	13.01	13.98	14.58	15.60	18.00	1.38	0.03	0.04	0.09	0.11	0.11	3.55
BFB-2	3286.07	Rotliegendes												
BFB-3	3298.99	Rotliegendes	14.47											
BFB-4	3308.36	Rotliegendes	18.41	20.05	23.05	23.90	27.92	1.52	0.18	0.19	0.18	0.23	0.23	1.25
BFC-1	3441.87	Rotliegendes	19.47	21.10	26.89	31.86	33.04	1.70	0.18	0.17	0.19	0.22	0.20	1.11
BFC-2	3446.98	Rotliegendes	18.06						0.22					
BFC-3	3451.90	Rotliegendes	28.54	29.55	32.55	34.56	35.90	1.26	0.19	0.20	0.23	0.20	0.24	1.26

Table 4.3: Elastic constants stress sensitivity data for samples from wells BFA, BFB and BFC.

Sample I.D.	Depth (m)	Reservoir Horizion	Confining Pressure (MPa)					Stress Ratio	Confining Pressure (MPa)					Stress Ratio
			σ_{c1}	σ_{c2}	σ_{c3}	σ_{c4}	σ_{c5}		σ_{c1}	σ_{c2}	σ_{c3}	σ_{c4}	σ_{c5}	
			Young's Modulus (GPa)						Poissons' Ratio					
CFA-1	1738.15	Kay	5.32	5.98	6.45	6.48	7.02	1.32	0.17	0.19	0.24	0.23	0.24	1.41
CFA-2	1739.98	Kay	4.50	4.83	5.72	5.92	6.32	1.40	0.07	0.14	0.17	0.16	0.17	2.43
CFA-6	1887.09	Kay	2.09	2.35	2.68	3.01	3.05	1.46	0.15	0.13	0.15	0.18	0.20	1.33
CFA-8	1889.76	Kay	5.24	5.66	6.01	6.55	6.98	1.33	0.16	0.19	0.18	0.24	0.23	1.44
CFA-9	1919.94	Kay	3.99	4.54	5.37	5.64	5.78	1.45	0.19	0.20	0.20	0.23	0.24	1.26

Table 4.4: Elastic constants stress sensitivity data for samples from well CFA.

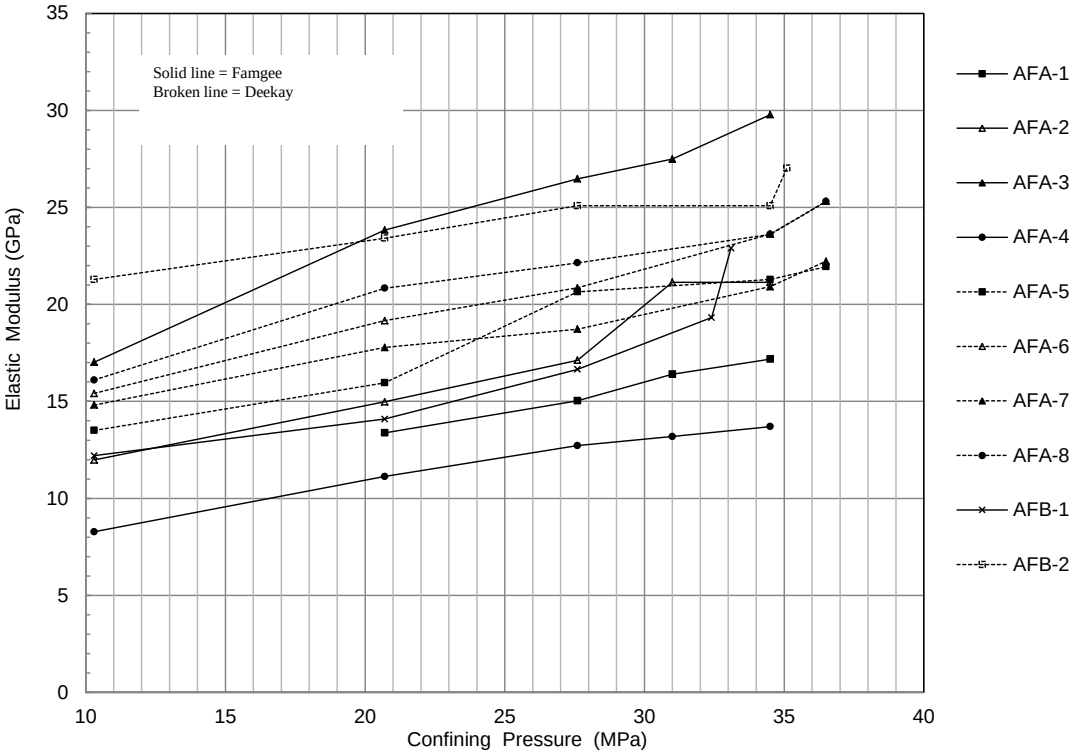

Figure 4.1: Effect of increasing confining pressure on elastic modulus for Famgee and Deekay samples from wells AFA and AFB.

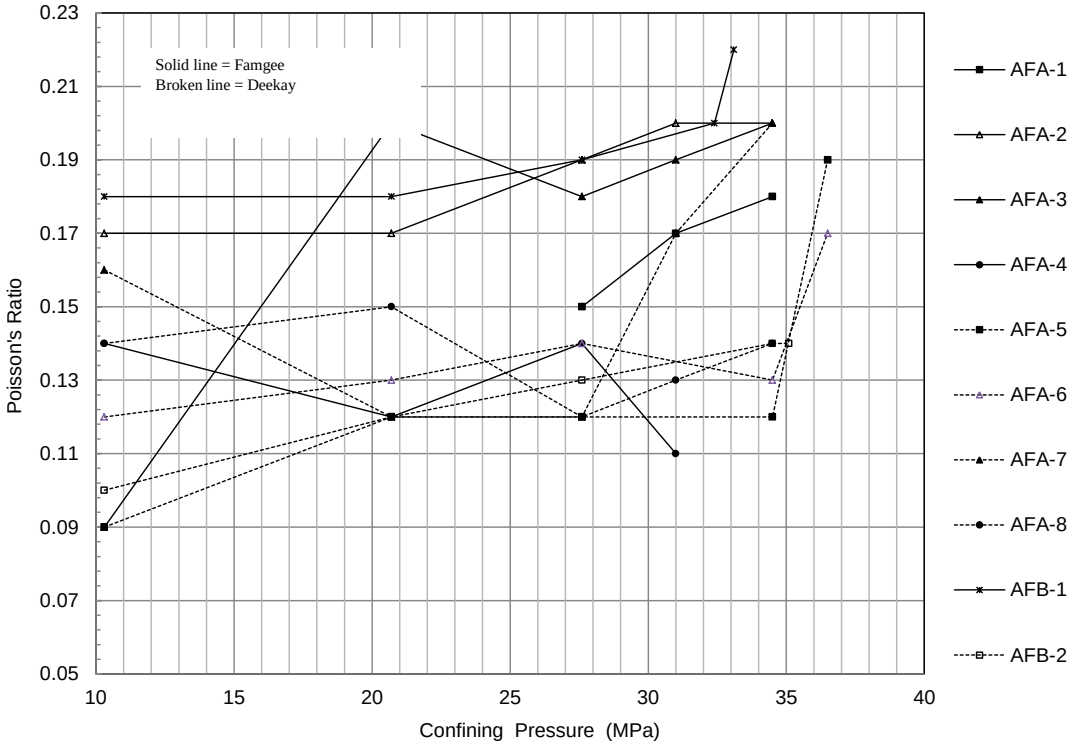

Figure 4.2: Effect of increasing confining pressure on Poisson's ratio for Famgee and Deekay samples from wells AFA and AFB.

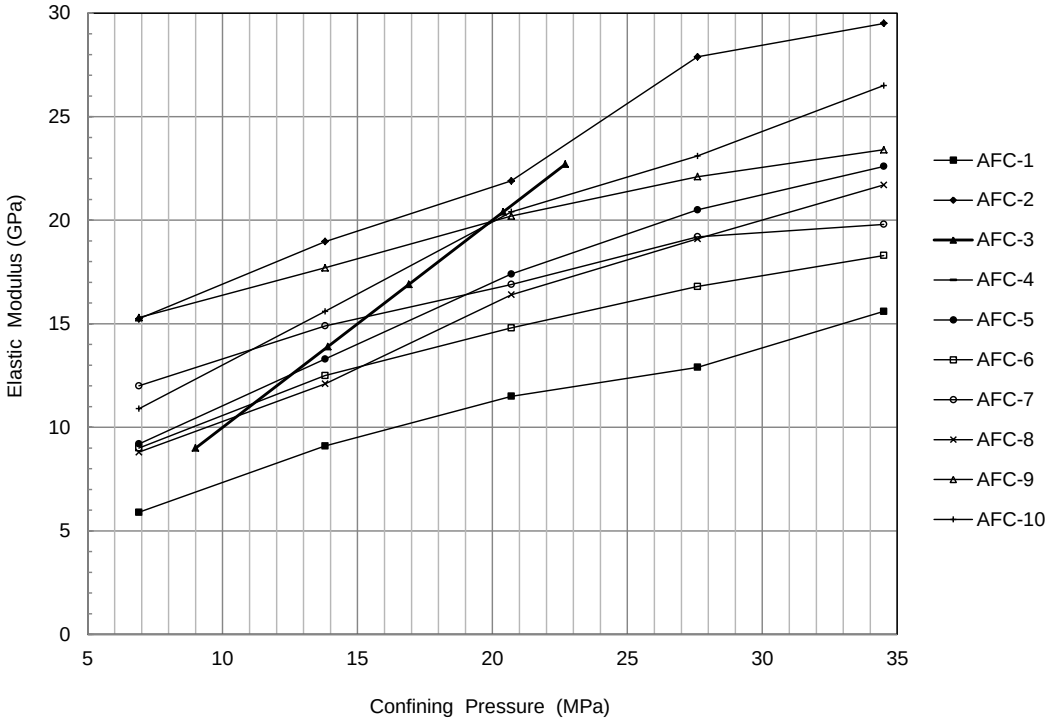

Figure 4.3: Effect of increasing confining pressure on elastic modulus on samples from well AFC.

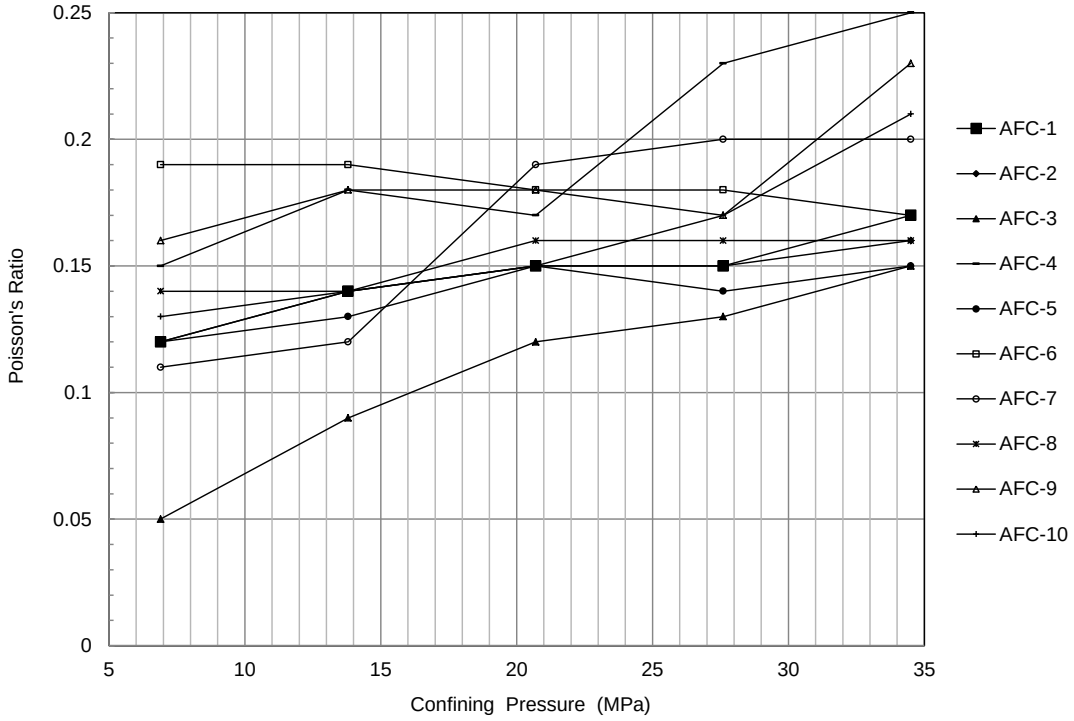

Figure 4.4: Effect of increasing confining pressure on Poisson's ratio for samples from well AFC.

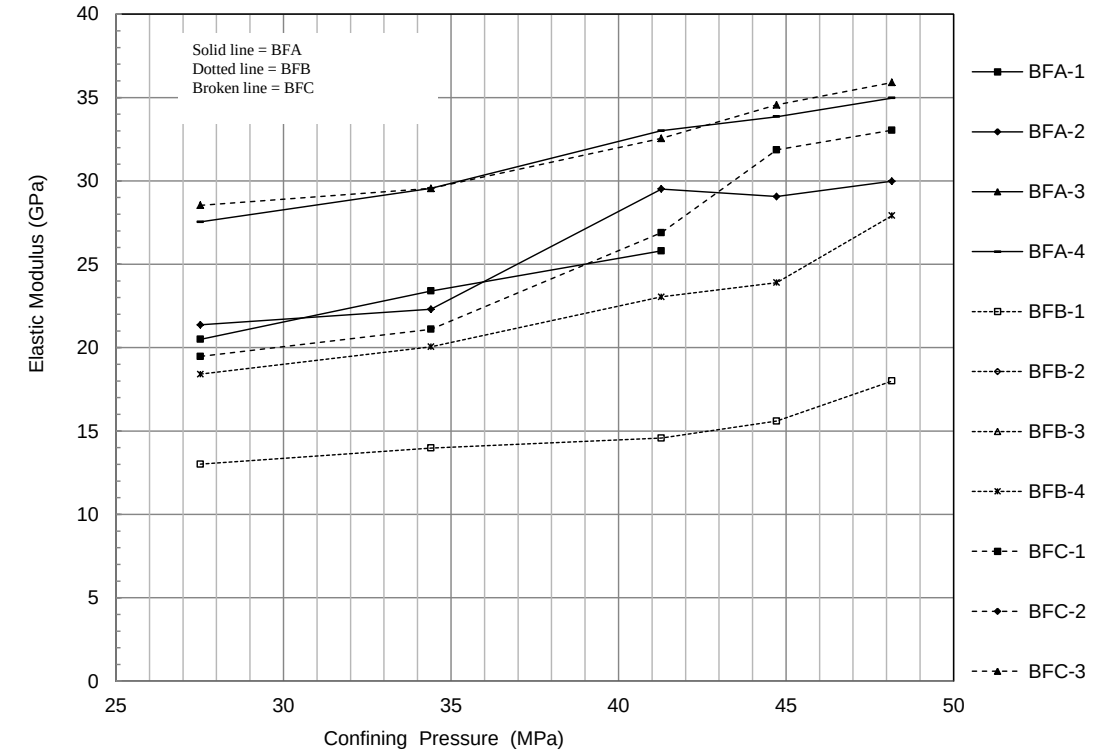

Figure 4.5: Effect of increasing confining pressure on elastic modulus for samples from wells BFA, BFB and BFC.

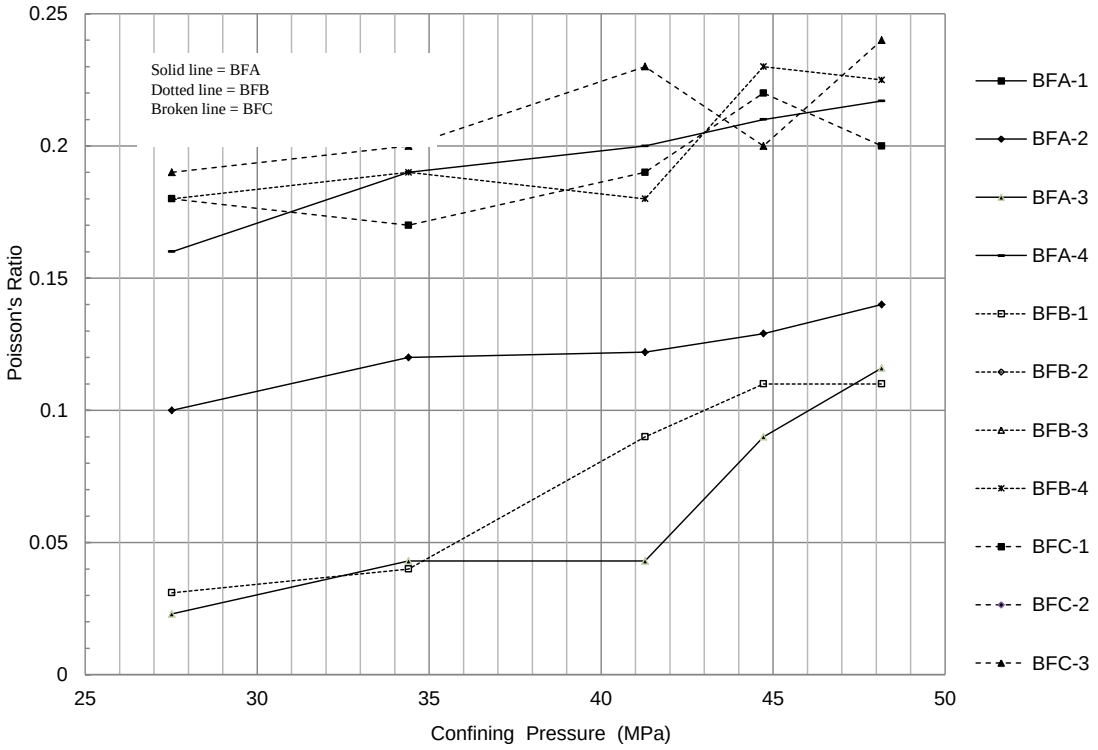

Figure 4.6: Effect of increasing confining pressure on Poisson's ratio for samples from wells BFA, BFB and BFC.

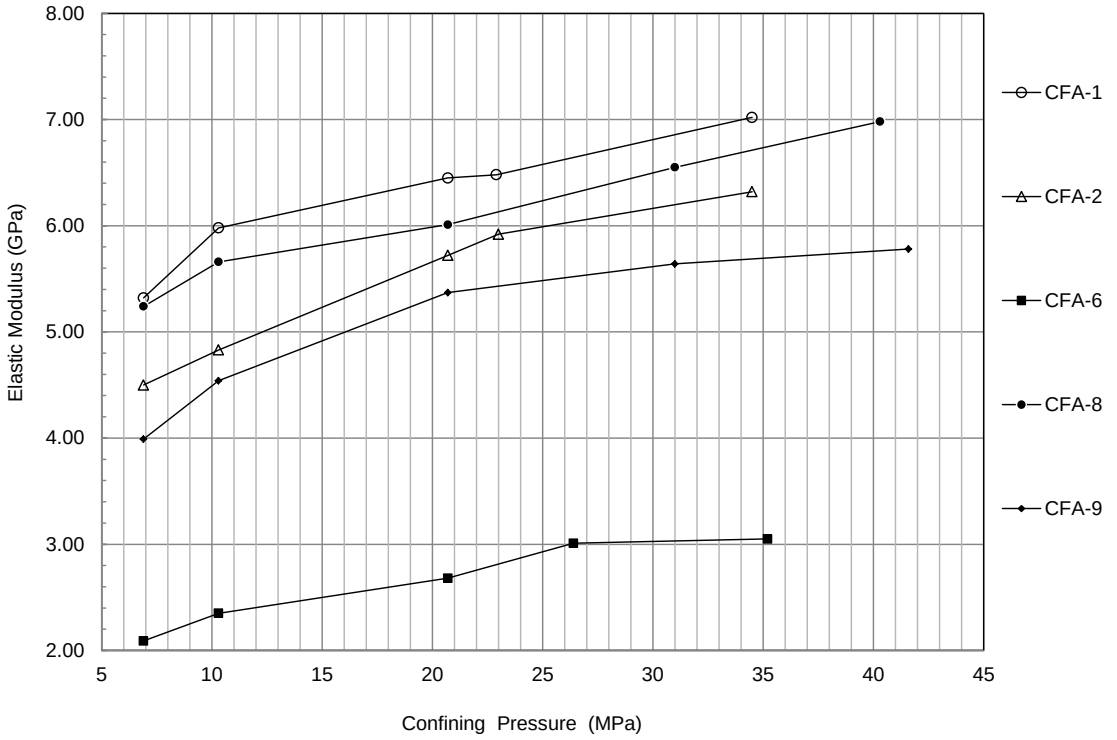

Figure 4.7: Effect of increasing confining pressure on elastic modulus for samples from well CFA.

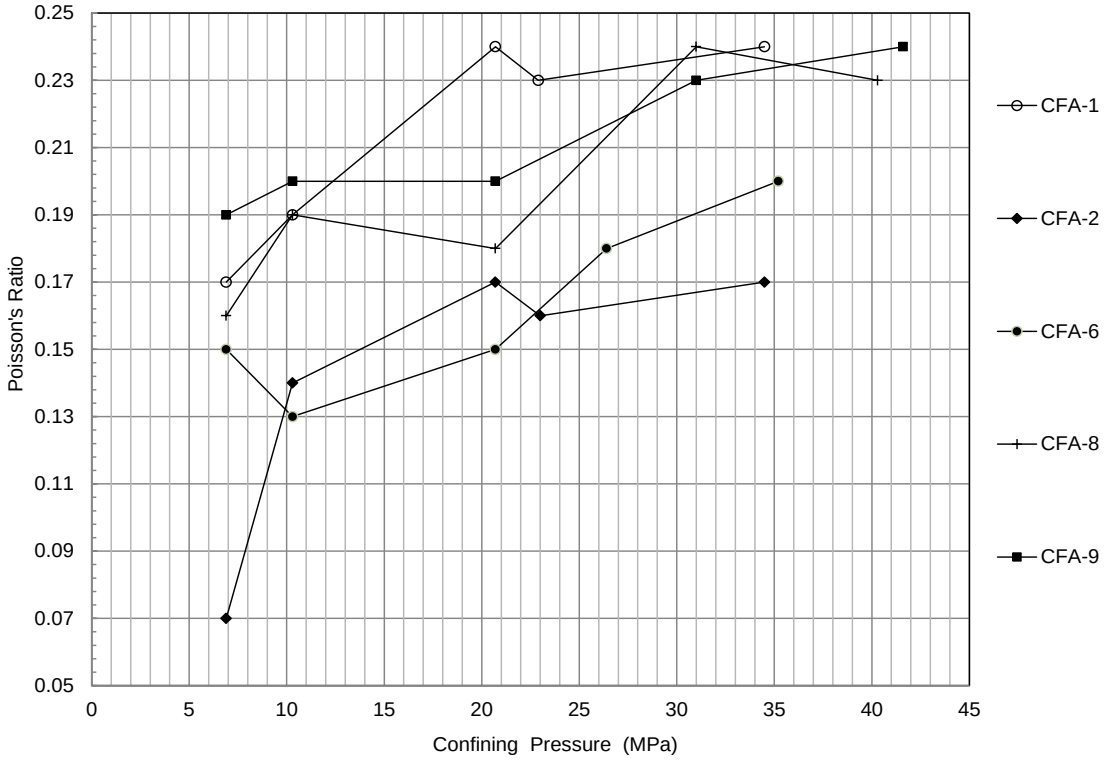

Figure 4.8: Effect of increasing confining pressure on Poisson's ratio for samples from well CFA.

4.2.2 Rupture and Mechanical Properties Stress Sensitivity

Axial stress data, failure properties and deformation mode of each sample under the effect of increasing confining pressure obtained from the multi-failure state testing are discussed in this section. The theoretical Mohr-Coulomb and the empirical Hoek-Brown failure criteria have been employed to describe the increase in compressive strength with confining pressure.

4.2.2.1 *Compressive Strength*

The rupture and mechanical properties of the reservoir samples were evaluated from multi-failure state test to define the failure criteria which describe the development of rock strength with increasing confining pressure. The tests were terminated at confining pressures representing the *in situ* effective stress magnitudes in each reservoir horizon (see Table 4.1) at which the samples are loaded to a complete failure, allowing shear displacement of the sample in order to create comminution debris for sand debris prediction analysis.

The peak or compressive strength which is the capacity of a material to withstand axially directed compressive forces is taken as the peak axial stress or axial stress at failure, σ_a. The peak axial stress was determined from the load-displacement curve as the maximum ordinate of the curve. Generally, a component of the axial stress is represented in the confining pressure. Thus, differential stress, σ_d or the difference between the axial stress and the confining stress ($\sigma_d = \sigma_a - \sigma_c$) can also be used to analyse rock strength as a function of confining stress, σ_c. The confined compression of rock material depends critically on the amount of the radial support or confining stress. A typical load-displacement curve from multi-failure state is shown in Figure 4.15.

Field A: The axial stress at failure, σ_a estimated at each confining pressure from the multi-failure state test for samples from wells AFA, AFB and AFC are summarised in Table 4.5 and the data presented graphically in Figure 4.9 and Figure 4.10 in principal stress space. The axial stress at failure for all the samples from this field ranged from as low as 24.30 to 73.20 MPa at the initial confining pressure of approximately 10.34 MPa and from 78.80 to 170.90 MPa at the final confining pressure of 34.50 MPa. The axial stress at failure increased with increasing confining pressure in all cases as expected. The compressive strength stress sensitivity behaviour of these sandstones ranged from 2.07 to 3.24, equivalent to an increase in strength of approximately 100% to over 200%. Stress

sensitivity of the samples was observed to decrease as the magnitude of strength is increased.

Field B: Table 4.6 and Figure 4.11 present the data and plots of the principal stress and stress sensitivity for samples from wells BFA, BFB and BFC (Field B). Recall that samples from this field were tested at a higher range of confining pressure and consequently are expected to show higher values of axial stress at failure. The axial stress at failure ranged from 122.40 to 219.10 MPa at the initial confining pressure of 27.58 MPa and from 173.70 to 298.00 MPa at the final confining pressure of 48.27 MPa. The stress sensitivity ratio for these samples which ranged from 1.29 to 1.42 is generally lower than previously observed in samples from Field A. This is owing to the fact that narrower range of confining pressure was applied to samples from this field.

Field C: Table 4.7 and Figure 4.12 display the data and plots of the principal stress and stress sensitivity for samples from well CFA. The axial stress at failure ranged from 9.40 to 22.90 MPa at the initial confining pressure of 6.90 MPa and from 67.00 to 152.00 MPa at the final confining pressure. It can be observed that the compressive strength of the samples increased with increasing confining pressure much more rapidly particularly at the around 13.79 to 20.69 MPa confining pressure. This is evident by the high stress sensitivity ratio which ranged from 4.64 to 9.27. Thus, in one of the sample the axial stress at failure increased by as much as 800% when the confining pressure was increased from 6.90 to 34.50 MPa.

4.2.2.2 *Failure Criteria*

The linear Mohr-Coulomb and non-linear Hoek-Brown failure criteria were used to describe the increase in compressive strength with increasing confining pressure for each sample. The two failure criteria can both be expressed in terms of maximum and minimum principal stresses, represented graphically as axial stress versus confining stress plot. A failure envelope which indicates a stable and unstable stress condition for a particular sample can be depicted from the stress plot. A comparison between the Mohr-Coulomb and Hoek-Brown failure envelop can be seen in Figure 4.13 where the two failure criteria are superimposed. This plot can also be used to demonstrate the principle of the multi-failure state test. Consider a point A (Figure 4.13) which lies just below the failure envelope. If this were to represent the state of stress acting on a sample during a multi-failure state test, it is apparent that if the confining pressure were held constant the axial stress which the sample could support would not increase beyond the value indicated by the failure envelope. The effect of increasing the confining pressure prior to failure can

be seen to return the sample to within the stable region (point B) where the sample can now support a greater axial load.

The multi-failure state data calculated from both the Mohr-Coulomb criteria (triaxial stress factor, k, and the uniaxial compressive strength, σ_0) and the non-linear Hoek-Brown (uniaxial compressive strength and constant, m) have been listed together with the compressive strength data in Table 4.5 to Table 4.7. The triaxial stress factor, k and the uniaxial compressive strength, σ_0 in the Mohr-Coulomb criterion are derived respectively from the intercept and slope of the multi-failure state plots. It is assumed that the index, s in the Hoek-Brown criterion for the principal stress plot is equal to 1 since none of the samples appeared to have any existing fracture prior to testing.

Field A: Uniaxial compressive strength values derived from all the samples were found to increase with increasing compressive strength. The uniaxial compressive strength for both Famgee and Deekay samples predicted by the Mohr-Coulomb failure criterion for samples from wells AFA, AFB and AFC ranged from 18.71 MPa to just over 71.93 MPa which is typical spread of values for sandstones over the range of porosity. The Hoek-Brown failure criterion predicted uniaxial compressive strength ranging from 14.43 to 69.18 MPa. This shows that samples from the two horizons exhibit similar range of strength. At lower confining pressures (sub 20.00 MPa) mechanical strength develops at a greater rate with increasing confining pressure amongst the Famgee samples than the Deekay samples. Both sets of samples from the two horizons were found to exhibit similar behaviour as the confining pressure approaches typical reservoir stress value. These results are also reflected in parameters k and m determined from Mohr-Coulomb and Hoek-Brown failure criteria respectively.

Field B: The range of uniaxial compressive strength for samples from wells BFA, BFB and BFC (Field B) as observed within each individual well can be seen in Table 4.6. In general, samples from well BFC tends to be weaker with Mohr-Coulomb derived uniaxial compressive strength values ranging from 55.20 to 85.44 MPa and an average triaxial stress factor of 2.34. Samples from wells BFA and BFB display a broader range of uniaxial compressive strength from 61.46 to 113.83 MPa. This indicates that although the rock type tested are of similar nature, there is quite a range of variability in the ultimate strength of these samples which can be related to several factors such as presence of microfractures. The range of uniaxial compressive strength derived from the Hoek-Brown criterion for all the samples in this field is from 13.24 to 83.52 MPa.

Field C: Uniaxial compressive strength values for samples from well CFA (Field C) derived from the Mohr-Coulomb criterion ranged from 2.70 to 13.81 MPa. The uniaxial compressive strength of the shale sample (CFA-6) is lower than the four sand samples.

4.2.2.3 *Failure Mode*

Porous sandstones under different loading conditions have been observed to exhibit one of the three macroscopic failure modes after the failure stress has been attained (Jamison and Stearns, 1982, Fisher et al., 1999). These failure modes have been classified as brittle, ductile and transitional failure (Bésuelle et al., 2000). Brittle failure results in the formation of discrete slip planes with macroscopic displacement which accommodates most of the strain, while ductile failure is characterised by distributed deformation and does not result in the formation of discrete slip surfaces, instead strain is accommodated throughout the sample (Fisher et al., 1999). Ductility has also been defined as a deformation without any loss of compressive strength (Byerlee, 1968), characterised by lack of major macroscopic plane of failure or shear zone (Scott and Nielsen, 1991). Distinction between the three failure modes is based on whether or not a sample is capable of undergoing a substantial permanent strain with or without macroscopic fracture (Paterson and Wong, 2005, Wong and Baud, 2012). The effective confining pressure is thought to be the dominant factor controlling the transition from brittle faulting to ductile flow (Handin et al., 1963b), however, since the evolution of porosity and stress are coupled, the initial porosity in addition to effective stress has been found to also play a critical role on the failure mode (Hirth and Tullis, 1989, Wong, 1990, Scott and Nielsen, 1991, Wong and Baud, 2012).

After each test, samples were carefully removed from the Hoek cell and examined for failure pattern. Generally, failure modes are defined based on visual observation of the shape of the load-displacement or the stress-strain curves recorded up to and beyond failure (Scott and Nielsen, 1991). In most of the samples tested, failure mode at the end of each test is representative of the brittle mode, this can be attributed to the range of the final confining pressures (approximately 34.50 to 48.27 MPa) employed in the tests which are relatively low stresses. However, a number of samples also exhibit ductile and transitional failure behaviour. Typical representation of the three modes of failure is shown in Figure 4.15 and stress-strain curves recorded during multi-failure state test for samples are shown in Figure 4.16. However, due to malfunctions of the strain gauges, stress-strain curves for samples from well CFA could not be obtained. In such cases failure modes was obtained from the load-displacement curves.

In wells AFA, AFB and AFC, eleven samples (which are the least porous) underwent brittle failure resulting in a single through-going shear fracture. Ductile failure by cataclastic flow was observed in seven samples, whilst the remaining two samples were observed to display failure characteristic of brittle/ductile transition. All the samples from wells BFA, BFB and BFC were found to display failure features in accordance with brittle failure mode. This can also be related to porosity as the range of porosity in these samples is from 8.20% to 18.20% with an average value of 12.71%. A similar scenario is observed in well CFA where only one sample (the least porous) failed in brittle mode while the remaining samples had failure characteristics which indicates ductile failure mode. This is an indication that samples display different failure modes which can be related to porosity (Farquhar et al., 1994).

Generally in the brittle failed samples, axial stress normally progress to a peak value, beyond which strain softening is observed, followed by a sharp down turn in the load-displacement curve to a residual value. The compressive strength of these samples shows a positive correlation with the confining pressure, which is typical of Mohr-Coulomb type of brittle failure (Paterson and Wong, 2005). Macroscopic observation of the brittle failed samples show that failure is characterised by a single diagonal, through-going fracture oriented at an angle of 21.0° to 58.0° to the direction of the maximum principal stress. This is probably due to the localisation of deformation on a shear fracture that characterised the brittle field (David et al., 2001). Shearing displacement along the plane of the fracture which often exhibited slickenside and gouge (shear debris) is the main feature of the failed samples. This failure mode is a qualitatively similar to fractures observed in brittle rocks under low to moderate confining pressure (Vajdova et al., 2004, Jaeger et al., 2007). Most of the brittle failed samples were cleanly separated into two fracture halves; however, few of the brittle failed samples retained some attraction within the fractures or shear bands (e.g. Wong et al., 1997).

The ductile failed samples failed by a combination of cataclasis with no shear localisation, which resulted in the end cones splitting into two or more pieces and in some cases complete disaggregation of the sample. Basically, the ductile failed samples were observed to show a macroscopic 'barrelled shape' upon retrieval from the Hoek cell. The load-displacement curve show absence of any sharp downward breaks in slope after yield point, but a slow transition from the strain softening toward the strain hardening behaviour is observed. These samples have higher failure angles (40.9° to 90.0°) than the brittle failed samples in respect to the direction of the maximum stress.

Failure behaviour in the transitional mode is characterised by development of conjugate shear bands as equally observed by Bésuelle et al. (2003). Post-failure observation of the samples shows a shear failure bands that are incomplete or incipient conjugates shear bands. There appears to be shear displacement within the fracture zone and the load displacement plots indicate stress softening after the axial stress reached a peak value. It is suggested that the failure mechanism in these samples must have switched from brittle to ductile failure resulting in cataclastic flow occurring mainly in the broken grains of the fracture zone.

Sample I.D.	Depth (m)	Reservoir Horizion	Confining Pressure (MPa)					Stress Ratio	Failure Criteria						Failure Mode	
			σ_{c1}	σ_{c2}	σ_{c3}	σ_{c4}	σ_{c5}		Mohr-Coulomb			Hoek-Brown				
			Axial Stress, σ_a (MPa)						σ_0	k	r_2	σ_0	m	r_2		
AFA-1	2787.15	Famgee	35.40	50.3	74.40	92.5	101.5	2.87	27.39	2.17	0.99	21.38	5.39	0.99	Ductile	
AFA-2	2791.66	Famgee	40.40	57.1	82.20	102	119.1	2.95	30.08	2.50	0.99	18.13	9.88	0.97	Brittle	
AFA-3	2796.84	Famgee	64.80	86.9	131.80	158.1	170.9	2.64	51.73	3.53	0.98	35.94	14.00	0.98	Brittle	
AFA-4	2818.18	Famgee	57.90	80.6	113.00	138.4	149.1	2.58	48.01	2.98	0.98	35.94	14.00	0.99	Brittle	
AFA-5	3709.11	Deekay	42.60	54.8	71.50	84.2	91.7	2.15	38.96	1.45	0.97	38.76	1.08	0.81	Ductile	
AFA-6	3722.83	Deekay	46.70	63.6	87.00	105.4	110.3	2.36	42.91	1.92	0.95	41.69	2.60	0.84	Ductile	
AFA-7	3724.32	Deekay	45.30	62.2	87.10	107.5	122.2	2.70	37.92	2.27	0.99	32.56	4.90	0.99	Transitional	
AFA-8	3727.52	Deekay	60.20	75.7	100.90	121.3	139.9	2.32	51.15	2.34	0.99	46.19	4.56	0.99	Brittle	
AFB-1	2750.30	Famgee	24.30	39.4	58.60	76	78.8	3.24	18.71	1.84	0.98	15.20	3.73	0.94	Ductile	
AFB-2	3427.81	Deekay	73.20	91.7	123.10	149.5	151.3	2.07	64.76	2.63	0.97	60.69	5.08	0.93	Briitle	
AFC-1	5494.05	Deekay	42.20	61.5	75.20	87.2	100	2.37	26.30	2.22	0.98	21.68	5.23	0.98	Ductile	
AFC-2	5498.59	Deekay	52.10	81.3	100.50	116.9	135.2	2.60	31.24	3.13	0.98	14.43	20.02	0.99	Transitional	
AFC-3	5509.41	Deekay	77.30	105.5	126.40	142.8	159.1	2.06	57.51	3.01	0.98	50.74	7.65	0.99	Brittle	
AFC-4	5520.93	Deekay	51.10	69.3	83.00	93	103.9	2.03	34.84	2.12	0.97	32.93	3.56	0.94	Ductile	
AFC-5	5561.32	Deekay	66.50	89.3	107.50	123.9	136.7	2.06	47.79	2.71	0.99	42.01	6.29	0.98	Brittle	
AFC-6	5572.05	Deekay	37.40	59.2	78.40	90.2	107.5	2.87	19.38	2.62	0.98	20.54	3.45	0.95	Ductile	
AFC-7	5573.48	Deekay	52.90	73.9	88.50	100.3	113.1	2.14	36.05	2.34	0.98	32.43	4.80	0.97	Brittle	
AFC-8	5585.95	Deekay	76.60	98.5	116.80	135.1	145.1	1.89	58.08	2.66	0.99	53.81	5.35	0.99	Brittle	
AFC-9	5601.77	Deekay	72.80	89.2	101.90	112.9	125.6	1.73	60.29	1.93	0.99	58.91	2.42	0.99	Brittle	
AFC-10	5692.23	Deekay	86.70	116.8	135.10	145.1	159.7	1.84	71.93	2.69	0.96	69.18	4.89	0.95	Brittle	

Table 4.5: Compressive strength, failure criteria and failure mode of samples from wells AFA, AFB and AFC. (*see Table 4.1 for values of the confining pressure levels).

Sample I.D.	Depth (m)	Reservoir Horizion	Confining Pressure (MPa)					Stress Ratio	Failure Criterion						Failure Mode	
			σ_{c1}	σ_{c2}	σ_{c3}	σ_{c4}	σ_{c5}		Mohr-Coulomb			Hoek-Brown				
			Axial Stress, σ_a (MPa)						σ_0	k	r_2	σ_0	m	r_2		
BFA-1	3020.27	Rotliegendes	169.70	193.4	213.10	221	230.90	1.36	90.70	2.93	1.00	57.13	10.99	0.99	Brittle	
BFA-2	3033.45	Rotliegendes	144.10	165.8	183.50	193.4	199.30	1.38	71.25	2.70	0.98	35.54	12.87	0.99	Brittle	
BFA-3	3036.14	Rotliegendes	153.90	173.7	189.50	197.4	203.30	1.32	89.37	2.40	0.99	73.64	5.37	0.98	Brittle	
BFA-4	3041.90	Rotliegendes	155.90	173.7	189.50	197.4	201.50	1.29	95.05	2.26	0.99	83.52	4.26	0.97	Brittle	
BFB-1	3282.15	Rotliegendes	219.10	246.7	276.30	286.2	298.00	1.36	113.83	3.86	0.99	44.67	28.28	0.99	Brittle	
BFB-2	3286.07	Rotliegendes	137.70	156.1	171.90	179.1	188.60	1.37	71.67	2.42	0.99	49.02	7.25	0.99	Brittle	
BFB-3	3298.99	Rotliegendes	173.70	197.4	217.10	231	238.80	1.37	86.89	3.18	0.99	33.60	21.89	0.99	Brittle	
BFB-4	3308.36	Rotliegendes	126.30	144.1	159.90	167.8	175.60	1.39	61.46	2.38	0.99	34.97	8.92	0.99	Brittle	
BFC-1	3441.87	Rotliegendes	153.90	171.7	189.50	197.4	205.30	1.33	85.44	2.50	0.98	65.26	6.52	0.99	Brittle	
BFC-2	3446.98	Rotliegendes	122.40	140.1	157.90	163.8	173.70	1.42	55.20	2.45	0.99	13.24	24.18	0.99	Brittle	
BFC-3	3451.90	Rotliegendes	134.20	152	167.80	173.7	175.60	1.31	79.05	2.08	0.97	69.27	3.69	0.92	Brittle	

Table 4.6: Compressive strength, failure criteria and failure mode of samples from wells BFA, BFB and BFC. (*see Table 4.1 for values of the confining pressure levels).

Sample I.D.	Depth (m)	Reservoir Horizion	Confining Pressure (MPa)					Stress Ratio	Failure Criterion						Failure Mode	
			σ_{c1}	σ_{c2}	σ_{c3}	σ_{c4}	σ_{c5}		Mohr-Coulomb			Hoek-Brown				
			Axial Stress, σ_a (MPa)						σ_0	k	r_2	σ_0	m	r_2		
CFA-1	1738.15	Kay	22.90	39.70	64.60	73.30	108.00	4.72	13.81	2.50	0.98	15.54	9.89	0.99	Ductile	
CFA-2	1739.98	Kay	21.30	37.30	63.90	70.30	105.00	4.93	10.93	2.40	0.99	12.54	13.54	0.99	Brittle	
CFA-6	1887.09	Kay	9.40	24.50	40.20	52.30	67.00	7.13	4.08	1.80	0.98	3.78	21.04	0.98	Ductile	
CFA-8	1889.76	Kay	19.50	32.20	54.00	73.00	90.40	4.64	13.09	1.90	0.97	14.32	4.57	0.97	Ductile	
CFA-9	1919.94	Kay	16.40	34.20	62.30	103.90	152.00	9.27	2.70	3.10	0.98	2.93	13.10	0.98	Ductile	

Table 4.7: Compressive strength, failure criteria and failure mode of samples from well CFA. (*see Table 4.1 for values of the confining pressure levels).

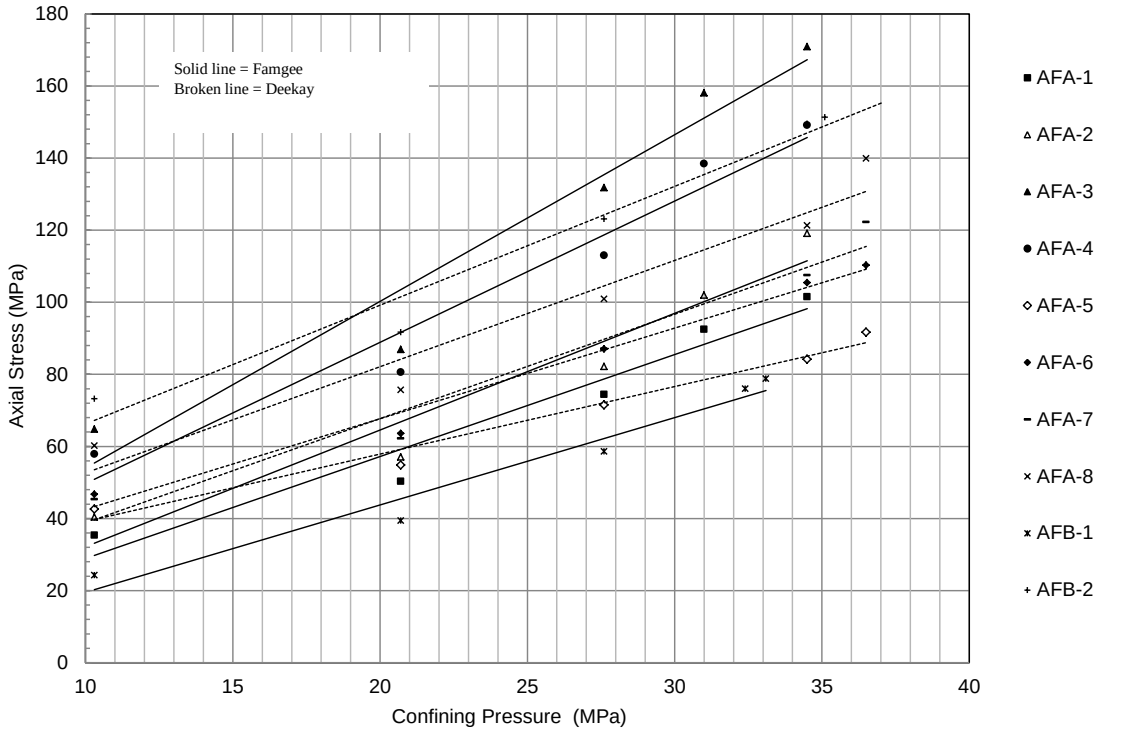

Figure 4.9: Principle stress plot resulting from multi-failure test for Famgee and Deekay samples from wells AFA and AFB.

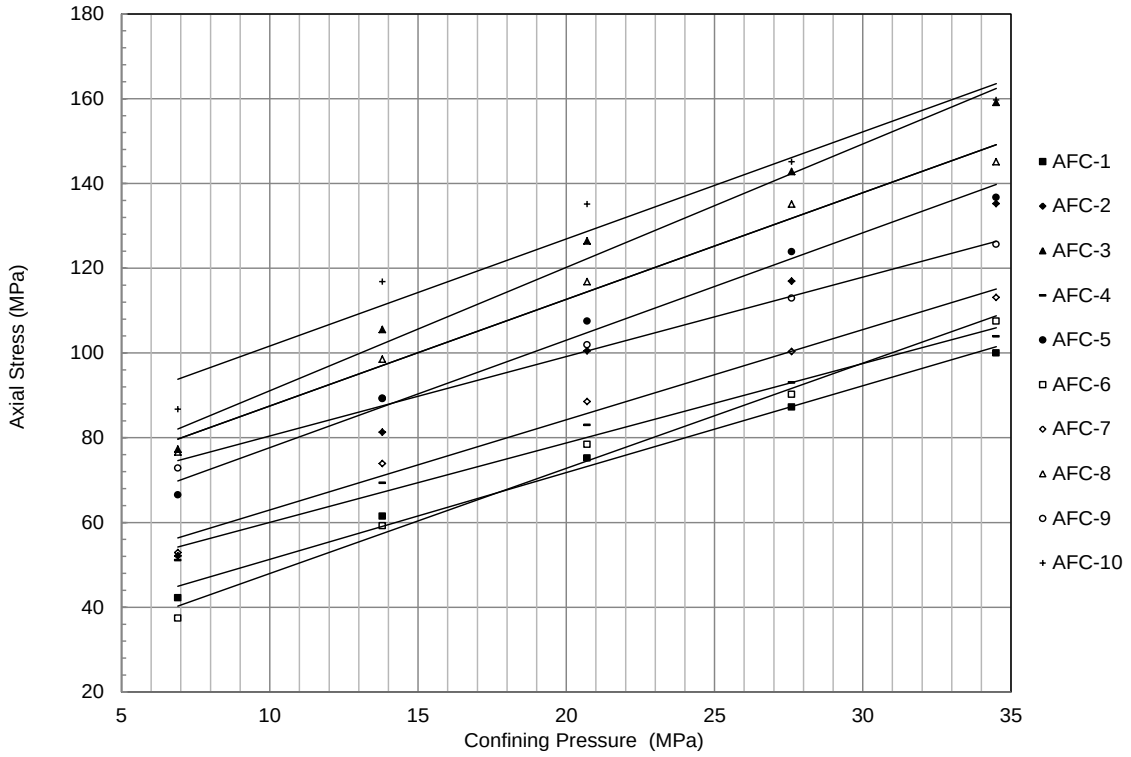

Figure 4.10: Principle stress plot resulting from multi-failure test for samples from well AFC.

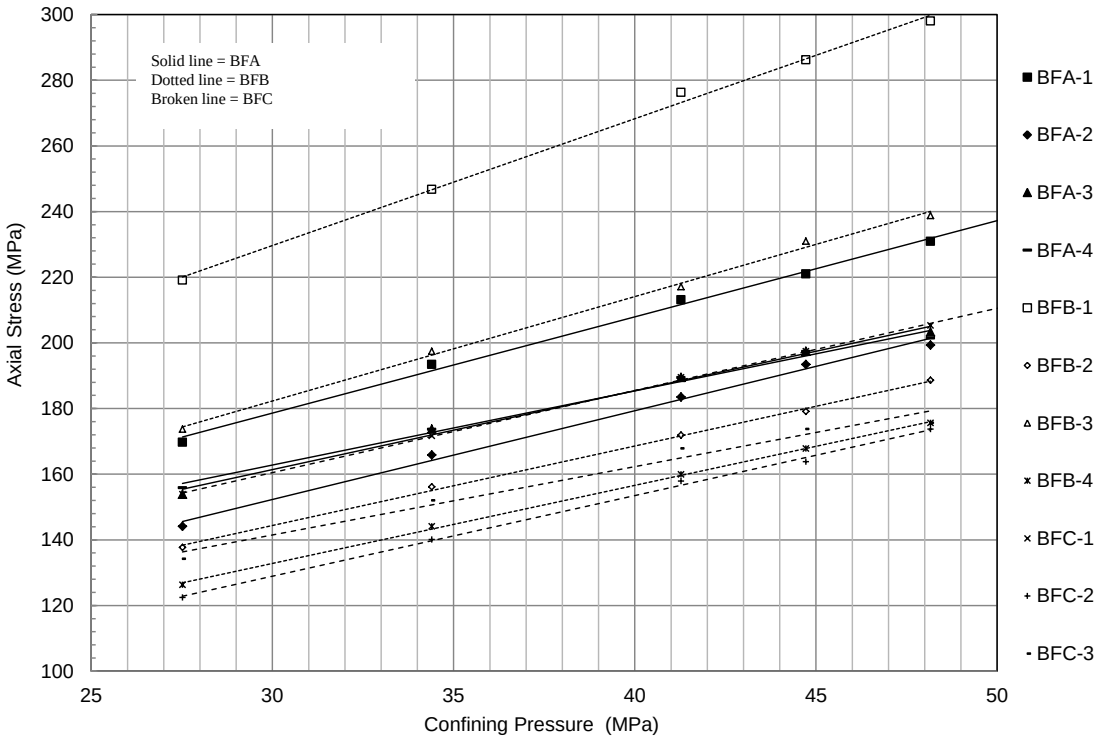

Figure 4.11: Principle stress plot resulting from multi-failure test for samples from wells BFA, BFB and BFC.

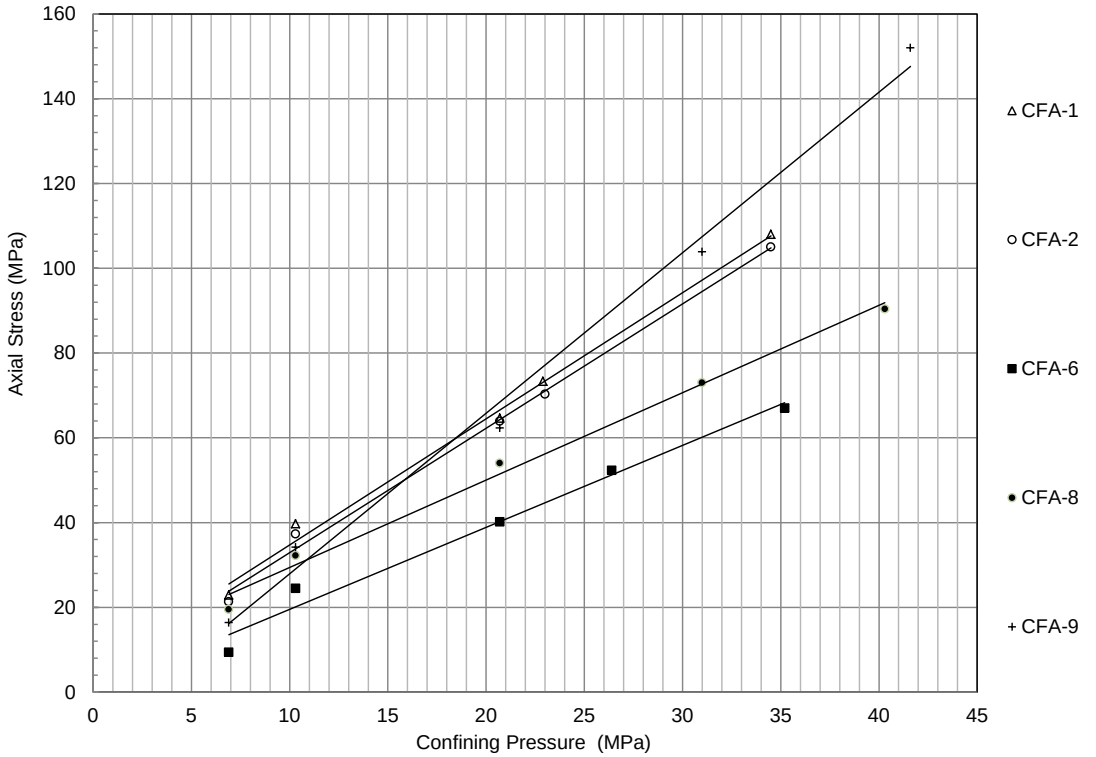

Figure 4.12: Principle stress plot resulting from multi-failure test for samples from well CFA.

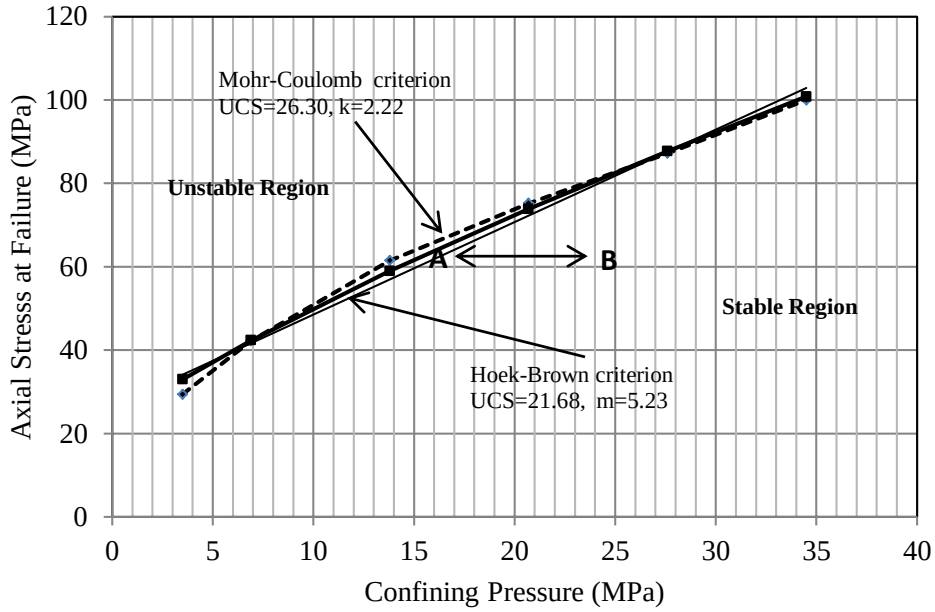

Figure 4.13: Demonstration of the multi-failure test using Mohr-Coulomb and Hoek-Brown failure criteria

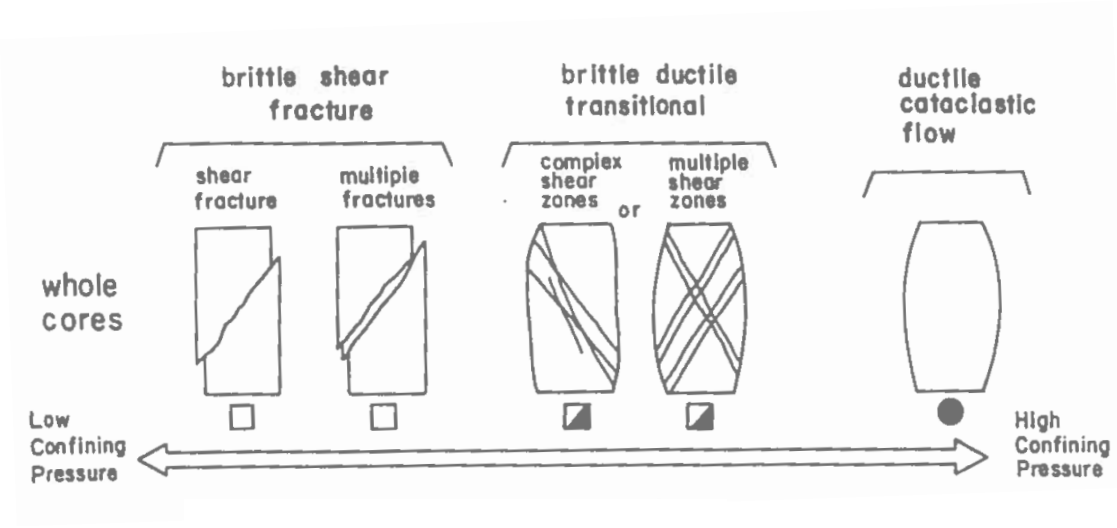

Figure 4.14: Deformation and failure mode of sandstones as a function of increasing confining pressure (after Scott and Nielsen, 1991).

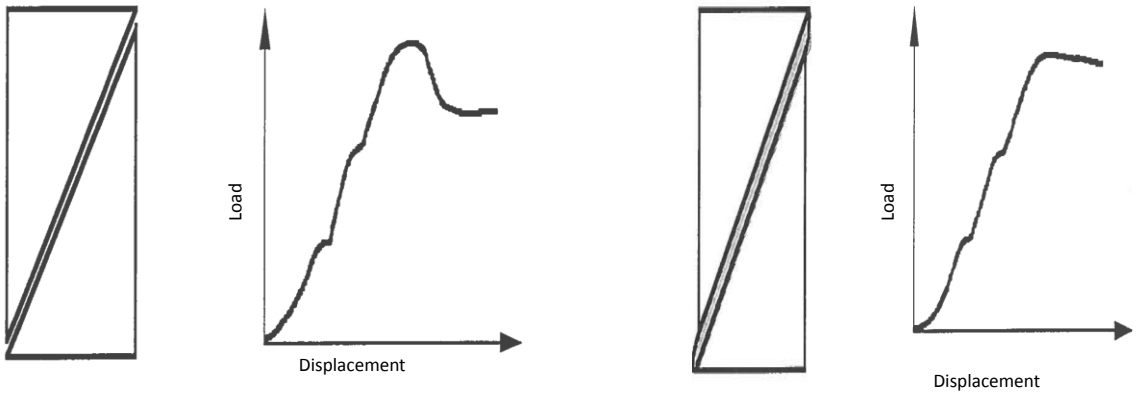

a) Brittle failure mode

b) Transitional failure mode

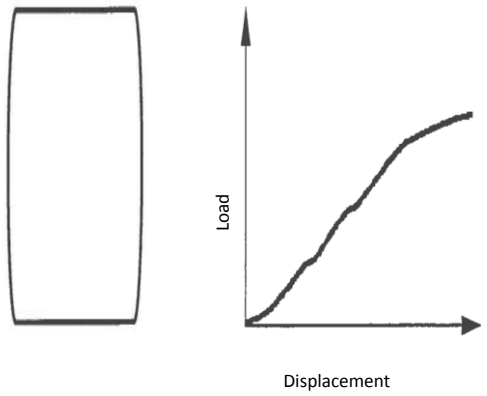

Figure 4.15: Representation of the three modes of failure.

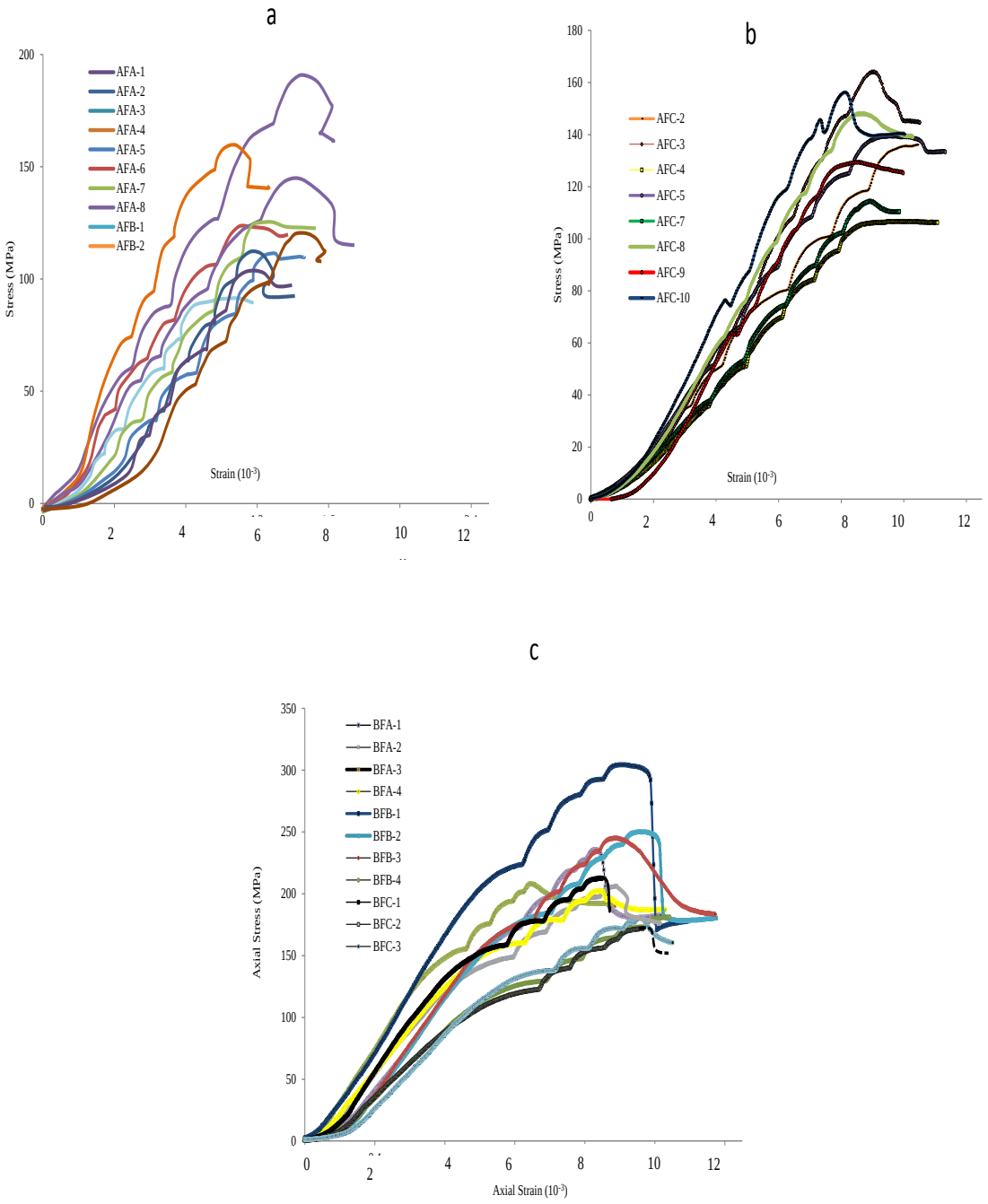

Figure 4.16: Stress-strain curves showing failure modes for samples from (a) well AFA and AFB, (b) well AFC and (c) wells BFA, BFB and BFC.

4.3 Geomechanical Characterisation of Analogue Sandstones

4.3.1 Introduction

The acquisition of core samples from entire reservoir interval are usually prohibitively expensive (Ameen et al., 2009), making the number of representative cores insufficient for a complete mechanical characterisation across the relevant interval of the reservoir (Holt et al., 2005). Reservoir analogue samples can offer an alternative means of evaluating reservoir mechanical properties. However, it is essential for the reservoir analogue sample to possess some salient and critical features of the original reservoir rock particularly in relation to the objective of the test and its application. In order to satisfy these requirements, it becomes absolutely necessary to establish both physical and mechanical relationships between the analogue and the original reservoir samples.

Following the mechanical appraisal of the reservoir sandstones (section 4.2), a thorough rock geomechanical characterisation was undertaken on five analogue sandstones to first assess their suitability as potential reservoir analogues particularly for the Famgee sandstone and secondly, their applicability in conducting laboratory studies on sand debris production prediction and wellbore stability. Core samples obtained from the Clashach, Doddington, Fife Silica, Lochaline and Locharbriggs sandstones described in section 3.2.2 were tested at confining pressure up to 34.50 MPa. This limit of confining pressure was dictated partly by the *in situ* effective stress magnitudes likely to be encountered in the UK North Sea reservoirs and partly by the rationale of the study; experiments were conducted under conditions which will induce brittle fractures with sufficient formation of comminution debris as opposed to distributed damage associated with ductile deformation. Since this range of stress is comparable to that found in the North Sea reservoirs, rupture and deformation characteristics of these sandstones at such stress can aid analysis of the North Sea sandstones by serving as reservoir analogues. Both the compressive strength and the rupture deformation mode are very important factors in determining whether a particular rock is a suitable mechanical analogue since the post-failure behaviour of brittle and ductile rocks are quite different and can have significant influence on the post-failure load bearing capability of the rock around a wellbore or perforation cavity.

4.3.2 Basic Petrophysical Characterisation of the Analogue Sandstones

In order to satisfy the requirements to be considered as analogue reservoir sandstone, the rock selected should possess similar fluid transport and storage capacity with the

original reservoir rock. This requirement is necessary because pore pressure changes and hence effective stresses acting in the reservoir will be influenced by the pressure drop which develops between the wellbore and the drainage boundaries. This pressure drop is dependent on permeability (and to a lesser extent porosity), thus a suitable analogue rock should match the fluid transport characteristics in addition to mechanical properties of the original reservoir rock. Ambient porosity and permeability data were determined for each of the sandstones using the equipment and procedure described in section 3.3. The five different sandstones were found to span a wide range of porosities and permabilities as shown in **Error! Reference source not found.**.

4.3.3 Mechanical Characterisation of the Analogue Sandstones

The elastic and mechanical properties of the analogue sandstones were determined from multi-failure state test at confining pressures of 6.90, 13.79, 20.69, 27.58 and 34.50 MPa using the same procedures and apparatus that were applied to the reservoir sandstones. The results of the mechanical characterisation of the analogue sandstones tested are summarised in Table 4.8 and Table 4.9.

4.3.3.1 *Clashach*

Four samples from the Clashach sandstone (CLS-1, CLS-2, CLS-3 and CLS-4) were tested. Figure 4.17 and Figure 4.18 display the evolution of elastic modulus and Poisson's ratio with confining pressure respectively. The elastic modulus ranged from 23.35 to 29.54 GPa at the initial confining pressure of 6.90 MPa and from 31.66 to 35.01 GPa at the final confining pressure of 34.50 MPa. The stress sensitivity ratio ranged from 1.19 to 1.36, representing an increase of 19% to 36%. Thus, the elastic modulus of the Clashach sandstones can be considered to be weakly pressure dependant. Poisson's ratio ranged from 0.14 to 0.19 at the initial confining pressure and from 0.17 to 0.21 at the final confining pressure. Both the elastic modulus and Poisson's ratio increased with increasing confining pressure although the increase in Poisson's ratio in some samples followed an erratic path.

Figure 4.19 shows the plots of the axial stress at failure versus increasing confining pressure for the Clashach sandstone. The axial stress at failure ranged from 66.98 to 92.40 MPa at the initial confining pressure and from 163.50 to 176.32 MPa at the final confining pressure. This shows an average stress sensitivity ratio of 100%. This result is in agreement with experiment conducted on the Clashach sandstone by Ngwenya et al. (2003) at similar range of confining pressure. Ojala et al. (2004) also reported a peak

strength of 123 MPa for Clashach sandstone tested at confining pressure of 13.5 MPa. The compressive strength of all the four samples are quite similar, however, sample CLS-2 is slightly weaker than the other three samples. A linear regression has been fitted to the data to produce uniaxial compressive strength and the triaxial stress factor for the Mohr-Coulomb failure criterion. Uniaxial compressive strength values ranged from 43.85 to 76.59 MPa.

Three of the Clashach samples (CLS-1, CLS-3 and CLS-4) failed in a brittle mode apparently due to the pervasive quartz cementation of the Clashach (Ojala et al., 2004). The brittle failed samples have a distinctive feature characterised by a single macroscopic failure plane and represented by a large distinct stress drop on the stress-strain curve (Figure 4.32a). However, sample CLS-2 failed in transitional mode, rather than producing a single fracture as in the other samples, failure resulted in a series of conjugate fractures.

4.3.3.2 *Doddington*

Five samples from the Doddington sandstone were tested. Elastic modulus and Poisson's ratio stress sensitivity plots of the Doddington samples are presented in Figure 4.20 and Figure 4.21 respectively. Essentially, both properties show linear increase with increasing confining pressure. The Doddington sandstone has been observed to exhibit isotropic elastic properties with little variation in the average values of the elastic modulus for the five samples. Infact, two of the samples (DDG-1 and DDG-2) exhibited very close values of both elastic modulus and Poisson's ratio at each of the confining pressure. This clearly indicates that the elastic properties of the Doddington sandstone are isotropic in nature. The elastic modulus at the initial and final confining pressure ranged from 22.97 to 24.02 GPa and from 35.11 to 36.05 GPa respectively. The stress sensitivity ratio of the Doddington samples ranged from 1.49 to 1.54 which again reflects the isotropic nature of this sandstone even at higher confining pressure. Poisson's ratios of the Doddington samples were also found to exhibit a consistent upward trend with increasing confining pressure.

Average axial stress at failure of the Doddington sandstone ranged from 104.91 MPa at the initial confining pressure to 207.63 MPa at the final confining pressure. These values are plotted in Figure 4.22 as stress sensitivity plots which shows that the average axial stress at failure increased by 100% over the range of applied confining pressure. Linear regression of the principal stress data provided values for the uniaxial compressive strength and triaxial stress factor for the Mohr-Coulomb failure criterion. Uniaxial compressive strength values obtained from this plot ranged from 77.23 to 87.34 MPa. It is

clear that the five samples are of similar strength. All of the samples were observed to fail in a classical brittle manner (as shown in Figure 4.32b) along a single plane of failure inclined at 43-55° to the maximum principal direction. Similar features were observed by Santarelli and Brown (1989) who tested the Doddington sandstones at confining pressure between 5.52 to 50.33 MPa and reported average values of elastic modulus and uniaxial compressive strength 20.73 GPa and 51.39 MPa respectively.

4.3.3.3 *Fife Silica*

Geomechanical characterisation was conducted on five Fife Silica sandstone samples. Figure 4.23 and Figure 4.24 show the plots of elastic constants with increasing confining pressure for all the samples. Elastic modulus measured on the Fife Silica samples varied between 19.87 to 22.54 GPa at the initial confining pressure and from 31.98 to 33.87 GPa at the final confining pressure. The value of the elastic modulus increased by over 50% as the confining pressure is increased from 6.90 to 34.50 MPa as represented by the range of stress ratio from 1.50 to 1.64. Poisson's ratio also correlates with increasing confining pressure but like in other sandstones, the pattern can be erratic. Average values of Poisson's ratio are 0.17 and 0.20 at the initial and final confining pressures respectively.

The axial stress at failure of the Fife Silica samples also increased as the confining pressure increase. The average value of the axial stress at failure ranged from 100.20 MPa at the initial confining pressure to 212.00 MPa at the final confining pressure. This indicates an increase of over 100% from the initial confining pressure to the final confining pressure. The resulting failure envelope is shown in Figure 4.25. The magnitudes of the mechanical properties of the Fife Silica sandstone are similar to those of the Doddington sandstone. As both rock types are of similar porosity this result is to be expected since porosity is well recognised as an index of geomechanical properties (Farquhar et al., 1994). The straight line in Figure 4.25 has been translated into a Mohr-Coulomb failure criterion, giving a range of extrapolated uniaxial compressive strength from 70.08 to 77.98 MPa which is typical spread of values for sandstones over this range of porosities. All of the Fife Silica samples underwent brittle failure (Figure 4.32c) resulting in a single through-going shear fracture. As the axial stress at failure is approached, localisation takes place and shear bands develop which eventually form a macroscopic shear plane through the sample.

4.3.3.4 *Lochaline*

Lochaline sandstones are generally associated with favourable porosity and permeability, however, the Lochaline samples characterised in this thesis were of the low porosity and permeability diagentically altered region (hard lenses). The elastic properties of the Lochaline samples are shown in Figure 4.26 and Figure 4.27. The value of the elastic modulus ranged from 33.98 to 38.88 GPa at the initial confining pressure and from 63.99 to 70.20 GPa at the confining pressure. The Lochaline samples tested here are by far the stiffest and strongest of all the analogue sandstones. The elastic modulus as expected increased with increasing confining pressure by as much as 90% in all the samples as shown by the range of the stress sensitivity (1.81-1.90). The response of the Poisson's ratio with increasing confining pressure can be considered to be fairly constant in most samples with an average value of 0.18 at the final confining pressure.

The axial stress at failure of the Lochaline samples ranged from 197.98 to 212.30 MPa at the initial confining pressure and from 379.80 to 396.50 MPa at the final confining pressure. Both elastic and mechanical properties of the Lochaline samples were observed to increase with increasing confining pressure. The strength of the Lochaline samples are found to also increase at a greater rate with increasing confining pressure as observed in other analogue sandstones. The stress sensitivity ratio of the axial stress at failure ranged from 1.83 to 1.94. This shared feature of rapid increase in strength among the analogue sandstones is most likely due to the very high quartz content found in these sandstones. The Lochaline and the Fife Silica sandstones in particularly have over 95% quartz, the reason why both sandstones are used in glass manufacturing. Failure envelope from the multi-failure state test is shown in Figure 4.28. A straight line has been translated into a Mohr-Coulomb failure criterion to obtain an extrapolated uniaxial compressive strength ranging from 152.57 to 175.96 MPa.

All the four Lochaline samples were observed to fail in a brittle mode (Figure 4.32d). However, while failure in three of the four samples is characterised by a single localised failure plane, one sample underwent a dispersed, non-localised failure resulting in eventual disintegration of the sample. It is thought that even though the load-displacement curve of this particular sample clearly shows a brittle failure, failure must have been initiated from multiple planes eventually resulted in the total disintegration of the sample.

4.3.3.5 *Locharbriggs*

Plots of the elastic constants stress sensitivity of the Locharbriggs sandstone are presented in Figure 4.29 and Figure 4.30. The effect of increasing confining pressure on

the Locharbriggs samples is marked by an increase in the elastic modulus. From the test result, the Locharbriggs sandstone can be divided into two groups based on porosity; high and low porosity Locharbriggs. The values of the elastic modulus of the high porosity Locharbriggs samples ranged from 18.54 to 20.04 GPa at the initial confining pressure and from 28.99 to 29.84 GPa at the final confining pressure, representing about 50% increase. Whereas values of elastic modulus of the low porosity Locharbriggs samples ranged from 23.55 to 25.31 GPa at the initial confining pressure and from 36.01 to 37.65 GPa at the final confining pressure. The magnitudes of the elastic modulus of the high porosity Locharbriggs samples are similar to those of the Clashach sandstone. The elastic modulus increase quite rapidly at the initial confining pressure and tends to flatten out as confining pressure is increased at around 20.69 MPa for most of the samples. The low porosity group is however, slightly stiffer and the response to increasing stress for this group is more pronounced at higher confining pressure. The Poisson's ratio of the Locharbriggs did not show any discernible pattern with increasing confining pressure with the exception of one low porosity sample.

Figure 4.31 presents the axial stress at failure versus increasing confining pressure and stress sensitivity plots for the Locharbriggs samples. The average values of the axial stress at failure of the high porosity Locharbriggs sample is 33.34 MPa at the initial confining pressure which increased to 101.91 MPa at the final confining pressure. The low porosity Locharbriggs samples on the other hand have an average axial stress at failure of 71.66 MPa at the initial confining pressure and 165.70 MPa at the final confining pressure. Average uniaxial compressive strength predicted from the Mohr-Coulomb criterion is 18.62 MPa and 47.99 MPa for the high and low porosity Locharbriggs samples respectively. These values roughly compare well with the other analogue sandstones, with the exception of the high strength Lochaline sandstone.

The low porosity Locharbriggs samples underwent brittle failure with a single plane of localised failure plane while the high porosity sample failed in a ductile manner as depicted from the stress-strain curves (Figure 4.32e). The failure mode found for each of the sample is indicated in Table 4.9.

Sample I.D.	Sandstone Type	Confining Pressure (MPa)					Stress Ratio	Confining Pressure (MPa)				
		6.90	13.80	20.70	27.60	34.50		6.90	13.80	20.70	27.60	34.50
		Young's Modulus (GPa)						Poisson's ratio				
CLS-1	Clashach	27.28	27.80	29.50	32.24	33.25	1.22	0.17	0.19	0.18	0.18	0.20
CLS-2	Clashach	23.35	24.06	25.78	27.01	31.66	1.36	0.17	0.19	0.18	0.20	0.17
CLS-3	Clashach	26.85	27.01	28.41	31.54	32.54	1.21	0.14	0.17	0.20	0.19	0.21
CLS-4	Clashach	29.54	30.17	33.57	34.89	35.01	1.19	0.19	0.18	0.19	0.18	0.18
DDG-1	Doddington	22.97	27.28	29.55	32.24	35.46	1.54	0.14	0.15	0.17	0.18	0.20
DDG-2	Doddington	23.37	25.28	29.50	32.18	35.40	1.51	0.15	0.14	0.17	0.18	0.20
DDG-3	Doddington	23.25	25.41	29.50	32.15	35.11	1.51	0.15	0.14	0.17	0.18	0.20
DDG-4	Doddington	23.90	25.91	29.57	32.87	35.68	1.49	0.14	0.16	0.17	0.19	0.21
DDG-5	Doddington	24.02	26.87	30.24	33.24	36.05	1.50	0.15	0.15	0.17	0.20	0.20
FSS-1	Fife Silica	20.60	25.10	29.33	30.50	32.22	1.56	0.17	0.17	0.19	0.17	0.19
FSS-2	Fife Silica	20.14	24.84	29.54	29.88	31.98	1.59	0.18	0.19	0.19	0.19	0.20
FSS-3	Fife Silica	22.54	26.99	30.85	32.55	33.87	1.50	0.17	0.17	0.19	0.21	0.20
FSS-4	Fife Silica	21.35	26.03	30.69	31.99	33.09	1.55	0.16	0.16	0.18	0.19	0.20
FSS-5	Fife Silica	19.87	23.98	29.00	30.31	32.54	1.64	0.17	0.17	0.18	0.20	0.19
LCS-1	Lochaline	33.98	39.99	48.79	50.67	63.99	1.88	0.19	0.21	0.20	0.19	0.20
LCS-2	Lochaline	35.07	43.50	49.78	53.24	65.01	1.85	0.19	0.19	0.17	0.21	0.21
LCS-3	Lochaline	35.10	43.90	50.10	55.98	66.74	1.90	0.10	0.06	0.10	0.11	0.11
LCS-4	Lochaline	38.88	49.90	58.20	62.36	70.20	1.81	0.22	0.14	0.17	0.17	0.20
LBG-1	Locharbriggs	19.34	21.03	25.18	25.98	29.84	1.54	0.18	0.19	0.18	0.20	0.20
LBG-2	Locharbriggs	23.55	25.87	28.99	34.10	36.03	1.53	0.17	0.17	0.21	0.18	0.19
LBG-3	Locharbriggs	24.99	26.54	29.78	34.55	36.58	1.46	0.15	0.17	0.16	0.19	0.21
LBG-4	Locharbriggs	25.31	27.47	31.99	35.65	37.65	1.49	0.21	0.16	0.15	0.20	0.23
LBG-5	Locharbriggs	24.01	25.87	28.01	32.41	36.01	1.50	0.21	0.15	0.14	0.21	0.25
LBG-6	Locharbriggs	20.04	22.43	25.87	26.78	29.10	1.45	0.17	0.17	0.19	0.20	0.22
LBG-7	Locharbriggs	18.54	21.89	24.99	25.22	28.99	1.56	0.16	0.17	0.20	0.19	0.19

Table 4.8: Elastic constants stress sensitivity data for analogues sandstones.

Sample I.D.	Sandstone Type	Confining Pressure (MPa)					Stress Ratio	Failure Criterion			Failure Mode	
		6.90	13.80	20.70	27.60	34.50		Mohr-Coulomb				
		Axial Stress (MPa)						σ_0	k	r_2		
CLS-1	Clashach	89.15	118.40	138.53	156.80	171.76	1.93	73.84	2.95	0.983	Brittle	
CLS-2	Clashach	66.98	92.60	117.97	142.27	163.50	2.44	43.85	3.85	0.998	Transitional	
CLS-3	Clashach	81.98	116.87	134.98	154.78	166.75	2.03	68.83	3.00	0.967	Brittle	
CLS-4	Clashach	92.40	121.40	142.01	159.03	176.32	1.91	76.59	2.97	0.986	Brittle	
DDG-1	Doddington	103.89	131.20	158.30	179.21	207.82	2.00	79.32	3.70	0.998	Brittle	
DDG-2	Doddington	101.56	124.53	153.97	180.99	205.63	2.02	73.95	3.83	0.998	Brittle	
DDG-3	Doddington	101.80	125.60	154.70	182.53	206.31	2.03	74.40	3.84	0.998	Brittle	
DDG-4	Doddington	105.35	126.01	155.74	183.68	207.08	1.97	77.23	3.78	0.997	Brittle	
DDG-5	Doddington	111.95	137.20	162.30	187.54	211.30	1.89	87.34	3.60	0.999	Brittle	
FSS-1	Fife Silica	97.57	123.98	152.33	184.63	204.92	2.10	70.08	3.99	0.996	Brittle	
FSS-2	Fife Silica	98.13	125.20	153.98	186.31	206.56	2.10	70.64	2.00	0.996	Brittle	
FSS-3	Fife Silica	104.60	142.98	170.04	198.70	228.31	2.18	77.98	4.39	0.996	Brittle	
FSS-4	Fife Silica	101.35	127.51	157.24	187.35	211.98	2.09	72.76	4.07	0.998	Brittle	
FSS-5	Fife Silica	99.35	126.34	154.06	187.24	208.21	2.10	71.45	4.02	0.996	Brittle	
LCS-1	Lochaline	197.98	244.57	287.58	335.65	379.80	1.92	152.57	6.59	0.999	Brittle	
LCS-2	Lochaline	209.99	249.78	313.32	355.68	383.54	1.83	166.56	6.56	0.984	Brittle	
LCS-3	Lochaline	212.30	271.9	326.30	364.9	396.50	1.87	175.96	6.68	0.982	Brittle	
LCS-4	Lochaline	210.65	255.45	328.98	361.54	387.35	1.84	170.94	6.65	0.966	Brittle	
LBG-1	Locharbriggs	37.58	52.75	73.84	84.50	106.32	2.83	20.22	2.45	0.992	Ductile	
LBG-2	Locharbriggs	65.09	84.25	109.21	136.21	157.54	2.42	39.40	3.43	0.997	Brittle	
LBG-3	Locharbriggs	67.84	90.57	118.35	139.89	159.87	2.36	45.29	3.38	0.996	Brittle	
LBG-4	Locharbriggs	79.51	105.10	130.81	152.92	175.47	2.21	56.84	3.47	0.998	Brittle	
LBG-5	Locharbriggs	74.21	98.01	124.02	147.80	169.90	2.29	50.43	3.49	0.999	Brittle	
LBG-6	Locharbriggs	35.47	55.74	71.25	86.99	103.56	2.92	20.37	2.43	0.997	Ductile	
LBG-7	Locharbriggs	29.97	49.35	63.87	78.34	95.84	3.20	15.26	2.32	0.997	Ductile	

Table 4.9: Compressive strength, failure criteria and failure mode of the analogues sandstones.

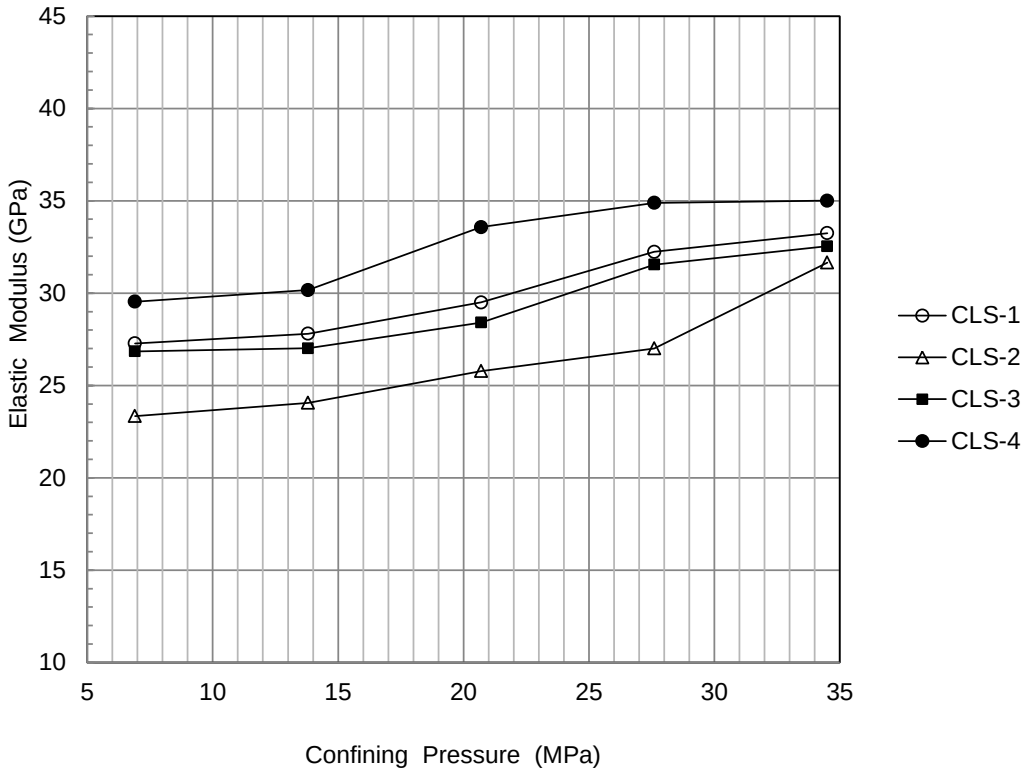

Figure 4.17: Effect of increasing confining pressure on elastic modulus for the Clashach sandstone.

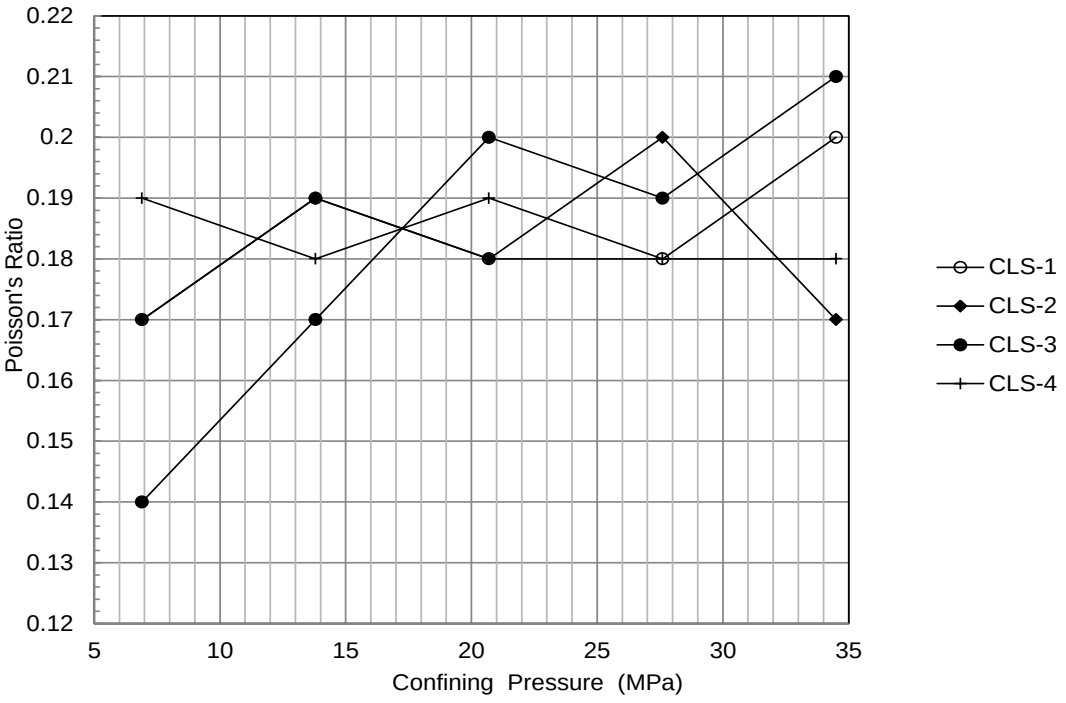

Figure 4.18: Effect of increasing confining pressure on Poisson's ratio for the Clashach sandstone.

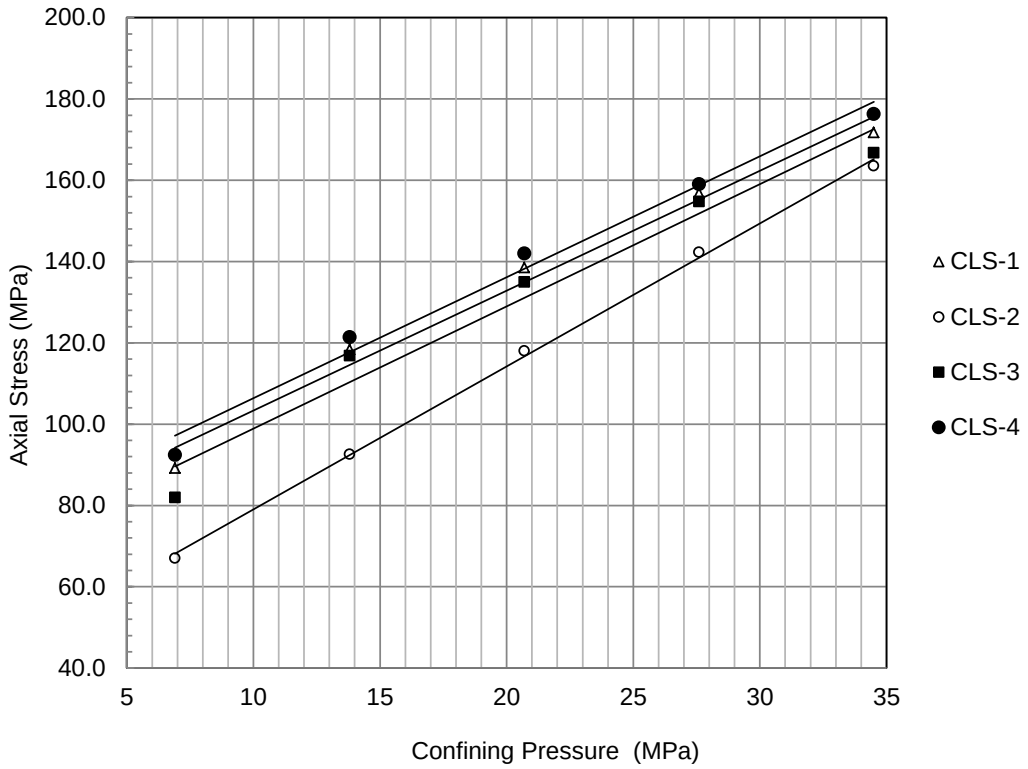

Figure 4.19: Principal stress plot resulting from multi-failure state test for the Clashach sandstone.

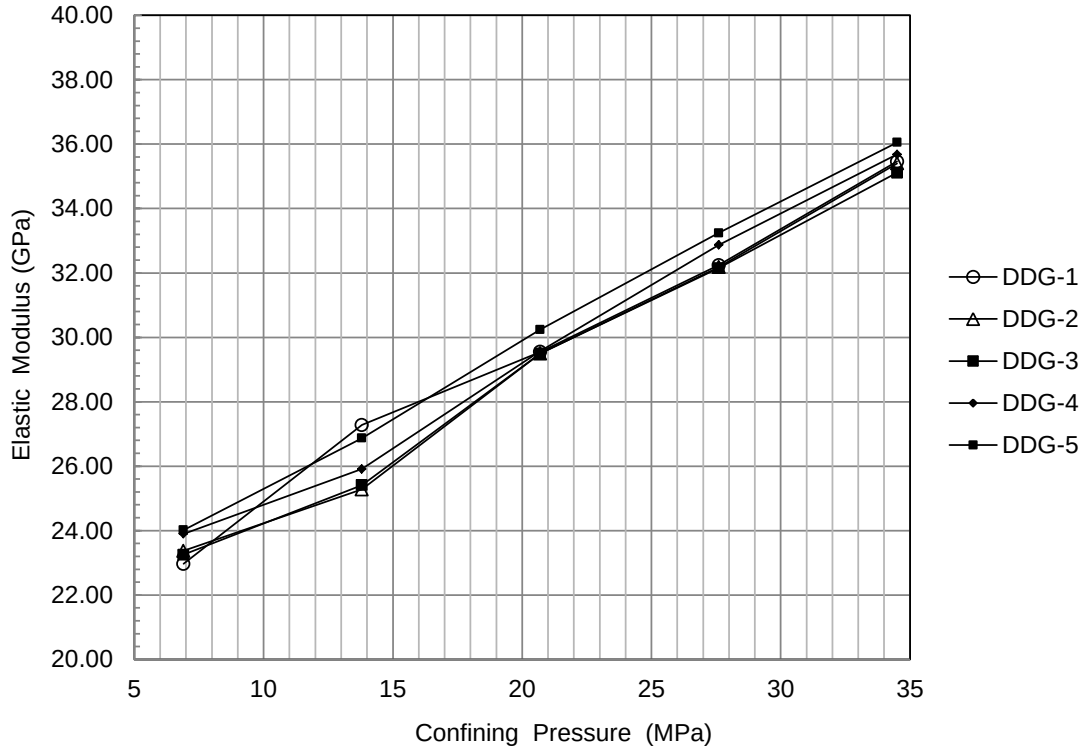

Figure 4.20: Effect of increasing confining pressure on elastic modulus for the Doddington sandstone.

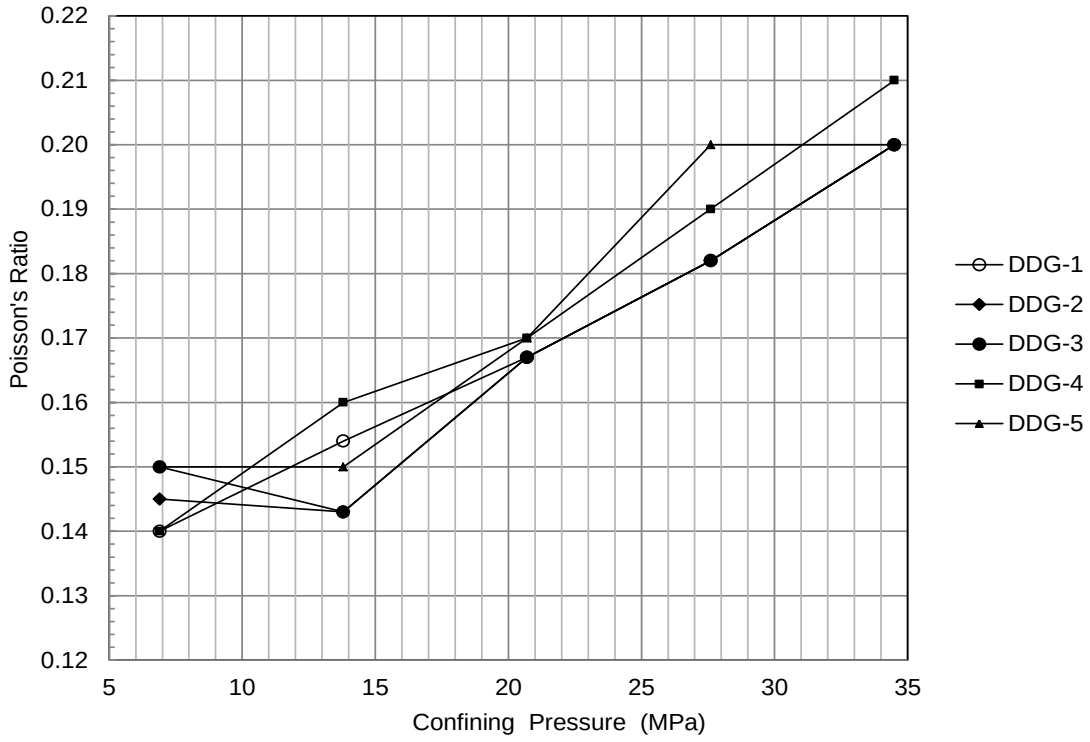

Figure 4.21: Effect of increasing confining pressure on Poisson's ratio for the Doddington sandstone.

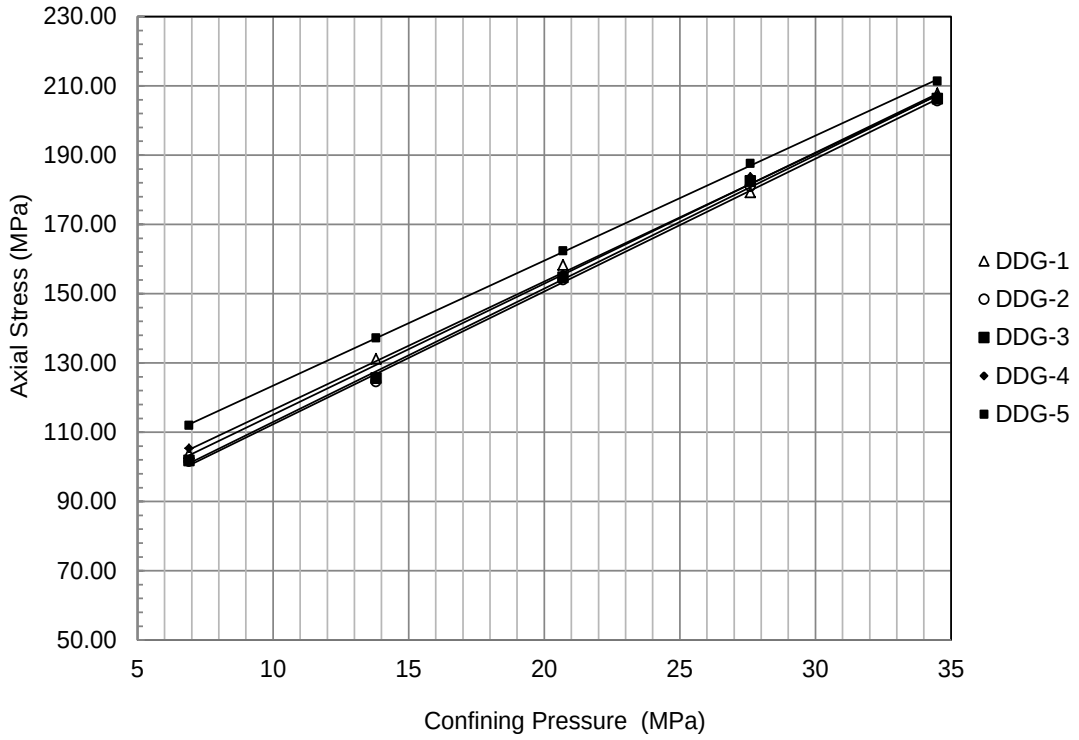

Figure 4.22: Principal stress plot resulting from multi-failure state test for the Doddington sandstone.

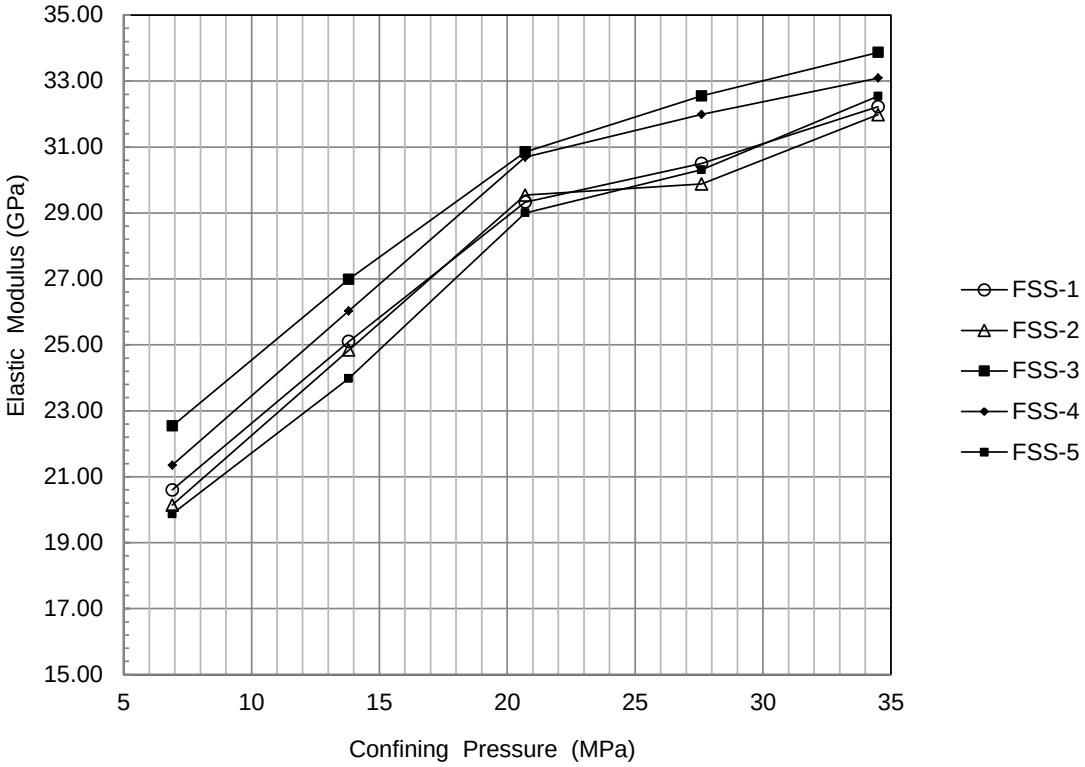

Figure 4.23: Effect of increasing confining pressure on elastic modulus for the Fife Silica sandstone.

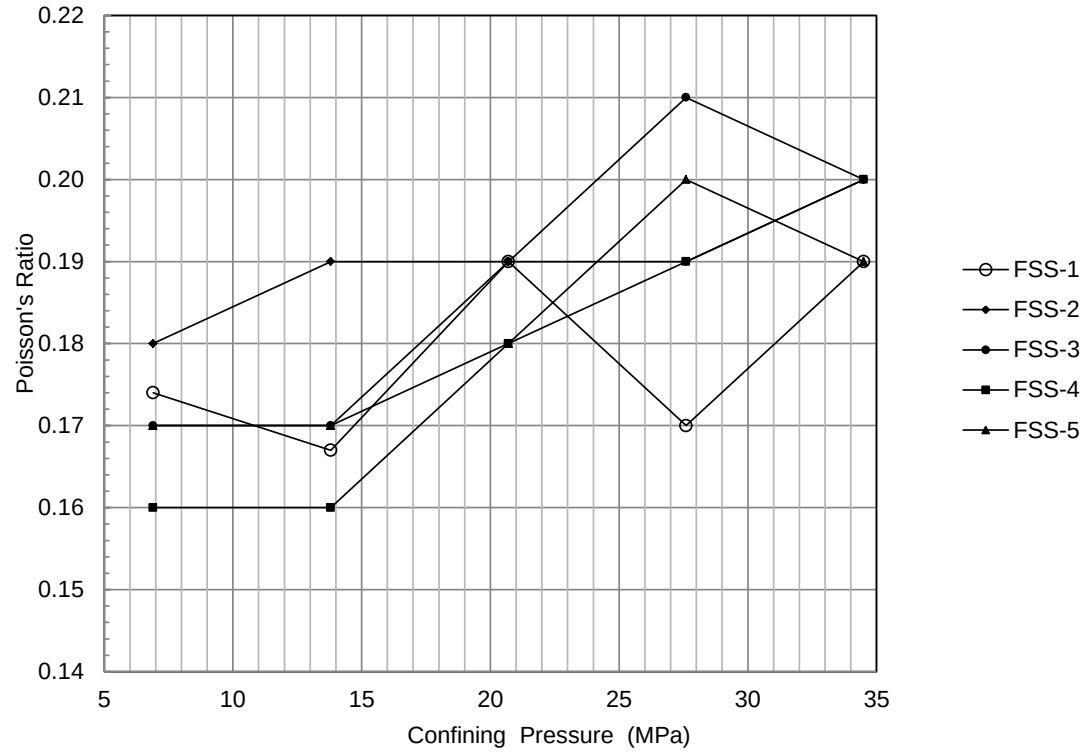

Figure 4.24: Effect of increasing confining pressure on Poisson's ratio for the Fife Silica sandstone.

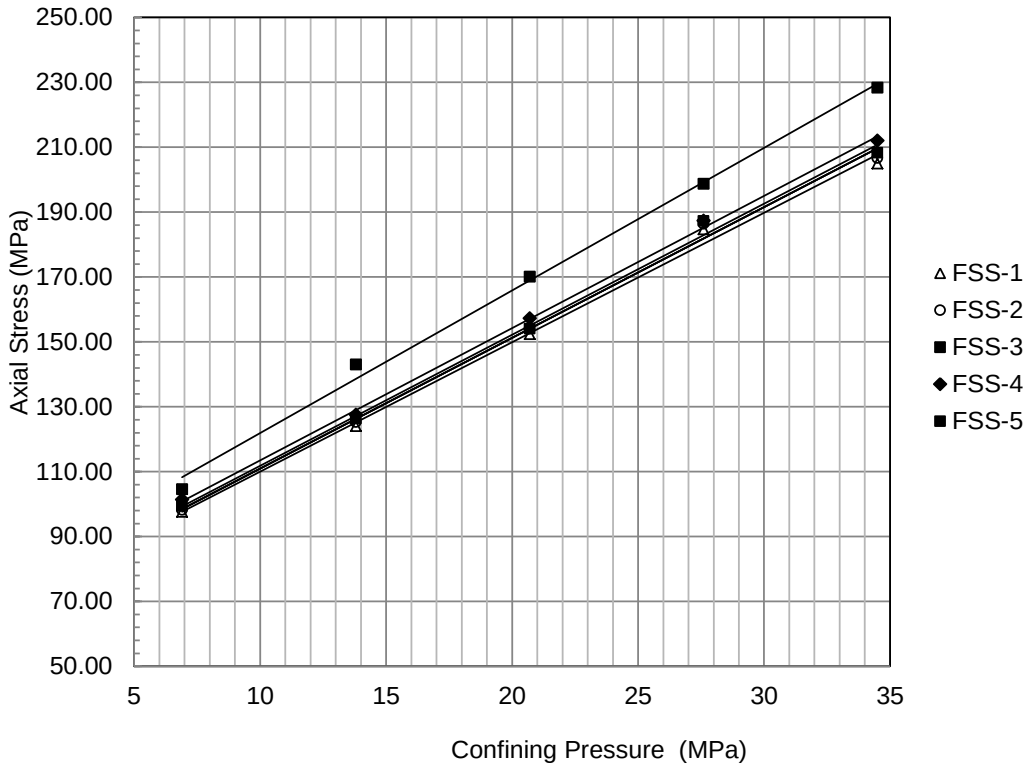

Figure 4.25: Principal stress plot resulting from multi-failure state test for the Fife Silica sandstone.

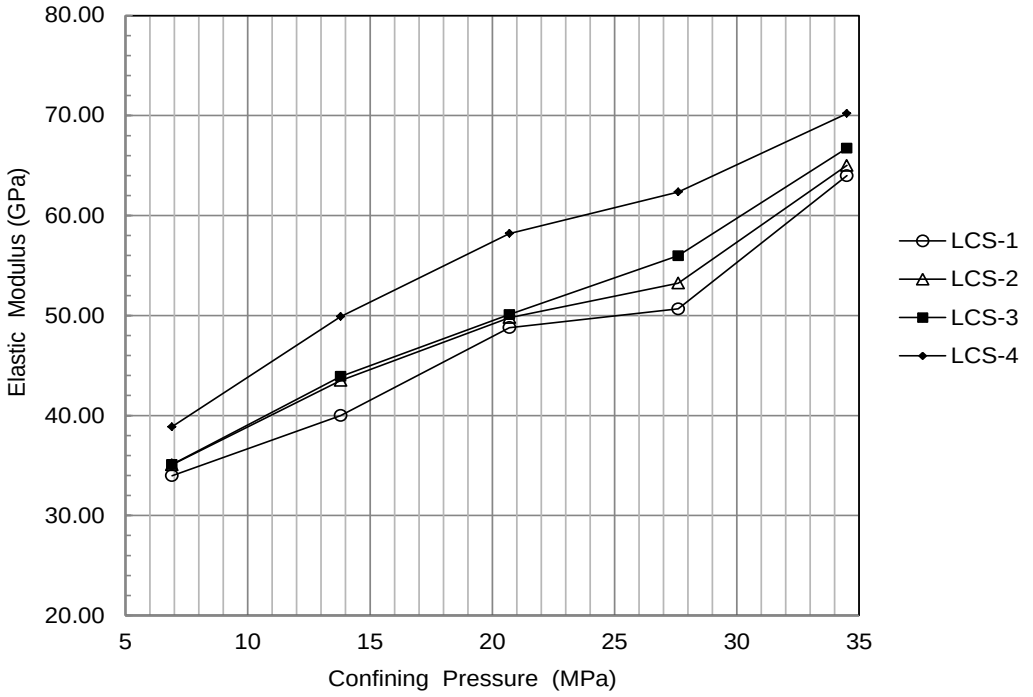

Figure 4.26: Effect of increasing confining pressure on elastic modulus for the Lochaline sandstone.

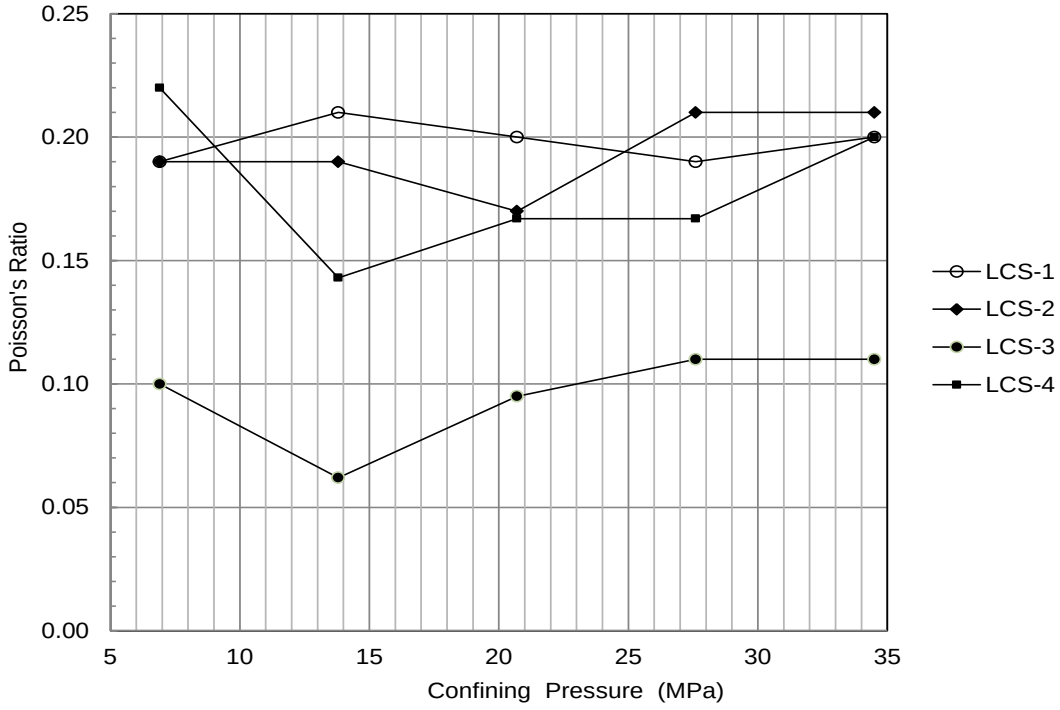

Figure 4.27: Effect of increasing confining pressure on Poisson's ratio for the Lochaline sandstone.

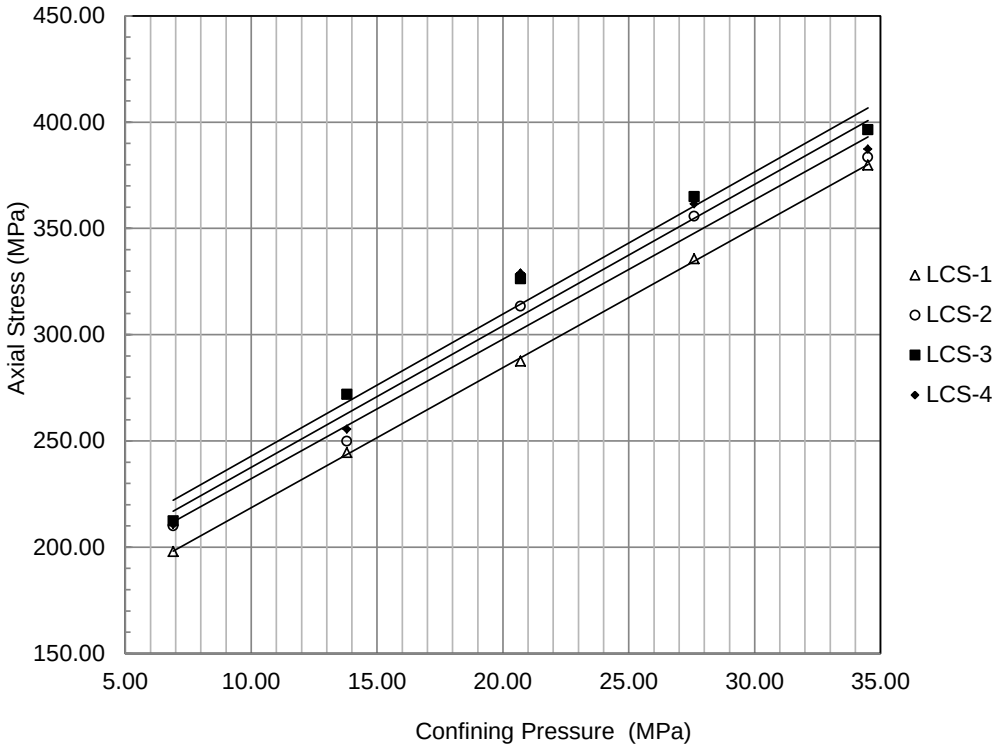

Figure 4.28: Principal stress plot resulting from multi-failure state test for the Lochaline sandstone.

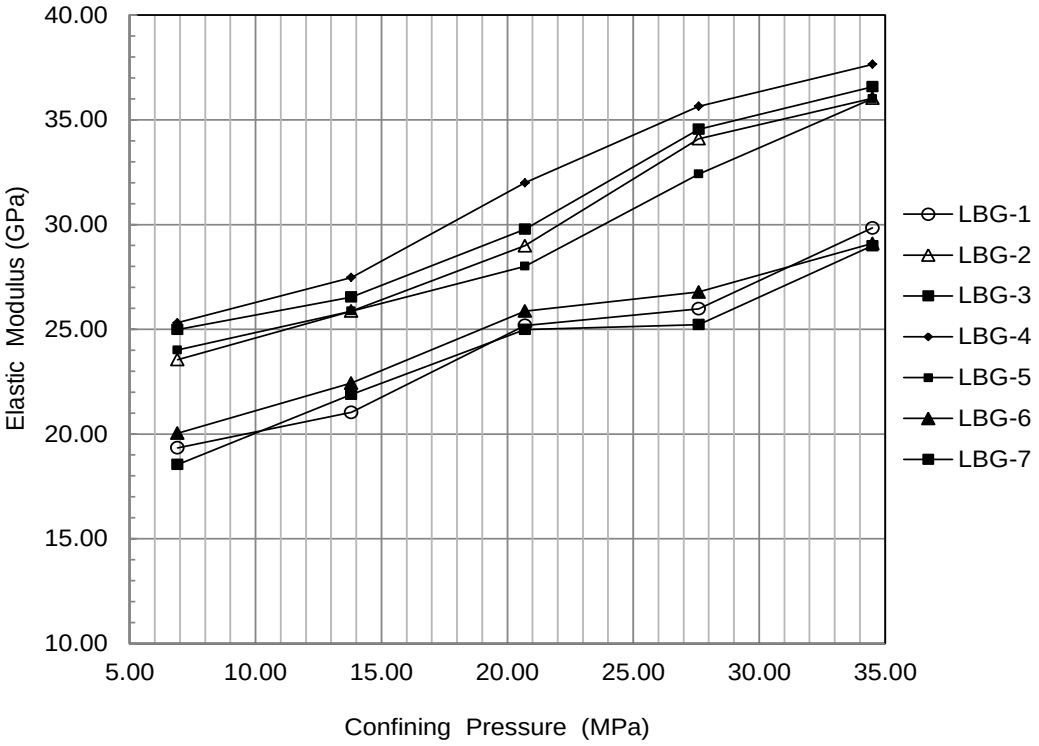

Figure 4.29: Effect of increasing confining pressure on elastic modulus for the Locharbriggs sandstone.

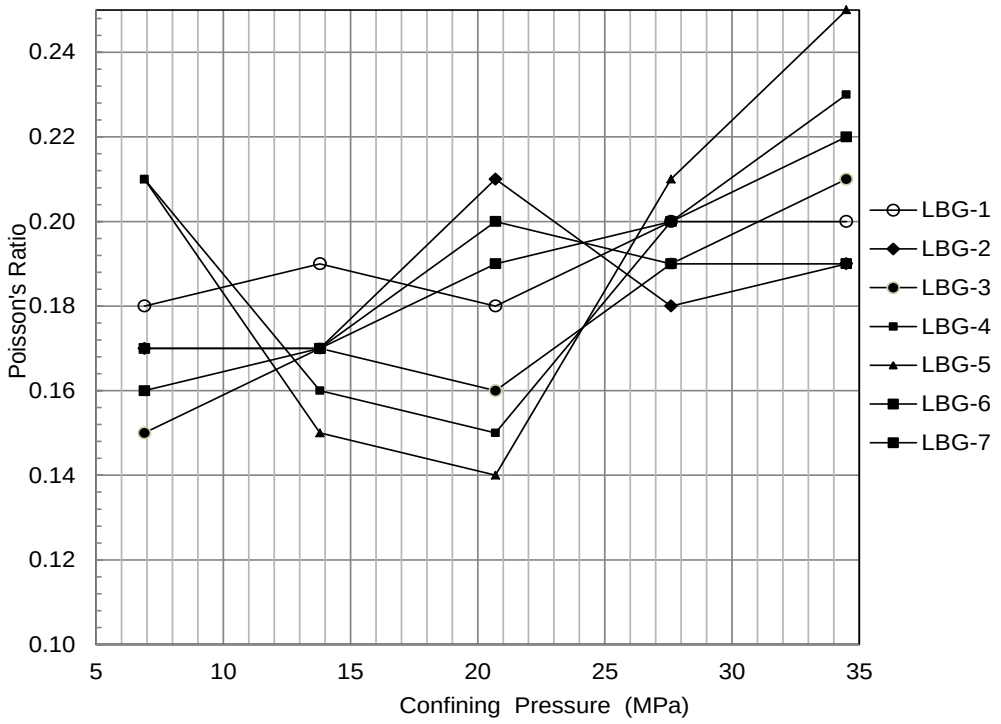

Figure 4.30: Effect of increasing confining pressure on Poisson's ratio for the Locharbriggs sandstone.

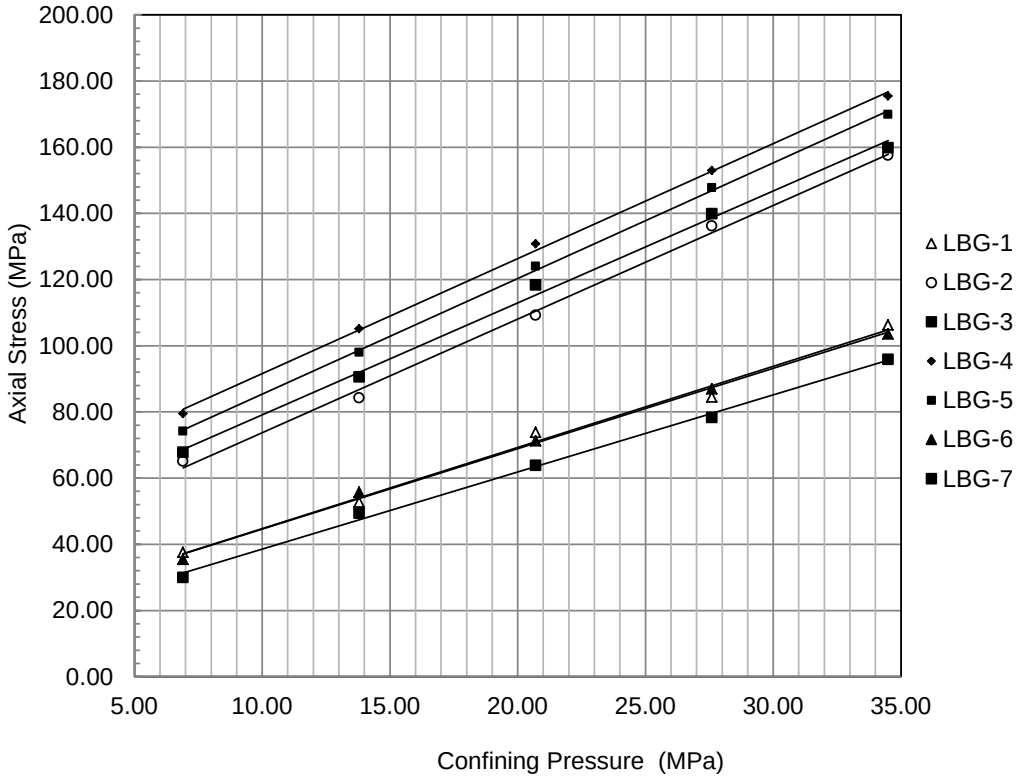

Figure 4.31: Principal stress plot resulting from multi-failure state test for the Locharbriggs sandstone.

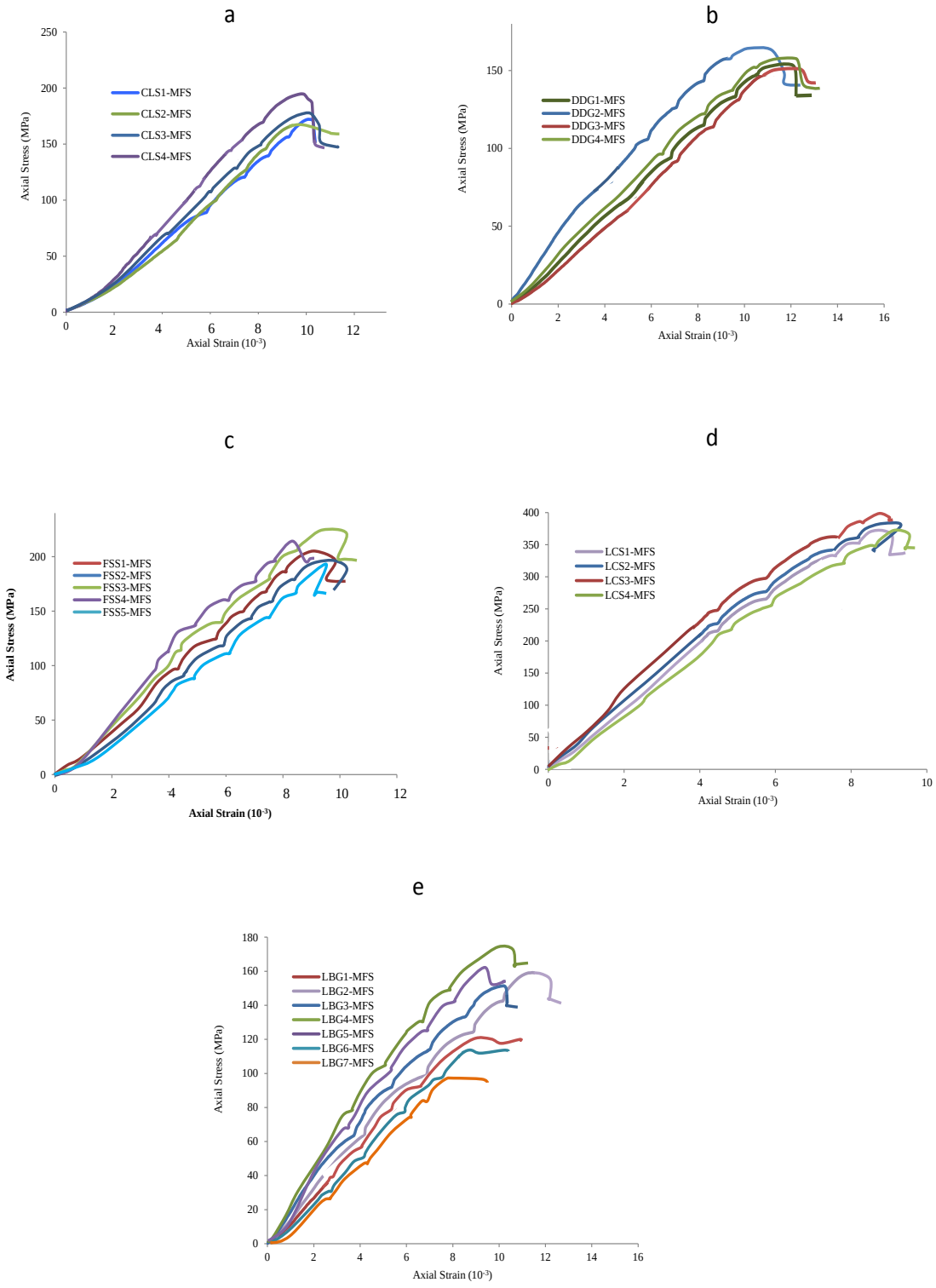

Figure 4.32: Stress-strain curve of analogue sandstones showing failure modes (a) Clashach, (b) Doddington, (c) Fife Silica, (d) Lochaline and (e) Locharbriggs sandstones.

4.4 Granulometric Characterisation of Comminution Debris

4.4.1 Introduction

Characterisation of the shear debris found on failure plane of a triaxially compressed sample is of particular importance in quantifying the energy that goes into comminution. After microscopic shear failure, the shear load usually falls to a residual strength equals to the frictional resistance of the sliding plane. In general, energy dissipation associated with the total energy budget expended occurs mainly by processes involving heat generation and grain comminution. The creation of new surface area in the form of shear debris (fault gouge) can be envisaged as a process with first order control on sand production potential of a formation.

Shear debris generated from triaxial compression testing (section 4.2 and 4.3) are analyse with regards to their particle size distributions. The influence of textural control, lithology, failure mode and confining pressure on resultant shear comminution products created during both brittle and ductile deformation is discussed. Relevant data required for sand production prediction (Chapter 5) are also extracted from the shear debris size distribution.

4.4.2 Theoretical Particle Size Distribution

Naturally, particle sizes of rock material have been found to follow well-defined mathematical laws in their distribution. As such number mathematical models have been developed to obtain distribution functions from experimental particle size distribution curves e.g. normal, log-normal, Rosin-Rammler (Rosin and Rammler, 1933) and Gate-Gaudin-Schuhmann (Schuhmann, 1940). The Rosin-Rammler and Gate-Gaudin-Schuhmann are adopted in this thesis since they have been successfully applied to analysis of comminution products (Taşdemir and Taşdemir, 2009). These two distribution functions are briefly discussed below.

4.4.2.1 *Rosin-Rammler Distribution*

The Rosin-Rammler distribution was originally developed to model size distribution of broken coal but has been widely applied to other materials like sand, cement, quartz, ores, clays and glass (Allen, 1975). From probability considerations (Rosin and Rammler, 1933) expressed the governing equation for particle size distribution as:

$$R = 100 \exp\left[-\left(\frac{x}{x_m}\right)^b\right] \qquad (4.1)$$

where R is the cumulative mass (in %) of material retained (cumulative oversize) on size x, x is the aperture size aperture or particle size, x_m is the mean particle size (size parameter) and b is the measure of the spread of particle sizes (distribution parameter) (Djamarani and Clark, 1997, Gupta and Yan, 2006). The value of b increases with increasing fineness where small values indicate scattered distribution, and large values imply uniform distribution (Herdan, 1960). Equation (4.1) can be rewritten as:

$$\frac{100}{R} = \exp\left[\left(\frac{x}{x_m}\right)^b\right] \tag{4.2}$$

The representation distribution of particle size based on Rosin-Rammler law was done using a linear regression of the data represented by taking the logarithm of equation (4.2) twice and rearranging to give:

$$\ln\left(\ln\frac{100}{R}\right) = \ln c \text{ (constant)} + b \ln x \tag{4.3}$$

Thus by plotting $\log\left(\frac{100}{R}\right)$ against particle size, x on a log-log scale a straight line is obtained. The resulting curve is known as the Rosin-Rammler curve (Gupta and Yan, 2006). It is possible from equation (4.3) to determine the Rosin-Rammler parameters, b and x_m from the slope of the straight line and the intercept at the horizontal line at $R = 36.79\%$ respectively. x_m is calculated as:

$$x_m = \exp\left[{(-\ln c)}/{b}\right] \tag{4.4}$$

4.4.2.2 *Gates-Gaudin-Schuhmann Distribution*

The Gates-Gaudin-Schuhmann distribution has also been widely applied to determine the size distribution of comminution debris (Taşdemir and Taşdemir, 2009). The distribution is given as (Gupta and Yan, 2006):

$$M = 100\left[\left({x}/{k}\right)^a\right] \tag{4.5}$$

where M is the cumulative mass (in %) passing size x (cumulative undersize), x is the aperture size, k is the size parameter and a is the distribution parameter. Theoretically, lower values of a suggest more fines and higher the value of a narrow distribution (Lu et al., 2003). In the Gates-Gaudin-Schuhmann method, the cumulative undersize data, M is plotted against the aperture size, x, on a log-log scale. Thus, taking the logs of both sides of equation (4.5) and rearranging it gives:

$$\ln(M/100) = a \ln x + \ln c \text{ (constant)} \tag{4.6}$$

On a log-log scale, a plot of the cumulative undersize, M against the aperture size, x gives a straight line. The slope of the straight line will be the distribution parameter, a and the intercept of the straight line, when M equals 100% will be the size parameter, k and it equals:

$$k = \exp\left[-\ln c/a\right] \tag{4.7}$$

4.4.3 Application of Fractal Concept to Particle Size Data of Shear Debris

Over the years, some interesting observation have emerged from the analyses of particle size distributions of natural and artificial sandstones (Engelder, 1974, Aydin, 1978, Aydin and Johnson, 1978, Sammis and Osborne, 1982, Sammis et al., 1987, Sammis et al., 1986, Sammis and Ashby, 1986, Chester and Logan, 1987, Antonellini et al., 1994, Anderson et al., 1980, Olgaard and Brace, 1983), experimental data (Shimamoto and Logan, 1981, Sammis et al., 1986, Biegel et al., 1989, Marone et al., 1990, Morrow and Byerlee, 1989, Marone, 1991, Beeler et al., 1996, Bos and Spiers, 2001, Mair and Marone, 1999, Mair K. et al., 2002, Mair et al., 2000) and comminuted chromites (Taşdemir and Taşdemir, 2009, Taşdemir, 2009). Particle size distributions of these materials may be self-similar (scale invariant) and in this case can be described by a power-law relationship (Mandelbrot, 1982) called the fractal dimension, D. An application of fractal mass distribution to the particle size distribution of the shear debris is discussed here.

4.4.3.1 *The Fractal Concept*

The concept of fractal was first introduced by Mandelbrot (1983) to described objects by a non-integral dimension called the fractal dimension. Generally, if the fractal dimension is an integer, it is equivalent to a Euclidean dimension. In Euclidean geometry, a point has an integer dimension of 0, a line 1, a square on a plane 2 and a solid cube 3. However, natural phenomena, such as the surfaces of mountains, coastlines, microstructure of rocks, rarely possess integral dimension and as such do not follow the Euclidean description due to the scale-dependent measures of length, area and volume. For example, the coastline of an island appears to be self-similar over a range of scales, but is limited by grain size on a microscopic scale, and by the size of the island on a macroscopic scale. Mandelbrot (1983) observed that the frequency size distribution of these systems exhibit a power law dependence, and he referred to such distributions as fractal. Turcotte (1992) has shown that the fractal dimension (D) exists if a number of

objects (N_n) have a characteristic linear dimension (r_n) that satisfies the following power-law relationship:

$$N_n = \frac{C}{r_n^D} \tag{4.8}$$

where C is a constant of proportionality.

4.4.3.2 *Fractal Dimension of Particle Size Data*

The power law relationship has been extensively used in describing particle size distributions since it does not include a characteristic length scale, thus it provide a scale invariant (fractal) relation. Mandelbrot (1983) suggested that fractal fragmentation could be quantified by measuring the fractal dimension through the equation:

$$N(> r) = Cr^{-D} \tag{4.9}$$

where $N(> r)$ is the number of fragments with a characteristic linear dimension greater than r, D is a fractal dimension and C is a constant chosen to fit the observe distribution.

Turcotte (1986) and Tyler and Wheatcraft (1992) proposed an equation for estimating the fractal dimension of comminution products, D_F, directly from mass size distribution data rather than particle number using the following equation:

$$M(X < x)/M_T = (x/X_L)^v \tag{4.10}$$

where $M(X < x)$ is the cumulative mass of particles with size X smaller than a given comparative sieve size x, X_L is the maximum particle size as defined by the largest sieve size opening, M_T is the total mass of particles and v is a constant exponent. X_L and v are the two main parameters for the particle size distribution of a fragmented material. The constant X_L shows the upper limit value of particle sizes. v is the slope of the best fitted line on a log $M(X < x)/M_T$ against log (x/X_L) graph:

$$\ln[M(X < x)/M_T] = v \ln x + \ln k \tag{4.11}$$

The power law relation of equation (4.10) and the linear fit of equation (4.11) produce estimates of v and k and it is related to the fractal dimension D_F in the following equation:

$$D_F = 3 - v \tag{4.12}$$

Therefore, the fractal dimension of particle size distribution of a fragmented rock sample can be determined from the slope of the fitted line by particle size analysis. The definition of fractal dimension given by equation (4.10) is similar to the Gates-Gaudin-Schuhmann equation which indicates that the Gates-Gaudin-Schuhmann equation is a fractal and the slope a of the Gates-Gaudin-Schuman line equals to the value of v in equation (4.12) (Lu et al., 2003, Ahmed and Drzymała, 2005).

4.4.4 Result of Granulometric Characterisation

Upon completion of the triaxial testing, samples were unloaded from the Hoek cell and the angle of the shear surface relative to the axis of each sample was measured and recorded. In order to obtain the particle size distribution of the original intact sample, sand samples were taken from the clean section of the tested plug avoiding any area which has produced comminution debris which would influence the results of the particle size distribution. The samples were first placed in a water bath and left to soak for 24 hours. The samples were then immersed in an ultra-sonic water bath for a further 2 hours. On removal from the water bath the samples were carefully disaggregated by hand, dried in an oven at 100℃. The particle size distribution of the intact rock sample is measured using the Malvern Particle Size Analyser (see section 3.5.4.2) with a lense-size of 600 – 0.2 μm to cover reasonable range of distribution. A model independent analysis using Fourier optics and the assumption of spherical particles was used to deconvolve the diffraction pattern into a multi-channel histogram of grain size by percentage volume. This type of distribution makes no assumptions about the form of the result with regards to its distribution, allowing multimodal distributions to be well characterised.

The shear debris, which was clearly visible on the surface as fine powder was carefully removed using a soft brush and the weight taken and recorded. Photographs of the deformed samples, failure surfaces and recovered debris are shown in Appendix C. It is accepted that not all of the debris collected is as a result of comminution. Part of the gross debris collected may consist of disaggregated grains or clusters of cemented grains which represent a disrupted region around the fracture surfaces. Comminuted debris are crushed original detrital grains and thus tends to be smaller than disaggregated grains. The appearance of the former also tends to be markedly different from the original grain shape, bearing a close resemblance to shards of broken glasses. Microscopic analysis was therefore conducted to identify the optimum sieve range to allow passage of comminuted debris but to retain the disaggregated detrital grains. It was found that only the debris in the sub 90 μm size range show the characteristics expected of the comminution products. The gross comminution products were then sieved to obtain sub 90 μm fraction and analysed in the Malvern Particle Size Analyser using lense-size of 80 – 0.5 μm in order to compare the distributions of different debris sample over the same size range.

Graphical representations of the particle size analysis for the comminuted sand debris for the sandstones are given in Figure 4.38 through to Figure 4.46 as both volume percentage and cumulative volume percentage against particle diameter. The particle size

distribution data for the intact undeformed samples are also included to facilitate comparison. The particle size distribution of the intact rock was obtained using lense-size of 600 – 0.2 μm, whereas that of the gross comminuted debris was obtained using lense-size of 80 – 0.5 μm to cover the appropriate ranges of distribution.

The convention for presenting particle size data widely used in the literature is to express grain diameter (measured in mm) in the phi (ϕ) scale (see Equation (2.4)). The measure of the mean value was obtained from the particle size analyser output. Sorting was calculated following the convention of Folk and Ward formula for graphic standard deviation (Folk and Ward, 1957) which is given as:

$$S_0 = \frac{\phi 84 - \phi 16}{4} + \frac{\phi 95 - \phi 5}{6.6} \qquad (4.13)$$

Increasing phi values therefore correspond to decreasing grain sizes whilst the sorting parameter (which measures the width of the distribution) reduces as sorting improves. The weight of the shear debris, angle of failure, sorting, sliding surface area and mean and specific surface area of comminution product smaller than 90 μm during rupture and post-peak strength shear sliding at the final confining pressure are presented in Table 4.13 through to Table 4.16. Resultant particle size data for the reservoir samples were also analysed using the Rosin-Rammler and Gate-Gaudin-Schuhmann size distribution methods. The estimated distribution parameters for characterising the Rosin-Rammler (RR) and Gate-Gaudin-Schuhmann (GGS) methods are shown in Table 4.17. The cumulative mass fractions of the reservoir samples are plotted as a function of particle diameter on the RR and GGS distribution scales as given in Figure 4.47 to Figure 4.50. These results tends to suggest that the initial mineralogy of the reservoir samples can be expected to affect the particle size distribution after triaxial compression test because there are different particle size distribution for the sample deformed at the same stress. A visual observation of the distribution curves show that both the RR and GGS curves for same sample show similar pattern.

The distribution constant, a from the GGS for each sample was converted to calculate inferred fractal dimensions, D using the linear relationship in equation (4.12). Due to the sigmoidal nature of some of these power-law distributions, straight line logarithmic regressions fits were calculated from the central linear portion of the curve. As such it was concluded that fractal theory was applicable to these data (e.g. Taşdemir, 2009).

4.4.5 Evolution of Debris Production as a Function of Confining Pressure

In order to analyse the influence of deformation at increasing confining pressure on the grain size distribution of comminuted sand debris, discrete tests were conducted on the Locharbriggs sandstones at confining pressures from 6.9 to 34.5 MPa. These stress levels were chosen to offer insight into the systematically changes in the size distribution of the sand debris produced with increasing confining pressure up to the brittle/ductile transition mode of the Locharbriggs sandstone.

The results from the discrete triaxial compression tests are presented as stress-strain (Figure 4.51). With the exception of sample tested at 34.5 MPa confining pressure, all samples display the same general behaviour of a classic example of brittle failure. The stress-strain plots show an initial non-linear deformation curve, usually attributed to the closure of pre-existing microcracks. The samples then show a linear elastic deformation response until yield point. Attaining the yield strength was accompanied by audible cracking. The yield point is marked by the departure from linear behaviour of the elastic curve and the beginning of the strength hardening phase. There was an indication of short period of strength hardening between the yield point and the peak stress. The load frame was sufficiently stiff that the phase of strain softening between peak stress and strain localisation could be recorded. This is then followed by a dynamic stress drop at failure which is typical of a Mohr-Coulomb brittle failure (Paterson and Wong, 2005), as strain was localised on a single fracture plane formed by coalescence of preferentially oriented microcracks. The stress drop associated with sample failure decreases systematically with increasing confining pressure. The sample deformed at the highest stress (34.5 MPa) is different from all other sample as it failed in the brittle-ductile transition mode (Figure 4.51), small amount of strain softening following the peak stress was noticed in this sample (e.g. Bésuelle et al., 2003). Rather than producing a single fracture as in previous tests, failure in this sample resulted in series of conjugate fractures. All the brittle failed samples are characterised by a through-going shear failure plane accommodating the axial displacement within a single shear debris zone. However, sample deformed at 34.5 MPa confining pressure developed conjugate failure zones. The change of failure angle with increasing confining pressure can be seen in Figure 4.52 - as the confining pressure increases from left to right in the picture the angle of fracture with respect to sample long axes (parallel to the direction of maximum principal stress) tends to increase, in agreement Besuelle et al. (2003).

Graphical representations of the particle size analysis of the gross comminuted debris are given in Figure 4.53 as both volume percentage and cumulative volume percentage against particle diameter. The particle size distribution data for the intact undeformed Locharbriggs sample is also included to facilitate comparison. The particle size distribution of the intact Locharbriggs sample is characterised by a major peak at 200 μm indicating over 70% of the grains have diameter ranging from 200 to 300 μm. Distribution parameter (degree of sorting) for both the intact material and comminuted debris was also calculated following the convention described by Folk and Ward (1957). A summary of the size distribution parameters is given in Table 4.18. Overall shapes (monomodal) of the particle size distributions are nearly the same for all the samples. The distributions of each of the comminuted debris sample show a peak between 20 to 50 μm and a long tail of finer particles. Particle size distributions of the comminuted debris collected from the samples reveal characteristic features depending on the level of the confining pressure. Particle size distribution of sample deformed at 6.9 MPa and 13.8 MPa both show a band ranging from 10– 110 μm with a peak at 50 μm suggesting the presence of some intact fine material from the relic grains. In contrast, sample deformed at confining pressure of 20.7 MPa include finer band of particles ranging from 1 μm to 100 μm. The amount of the grains less than 20 μm are much increased while the amount of grains greater than 20 μm are reduced compared to the intact material. Sample tested at confining pressure of 27.6 MPa and 34.5 MPa produced the largest amount of comminuted lower size-range fines (<10 μm). There is a systematic trend towards distributions with smaller peaks at 20 μm and more grains with <10 μm at increasing confining pressure. As the confining pressure increases up to the brittle/ductile transition, the sliding produced strain hardening as the fracture locked up and the attendant increase comminution of material to fine debris. Thus the rate of this attendant change in particle size distribution was seen to be stress dependent, with the greatest change being seen at the higher confining pressure.

4.5 Discussion

4.5.1 Geomechanical Appraisal of Sandstone

Generally, it has been shown from the geomechanical appraisal of both the reservoir analogue sandstones shows that elastic modulus increased with increasing confining stress while Poisson's ratio shows no consistent variation with increasing stress. This may be related to strain reduction generated for a given load due to more efficient distribution of

stress throughout the load bearing structure as a result of closer grain packing and the closure of intergranular cracks (Farquhar et al., 1993). The results obtained conform well with past studies undertaken by Cleary (1959), Senseny (1983b) and Farquhar et al. (1993) who conducted similar experiment and concluded that elastic modulus increases with increasing stress while Poisson's ratio show no clear sensitivity with increasing stress. The values of elastic modulus of sandstones measured from these studies (in the region of 34.50 MPa confining pressure) vary widely between 10 GPa to a high value of 70 GPa. Most of the reservoir samples measured in this study falls within the middle part of this range with values between 20 to 30 GPa. Similar values were obtained for the Rotliegendes sandstones (Yale et al., 1995, Collins, 2002, Farquhar et al., 1993) and other North Sea sandstones (Anderson and Jones Jr, 1985, Wong et al., 1994b, Somerville and Smart, 1991). The high end of the range consists of low permeability sandstones (Senseny, 1983b) due to their high contents of quartz (Cleary, 1959). However, low values of elastic modulus measured from some North Sea wells have also been reported (Russell et al., 2006, Wong et al., 1994b). Theoretically, Poisson's ratio for sandstones can range from zero to 0.50. Commonly reported values in the literature are from 0.20 to 0.35 (Senseny, 1983a, Anderson and Jones Jr, 1985, Sattler, 1989). Poisson's ratio measured in this thesis at approximately 34.50 MPa confining pressure falls within the range of values quoted in the literature.

The ranges of mechanical properties exhibited by the reservoir and analogue samples tested in this thesis are similar to those observed for other North Sea sandstones of comparable porosity (e.g. Farquhar et al., 1993). Little variation was observed in the mechanical properties between different wells and reservoir horizons with regards to average values of the properties. This is consistent with the observation reported previously for the Rotliegendes sandstones by Farquhar et al. (1993) and several low permeability gas bearing sandstones by Senseny (1983a) and Sattler (1989). Compressive strength of porous sandstones at confining pressure between 20.69 to 48.27 MPa as reported in the literature ranged from 70.00 MPa to over 650.00 MPa, however, an upper limit of 300.00 MPa is usually reported. The compressive strength of the samples tested in this thesis ranged from 78.80 to 170.90 MPa at 34.50 MPa and from 173.70 to 298.00 MPa at 48.27 MPa. These values correspond to the range of values found in the literature.

The uniaxial compressive strength of sandstones reported in the literature covers a very wide range of values from as low as 10.00 MPa up to 200.00 MPa. Uniaxial compressive strength predicted for the reservoir samples tested in this thesis ranged from 2.70 to

113.83 MPa. The range of uniaxial compressive strength exhibited by samples from Field A (Palaeocene and Upper Jurassic) and Field B (Permian) is comparable with the values reported for North Sea Jurassic (Holt et al., 1989) and Brent formation (Wong et al., 1994a) measured on samples from similar depth. It should be noted that the values of uniaxial compressive strength were derived from the from the Mohr-Coulomb criterion for each sample.

4.5.2 Identification of a Suitable Geomechanical Reservoir Analogue

One of the main objectives of the geomechanical characterisation of the analogue sandstones is to identify a suitable reservoir analogue for the Famgee sandstone. It is desirable for a reservoir analogue to match as closely as possible many features of the original rock which it's intend to represent. However, depending on the scale of observation, it may be possible to represent a reservoir analogue for a specific purpose even when it would be quite unacceptable as a model at some other scale. Mineral composition, textural aspects, such as grain size and grain interlocking, cementation and porosity are thought to have great influence on rock strength (Dyke and Dobereiner, 1991, Plumb, 1994).

The range of the properties measured on the analogue sandstones are compared with equivalent range determined for the Famgee sandstone. A comparison of the petrophysical and mechanical characteristics of the analogue sandstones with the Famgee sandstones is summarised in Table 4.10. In general, it can be seen that the range of geomechanical properties of the analogue sandstones overlaps the values displayed by the Famgee sandstone. However, based on geomechanical properties of the individual analogue sandstones none was observed to possess all the requirements and/or display a sufficiently broad range of porosities to represent the variability among the Famgee samples. In order to facilitate comparison of the stress sensitivity, average values of the analogue sandstone and the upper and the lower limits of the mechanical properties of the Famgee sandstones are plotted in Figure 4.33 to Figure 4.35. The general trends in the properties with increasing stress are similar for both groups of sandstones; however, the analogue sandstones reflect the upper limits of elastic modulus and compression strength of the Famgee sandstone.

The failure mode of sandstone is an important parameter regarding the sand production behaviour. It was noted from section 4.2.2.3 that the Famgee sandstone can be separated into two groups according to their failure mode. One group consisted of samples which underwent brittle failure (indicated by a post-failure loss in strength) resulting in the

development of through-going fractures. The other group consisted of samples which underwent either ductile failure and associated work hardening or sample which display transitional and ductile failure at a typical reservoir stress level. The failure mode of the sandstone also appears to be porosity dependent and the transition between brittle and ductile failure is influence by confining pressure and porosity as previously observed by Scott and Nielsen (1991) (See Figure 4.36). Accordingly, the high porosity (> 25%) Locharbriggs samples which tend to undergo ductile or transitional deformation could be employed as a suitable analogue for the ductile group of the Famgee sandstone whilst the low porosity Locharbriggs samples would fulfil the requirements for brittle Famgee sandstone. However, the Lochaline sandstone is not suitable as an analogue for the reservoir rock due to its relatively high stiffness and strength, which inhibit yielding at stresses representative of the Famgee reservoir. The tendency of the Lochaline sandstone to disintegrate readily after rupture may be useful in some perforation studies where a large volume of fairly uniform sized grains are required to be produced. Thus in the absence of suitable and accessible Paleocene submarine fan outcrop and provided that the Locharbriggs sandstone is sampled to include the appropriate porosity range as the Famgee sandstone, the Locharbriggs sandstone may suffice as a suitable geomechanical analogue of the Famgee sandstone. Both set of sandstones were found to exhibit both brittle and ductile failure modes.

The Locharbriggs sandstone is deposited in an aeolian environment and is of Permian age. It is in this respect closer to the Rotliegendes sandstone (Field B). However, justification for its use as a geomechanical analogue for the Famgee sandstone which is of Palaeocene age can further be highlighted by examining the relationship between porosity and mechanical properties. Farquhar et al. (1994) has identified porosity to be an important geomechanical index. Figure 4.37 shows the general relationship between porosity and uniaxial compressive strength for a wide selection of sandstones. The porosity of the Famgee sandstone ranged between 20% to over 30%. This range of porosity can be matched by the Locharbriggs samples which have undergone less extensive diagenesis than their Rotliegendes counterpart. Elastic modulus and failure criteria parameters such as triaxial stress factor have also been observed to be porosity dependent (Farquhar et al., 1994), regardless of the depositional origin. Thus at core sample scale the geomechanical characteristics of sandstones appears to be less sensitive to the specifics of the depositional environment.

As noted earlier, textural parameters are thought to influence the mechanical properties of sandstones at microscopic scale (Plumb, 1994). The grain size, sorting and grain shape are thought to be the most important textural parameters. These parameters influence the packing arrangement of grains and thus the density of the grain to grain contact in the primarily mineral framework (see section 2.1.1.3 for a detail discussion). The number of contacts per grain ultimately controls the distribution of the stress and strain throughout the rock and thus the rupture characteristics. A comparison between the textural properties of the Famgee sandstone and the analogue sandstone is presented in Table 4.11. It is evident that there is a fair degree of similarities between the textural composition of the Locharbriggs and the Famgee sandstone, therefore it might be expected that the mechanical properties will be subject to similar granulometric controls. At the scale of investigation (up to whole core size) textural and porosity controls are probably more important than factors such as mineral composition, sandbody geometry and bedding structures which would be expected to vary considerably between submarine fan and aeolian sandstones.

4.5.3 Granulometric Characterisation

The particle size distribution plots of comminuted debris samples for both the reservoir and analogue sandstones display a number of characteristics which can be correlated to the textural parameters (grain size and sorting), stratigraphic age, mode of failure and possibly mineralisation. The particle size distribution curves for the analogue samples have very similar characteristic curves (depending on the rock type) which exhibit both the same peak value, indicating significant grain size reduction with respect to the undeformed sample, and a similar range of grain sizes. The particle size distribution curves are all characterised by peak ranging from 10 μm to 20 μm, interpreted as the most frequent grain diameter. Both brittle and cataclastic failure mechanisms are responsible for the grain size reduction with respect to the original intact rock due to comminution of debris. The mean grain size of the comminuted debris is directly related to the sorting parameter. As the mean diameter decreases the sorting parameter increases, indicating reduced sorting. The fine details of the comminuted debris curves may differ for the different rock type but the main characteristics are strikingly similar. Laboratory and field investigations of gouge comminution mechanisms show that loading conditions and lithology affect the processes of gouge grain breakage (Marone and Scholz, 1989).

The comminution efficiency of the ductile and transitional failed samples is reduced at small particle size compared to the brittle failed samples. This is probably due to the fact

that plastic deformation as opposed to fracturing and increase in new surface area is responsible for deformation in the ductile failed samples. Comminution efficiency in terms of particle size of the three wells in Field B are all peculiar to individual well which is a reflection of effect of mineralisation.

A relationship between failure mode and the weight percentage of comminution product can be observed from the comminution characteristics of the various sandstones. Samples that underwent brittle failure have a lesser weight of debris relative to the weight of the original sample compared to ductile and transitional failure modes samples, with the exception of one of the Lochaline sample which even though it underwent brittle failure produced an anomalously high quantity of sub 90 μm fines and underwent near complete disaggregation when the sample was removed from the Hoek cell. This result is probably related to the fact that grain fracture and comminution is localised to the shear fracture surfaces in the case of brittle failure whereas comminution is distributed throughout the sample in the case of ductile failure. A lesser weight of fine relative to the weight of the original sample is associated with brittle failure and the development of a through-going shear fractures compared to ductile and transitional failure modes. This result is probably related to the fact that grain fracture and comminution is localised to the shear fracture surfaces in the case of brittle failure whereas comminution is distributed throughout the sample in the case of ductile failure. There is a strong indication particularly for samples from Field A that comminution products resulting from both brittle and ductile failure may be characterised according to stratigraphic age. The size distribution of the Famgee (Paleocene) samples in the sub 90 μm fraction being monomodal whilst that for the Deekay (Jurassic) sandstones appears to be somewhat bimodal.

The fractal concepts results show that comminuted shear debris products from both the reservoir and analogue sandstones have power-law distributions, with fractal dimensions varying between 2.15 and 2.33. These results are consistent with the theoretical values predicted by micromechanical models of fragmentation (Turcotte, 1986) and range of published values found in the literature (Marone and Scholz, 1989, Rawling and Goodwin, 2003, Taşdemir, 2009, Carpinteri et al., 2003, Carpinteri and Pugno, 2002). The magnitude of the fractal dimension was obtained by first developing an $M(X < x)/M_T$ against log (x/X_L) on log–log plot and determining the slope of the best-fit line through the data points using linear regression (e.g. Taşdemir, 2009). The determination

coefficients, R^2 of the linear regressions are mostly greater than 0.95. This indicates that the fractal model of accumulative mass–size distribution is applicable.

Even though both the RR and GGS models have shown to adequately describe particle size distribution for the different sandstone samples, the GGS model has been considered for characterising of particle size distribution for fragmentation analysis since the GGS model is similar to the definition of fractal dimension.

4.5.4 Influence of Confining Pressure on Development of Debris

The influence of confining pressure on deformation shows that the magnitude of the stress drop associated with failure reduced at higher confining pressures until, at the highest confining pressure of 34.5 MPa, pairs of conjugate fractures were produced rather than a single fracture plane, as the frictional energy approached the failure energy (the brittle/ductile transition). At low confining pressure, post-fracture residual sliding was associated with slip weakening. The sample tested at the lowest effective pressure showed the least particle comminution and the greatest propensity to preserve relict intact grains. Sample deformed at the highest confining pressure (34.5 MPa) produced the largest amount of comminuted lower size-range debris (<20 μm). Sammis et al. (1986) attributed the decrease in particle size with increasing confining pressure to a suppression of axial extension of individual microcrack and subsequent scaling down of the length and spacing of the cracks.

Generally, there is a systematic change towards a greater volume of fraction of smaller particles with increasing confining pressure. This can also is associated with a reduction in the height of the peak in the distribution at the diameter at which it occurs. The mean particle size within the comminuted debris reduced by a factor of four during deformation. The marked increase in at elevated stress indicates the significant reduction in upper grain size of the smallest 5% of the distribution or, alternatively, the longer tail of smaller particles produced at higher stress. The key indicator however, is the sorting parameter. This measures the width of the distribution or the degree to which particle differ significantly from the mean size. This is also seen to increase with confining pressure.

4.6 Summary and Conclusions

In summary, the petrophysical and mechanical properties of several reservoir and analogue sandstones have been characterised in this chapter. The main aim of the characterisation is primarily to derive input data for sand production prediction and

wellbore stability evaluation; however the data have been analysed to provide a better understanding of the effects of increasing stress on rock properties. Also, further analysis of the geomechanical parameters of the analogue sandstones was undertaken to identify potential reservoir analogue for the Famgee sandstone. The following points are the main conclusions drawn from this chapter:

I. The geomechanical responses of both the reservoir and analogue sandstones were found to show stress sensitivity similar to what is found in the literature for sandstones.

II. In all cases the elastic modulus and compressive strength increased with increasing confining pressure. Poisson's ratio was only slightly influenced by increasing stress and not all the samples exhibited a consistent increase with increasing confining pressure.

III. Geomechanical appraisal of the sandstones indicates that samples display different failure modes which can be related to porosity. This upholds the relationship which has been observed between porosity and the mechanical characteristics of sandstones (Farquhar et al., 1994). The least porous samples underwent brittle failure resulting in a single through-going shear fracture. Both ductile failure by cataclastic flow and failure behaviour characteristic of brittle/ductile transition were also observed.

IV. The Locharbriggs sandstones can be considered as possible mechanical analogue for the Famgee sandstone as they display the same variability in porosity noted among the Famgee sandstone. In particular the low porosity Locharbriggs sandstone may be used as analogue for the stronger Famgee reservoir rocks, which would be expected to display brittle rupture. Whereas the high porosity Locharbriggs sandstone could be used as an analogue for high porosity (> 25%) Famgee reservoir rock which tend to undergo ductile or transitional deformation.

V. The particle size distribution of comminuted debris is influence by initial mineralogical properties, particle size, sorting, confining pressure, and dominant failure mode. A lesser weight of fine relative to the weight of the original sample is associated with brittle failure and the development of through-going shear fractures compared to ductile and transitional failure modes. There is a systematic change towards a greater volume of fraction of smaller particles with increasing confining pressure.

VI. Fractal fragmentation theory has been used to quantify comminution shear debris from triaxial tests. The particle size distributions of comminution shear debris from the triaxial tests exhibit fractal behaviour, and the derived empirical fractal dimension lies within 2.15–2.63 consistent with literature.

Sandstone Type	Stratigraphic Age	Ambient Porosity (%)	Klinkenberg Permeability (mD)	Elastic Modulus (GPa)	UCS (MPa)	Triaxial Stress Factor, k	Failure Mode
Famgee (High Porosity)	Paleocene	31.26	591.1	17.18	27.39	2.17	Ductile
Famgee (Low Porosity)	Paleocene	20.55	550.5	21.14	49.87	3.26	Brittle
Clashach	Permo-Triassic	22.52	403.43	33.11	65.78	3.19	Brittle
Doddington	Carboniferous	19.89	449.36	35.42	78.45	3.15	Brittle
Fife Silica	Carboniferous	22.22	318.09	31.05	72.58	3.69	Brittle
Lochaline	Cretaceous	5.43	6.45	55.56	166.51	6.62	Brittle
Locharbriggs (High Porosity)	Permian	28.85	305.41	29.18	20.61	2.99	Ductile
Locharbriggs (Low Porosity)	Permian	20.04	513.74	35.83	53.64	3.48	Brittle

Table 4.10: Comparison of the geomechanical characteristics of the Field A and the analogue sandstones. * Average values.

Sandstone Properties	Field A (Famgee)	Locharbriggs
Stratigraphic age	Paleocene	Permian
Depositional Environment	submarine fan	aeolian
Classification	quartz arenite	aub-arkose
Size Range	coarse to fine	medium to fine
Sorting	moderately poor to well	poorly to very well
Shape	angular to rounded	rounded
Primary Porosity	good	good
Secondary Porosity	minor (feldspar dissolution)	minor (feldspar dissolution)

Table 4.11: Comparison of petrographic properties of Famgee and Locharbriggs sandstones.

Sandstone Type	Weighjt of debris <90 µm/Weight of sample (%)	Failure Mode
Famgee (High Porosity)	2.46-0.52	Brittle
Famgee (Low Porosity)	10.04-35.39	Ductile/Transitional
Clashach	3.25-23.48	Ductile/Transitional
Doddington	0.98-2.27	Brittle
Fife Silica	1.08-4.26	Brittle
Lochaline	3.84-35.30*	Brittle
Locharbriggs (High Porosity)	3.54-19.25	Ductile/Transitional
Locharbriggs (Low Porosity)	1.25-2.49	Brittle

Table 4.12: Comminution products related to failure mode.

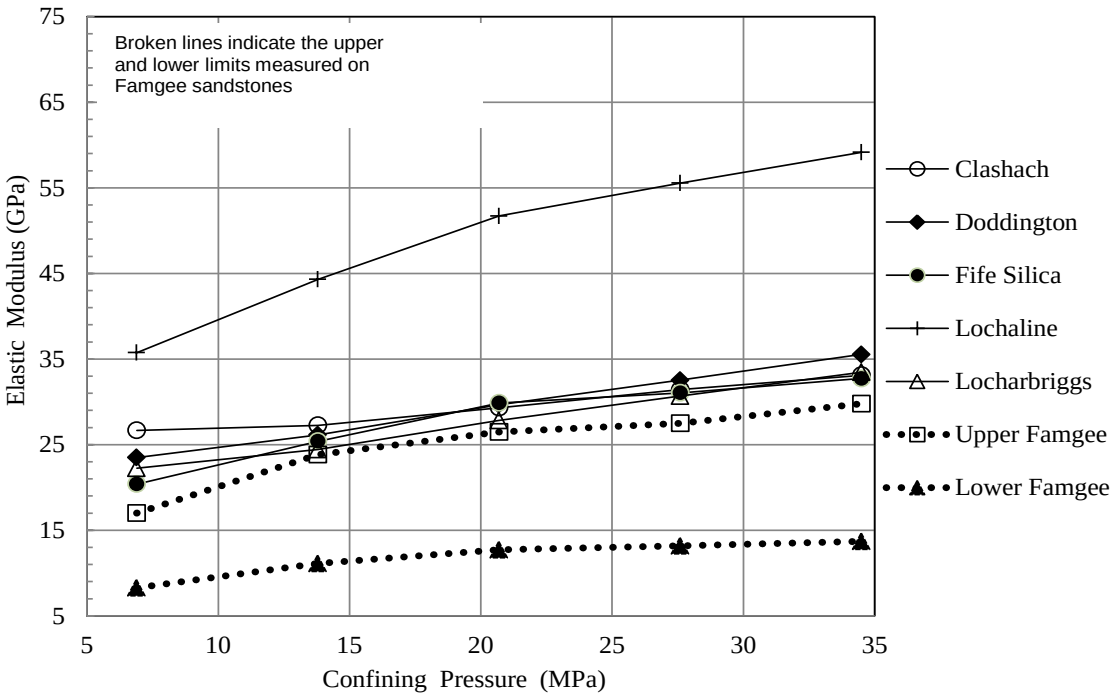

Figure 4.33: Comparison between average values of elastic modulus for the analogue sandstone with the reservoir sandstones.

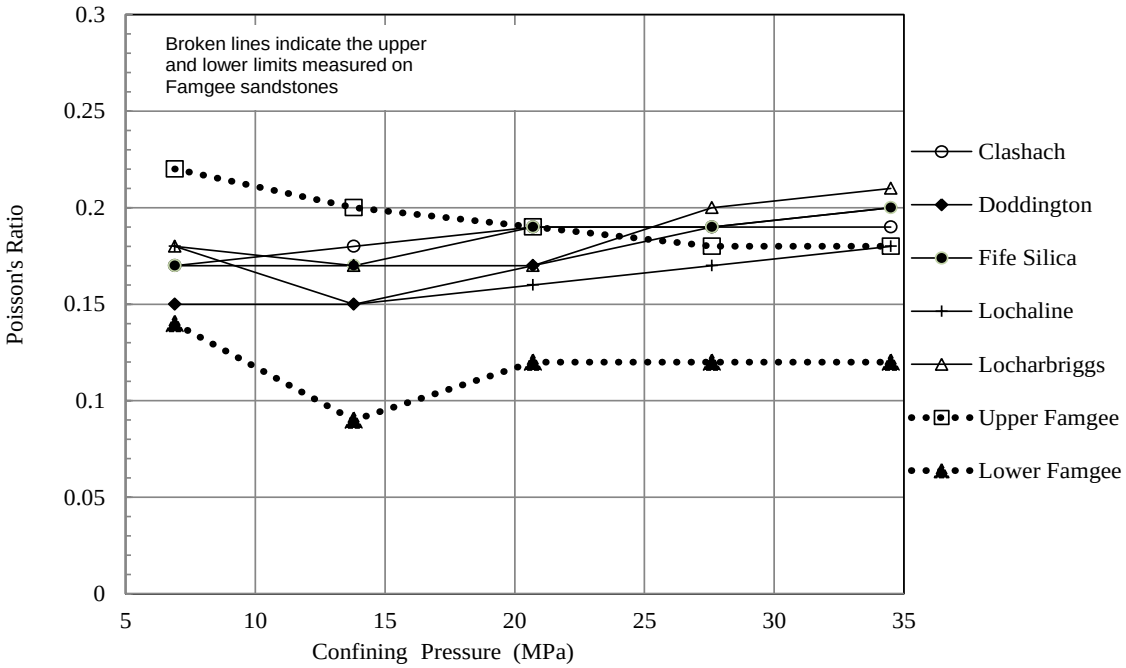

Figure 4.34: Comparison between average values of Poisson's ratio for the analogue sandstone with the reservoir sandstones.

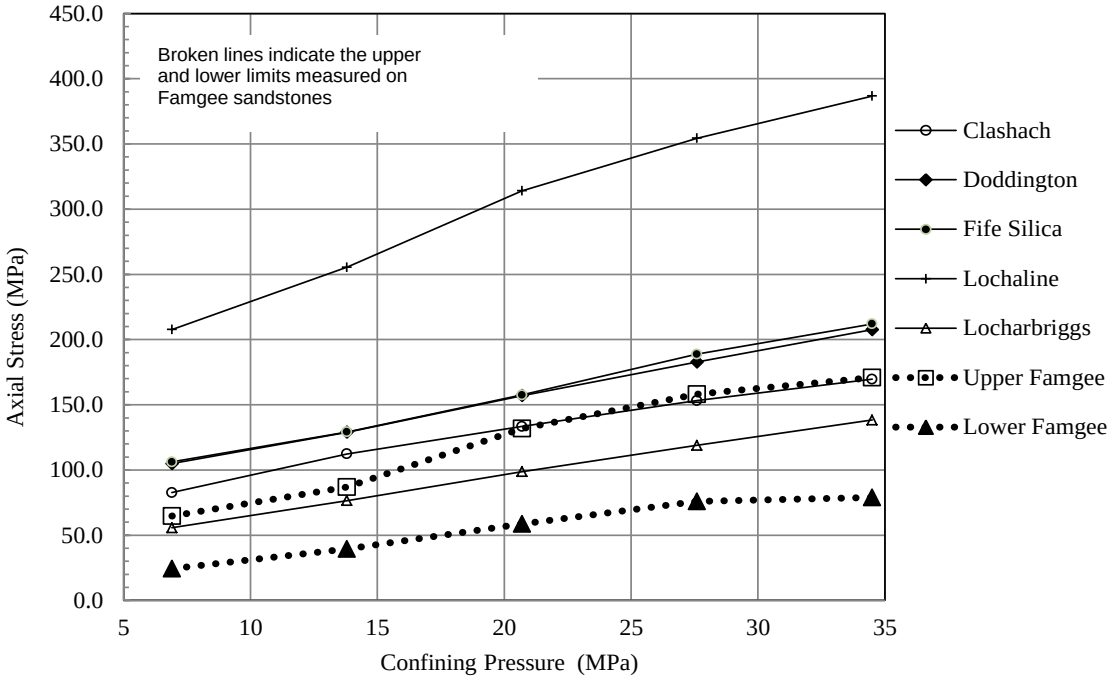

Figure 4.35: Comparison between average values of compressive strength for the analogue sandstone with the reservoir sandstones.

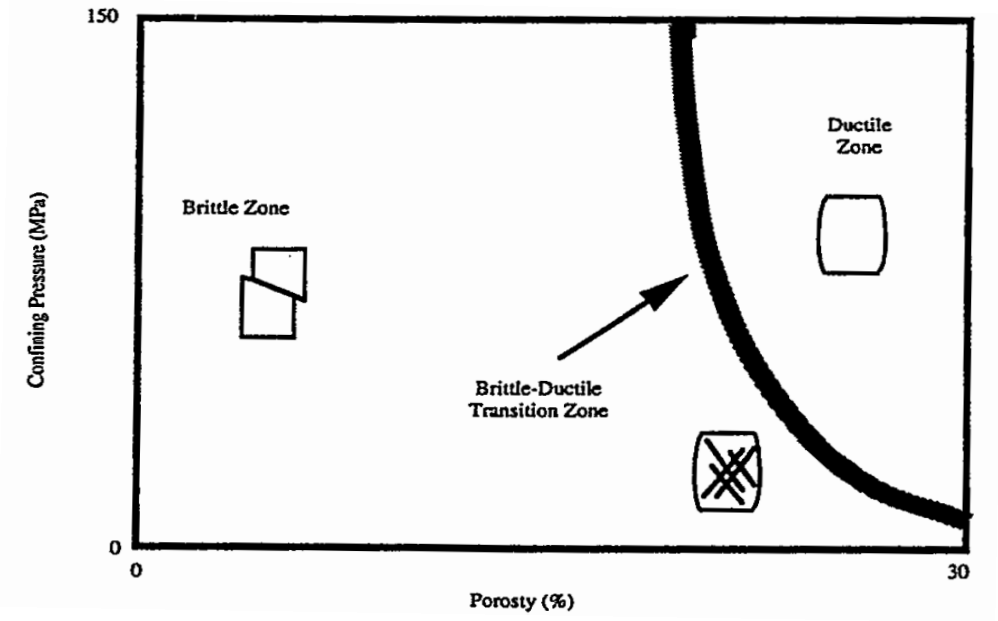

Figure 4.36: Influence of confining pressure and porosity on brittle-ductile transition for sandstones (after Scott and Nielsen, 1991).

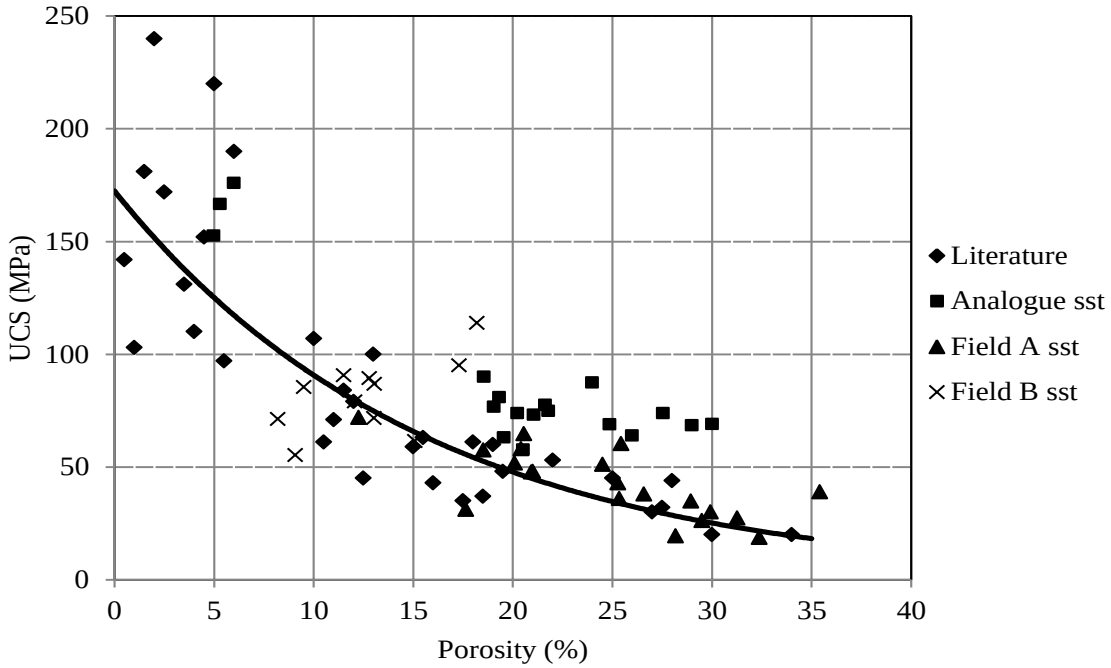

Figure 4.37: General correlation between porosity and uniaxial compressive strength (UCS) of sandstones.

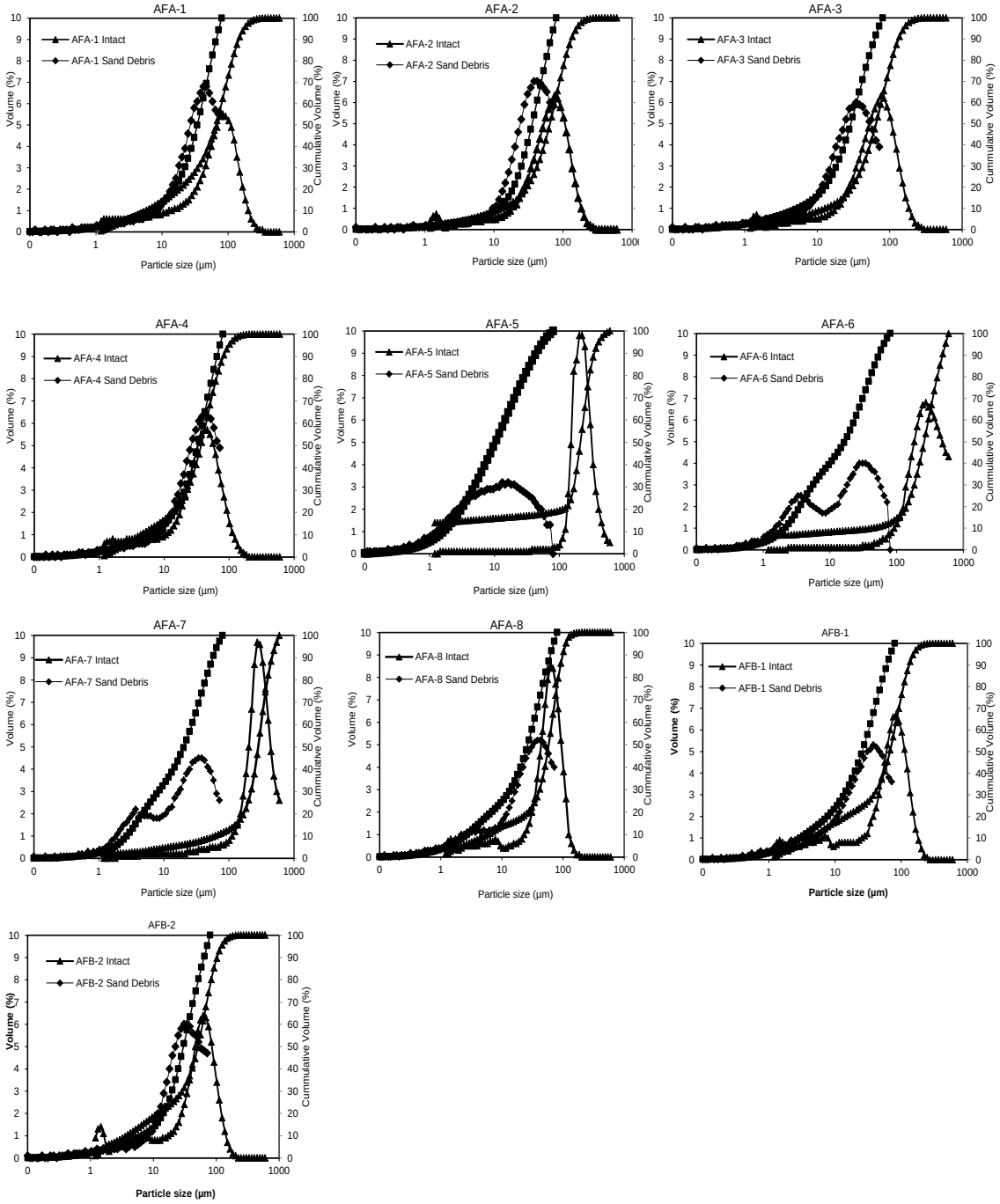

Figure 4.38: Particle size distribution of intact and comminution debris– wells AFA and AFB (Field A).

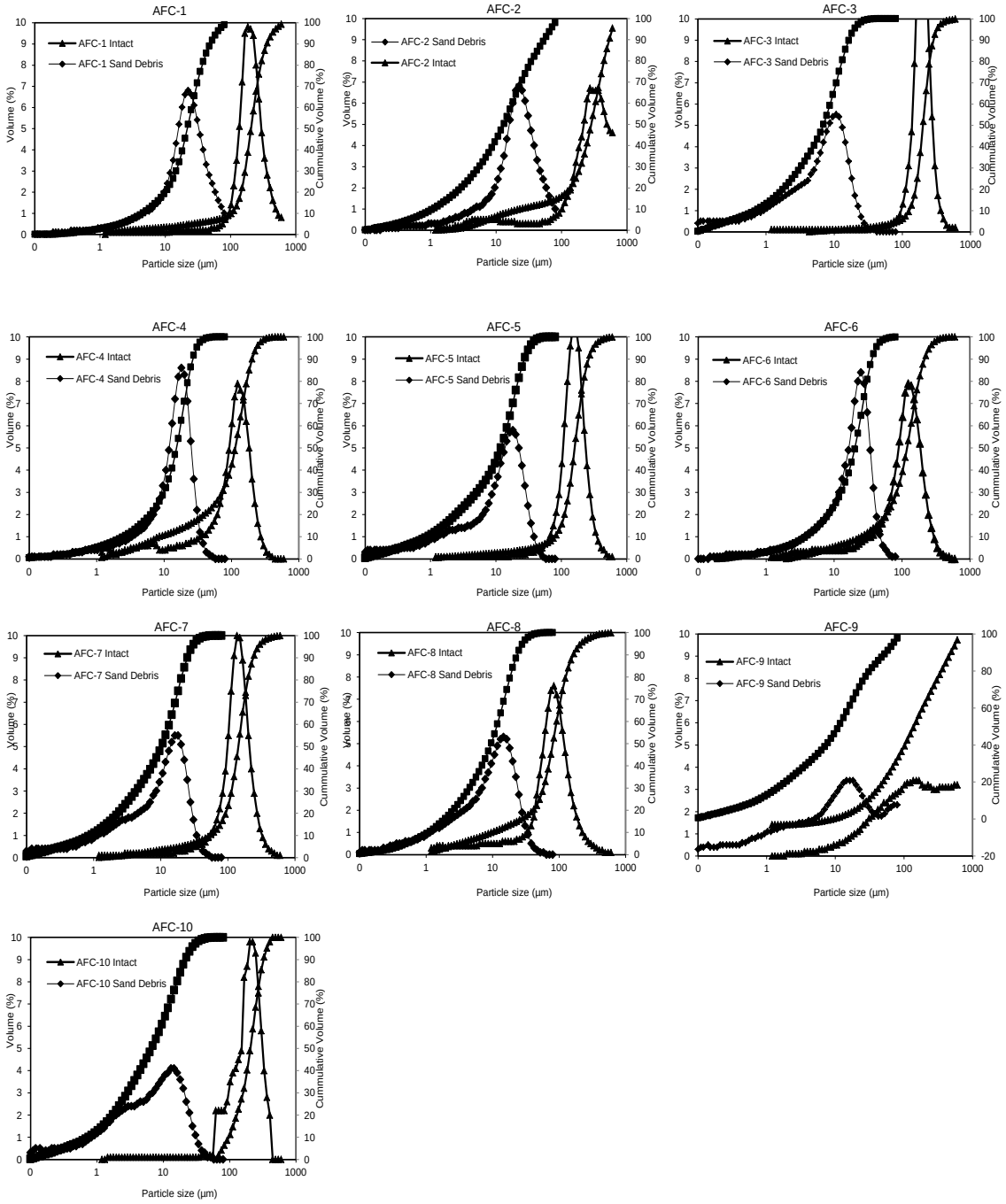

Figure 4.39: Particle size distribution of intact and comminution debris– well AFC (Field A).

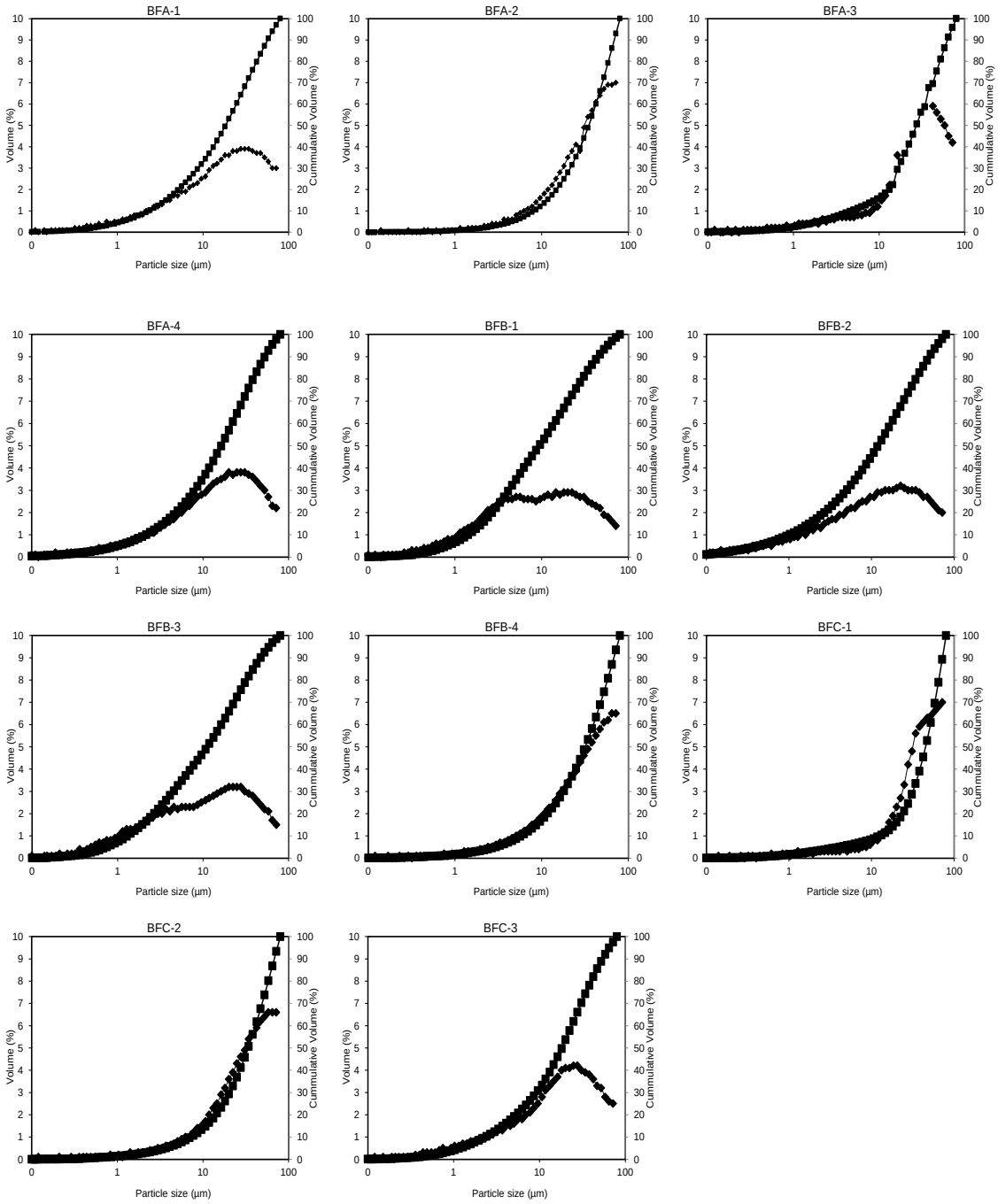

Figure 4.40: Particle size distribution of comminution debris–well BFA, BFB and BFC (Field B).

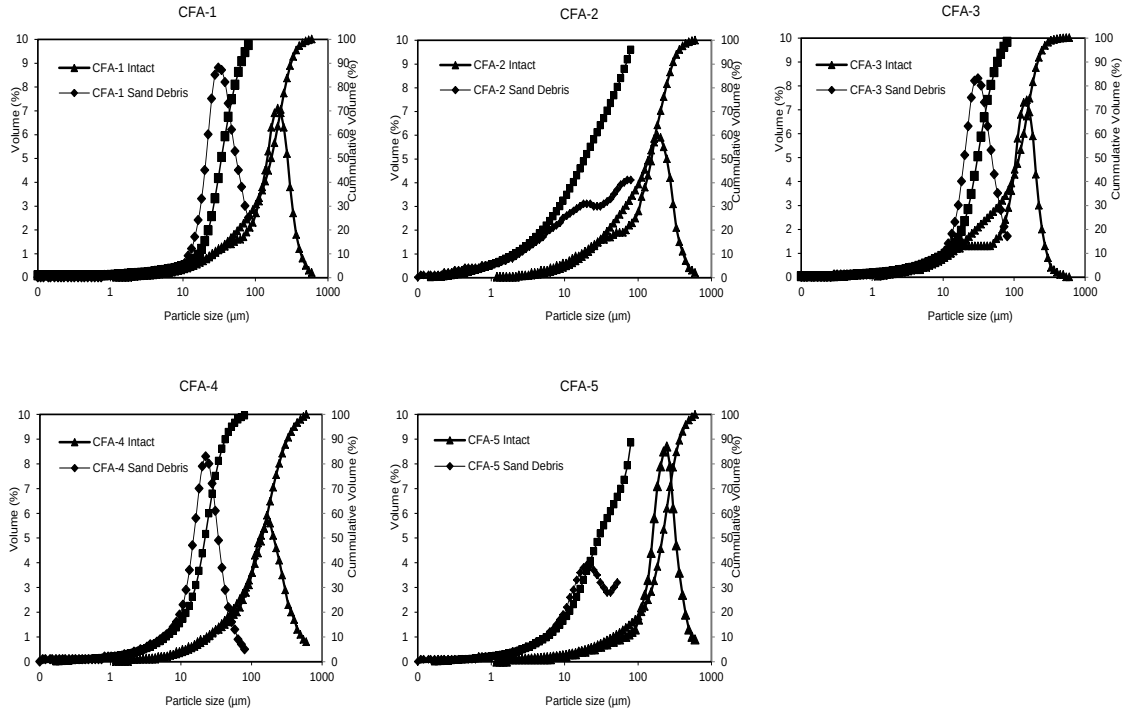

Figure 4.41: Particle size distribution of intact and comminution debris– well CFA (Field C).

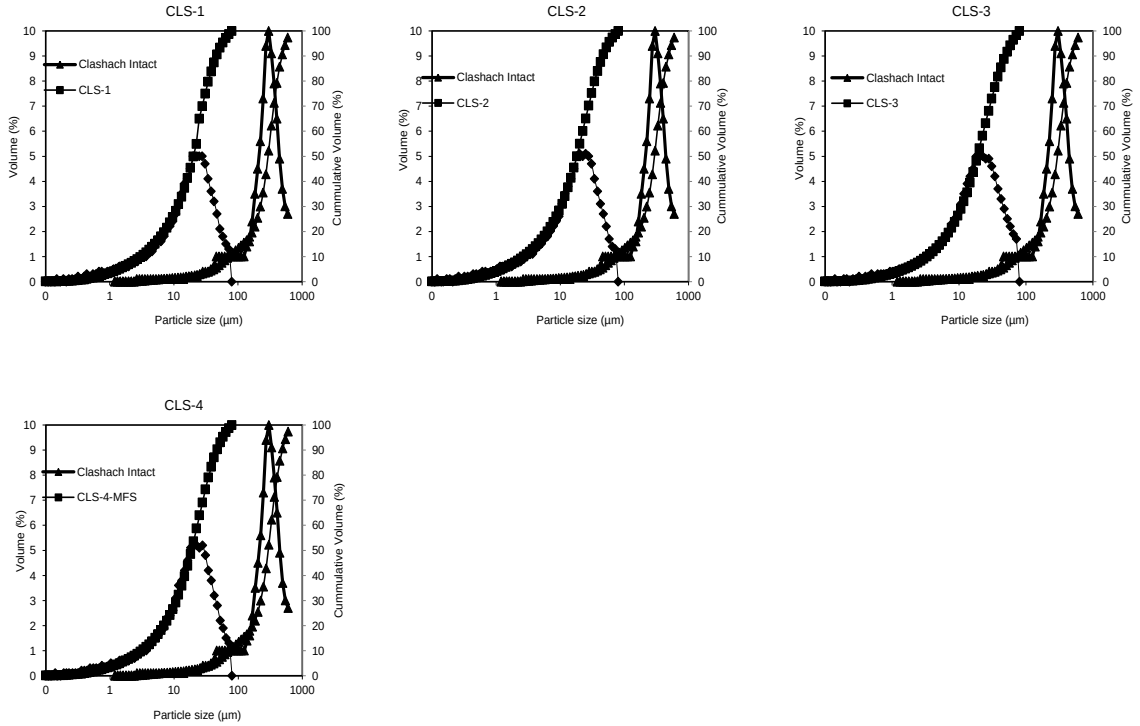

Figure 4.42: Particle size distribution of intact and comminution debris– Clashach sandstone samples.

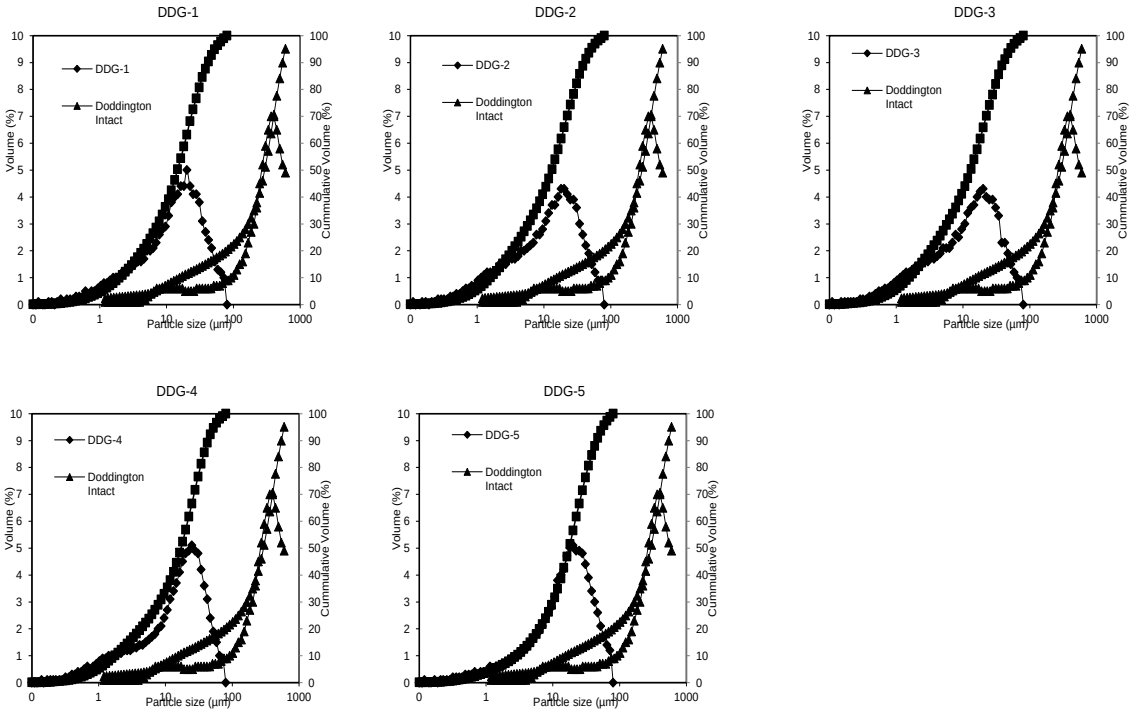

Figure 4.43: Particle size distribution of intact and comminution debris– Doddington sandstone samples.

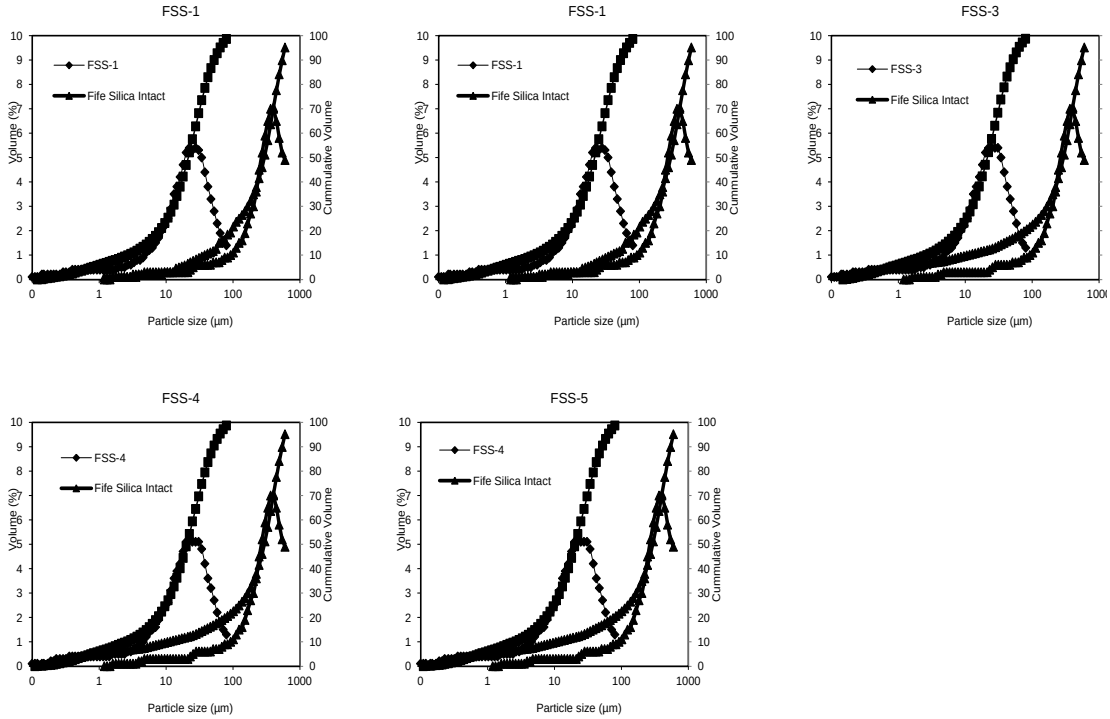

Figure 4.44: Particle size distribution of intact and comminution debris– Fife Silica sandstone samples.

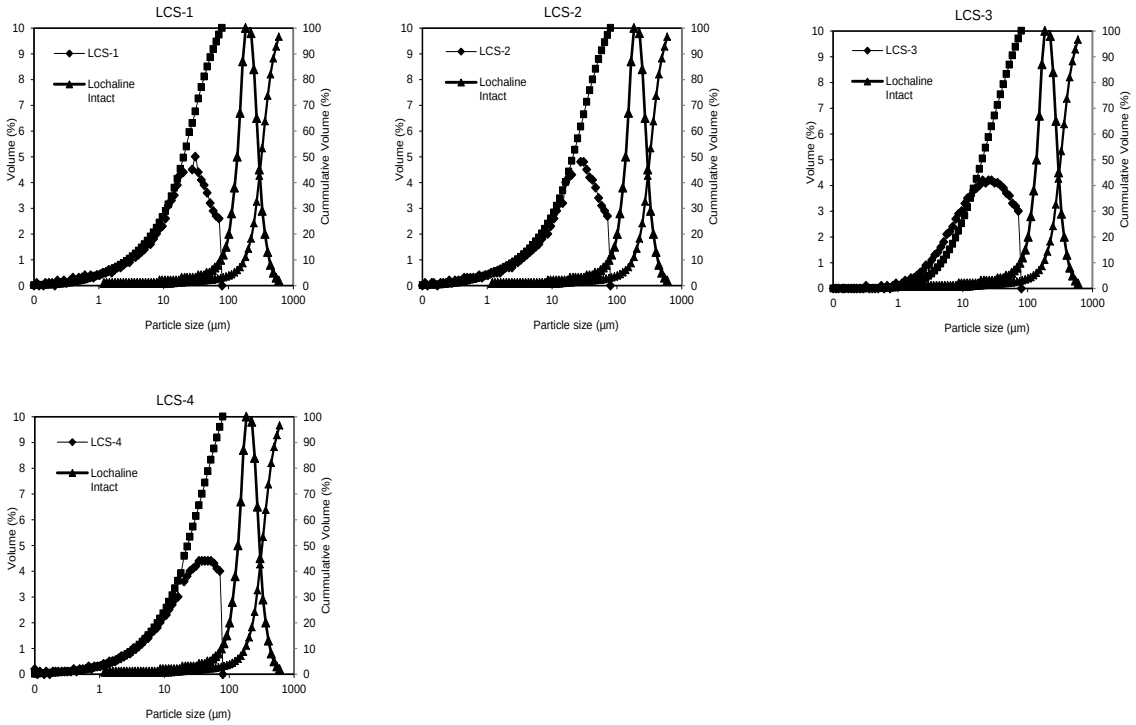

Figure 4.45: Particle size distribution of intact and comminution debris – Lochaline sandstone samples.

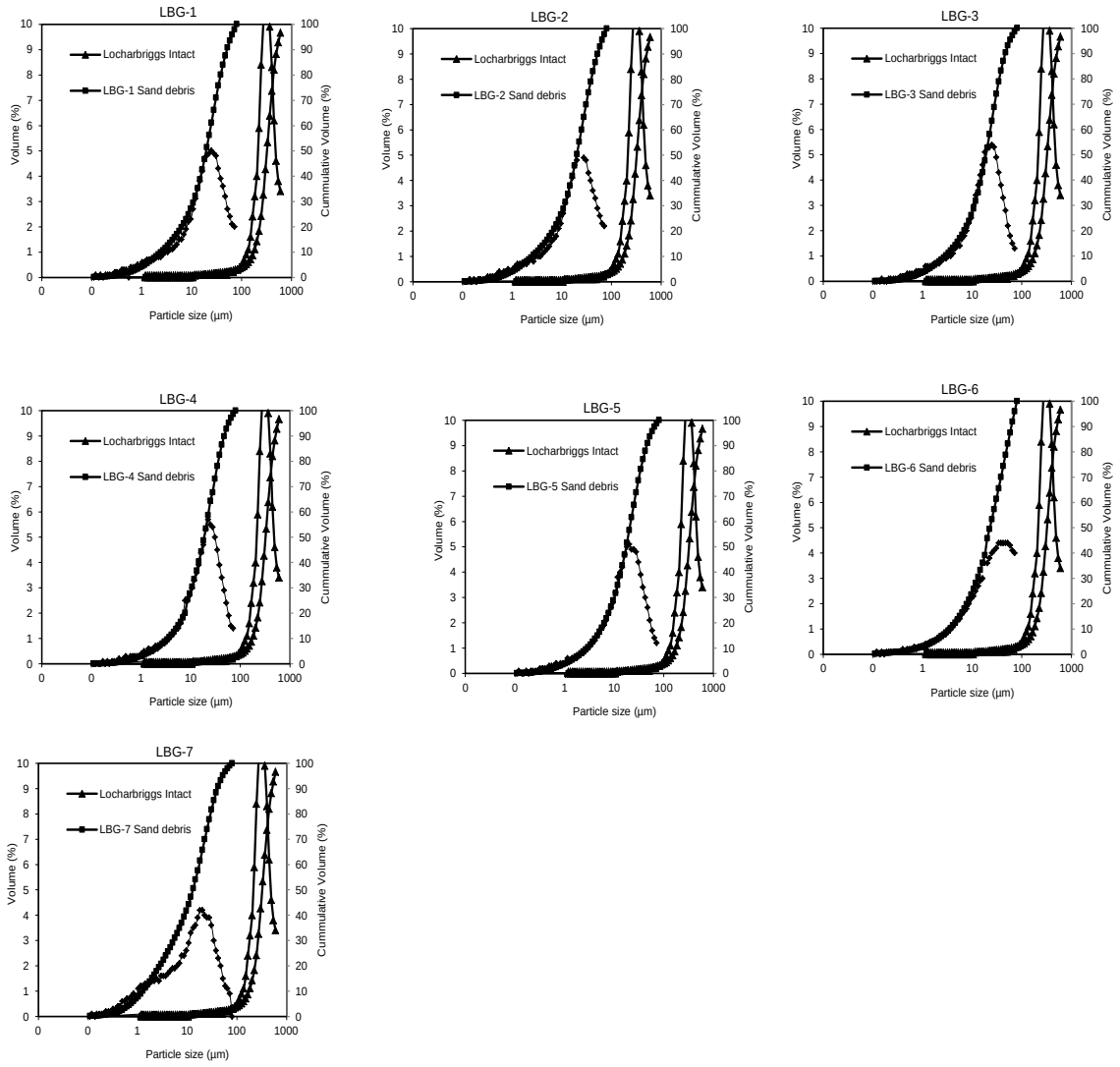

Figure 4.46: Particle size distribution of intact and comminution debris – Locharbriggs sandstone samples.

Sample I.D.	Depth (m)	Reservoir Horizion	Mass of sub 90 µm Debris (g)	Failure Angle (deg)	Sliding Surface Area (m^2)	Specific Surface Area (m^2/g)	Mean Diameter (µm)	Sorting	Distribution Mode
AFA-1	2787.15	Famgee	2.78	45.00	0.004817	0.0667	12.74	1.370	monomodal
AFA-2	2791.66	Famgee	0.66	38.70	0.004233	0.0647	12.70	1.371	monomodal
AFA-3	2796.84	Famgee	0.73	55.00	0.004601	0.0873	11.00	1.379	monomodal
AFA-4	2818.18	Famgee	0.84	56.40	0.004483	0.0809	11.88	1.379	monomodal
AFA-5	3709.11	Deekay	24.06	37.54	0.004801	0.1846	6.39	1.435	platykurtic
AFA-6	3722.83	Deekay	6.98	40.90	0.004681	0.1474	8.06	1.411	bimodal
AFA-7	3724.32	Deekay	1.78	45.87	0.004677	0.0926	10.93	1.389	bimodal
AFA-8	3727.52	Deekay	0.87	52.36	0.004470	0.1143	9.86	1.399	slightly
AFB-1	2750.30	Famgee	4.03	55.88	0.004804	0.1067	10.22	1.411	monomodal
AFB-2	3427.81	Deekay	0.43	55.74	0.004763	0.0986	11.16	1.402	monomodal
AFC-1	5494.05	Deekay	12.00	90.00	0.004536	0.0402	30.51	1.354	monomodal
AFC-2	5498.59	Deekay	16.70	45.00	0.009192	0.1065	25.32	1.351	monomodal
AFC-3	5509.41	Deekay	0.20	70.00	0.008950	0.1644	10.32	1.408	monomodal
AFC-4	5520.93	Deekay	5.70	60.00	0.004650	0.0668	16.23	1.364	monomodal
AFC-5	5561.32	Deekay	0.30	55.00	0.004775	0.1375	22.54	1.352	monomodal
AFC-6	5572.05	Deekay	35.60	45.00	0.009192	0.0460	31.24	1.347	monomodal
AFC-7	5573.48	Deekay	0.40	55.00	0.006447	0.1325	17.89	1.359	monomodal
AFC-8	5585.95	Deekay	0.60	45.00	0.005969	0.1013	12.35	1.375	monomodal
AFC-9	5601.77	Deekay	0.50	43.00	0.007282	0.1459	17.56	1.343	monomodal
AFC-10	5692.23	Deekay	0.20	58.00	0.013302	0.1571	12.30	1.377	monomodal

Table 4.13: Granulometric analysis of sub 90 µm comminution debris for samples from wells AFA, AFB and AFC.

Sample I.D.	Depth (m)	Reservoir Horizion	Mass of sub 90 µm Debris (g)	Failure Angle (deg)	Sliding Surface Area (m^2)	Specific Surface Area (m^2/g)	Mean Diameter (µm)	Sorting	Distribution Mode
BFA-1	3020.27	Rotliegendes	0.82	31.50	0.003318	0.14	10.10	1.238	monomodal
BFA-2	3033.45	Rotliegendes	3.74	25.00	0.002695	0.06	11.32	1.217	monomodal
BFA-3	3036.14	Rotliegendes	1.58	24.00	0.003757	0.09	10.86	1.224	monomodal
BFA-4	3041.90	Rotliegendes	0.55	35.50	0.003223	0.18	9.77	1.257	monomodal
BFB-1	3282.15	Rotliegendes	0.69	33.00	0.003848	0.20	5.68	1.327	monomodal
BFB-2	3286.07	Rotliegendes	0.65	34.00	0.003534	0.31	7.54	1.300	monomodal
BFB-3	3298.99	Rotliegendes	0.81	26.50	0.003732	0.20	5.98	1.324	monomodal
BFB-4	3308.36	Rotliegendes	3.55	34.50	0.002695	0.80	8.25	1.298	monomodal
BFC-1	3441.87	Rotliegendes	3.41	21.00	0.002450	0.06	13.21	1.214	monomodal
BFC-2	3446.98	Rotliegendes	4.84	35.00	0.002312	0.07	11.57	1.219	monomodal
BFC-3	3451.90	Rotliegendes	0.53	39.00	0.003377	0.13	12.47	1.213	monomodal

Table 4.14: Granulometric analysis of sub 90 µm comminution debris for samples from wells BFA, BFB and BFC.

Sample I.D.	Depth (m)	Reservoir Horizion	Mass of sub 90 µm Debris (g)	Failure Angle (deg)	Sliding Surface Area (m^2)	Specific Surface Area (m^2/g)	Mean Diameter (µm)	Sorting	Distribution Mode
CFA-1	1738.2	Kay	0.89	49.80	0.003556	0.4060	15.87	1.258	monomodal
CFA-2	1740.0	Kay	0.57	55.00	0.004737	0.3000	9.87	1.547	monomodal
CFA-6	1887.1	Kay	0.99	53.50	0.003319	0.7814	12.60	1.324	monomodal
CFA-8	1889.8	Kay	1.54	49.00	0.004353	0.5885	18.74	1.201	monomodal
CFA-9	1919.9	Kay	1.31	50.89	0.004600	0.2428	24.55	1.199	monomodal

Table 4.15: Granulometric analysis of sub 90 µm comminution debris for samples from well CFA.

Sample I.D.	Sandstone Type	Mass of sub 90 µm Debris (g)	Failure Angle (deg)	Sliding Surface Area (m^2)	Specific Surface Area (m^2/g)	Mean Diameter (µm)	Sorting	Distribution Mode
CLS-1	Clashach	0.58	65.00	0.000951	0.1233	14.10	1.301	monomodal
CLS-2	Clashach	5.70	60.00	0.004650	0.0668	11.00	1.374	monomodal
CLS-3	Clashach	0.98	48.00	0.000974	0.1250	16.51	1.101	monomodal
CLS-4	Clashach	0.30	55.00	0.004775	0.1375	14.51	1.299	monomodal
DDG-1	Doddington	1.46	55.00	0.002219	0.1556	11.54	1.597	monomodal
DDG-2	Doddington	1.66	45.00	0.002373	0.1445	13.47	1.499	monomodal
DDG-3	Doddington	1.38	43.00	0.002623	0.1809	15.89	1.384	monomodal
DDG-4	Doddington	0.98	51.00	0.002623	0.1809	17.58	1.311	monomodal
DDG-5	Doddington	1.03	50.50	0.003026	0.1809	12.55	1.580	monomodal
FSS-1	Fife Silica	1.94	58.00	0.002762	0.1763	15.70	1.301	monomodal
FSS-2	Fife Silica	0.98	45.00	0.002655	0.3123	13.54	1.458	monomodal
FSS-3	Fife Silica	1.54	45.00	0.002521	0.1937	18.92	1.232	monomodal
FSS-4	Fife Silica	1.09	48.00	0.002352	0.1798	18.01	1.219	monomodal
FSS-5	Fife Silica	1.25	52.00	0.002742	0.1057	17.89	1.298	monomodal
LCS-1	Lochaline	0.84	56.40	0.004483	0.0809	11.60	1.214	monomodal
LCS-2	Lochaline	24.06	37.54	0.004801	0.1846	10.89	1.099	monomodal
LCS-3	Lochaline	2.37	40.90	0.004681	0.1320	15.98	1.741	monomodal
LCS-4	Lochaline	2.98	45.87	0.004677	0.1370	15.24	1.725	monomodal
LBG-1	Locharbriggs	2.24	45.00	0.005753	0.1760	16.60	1.159	monomodal
LBG-2	Locharbriggs	1.01	38.70	0.005022	0.3245	19.87	1.099	monomodal
LBG-3	Locharbriggs	1.19	55.00	0.005576	0.2578	10.89	1.413	monomodal
LBG-4	Locharbriggs	0.99	38.70	0.005022	0.3245	16.88	1.162	monomodal
LBG-5	Locharbriggs	1.25	50.50	0.004535	0.3245	12.87	1.356	monomodal
LBG-6	Locharbriggs	5.11	49.00	0.004961	0.3245	15.54	1.211	monomodal
LBG-7	Locharbriggs	3.21	45.00	0.004781	0.3245	10.25	1.452	monomodal

Table 4.16: Granulometric analysis of sub 90 µm comminution debris for the analogue sandstones.

Sample I.D.	Depth (m)	Reservoir Horizion	Distribution Model						
			Rosin-Rammler (RR)			Gates-Gaudin-Schuhmann (GGS)			
			b	x_m	r_2	a	k	r_2	D
AFA-1	2787.15	Famgee	1.06	57.44	0.981	0.99	81.01	0.988	2.010
AFA-2	2791.66	Famgee	1.13	50.37	0.983	0.97	69.78	0.985	2.030
AFA-3	2796.84	Famgee	1.13	35.22	0.986	0.95	51.34	0.979	2.050
AFA-4	2818.18	Famgee	1.02	44.60	0.983	0.97	59.70	0.982	2.030
AFA-5	3709.11	Deekay	1.15	16.06	0.988	0.91	29.26	0.953	2.090
AFA-6	3722.83	Deekay	1.21	18.14	0.969	0.95	29.46	0.937	2.050
AFA-7	3724.32	Deekay	1.24	22.64	0.984	0.89	34.25	0.960	2.110
AFA-8	3727.52	Deekay	1.23	23.05	0.981	0.87	33.81	0.953	2.130
AFB-1	2750.30	Famgee	1.08	30.12	0.988	0.95	47.73	0.972	2.050
AFB-2	3427.81	Deekay	1.14	39.09	0.982	0.68	56.07	0.972	2.320
AFC-1	5494.05	Deekay	1.18	27.74	0.983	0.93	46.07	0.961	2.070
AFC-2	5498.59	Deekay	0.89	18.54	0.970	0.74	35.14	0.931	2.260
AFC-3	5509.41	Deekay	0.96	7.57	0.980	0.61	28.62	0.960	2.390
AFC-4	5520.93	Deekay	0.75	12.77	0.962	0.55	42.85	0.981	2.450
AFC-5	5561.32	Deekay	0.90	12.23	0.973	0.69	33.07	0.956	2.310
AFC-6	5572.05	Deekay	1.21	21.73	0.975	0.55	14.51	0.963	2.450
AFC-7	5573.48	Deekay	0.92	10.62	0.982	0.69	31.14	0.963	2.310
AFC-8	5585.95	Deekay	1.05	10.75	0.992	0.80	27.42	0.952	2.200
AFC-9	5601.77	Deekay	0.77	16.16	0.986	0.63	63.96	0.957	2.370
AFC-10	5692.23	Deekay	0.96	8.57	0.988	0.69	25.71	0.935	2.310
BFA-1	3020.27	Rotliegendes	1.12	22.06	0.980	0.79	37.44	0.962	2.210
BFA-2	3033.45	Rotliegendes	1.27	47.69	0.997	0.85	57.46	0.996	2.150
BFA-3	3036.14	Rotliegendes	1.07	40.14	0.982	0.98	52.78	0.979	2.020
BFA-4	3041.90	Rotliegendes	0.97	22.92	0.998	0.86	37.40	0.990	2.140
BFB-1	3282.15	Rotliegendes	1.16	13.89	0.969	1.00	22.71	0.937	2.000
BFB-2	3286.07	Rotliegendes	0.81	18.1	0.997	0.681	35.64	0.984	2.319
BFB-3	3298.99	Rotliegendes	1.13	14.66	0.961	0.95	56.43	0.995	2.050
BFB-4	3308.36	Rotliegendes	1.10	43.45	0.997	0.93	56.43	0.995	2.070
BFC-1	3441.87	Rotliegendes	1.01	77.9	0.979	0.95	103.61	0.991	2.050
BFC-2	3446.98	Rotliegendes	1.19	43.49	0.993	0.93	59.89	0.991	2.070
BFC-3	3451.90	Rotliegendes	1.11	22.51	0.987	0.95	54.00	0.954	2.050
CFA-1	1738.15	Kay	1.05	36.24	0.978	0.95	35.31	0.954	2.050
CFA-2	1739.98	Kay	0.15	12.69	0.951	0.34	35.31	0.948	2.660
CFA-6	1887.09	Kay	1.10	14.01	0.988	0.88	29.22	0.936	2.120
CFA-8	1889.76	Kay	1.02	21.06	0.997	0.61	32.51	0.982	2.390
CFA-9	1919.94	Kay	1.26	30.52	0.979	0.9	51.41	0.974	2.100

Table 4.17: Particle size distribution parameters of Rosin-Rammler and Gates-Gaudin-Schuhmann models for the shear debris.

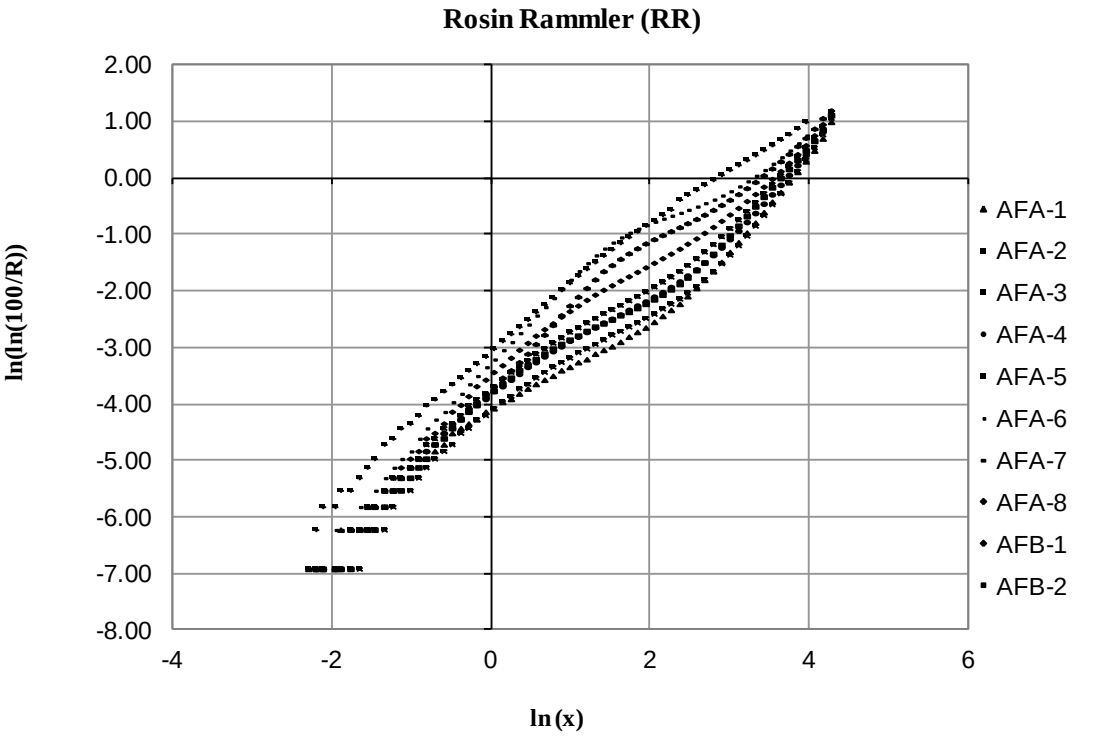

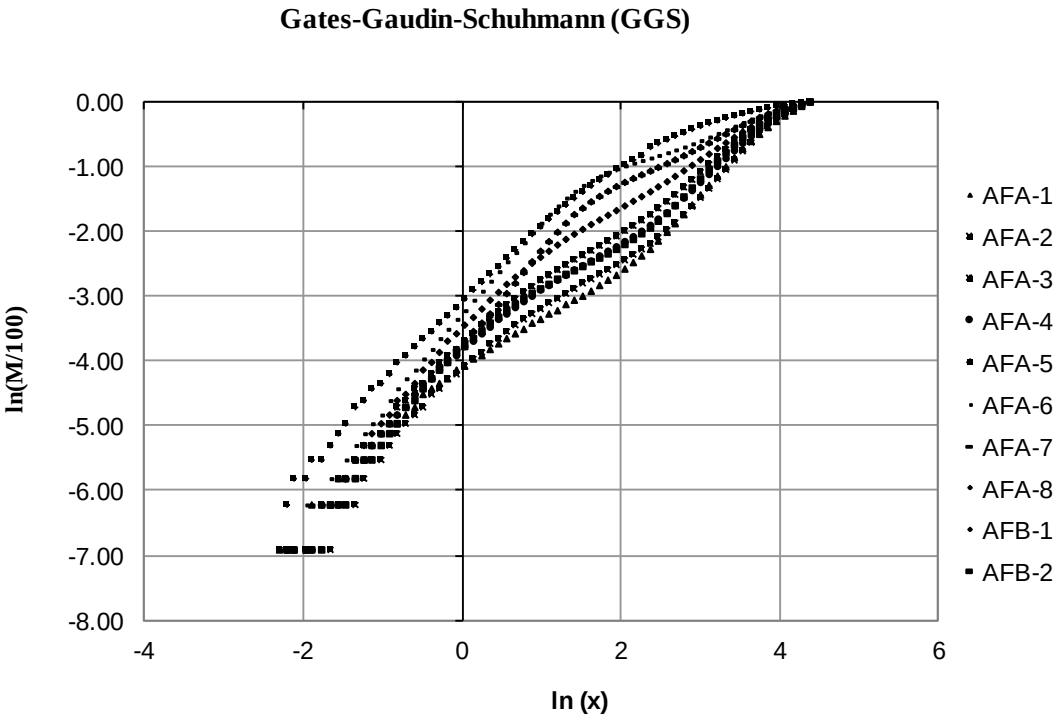

Figure 4.47: Rosin-Rammler and Gate-Gaudin-Schuhmann plots of particle size distributions for shear debris samples from wells AFA and AFB.

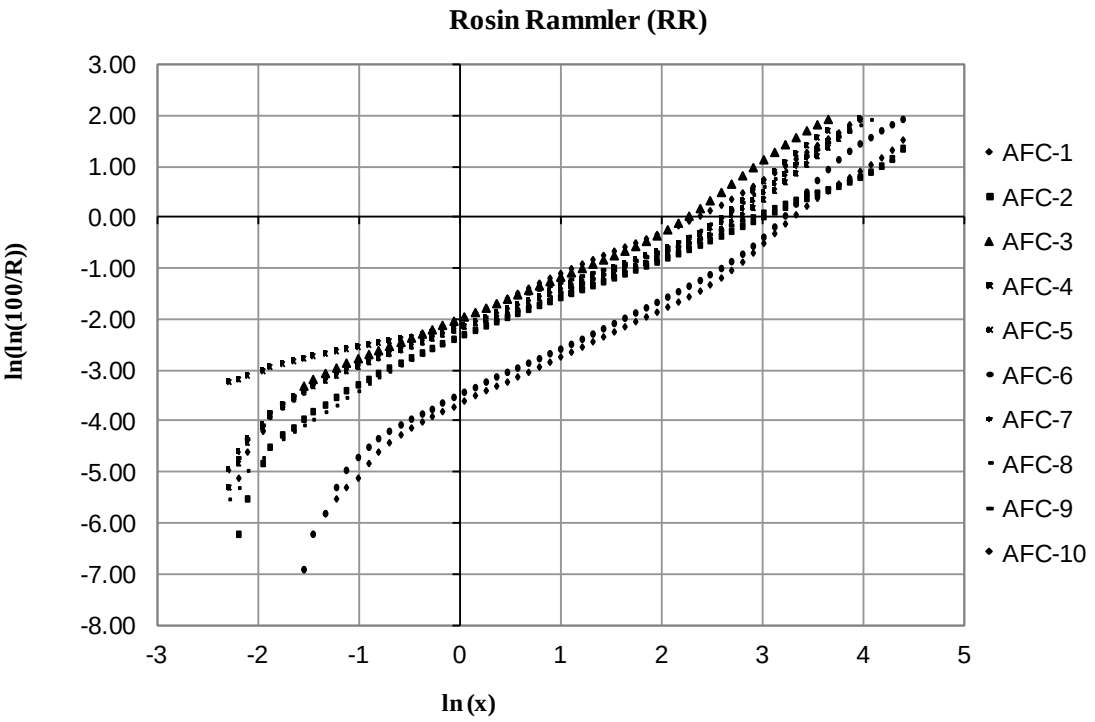

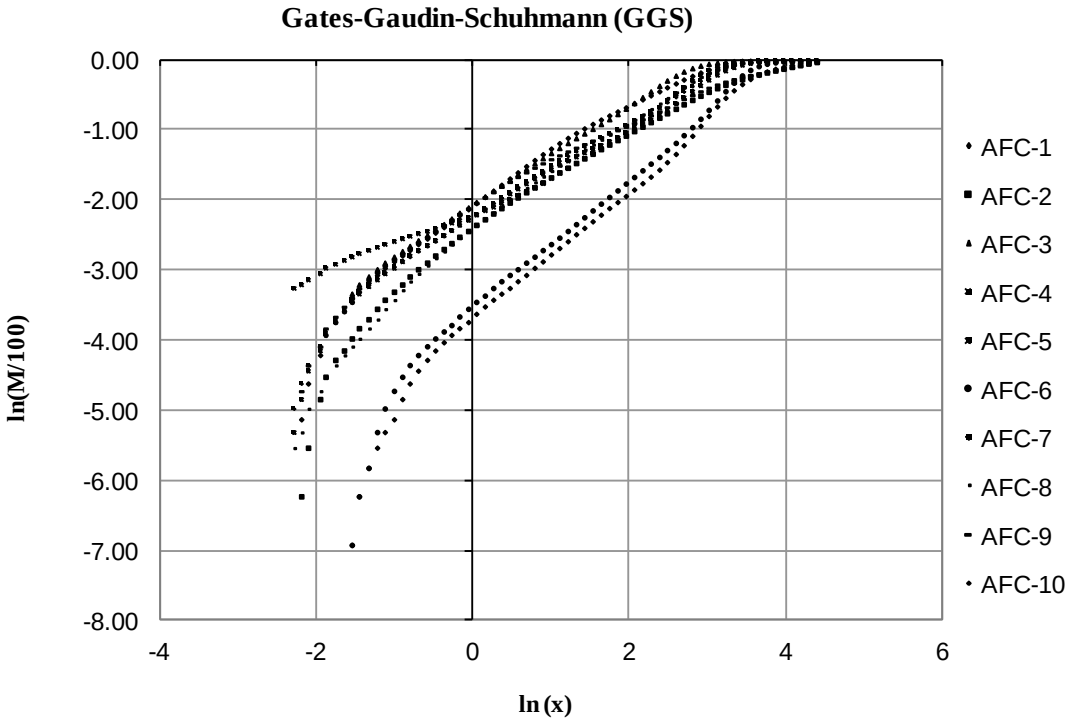

Figure 4.48: Rosin-Rammler and Gate-Gaudin-Schuhmann plots of particle size distributions for shear debris samples from well AFC.

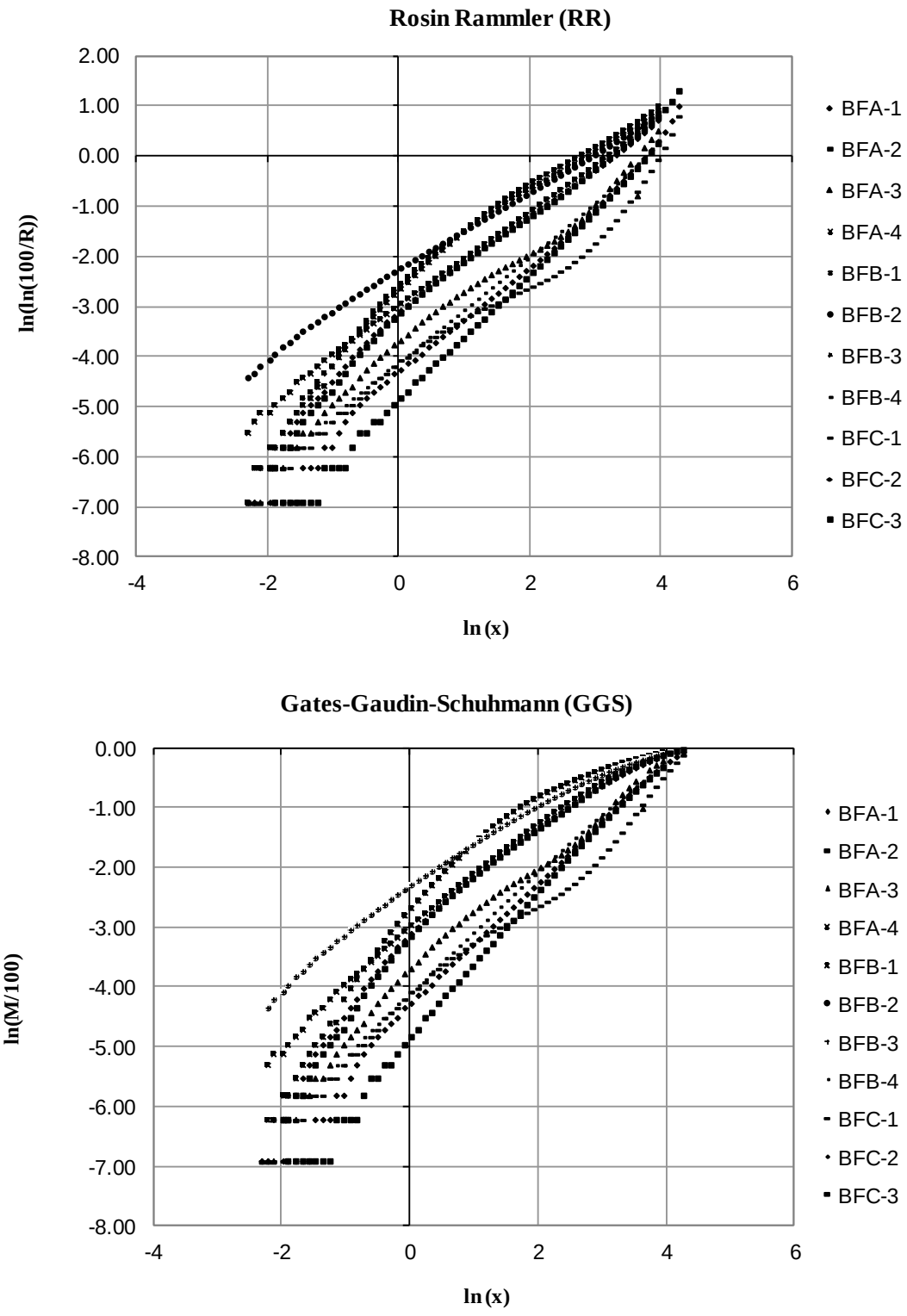

Figure 4.49: Rosin-Rammler and Gate-Gaudin-Schuhmann plots of particle size distributions for shear debris samples from wells BFA, BFB and BFC.

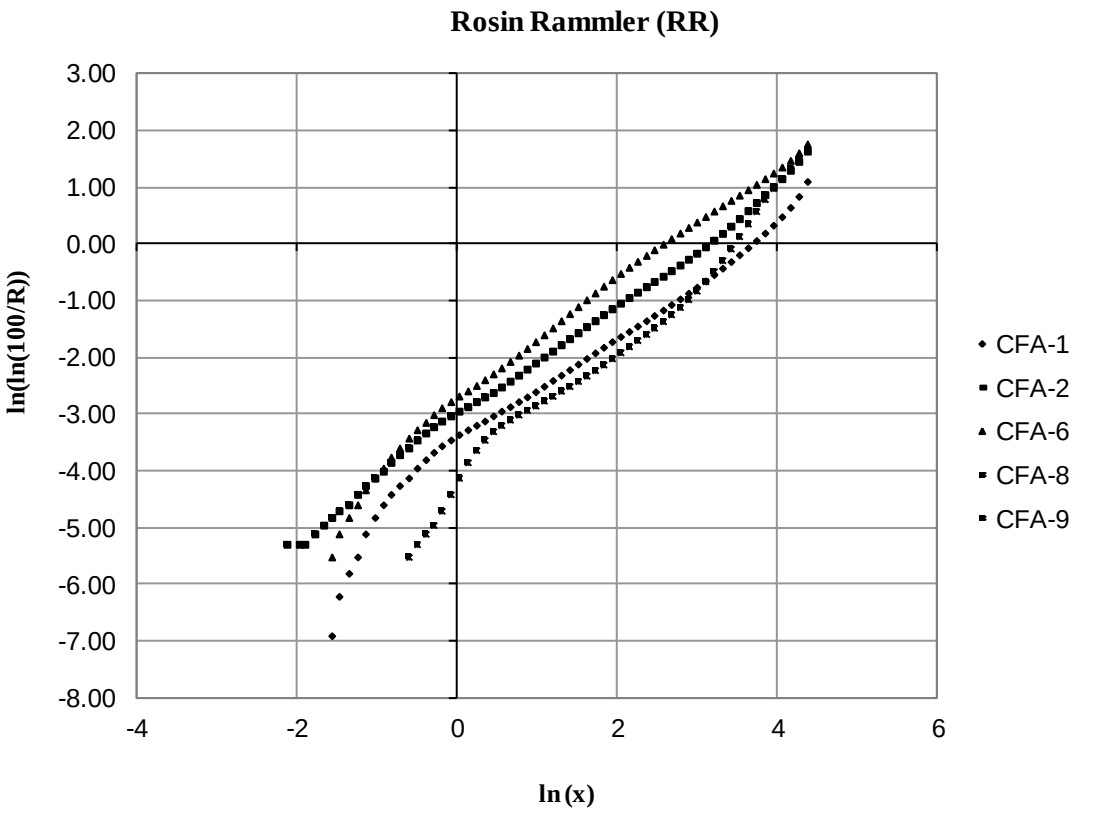

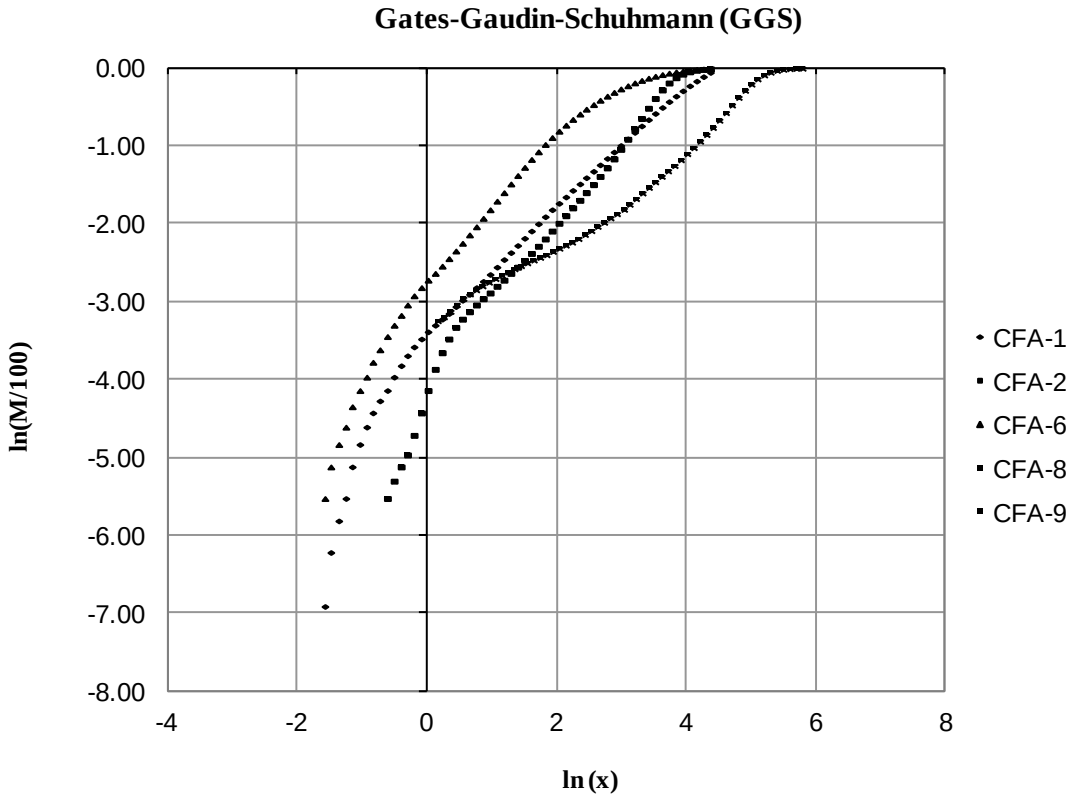

Figure 4.50: Rosin-Rammler and Gate-Gaudin-Schuhmann plots of particle size distributions for shear debris samples from well CFA

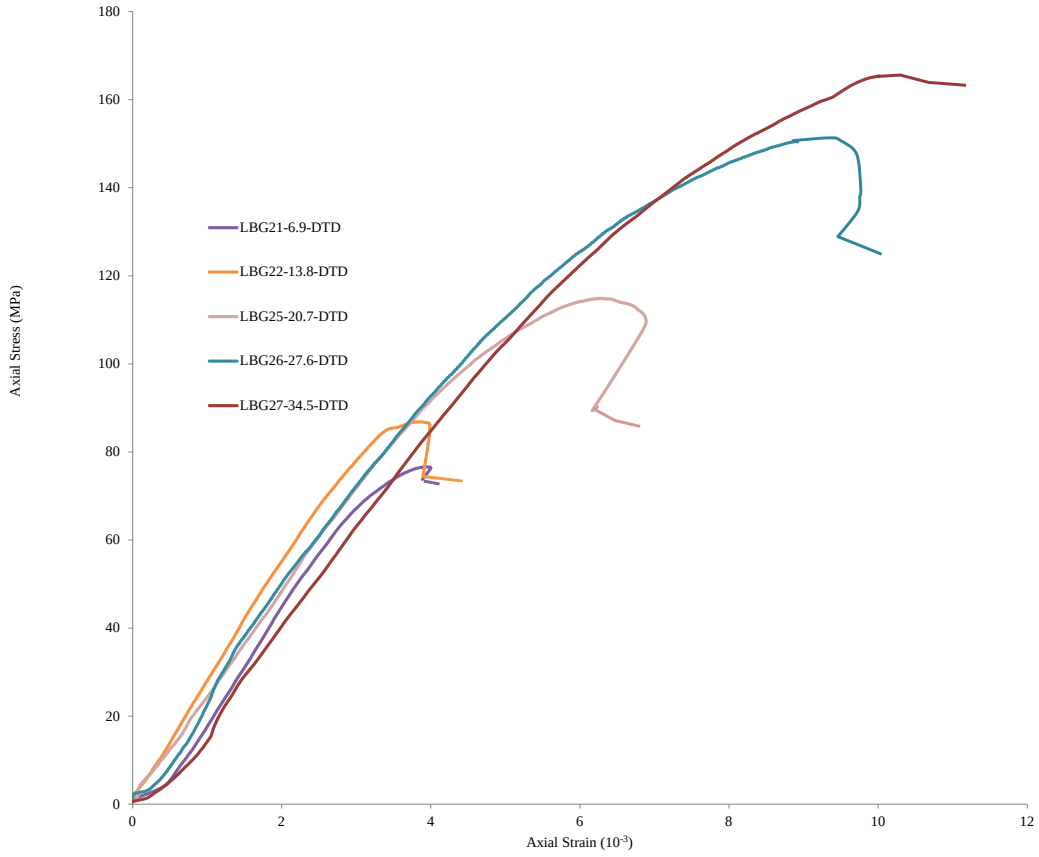

Figure 4.51: Stress-strain curve of the discrete tests for the Locharbriggs samples tested at different confining pressure.

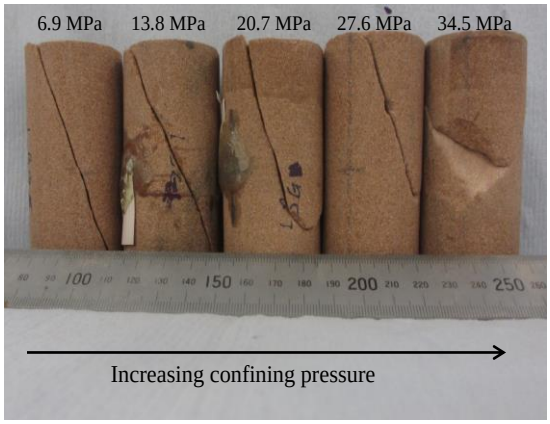

(a) deformed samples

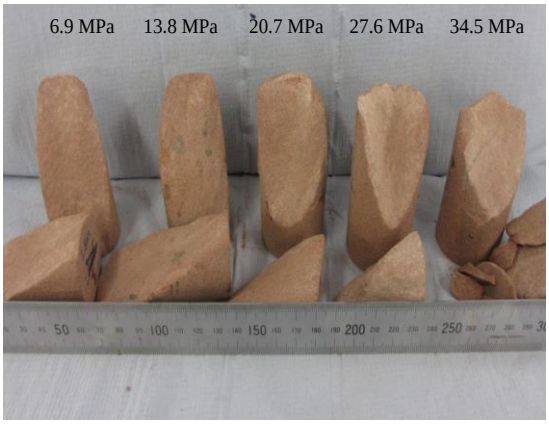

(b) failure surfaces of deformed samples

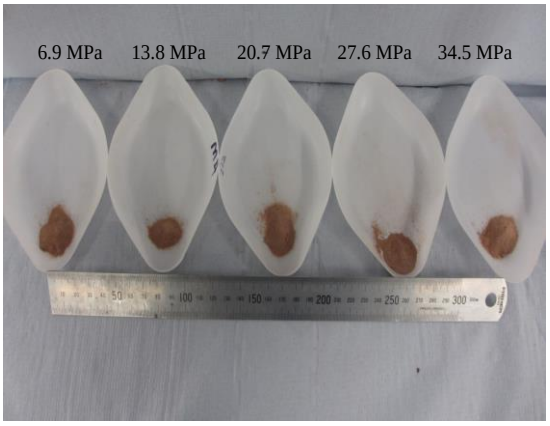

(c) debris recovered from failure surfaces of deformed samples

Figure 4.52: Photographs of Locharbriggs samples tested at increasing confining pressure showing, (a) deformed samples, (b) failure surface of deformed samples and (c) debris recovered from deformed samples.

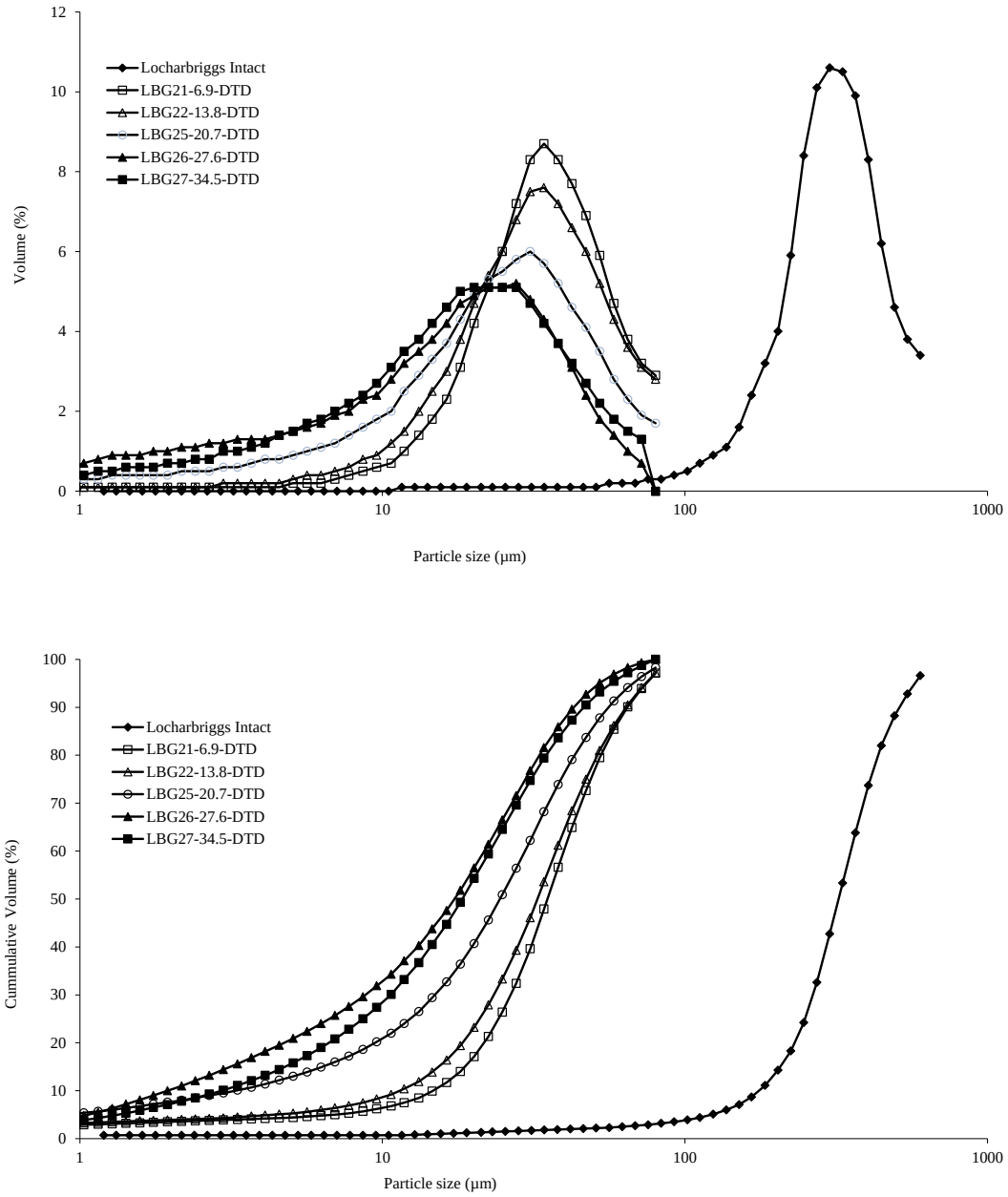

Figure 4.53: Particle size distribution of intact Locharbriggs sandstone and comminuted debris from discrete tests samples deformed at increasing confining pressure.

Confining Pressure (MPa)	Mean (μ)	Sorting
Intact Material	201	0.354
6.9	19.4	0.641
13.8	17.5	1.342
20.7	15.4	1.501
27.6	9.5	1.825
34.56	9.6	1.831

Table 4.18: Distribution parameters for both intact Locharbriggs sandstone and comminuted debris from shear induced fracture.

5 Development of the Strain Energy Approach to Sand Production Prediction

5.1 Introduction

Sand production has always been a problem in unconsolidated to loosely consolidated sandstones (Tippie and Kohlhaas, 1973, Antheunis et al., 1976b, Perkins and Weingarten, 1988, Vaziri, 2004, Wu et al., 2004, Nouri et al., 2006a, Adeyanju and Oyekunle, 2011, Wang and Papamichos, 2012a, Volonte et al., 2013). However, sand production has also been observed in formation which would be considered to be moderately consolidated and competent (Papamichos, 2002, Andrews et al., 2005). The failure mechanism associated with such moderately consolidated and competent formation is quite different from the sand arch mechanism (Hall and Harrisberger, 1970, Risnes et al., 1982a, Arii et al., 2005) which prevails in unconsolidated formation. The occurrence of shear fractures similar to that observed in triaxial testing in the laboratory has been reported (e.g. Al-Awad and Desouky, 1997). Accordingly, sand production from these shear fractures are product of comminuted debris resulting from shear sliding of the fracture planes. Therefore, in order to mitigate sand production and maximise the recovery of hydrocarbon reservoirs, it is necessary to accurately assess the potential of a rock formation to produce sand during the initial field developmental stage.

The overall majority of currently available sand prediction models (Weissenburger et al., 1987, Morita et al., 1989a, Morita et al., 1989b, Weingarten and Perkins, 1995, Sanfilippo et al., 1997, Tronvoll et al., 1997, Papamichos and Malmanger, 1999, Papamichos, 2002, Vaziri et al., 2002, Wu and Tan, 2002, Vaziri, 2004, Wu et al., 2004, Nouri et al., 2006a, Nouri et al., 2006b, Palmer et al., 2006, Papamichos, et al., 2008, Khaksar et al., 2008, Palmer et al., 2008, Nouri et al., 2009, Wang and Papamichos, 2012a, Wang and Papamichos, 2012b, Volonte et al., 2013) are developed for unconsolidated and loosely consolidated formation. These models are usually based on conventional failure criteria to predict the 'onset' of sand prediction where the maximum effective stress exceeds the strength of the formation. However, sand production is a consequential effect of continuous changes occurring in the wellbore and around the perforation region. In this chapter, a new sand prediction approach based on comprehensive analysis of the energy changes (accumulation and dissipation) that occur during rock failure is presented. In this chapter, a novel method of predicting sand

production potential of a formation based on a comprehensive analysis of the energy changes (accumulation and dissipation) that occur during rock failure is presented.

5.2 Sand Failure Mechanisms

The sand surrounding a wellbore can fail due to compressive failure as a result of depletion and drawdown usually analysed by continuum modeling (Antheunis et al., 1976b, Nordgren, 1977, Coates and Denoo, 1981, Edwards et al., 1983, Geertsma, 1985, Peden and Yassin, 1986, Morita et al., 1989a, Morita et al., 1989b, Dusseault and Santarelli, 1989) or tensile failure as a result of drawdown (fluid drag) alone (Bratli and Risnes, 1981, Risnes et al., 1982b, Perkins and Weingarten, 1988, Vaziri, 1988, Morita et al., 1989a, Morita et al., 1989b, Dusseault and Santarelli, 1989). Failure as a result of erosion which considers the dislodging of individual grains due to excessive fluid pressure and thus accounts for individual grain-to-grain interactions has also been proposed (e.g., Dusseault and Santarelli, 1989).

In the event of compressive failure, an excessive, near cavity wall, (compressive) tangential stress causes shear failure of the formation material (Figure 5.1). This is dependent on both the *in situ* stresses (depletion of reservoir pressure) and drawdown pressure applied locally to the wellbore. Tensile failure refers to a situation where the tensile radial stress exceeds the tensile failure envelope and is normally triggered exclusively by drawdown pressure. Laboratory sand production experiments support the existence of both types of failure; tensile failure predominates in unconsolidated sands, while compressive failure predominates in consolidated sandstone (Veeken, 1991). Erosion occurs when the drag forces exerted on a particle at the sand face exceed its apparent cohesion which can be considered as a special form of tensile failure.

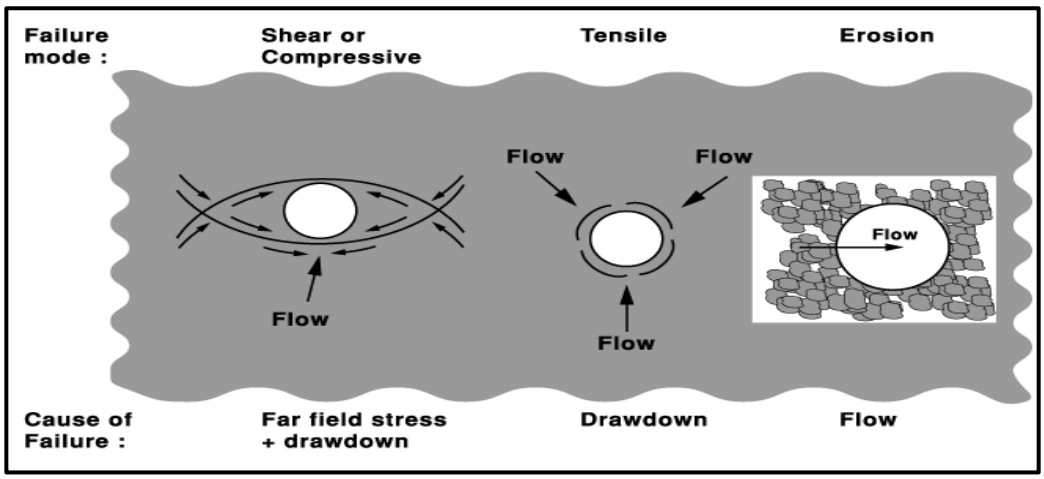

Figure 5.1: Sand Failure model (Veeken et al., 1991).

5.3 Sand Prediction Methods

Over past decades numerous studies have been undertaken in order to be able to predict whether a well will produce fluids with or without producing sand. These approaches are based on empirical method from field observation, laboratory experiments and theoretical modeling (Veeken et al., 1991, Kessler et al., 1993, Sanfilippo et al., 1995, Ranjith et al., 2013).

5.3.1 Empirical Method using Field Observation

Sand prediction techniques based on field experience rely on establishing a correlation between sand production well data and field and operational parameters including formation data e.g. strength, *in situ* stresses; reservoir data, e.g. pore pressure, fluid composition, drainage radius, reservoir thickness; completion data e.g. wellbore orientation and diameter, perforation policy, under/overbalance, completion fluids and production data such as flowrate, drawdown pressures and formation damage. The technique most frequently used for prediction of sand production is analogy with other wells in the same horizon, field, or area. The data are then correlated to produce simple relationship between, for instance, unconfined compressive strength with depth criteria, compressional sonic wave transit time and results obtained from rock compressional tests (Stein and Hilchie, 1972, Stein et al., 1974, Tixier et al., 1975, Stein, 1976, Ghalambor et al., 1989, Veeken et al., 1991, Sanfilippo et al., 1995, Tronvoll et al., 1997). This method has largely been adopted by most oil companies around the world as a means of sand prediction for the simple fact that it can relate sand production well and field data with operational parameters (Veeken et al., 1991).

The Mechanical properties approach (Mechpro) is one of the most used empirical methods of sand prediction. Tixier et al. (1975) conducted field tests on Gulf of Mexico formations to develop a sand strength criterion based on sonic and density log derived parameter, G/C_b (ratio of shear modulus to bulk compressibility). A limit value was proposed as the threshold criterion of sand production. Sand production is expected when G/C_b exceeds 0.8 $x10^2$ psi^2. This technique gives a general estimate as to whether or not sanding may take place, but it does not indicate at what pressure drawdown or production rate sanding should be expected.

5.3.2 Theoretical Methods

Generally, most of the existing sand prediction methods are based on analytical and numerical models (e.g., Risnes et al., 1982b, Perkins and Weingarten, 1988, Morita et al., 1989b, Dusseault and Santarelli, 1989, Sanfilippo et al., 1995, Vaziri et al., 1997). Compressive strength based models ranging from simple and easy to implement elastic brittle failure (eg., Coates and Denoo, 1981, Edwards et al., 1983, Nordgren, 1977) to more realistic elastic-plastic material (e.g., Antheunis et al., 1976b, Peden and Yassin, 1986, Morita et al., 1989a, Morita et al., 1989b, Dusseault and Santarelli, 1989) have been proposed. The elastic-plastic models provide a more realistic description of the material behaviour at the expense of high computational effort (Nouri et al., 2006a). As reported by Veeken et al. (1991), the majority of the sand failure analyses in the literature are carried out using either Mohr-Coulomb (Coates and Denoo, 1981, Peden and Yassin, 1986) or Drucker-Prager (Antheunis et al., 1976b, Morita et al., 1989b) failure criteria.

5.3.3 Experimental Sand Prediction Methods

Laboratory sand prediction method such as sand production experiments to simulate the process that may be involved in sand production in a controlled environment (Perkins and Weingarten, 1988, Cook et al., 1994, Presles and Creusot, 1997, Tronvoll et al., 1997, Morita and Fuh, 1998, Ranjith et al., 2013) and thick-walled cylinder tests (Antheunis et al., 1976a, Geertsma, 1985, Cook et al., 1994, van den Hoek et al., 1996) are common sand prediction approach.

Laboratory sand production tests have been carried out using both unconsolidated sand (Hall and Harrisberger, 1970, Tippie and Kohlhaas, 1973, Durrett et al., 1977, Clearly et al., 1979, Wood, 1979, Bratli and Risnes, 1981) and friable-consolidated sandstone (Vriezen et al., 1975) on perforation cavity (Tronvoll, 1992, Tronvoll et al., 1992, Tronvoll and Fjaer, 1994, Tronvoll and Halleck, 1994). In the tests on unconsolidated

material, the formation of stable arches around a perforation is widely believed to inhibit sand production. Typically, majority of these experiments simulate small scale formation and stability of sand arches or flow through perforation or cylindrical cavities in a stressed cylindrical core sample. Large experiments (Kooijman et al., 1992) and even full scale experiments on artificial well (Behrmann et al., 1993) under realistic and controlled conditions have been performed to narrow the gap between small-scale laboratory experiments and field observations.

5.4 Strain Energy Approach to Sand Prediction

The strain energy approach is a new sand prediction method based on the concept of energy accumulation and dissipation during rock failure. This method uses an estimate of the strain energy dissipated in shear debris production as a means of assessing sand production associated with failed rock surrounding a wellbore.

When a rock is subjected to loading conditions in a triaxial cell, the rock sample exhibits elastic behaviour before failure, storing strain energy as it is compressed, determined by elastic properties of the rock. During failure, especially in a brittle mode, the strain energy stored in the rock between the ultimate load bearing capacity and the residual strength of the rock represent the energy which is dissipated during the development of a macroscopic fracture. This process is illustrated in Figure 5.2. The principal factors that account for the elastic strain energy dissipation are heat energy, seismic energy and also some of the energy that may be available for the creation of new surface area through comminution of the mineral grains present. Frictional sliding of brittle shear zones at shallow depth is usually accompanied by production, accumulation and evolution of fault gouge. The shearing action between the faces of the shear fracture planes of deformed sample in the laboratory results in the comminution of the sand grains adjacent to the shear fractures. It is postulated that such debris is potential source of producible sand. Griffith's fracture theory states that a fracture in a mineral grain can only propagate when there is sufficient energy available to account for surface energy requirement of the new surface created (Griffith, 1924). The comminution of sand-sized particles on the fracture surface of brittle sandstones can be analysed from the consideration of the energy associated with comminution. The resultant debris are then available as a source for sand production. Some elastic energy may remain stored in the larger fragments of the rock which continue to accept load by virtue of the confining pressure applied to them by the cell in a triaxial test or *in situ* by the surrounding rock.

Comminution theory states that the area of the new surface created is directly proportional to the energy required for fragmentation and that the energy requirement remain constant for a unit of surface energy produced (von Rittenger, 1867, Temmerman et al., 2013). Using appropriate mineral constants (density and the specific surface energy of the mineral phase present) and the surface area of debris produced, the proportion of energy associated with fracturing which is related to fragmentation can be calculated. Considerable experimental evidence exists to support this assumption and the Rosin-Rammler (Rosin and Rammler, 1933), Gates-Guadin-Schuhmann and log-normal distributions have proved to give an adequate description of particle size distribution resulting from comminution process (Taşdemir and Taşdemir, 2009). From the geometry of the fracture surface (normally approximated to an ellipse), the energy dissipated in creating the debris per unit sliding surface area, E_A (Jm^{-2}) can be estimated. This can be related to the total energy dissipated during frictional sliding along the fracture surface or the critical energy release rate G_{IIC} (Jm^{-2}). A portion of this energy is responsible for driving the comminution process.

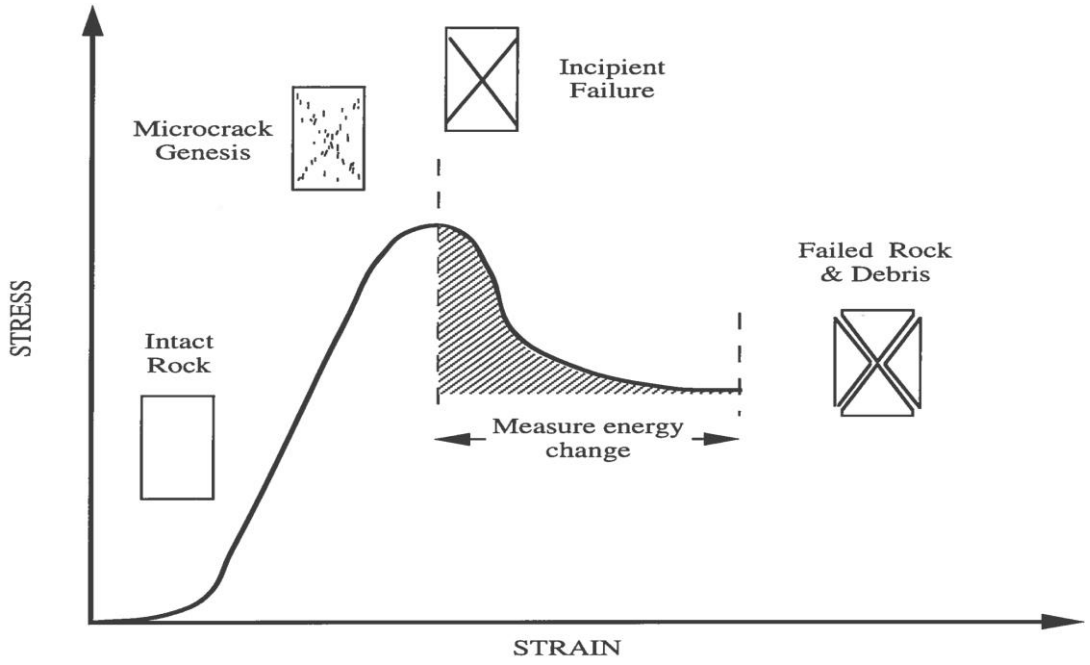

Figure 5.2: Triaxially compressed rock sample undergoing brittle failure showing the measured energy change.

The ratio of E_A/G_{IIC} is the energy dissipated in creating debris per unit area of the sliding surface referred to in this thesis as the comminution efficiency factor, CEF. The

CEF gives an indication of the fraction of energy which has been used for debris production and quantifies the potential for shear debris creation by giving an indication of how much energy was involved in creation of shear debris. In other words, this is considered to be the efficiency of a particular rock in creating potential producible sand debris and, as employed in this thesis, serve as a means to assess the sanding potential of a formation.

5.4.1 Determination of Energy Expended in Shear Debris Production per Unit Sliding Area (E_A)

Expression for the work done in breaking bonds of shear debris to create new surface area was first given by Engelder et al. (1975). Olgaard and Brace (1983) adapted the expression to study the portion of the total energy released during earthquake that is allocated to creating new surfaces. Following the same concept, Smart and Crawford (1990) estimated the energy expended in shear debris creation during a direct shear test. The energy density, W_A assuming the shear debris consists of pure quartz is given as:

$$W_A = S_W \times \rho \times \gamma \tag{5.1}$$

where S_W is the surface area per gram of debris (m^2g^{-1}), ρ the density of single mineral phase (quartz = 2.65 x 10^6 gm^{-3}) and γ the specific surface energy of single crystals determined in tension (quartz = 0.68 Jm^{-2})

The energy expended in creating measured volume of the debris, E (J) is given as:

$$E = W_A \times V \tag{5.2}$$

where V is the volume of the debris.

For the purpose of this analysis, the region of the fracture surface is approximated to be represented by an ellipse with a semi major axis, a and a semi minor axis, b. This gives an energy dissipated per unit sliding area (Jm^{-2}) as:

$$E_A = \frac{E}{\pi ab} \tag{5.3}$$

5.4.2 Determination of the Fracture Surface Energy (G_{IIC})

Traditionally, fracture surface energy has been estimated from seismological data (Rice, 1980, Aki and Richards, 1980, Rudnicki, 1980), laboratory studies of post-failure behaviour under conventional triaxial compression test (Wong, 1982, Guatteri et al., 2001, Rice et al., 2005, Abercrombie and Rice, 2005) and large-scale biaxial test (Okubo and Dieterich, 1984). Since most of the deformation in a triaxially compressed sample is taking place along the failure plane, the post-failure process is usually characterised by

the stress and slip along the localised zone, from which the slip-weakening curve can be obtained (Wong, 1982).

The slip-weakening model provides a means of interpreting the shear fracture energy, G as defined by theory of elastic fracture mechanics by integrating the area under the post-failure stress-displacement curve (Wong, 1986). In physical sense, the quantity, G represents the energy flux or 'breakdown' process at the crack tip (Rice, 1980). This crack extension force or strain energy release rate, G is the loss of energy per unit area of new crack sliding area formed during an increment of crack extension. Rice (1968) based on J-integral concept and, Willis (1967) from linear elasticity proved that this model is analogous to the critical energy release rate criterion in linear fracture mechanic as long as the size of the slip zone is small relative to the crack size.

Consider a distribution near the tip of a mode II in-plane shear fracture with a peak strength (τ^p) shear stress (τ) and slip (δ_s) as shown in Figure 5.3.

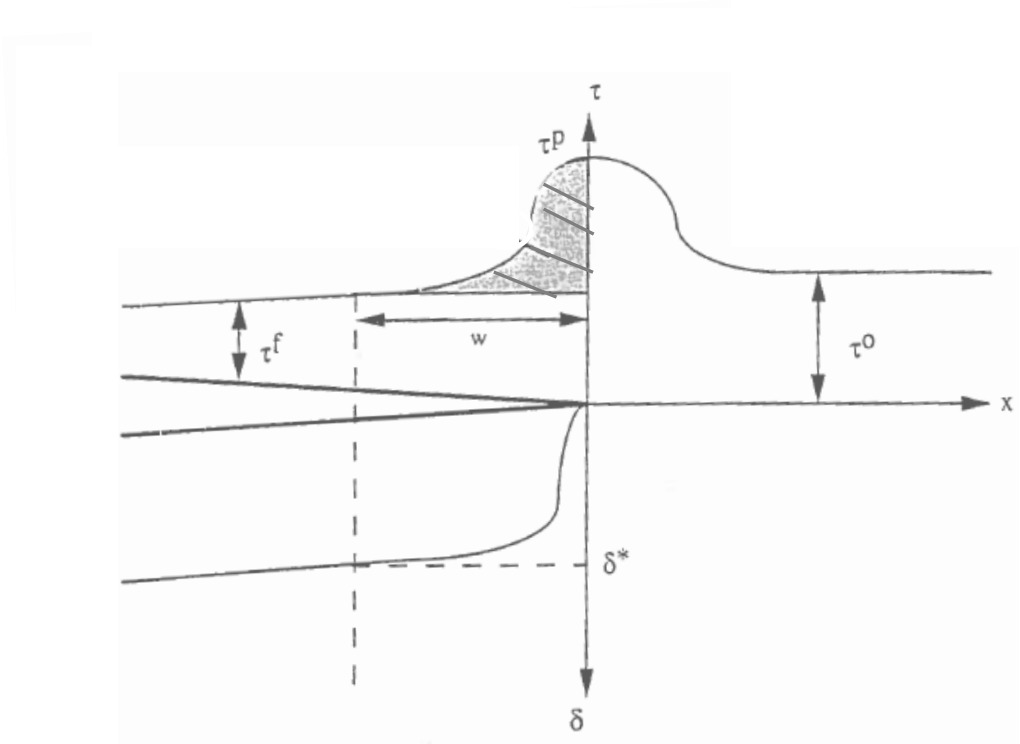

Figure 5.3: Slip weakening model showing distribution of stresses as applied in the field (after Rice, 1980).

A breakdown zone at the shear crack tip of dimension, w contains the stress degradation from the peak strength, τ^p to a constant residual frictional strength, τ^f at which slip has reached a critical level, δ_s^*. The post-failure stress and slip along the localised zone are considered where most of deformation occurs. The slip-weakening model provide a straight forward interpretation of the shear fracture energy, G as defined in elastic crack mechanics. Where the breakdown zone dimension is small relative to the fault length, then G is simply given by an integral under the slip-weakening curve (Wong, 1986).

The crack extension force, or strain energy release rate, G under mode II loading condition is defined as the loss of energy per unit of new crack separation area (Jm^{-2}) formed during an increment of crack extension (Rice, 1980, Wong, 1982). A key concept in fracture mechanics is that the extension of a fracture will occur once a critical value of crack extension force, G_C has been reached.

$$G = \int_0^{\delta_s^*} \left[\tau(\delta_s) - \tau^f\right] . d(\delta_s) \qquad (5.4)$$

The crack extension force is just the shaded area under the slip weakening curve as shown in Figure 5.3. Rewriting equation (5.4) as:

$$G = (\tau^p - \tau^f)\delta_s \qquad (5.5)$$

in which the nominal slip distance,

$$\delta_s = \frac{1}{\tau^p - \tau^f} \int_0^{\delta_s^*} \left[\tau(\delta_s) - \tau^f\right] . d(\delta_s) \qquad (5.6)$$

implies that the slip weakening model in the limit when w is small, is consistent with an elastic brittle crack model. Hence:

$$G_{IIC} = (\tau^p - \tau^f)\delta_s \qquad (5.7)$$

Experimentally, it is known that a triaxially compressed rock near the peak strength under brittle regime may experience post-peak strain localisation and the formation of a through-going fault at an angle, θ to the major principal stress, σ_1 as shown in Figure 5.4.

After failure the measured deformation is mostly taken along the failure plane. The shear stress, τ and the slip, δ can be expressed in terms of the differential stress $(\sigma_1 - \sigma_3)$ by:

$$\tau = \frac{\sigma_1 - \sigma_3}{2} \sin 2\theta \qquad (5.8)$$

and the shear slip, δ is described in terms of the post-failure axial displacement as follows:

$$\delta = \frac{\Delta L_s}{\sin\theta} \tag{5.9}$$

In Figure 5.5, the transformation of the post-failure stress-displacement curve into a $\tau - \delta$ curve is represented schematically. This shows the plot of shear stress as a function of amount of sliding from which the critical energy release rate can be derived.

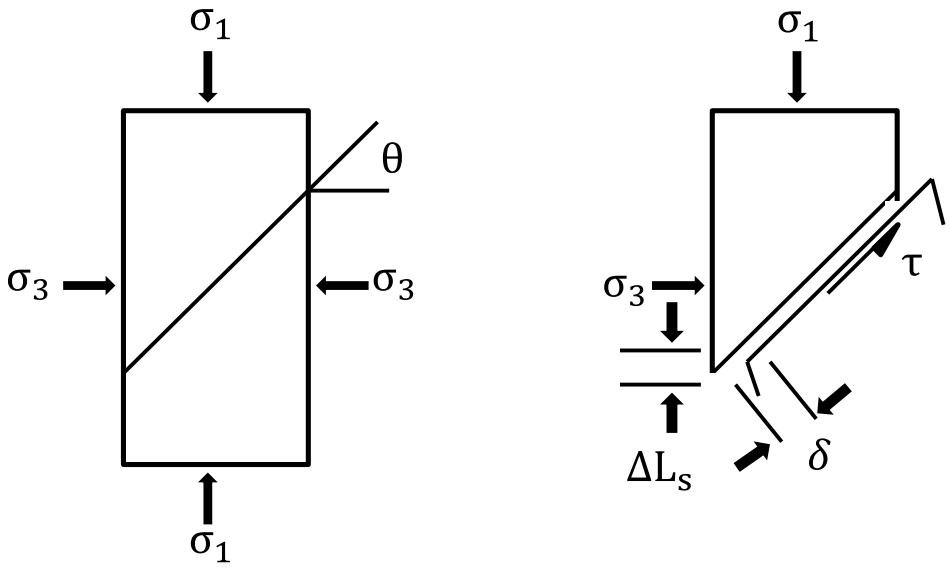

Figure 5.4: Slip weakening model in the laboratory for a loaded sample in a triaxial cell showing relationship between axial relative movement of sliding surface and slip for a triaxially failed sample.

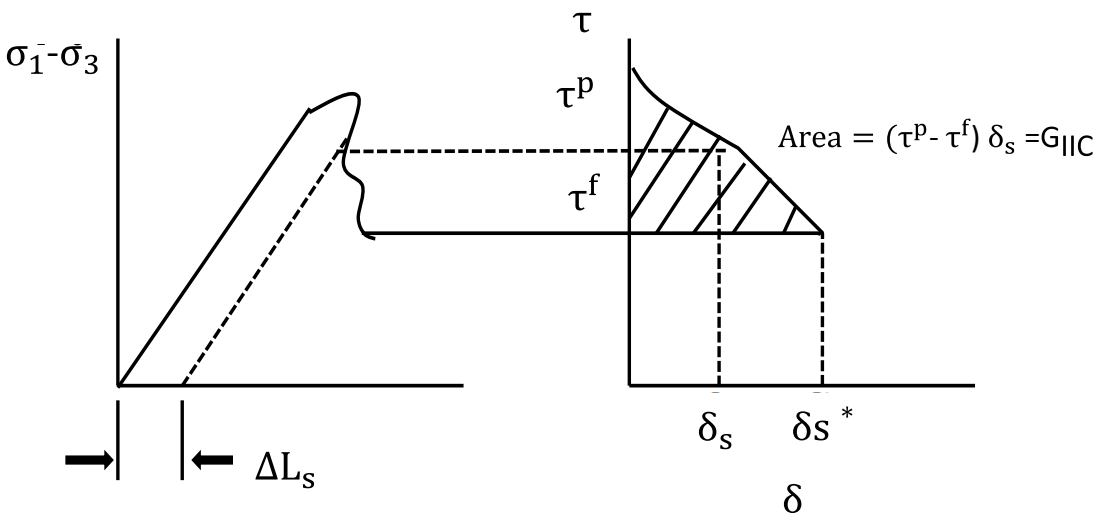

Figure 5.5: Representation of the transformation of the post-failure stress-strain curve into a $\tau - \delta$ used in derivation of slip-weakening curve from experimental output (after Rice, 1980).

5.5 Application of the Strain Energy Approach

The strain energy approach has been applied to evaluate the sand debris production potential of both the reservoir and analogue sandstones utilising the mechanical data obtained in chapter 4. The application of the strain energy approach is demonstrated here using a deformed sample with a triaxially-induced through-going fault (post-peak localisation of shear deformation). The sample is removed from the Hoek cell and the failure surface examined upon the completion of the triaxial test. The angle of shear failure was measured and shear debris on the failure surface was carefully collected and sieved to provide a < 90 μm fraction weighing 1.7081 g, for which specific surface area of 0.0426 m^2g^{-1} was directly measured using a Malvern Laser Particle Sizer assuming a Rosin-Rammler exponential distribution (see section 4.4).

Calculation of Energy Expanded in Shear Debris (E_A)

Assuming that the shear debris consisted of pure quartz, the energy density, W_A is first obtained using equation (5.1):

$$W_A = 0.0426 \times 2.65 \times 10^6 \times 0.68 = 7.68 \times 10^4 \ \text{Jm}^{-3}$$

The volume of the debris is obtained as:

$$V = \frac{1.7081}{2.65 \times 10^6} = 6.445 \times 10^{-7}\ \text{m}^3$$

multiplying the energy density by the volume of debris produced gives a measure of the energy expended in creating the less than 90 μm shear debris fraction (equation (5.2)).

$$E = 7.68 \times 10^4 \times 6.445 \times 10^{-7} = 4.95 \times 10^{-2}\ \text{J}$$

with the area, A of the shear fracture of θ = 50° approximating to that of ellipse of semimajor axis, a =19.95 mm and semiminor axis, b = 12.83 mm, so that:

$$A = \pi ab = 803.7 \times 10^{-6}\ \text{m}^2$$

The energy dissipated in shear debris formation per unit area of sliding surface E_A is estimated from equation (5.3):

$$E_A = \frac{4.95 \times 10^{-2}}{803.7 \times 10^{-6}} = 62\ \text{Jm}^{-2}$$

Calculation of Fracture Surface Energy (G_{IIC})

The fracture surface energy (G_{IIC}) for the sample was determined by monitoring the axial shortening of the triaxially compressed sample as the axial stress is increased to, and past failure of the sample. Shear fracture energy for samples with a triaxially-induced through-going fault (post-peak localisation of shear deformation) can be determined by measuring the area of the slip-weakening curve as illustrated in Figure 5.5. Under a

constant confining pressure of 68.9 MPa an axial displacement failure curve was generated which provided the raw data required to calculated the parameters recorded in Table 4.2.

Axial Load (kN)	σ_1 (MPa)	$(\sigma_1-\sigma_{3)}$ (MPa)	τ (MPa)	ΔL_s (mm)	δ (mm)
89.00	172.20*	108.30	53.30	0.00	0.00
88.00	170.30	101.40	49.90	0.10	0.13
81.00	156.80	87.90	43.30	0.15	0.20
71.00	137.40	68.50	33.70	0.20	0.26
70.00	135.50	66.60	32.80	0.40	0.39

Table 5.1: Shear fracture parameters derived from axial load-displacement curved produced in triaxial test on Sample. *peak axial stress.

The values of the shear stress and shear displacement are calculated using equation (5.8) and equation (5.9) respectively. This is then used to construct the slip-weakening curve from which the value of G_{IIC} is obtained by integration of the area under the curve (see section 5.4.2).

The slip-weakening curve constructed from Table 5.1 is shown in Figure 5.6 from which G_{IIC} value of 0.4 x 10^4 Jm^{-2} was determined for the sample. This compares favourably with values of G_{IIC} found in the literature (e.g. Wong 1982). This relative high value of G_{IIC} is due to the greater degree of fragmentation involved in created shear zone, compared with purely tensile mode-I opening cracks and frictional work, as there exist a large compressive normal stress across the shear zone. Rice (1984) recognised that the values of peak and residual stress are affected by normal stress acting across a fault. He suggested a correction for triaxial compression data based on Mohr circle analysis. A similar scheme was devised by Wong (1986) to determine the expected shear fracture surface energy of triaxial raw data under normal stress dependence. This is usually higher by a factor of two when compared with the expected values from biaxial tests with the normal stress maintained constant. The application of this reduction scheme is not

appropriate for the purpose of this study. Hence the raw triaxial data have not been adjusted to the condition of constant normal stress.

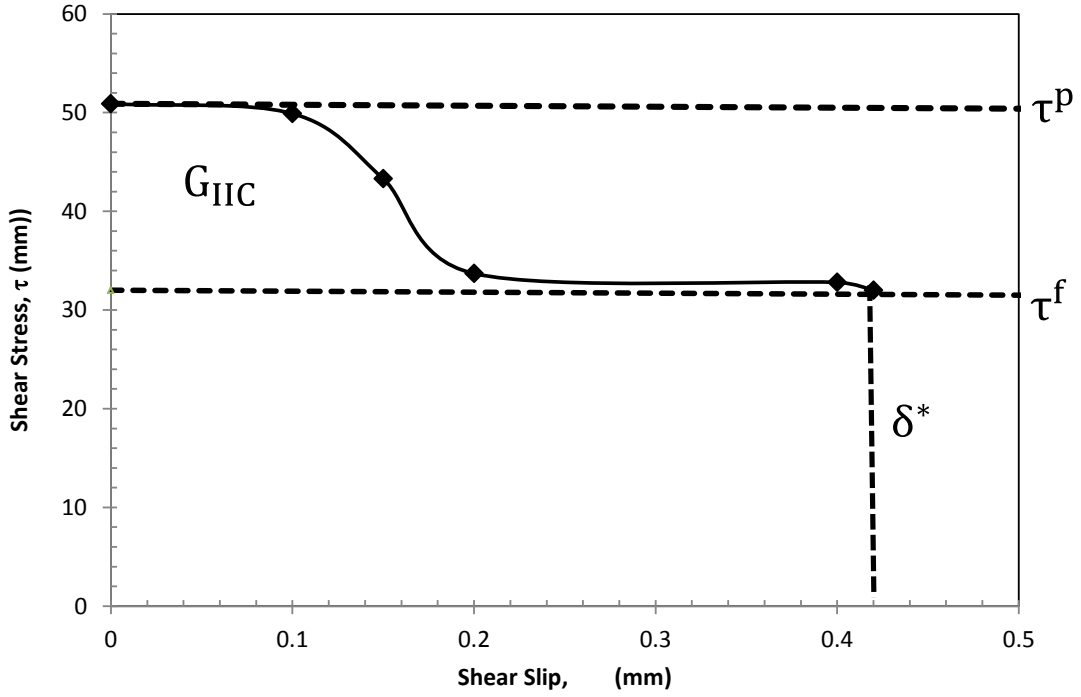

Figure 5.6: Slip-weakening behaviour defining fracture surface energy.

Propensity of Sand Debris Production

Thus an estimate of energy expended purely in shear debris creation (sand production) as a percentage of the total fracture surface energy, per unit area of sliding surface is givens as:

$$\frac{E_A}{G_{IIC}} \times 100 = 1.5\% = CEF$$

5.5.1 Results and Discussions

Using the same approach the CEF of all the reservoir and analogue samples tested are calculated and presented in Table 5.2 through to Table 5.4. In the case of ductile deformed samples where the sample completely failed and produced sand; the CEF becomes greater than 100% which is taken as an indicator of complete failure of the formation.

Field A: Table 5.2 shows the result of sand prediction for wells AFA, AFB and AFC. Sand prediction analysis conducted for the eleven samples that failed in brittle manner shows that samples AFA-3, AFB-4, AFB-2, AFC-3, AFC-5, AFC-7, AFC-8, AFC-9 and

AFC-10 were found to have CEF ranging from 5%-15%, while samples AFA-2 and AFA-8 exhibited CEF of over 40% at the same confining pressure as shown in Table 5.2. This implies that when samples AFA-2 and AFB-8 were deformed, more of the energy dissipated during post-failure was used in creation of shear debris and therefore these samples have greater propensity for sand production. The remaining samples in these wells failed in ductile manner with CEF of over 100% and there was no apparent release of energy to create debris. The ductile samples produced debris without reduction of stress and slip along a localised fracture surface. These samples either totally disintegrated or are characterised by many shear fractures within the sample. In some cases, the samples are deformed plastically and almost all the sample reduced to debris. Samples AFA-7 and AFC-2 failed in a transitional mode. A reduction in the applied stress was observed in these cases, but it was much less than when the samples failed in a purely brittle manner.

Field B: Table 5.3 shows the sand prediction result from the three wells (BFA, BFB and BFC) in Field B. All of the samples from these three wells failed in brittle manner by breaking into competent wedges along a localised failure planes with sand debris produced on the failure surfaces. The potential for sand debris production in terms of the CEF for most of the sample is less than 10% with the exception of samples BFB-4 and BFC-2 which show CEF of 22% and 43% respectively.

Field C: The result for sand production prediction for well CFA in Field C is given in Table 5.4. The potential for sand debris of samples from well CFA under triaxial condition indicates that the brittle failed sample (CFA-2) will produce little amount of debris coming from the localised plane of failure with CEF of 5%. The remaining samples failed in a ductile manner with a potential of producing high volume of debris as these samples deformed plastically.

Analogue Sandstones: The results of sand prediction in terms of CEF calculated for the analogue sandstones are presented in Table 5.5. All of the data refer to the rupture of the sandstones at a confining pressure of 34.50 MPa and subsequent sliding of the shear fracture surfaces. There are close similarities between the comminution process which occur in the brittle failed Fife Silica, Doddington, and Locharbriggs sandstones. This feature was noted previously from the particle size data. It was found that CEF for these three sandstones is in the range of 2.74% to 4.72%. It is evident that the Clashach sandstone is the most efficient producer of sub 90 μm debris with CEF of over 10%. The Lochaline samples on the hand are the least efficient in terms of energy efficiency;

however, one of the Lochaline samples produced a comparatively large mass of debris. This is due to the fact that much of the debris from this particular Lochaline sample are created by dispersed, non-localised fracture events resulting in the eventual disintegration of the sample, as opposed to the creation of two fracture halves of intact material. Three Locharbriggs and one Clashach samples were found to have failed in a ductile manner with CEF greater than 100%.

5.5.2 Comparison with other Sand Indicator Models

It is necessary to validate the strain energy approach for sand debris prediction by comparing the results obtained with some existing sand prediction models. As such, the strain energy approach is compared with the Uniaxial Compressive Strength (UCS) and Mechpro (Tixier et al., 1975) sand prediction methods. These methods are chosen since the derived rock mechanical parameters can be utilised as their input parameters. The static Mechpro ratio, $(G/C_b)_s$ was determined using data from stress-sensitive elastic constants (section 4.2.1) and the shear modulus and bulk compressibility were calculated from equation (2.35) and equation (2.38) respectively. Table 5.6 shows the result of the derived static Mechpro ratio, $(G/C_b)_s$. Since P and S-wave velocities were not determined for any of the test reservoir samples, a general correlation from Biot's theory of acoustic wave propagation (Biot, 1956) based on empirically derived Geertsma-Smit formula (White, 1983) as shown in Fjaer et al. (2008) was used to determined P and S-wave velocities from measured porosity. The P and S-wave velocities were used in equation (2.48) and in equation (2.49) to determine the shear modulus and bulk compressibility respectively, from which the dynamic Mechpro ratio $(G/C_b)_d$ was derived.

The result comparing the three methods (UCS, $(G/C_b)_d$ and CEF) for each sample tested from Field A, Field B and Field C are shown in Table 5.7, Table 5.8 and Table 5.9 respectively. The values of $(G/C_b)_d$ are those calculated from the Biot's theory of acoustic wave propagation and the values of P and S-wave velocities determined from the core porosities are also shown. These data with the density and the porosity are plotted against depth for each well.

Field A: Figure 5.8 presents the data for $(G/C_b)_d$, UCS and CEF plotted for samples from well AFA. There is a strong correlation between porosity and density as these two properties are inversely proportional. At the depth of 2800 m, there is an increase in density from 2640 to 2660 kg/m^3 which corresponds to a decrease in porosity from 32% to 20%. This is associated with an increase in the UCS from 30 to 80 MPa. CEF reduced

from a value in excess of 100% to 5% which corresponds to an increase in $(G/C_b)_d$ from 30 to 53 GPa^2. This is an indication that this section of the well would likely fail and produce sand. Further down the well at depth of 3700 m, the value of the density slightly increased from 2614 to 2656 kg/m^3 which is then followed by an associated decrease in porosity from 35% to 25%. The UCS decreased from 50 to 41 MPa with an associated decrease in CEF from +100% to 39% and a reduction in $(G/C_b)_d$ from 41 to 25 GPa^2. Generally, there is an agreement between the three sand prediction methods, indicating that there appears to be two sections (around 2800 and 3700 m) in this well where sand production is expected The CEF indicates that the amount of sand will be substantial as the rock is expected to fail plastically.

The data from the three different methods for well AFC are plotted in Figure 5.9. In this well however, there is a greater variation in the three sand prediction methods, which may be a reflection of the sampling procedure followed to choose representative core material. From a depth of 5480 to 5510 m, the density increased from 1870 to 2150 kg/m^3 corresponding to a decrease in porosity from 30% to 17%. UCS increased from 26 to 57 MPa and CEF reduced from an excess of +100% to 1%. $(G/C_b)_d$ was observed to have increased from 16 to 39 GPa^2. In Comparison with depth 2773 m in well AFA, $(G/C_b)_d$ is lower in this well (indicating a greater propensity of failure) yet the CEF is lower at 1% compared to +100% in well AFA. This indicates that the rock from this section of the well will fail in brittle manner and all of the sand production will come from a localised shear failure surfaces rather than the rock deforming plastically and being produced as sand.

At depth of 5518 m there is an agreement between the three sand indicators: low density value of 1860 kg/ m^3, high porosity of 29%, low $(G/C_b)_d$ of 16 GPa^2, low UCS of 35 MPa, and high CEF of 50%. This indicates a potential failure area: the CEF is still indicative of brittle failure, but the material is weak and a lot of debris will be produced.

At depth 5735 m, the density decreased from 2090 to 1880 kg/m^3 with corresponding increase in the porosity from 21% to 28%. UCS decreased from 47 to 19 MPa and CEF increased from 9% to +100% with a decrease in $(G/C_b)_d$ from 31 to 18 GPa^2. This indicates a weak zone which will fail in a ductile manner.

Field B: The correlation between the three sand indicators for samples from well BFB is presented in Figure 5.10. There is quite a good correlation between density and porosity and reasonable agreement amongst the three sand indicators across the depth covering the four samples from 3020 to 3042 m. Both $(G/C_b)_d$ and UCS values are high with low CEF

at less than 4%, indicating a fairly competent formation with very low risk of sand production. Similar features were also observed across well BFB (Figure 5.11) and well BFC (Figure 5.12) where the $(G/C_b)_d$ is above the threshold value of 38 GPa^2 and UCS above 55 MPa.

Field C: Figure 5.13 shows the correlation for samples from well CFA where porosity is much lower than in the other wells. It can be seen that from depth of 1737 to 1885 m, density decreased from 2210 to 2010 kg/m^3 with an increase in porosity from 5% to 10%. Overall, UCS decreased from 14 to 4 MPa from depth of 1737 to 1885 m but increased to 13 MPa at 1887 m. CEF is recorded at +100% for all of the section except at depth 1740 m indicating that there will be plastic deformation and a high potential for sand production. The values of $(G/C_b)_d$ are consistent in that these values are well above 38 GPa^2 threshold. Neglecting the results of the $(G/C_b)_d$, the whole section appears weak and failure involves plastic deformation leading to the greater potential for sand production.

5.5.3 General Correlations

The relationship between the CEF and the mass of sub 90 μm debris normalised to the mass of the sample is presented in Figure 5.14. The result shows that as the CEF increases (i.e. more of the available energy is used for comminution) the ratio of the mass of sub 90 μm debris to the mass of the bulk sample increases. The mass of the sub 90 μm debris created per m^2 is also observed to increase as the CEF increases (Figure 5.15). This relationship between CEF and the debris characteristics of the sandstones yields some general information on the comminution process and validates the strain energy approach to comminution since it is consistent with both the theoretical and the practical considerations. Secondly, and more importantly, these data indicate that consistent and predictable information on comminution can be obtained from the strain energy approach for a range of different sandstones.

Figure 5.16 shows the variation of CEF with porosity. In this case only brittle failed samples are included (i.e. those with strain energy less than 100%). There is no clear trend from the plotted values; the values most be affected by other factors such as mineralogy. There is an indication of a strong link between CEF and the triaxial stress factor. As shown in Figure 5.17 (for brittle failed samples only), the stronger the sample, the less the energy that goes into debris production. Thus competent rocks release less energy into the fracture to create debris than least competent ones.

Figure 5.18 shows the relationship between CEF and UCS. The samples from wells AFA, AFB and AFC appear to follow trends which are specific to the individual wells probably reflecting the mineralogy of each well. This result again shows that stronger samples are less prone to comminution of debris. The sample from well CFA is more closely aligned with samples from well AFB. Poor correlation is observed for samples from wells BFA, BFB and BFC.

Figure 5.19 illustrates the relationship between CEF and the fractal dimensions describing the particle size distribution of the reservoir sandstones. It can be seen that the fractal dimension, D increases with increasing CEF. This means that an increase in the value of D is reflected by higher CEF as more energy goes into the comminution of shear debris. The larger the value of the fractal dimension, the wider the range of particle size. It follows that the fractal dimension could yield a quantitative indicator of energy that goes into shear debris production. Accordingly, higher fractal dimension indicates higher amount of fine particles as previously noted by other researchers (Lu et al., 2003, Cui et al., 2006).

5.6 Summary and Conclusions

A new approach for predicting sand debris production based on strain energy dissipation of experimentally produced shear fractures, created under various triaxial stress states has been presented. The approach has been applied to assess the sanding potential of several reservoir and analogue sandstone samples. The technique equates the energy released by a rock sample during rock failure to the amount of debris produced on the failure surface. In the case of a brittle failure and formation of a thorough-going shear fractures, comminution is largely restricted to the fracture surface where shear sliding along the fracture surface can produce very fine comminution debris. Ductile failure is however characterised by grain rotation and fracturing which result in dispersed comminution products. The main conclusions derived from this chapter are:

I. A new approach for predicting sand debris production based on strain energy dissipation of experimentally produced shear fractures, created under various triaxial stress states has been presented. The approach has been applied to assess the sanding potential of several reservoir and analogue sandstone samples. The strain energy has shown good correlation with other sand prediction techniques.

II. Failure in a compressed rock occurs when the internal energy level increases beyond an acceptable level for that material. During failure, the energy is

converted into seismic, heat and in the context of sand production surface energy, by creation of micro-fractures.

III. The proportion of energy which accounts for the generated debris or comminution efficiency factor (CEF) has been estimated from the ratio of the energy dissipated in the creation of debris (E_A) to the fracture surface energy (G_{IIC}) required for the extension of the failure surface.

IV. The fracture surface energy (G_{IIC}) and the energy expended in shear debris production (E_A) have been obtained from fracture mechanics theory applied to triaxial compressed samples and dynamic fragmentation theory respectively.

V. Samples that failed in a purely brittle manner were found to have a CEF between 0 – 100% while ductile failed samples were found to have a CEF of over 100%, indicating that there was no apparent release of energy to create debris.

VI. Most of the brittle failed samples have a CEF of less than 10%, indicating that the energy that goes into comminution of debris forms a small fraction of the total energy budget.

VII. The relationship between the comminution efficiency factor, CEF and the mass of sub 90 μm debris normalised to the mass of the sample shows that as the CEF increases (i.e. more of the available energy is used for comminution) the ratio of the mass of sub 90 μm debris to the mass of the bulk sample increases. The mass of the sub 90 μm debris created per m^2 is also observed to increase as comminution efficiency factor, CEF, increases.

VIII. The strain energy method has shown the potential of sandstone to produce debris is a function of the mechanical properties of the rock. There is a good correlation between the comminution efficiency factor, CEF, and rock properties such as porosity, uniaxial compressive strength and triaxial stress factor.

IX. There is a strong correlation between the fractal dimension, D, and CEF since both parameters measure the degree of comminution. The greater the fragmentation fractal dimension, the greater the amount of energy apportioned to debris comminution.

Sample I.D.	Depth (m)	Reservoir Horizion	Energy Expended (J)	Energy Expended/unit area of slip, E_A (J/m^2)	Fracture Surface Energy G_{IIC} (J/m^2)	Comminution Efficiency Factor (CEF) %
AFA-1	2787.2	Famgee	0.13	26.14	0.21	12740.08
AFA-2	2791.7	Famgee	0.03	6.87	15.62	44.00
AFA-3	2796.8	Famgee	0.04	9.42	188.30	5.00
AFA-4	2818.2	Famgee	0.05	10.30	68.64	15.00
AFA-5	3709.1	Deekay	3.02	628.99	247.64	254.00
AFA-6	3722.8	Deekay	0.70	149.53	26.80	558.00
AFA-7	3724.3	Deekay	0.11	24.02	12.85	187.00
AFA-8	3727.5	Deekay	0.07	15.20	38.97	39.00
AFB-1	2750.3	Famgee	2.90	604.55	5.88	10281.48
AFB-2	3427.8	Deekay	0.03	6.03	40.20	14.99
AFC-1	5494.05	Deekay	0.33	72.31	36.46	198.35
AFC-2	5498.59	Deekay	1.21	131.57	40.42	325.54
AFC-3	5509.41	Deekay	0.02	2.50	756.98	0.33
AFC-4	5520.93	Deekay	0.26	55.69	22.68	245.54
AFC-5	5561.32	Deekay	0.03	5.87	61.51	9.55
AFC-6	5572.05	Deekay	1.11	121.14	22.67	534.45
AFC-7	5573.48	Deekay	0.04	5.59	109.40	5.11
AFC-8	5585.95	Deekay	0.04	6.92	455.54	1.52
AFC-9	5601.77	Deekay	0.05	6.81	108.99	6.25
AFC-10	5692.23	Deekay	0.02	1.61	247.12	0.65

Table 5.2: Sand debris production potential of samples from Field A.

Sample I.D.	Depth (m)	Reservoir Horizion	Energy Expended/unit area of slip, EA (J/m^2)	Fracture Surface Energy G_{IIC} (J/m^2)	Comminution Efficiency Factor (CEF) %
BFA-1	3020.27	Rotliegendes	23.25	1873.25	1.24
BFA-2	3033.45	Rotliegendes	53.11	2228.21	2.38
BFA-3	3036.14	Rotliegendes	25.56	769.03	3.32
BFA-4	3041.90	Rotliegendes	20.35	885.08	2.30
BFB-1	3282.15	Rotliegendes	24.22	12294.11	0.20
BFB-2	3286.07	Rotliegendes	38.50	5120.09	0.75
BFB-3	3298.99	Rotliegendes	29.51	7200.14	0.41
BFB-4	3308.36	Rotliegendes	715.55	3316.01	21.58
BFC-1	3441.87	Rotliegendes	58.25	1124.33	5.18
BFC-2	3446.98	Rotliegendes	92.86	218.35	42.53
BFC-3	3451.90	Rotliegendes	14.36	1228.45	1.17

Table 5.3: Sand debris production potential of samples from Field B.

Sample I.D.	Depth (m)	Reservoir Horizion	Energy Expended/unit area of slip, EA (J/m^2)	Fracture Surface Energy G_{IIC} (J/m^2)	Comminution Efficiency Factor (CEF) %
CFA-1	1738.2	Kay	145.59	30.68	474.55
CFA-2	1740.0	Kay	51.06	1019.23	5.01
CFA-6	1887.1	Kay	158.48	0.39	40636.61
CFA-8	1889.8	Kay	141.56	0.89	15905.88
CFA-9	1919.9	Kay	47.02	1.65	2849.80

Table 5.4: Sand debris production potential of samples from Field C.

Sample I.D.	Sandstone Type	Energy Expended/unit area of slip, E_A (J/m^2)	Fracture Surface Energy G_{IIC} (J/m^2)	Comminution Efficiency Factor (CEF) %
CLS-1	Clashach	199.23	1954.78	10.19
CLS-2	Clashach	244.50	150.08	162.91
CLS-3	Clashach	178.22	1547.14	11.52
CLS-4	Clashach	187.98	1678.99	11.20
DDG-1	Doddington	69.61	1595.55	4.36
DDG-2	Doddington	68.73	1454.65	4.72
DDG-3	Doddington	54.25	1254.65	4.32
DDG-4	Doddington	45.96	1127.87	4.08
DDG-5	Doddington	41.67	1087.51	3.83
FSS-1	Fife Silica	84.22	1954.87	4.31
FSS-2	Fife Silica	78.37	1958.35	4.00
FSS-3	Fife Silica	80.45	2019.59	3.98
FSS-4	Fife Silica	56.67	2020.59	2.80
FSS-5	Fife Silica	56.01	2021.59	2.77
LCS-1	Lochaline	140.30	17537.50	0.80
LCS-2	Lochaline	78.90	8134.02	0.97
LCS-3	Lochaline	29.54	2978.21	0.99
LCS-4	Lochaline	68.97	8748.50	0.79
LBG-1	Locharbriggs	175.89	101.50	173.29
LBG-2	Locharbriggs	44.38	1589.57	2.79
LBG-3	Locharbriggs	50.90	1357.21	3.75
LBG-4	Locharbriggs	43.50	1589.00	2.74
LBG-5	Locharbriggs	69.54	2541.54	2.74
LBG-6	Locharbriggs	174.54	152.14	114.72
LBG-7	Locharbriggs	187.54	125.87	148.99

Table 5.5: Sand debris production potential of the analogue sandstones.

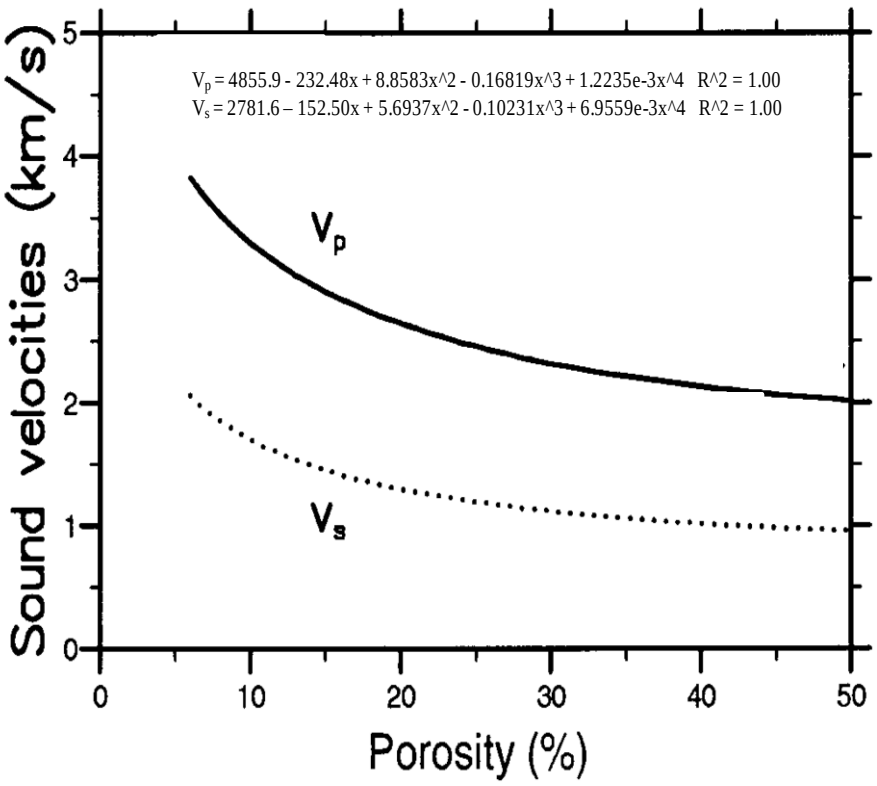

Figure 5.7: Correlation of P and S wave velocities versus porosities (Biot, 1956)

Sample I.D.	Depth (m)	Reservoir Horizion	$(G/Cb)_s$ (GPa^2)					
			σ_{c1}	σ_{c2}	σ_{c3}	σ_{c4}	σ_{c5}	σ_{c6}
AFA-1	2787.15	Famgee	N/A	N/A	40.00	48.56	59.36	N/A
AFA-2	2791.66	Famgee	31.08	48.56	66.05	103.06	103.06	98.25
AFA-3	2796.84	Famgee	65.28	131.12	154.98	131.73	n/a	183.99
AFA-4	2818.18	Famgee	13.99	24.12	32.75	33.54	N/A	N/A
AFA-5	3709.11	Deekay	37.01	47.74	83.90	88.83	88.83	93.91
AFA-6	3722.83	Deekay	51.19	77.89	85.53	111.01	129.97	129.97
AFA-7	3724.32	Deekay	47.28	73.34	73.89	85.53	96.50	121.23
AFA-8	3727.52	Deekay	52.63	89.57	95.63	111.01	129.97	129.97
AFB-1	2750.30	Famgee	23.91	34.45	44.91	61.55	73.91	139.84
AFB-2	3427.81	Deekay	58.67	88.83	109.14	127.93	127.93	150.93
AFC-1	5494.05	Deekay	25.62	23.63	37.07	58.67	78.32	91.35
AFC-2	5498.59	Deekay	12.73	14.29	36.03	55.92	82.95	106.69
AFC-3	5509.41	Deekay	556.32	588.18	735.20	1159.65	1687.24	1696.30
AFC-4	5520.93	Deekay	8.64	16.57	35.26	62.68	85.33	105.75
AFC-5	5561.32	Deekay	98.91	29.24	42.74	51.73	72.18	81.17
AFC-6	5572.05	Deekay	9.00	15.72	29.73	56.83	77.08	99.50
AFC-7	5573.48	Deekay	34.08	49.46	107.52	90.05	105.42	118.18
AFC-8	5585.95	Deekay	13.91	23.68	49.42	86.16	126.72	151.57
AFC-9	5601.77	Deekay	8.90	18.28	39.92	99.30	61.06	183.88
AFC-10	5692.23	Deekay	14.82	18.30	35.30	48.34	62.29	72.28
BFA-1	3020.27	Rotliegendes	N/A	N/A	N/A	N/A	N/A	N/A
BFA-2	3033.45	Rotliegendes	93.26	98.58	171.11	168.01	169.42	N/A
BFA-3	3036.14	Rotliegendes	105.60	N/A	N/A	N/A	N/A	N/A
BFA-4	3041.90	Rotliegendes	171.33	185.66	252.24	227.97	295.89	N/A
BFB-1	3282.15	Rotliegendes	32.21	36.01	36.64	42.39	60.42	N/A
BFB-2	3286.07	Rotliegendes	N/A	N/A	N/A	N/A	N/A	N/A
BFB-3	3298.99	Rotliegendes	N/A	N/A	N/A	N/A	N/A	N/A
BFB-4	3308.36	Rotliegendes	85.05	99.44	120.89	126.06	176.09	N/A
BFC-1	3441.87	Rotliegendes	83.66	96.09	163.34	247.62	252.69	N/A
BFC-2	3446.98	Rotliegendes	79.57	N/A	N/A	N/A	N/A	N/A
BFC-3	3451.90	Rotliegendes	193.44	197.25	265.86	276.48	333.13	N/A
CFA-1	1738.15	Kay	3.85	11.44	4.48	7.61	N/A	N/A
CFA-2	1739.98	Kay	3.67	5.04	6.64	6.59	N/A	N/A
CFA-6	1887.09	Kay	0.62	2.48	3.05	3.63	N/A	N/A
CFA-8	1889.76	Kay	6.06	6.91	7.37	9.51	8.59	N/A
CFA-9	1919.94	Kay	N/A	N/A	11.21	9.41	8.38	N/A

Table 5.6: Stress sensitivity values of $(GC/Cb)_s$ for reservoir sandstones.

Sample I.D.	Depth (m)	Reservoir Horizion	Density (kg/m^3)	Porosity (%)	Vp (m/s)	Vs (m/s)	G (GPa)	C_b ($1/GPa^2$)	G/C_b (GPa^2)	UCS (MPa)	CEF (%)
AFA-1	2787.15	Famgee	2655	31.26	2275.00	1117.00	3.31	0.11	30.89	31.60	12740.08
AFA-2	2791.66	Famgee	2649	29.92	2306.00	1133.00	3.40	0.10	32.48	43.20	44.00
AFA-3	2796.84	Famgee	2652	20.09	2596.00	1300.00	4.48	0.08	53.32	80.30	5.00
AFA-4	2818.18	Famgee	2660	21.01	2560.00	1278.00	4.34	0.09	50.57	65.30	15.00
AFA-5	3709.11	Deekay	2614	35.42	2187.00	1072.00	3.00	0.12	25.53	50.30	254.00
AFA-6	3722.83	Deekay	2656	25.27	2423.00	1196.00	3.80	0.09	40.00	43.50	558.00
AFA-7	3724.32	Deekay	2645	26.59	2387.00	1177.00	3.66	0.10	37.32	43.10	187.00
AFA-8	3727.52	Deekay	2644	24.51	2444.00	1209.00	3.86	0.09	41.12	48.90	39.00
AFB-1	2750.30	Famgee	2639	32.37	2251.00	1105.00	3.22	0.11	29.24	21.40	1034.16
AFB-2	3427.81	Deekay	2610	20.55	2578.00	1288.00	4.33	0.09	50.11	60.00	14.99
AFC-1	5494.05	Deekay	1850	29.49	2316.00	1138.00	2.40	0.15	16.12	26.30	198.35
AFC-2	5498.59	Deekay	2100	17.65	2706.00	1369.00	3.94	0.10	39.87	31.20	325.54
AFC-3	5509.41	Deekay	2150	18.52	2664.00	1342.00	3.87	0.10	39.09	57.50	0.33
AFC-4	5520.93	Deekay	1860	28.95	2328.00	1145.00	2.44	0.15	16.65	34.90	245.54
AFC-5	5561.32	Deekay	2090	20.93	2563.00	1279.00	3.42	0.11	31.35	47.50	9.55
AFC-6	5572.05	Deekay	1880	28.18	2347.00	1155.00	2.51	0.14	17.59	19.40	534.45
AFC-7	5573.48	Deekay	1960	25.35	2420.00	1195.00	2.80	0.13	21.68	36.10	5.11
AFC-8	5585.95	Deekay	2110	20.42	2583.00	1291.00	3.52	0.11	33.02	58.10	1.52
AFC-9	5601.77	Deekay	1960	25.43	2418.00	1194.00	2.79	0.13	21.61	60.30	6.25
AFC-10	5692.23	Deekay	2230	12.26	3055.00	1595.00	5.67	0.08	75.16	71.90	0.65

Table 5.7: Values G/C_b, UCS and CEF for Field A samples.

Sample I.D.	Depth (m)	Reservoir Horizion	Density (kg/m^3)	Porosity (%)	Vp (m/s)	Vs (m/s)	G (GPa)	C_b ($1/GPa^2$)	G/C_b (GPa^2)	UCS (MPa)	CEF (%)
BFA-1	3020.27	Rotliegendes	2110.00	13.00	2996.14	1556.43	5.11	0.08	61.98	90.70	1.24
BFA-2	3033.45	Rotliegendes	2215.00	12.00	3076.47	1609.12	5.74	0.08	76.38	71.25	2.38
BFA-3	3036.14	Rotliegendes	2010.00	12.80	3011.62	1566.57	4.93	0.09	57.48	89.37	3.32
BFA-4	3041.90	Rotliegendes	2150.00	15.00	2856.12	1465.10	4.62	0.09	52.54	95.05	2.30
BFB-1	3282.15	Rotliegendes	2010.00	16.35	2775.20	1412.82	4.01	0.10	40.65	113.83	0.20
BFB-2	3286.07	Rotliegendes	2110.00	13.02	2994.61	1555.42	5.10	0.08	61.85	71.67	0.75
BFB-3	3298.99	Rotliegendes	1960.00	13.05	2992.32	1553.92	4.73	0.09	53.19	86.89	0.41
BFB-4	3308.36	Rotliegendes	2100.00	15.09	2850.40	1461.39	4.48	0.09	49.70	61.46	21.58
BFC-1	3441.87	Rotliegendes	2510.00	9.50	3312.57	1764.65	7.82	0.06	133.82	85.44	5.18
BFC-2	3446.98	Rotliegendes	2500.00	9.08	3357.72	1794.46	8.05	0.06	140.49	55.20	42.60
BFC-3	3451.90	Rotliegendes	2110.00	12.07	3070.61	1605.27	5.44	0.08	68.75	79.05	1.17

Table 5.8: Values G/C_b, UCS and CEF for Field B samples.

Sample I.D.	Depth (m)	Reservoir Horizion	Density (kg/m^3)	Porosity (%)	Vp (m/s)	Vs (m/s)	G (GPa)	C_b ($1/GPa^2$)	G/C_b (GPa^2)	UCS (MPa)	CEF (%)
CFA-1	1738.15	Kay	2160.00	13.60	2951.00	1527.00	5.04	0.08	60.92	13.81	474.55
CFA-2	1739.98	Kay	2230.00	4.80	3926.00	2170.00	10.50	0.05	213.91	10.93	5.01
CFA-6	1887.09	Kay	2120.00	16.10	2789.00	1422.00	4.29	0.09	46.19	4.08	40636.61
CFA-8	1889.76	Kay	2250.00	9.90	3271.00	1737.00	6.79	0.07	101.98	13.09	15905.88
CFA-9	1919.94	Kay	2010.00	9.30	3334.00	1779.00	6.36	0.07	88.17	2.70	2849.80

Table 5.9: Values G/C_b, UCS and CEF for Field C samples.

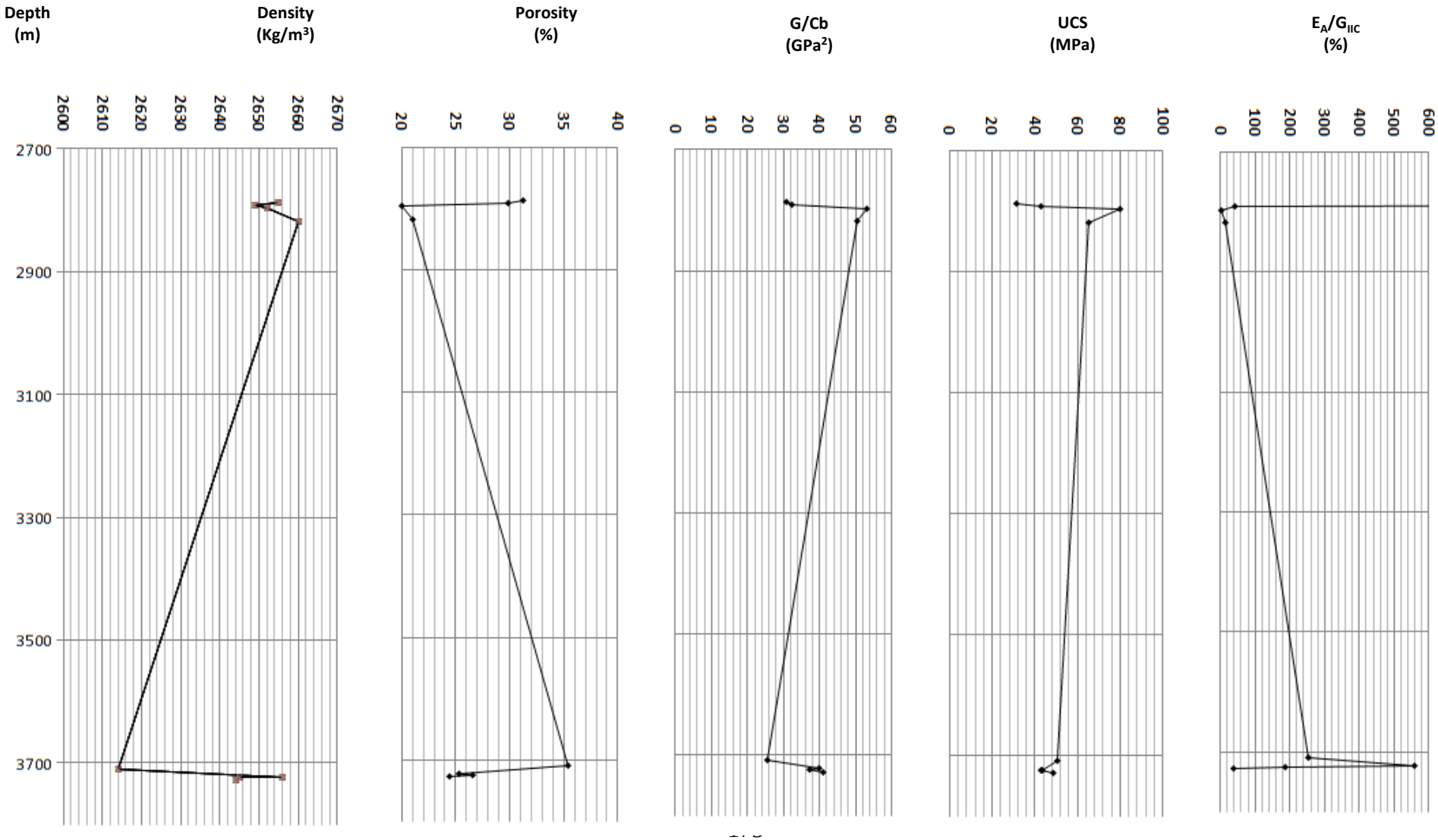

Figure 5.8: Comparison of different laboratory sand indicator for samples from well AFA in Field A.

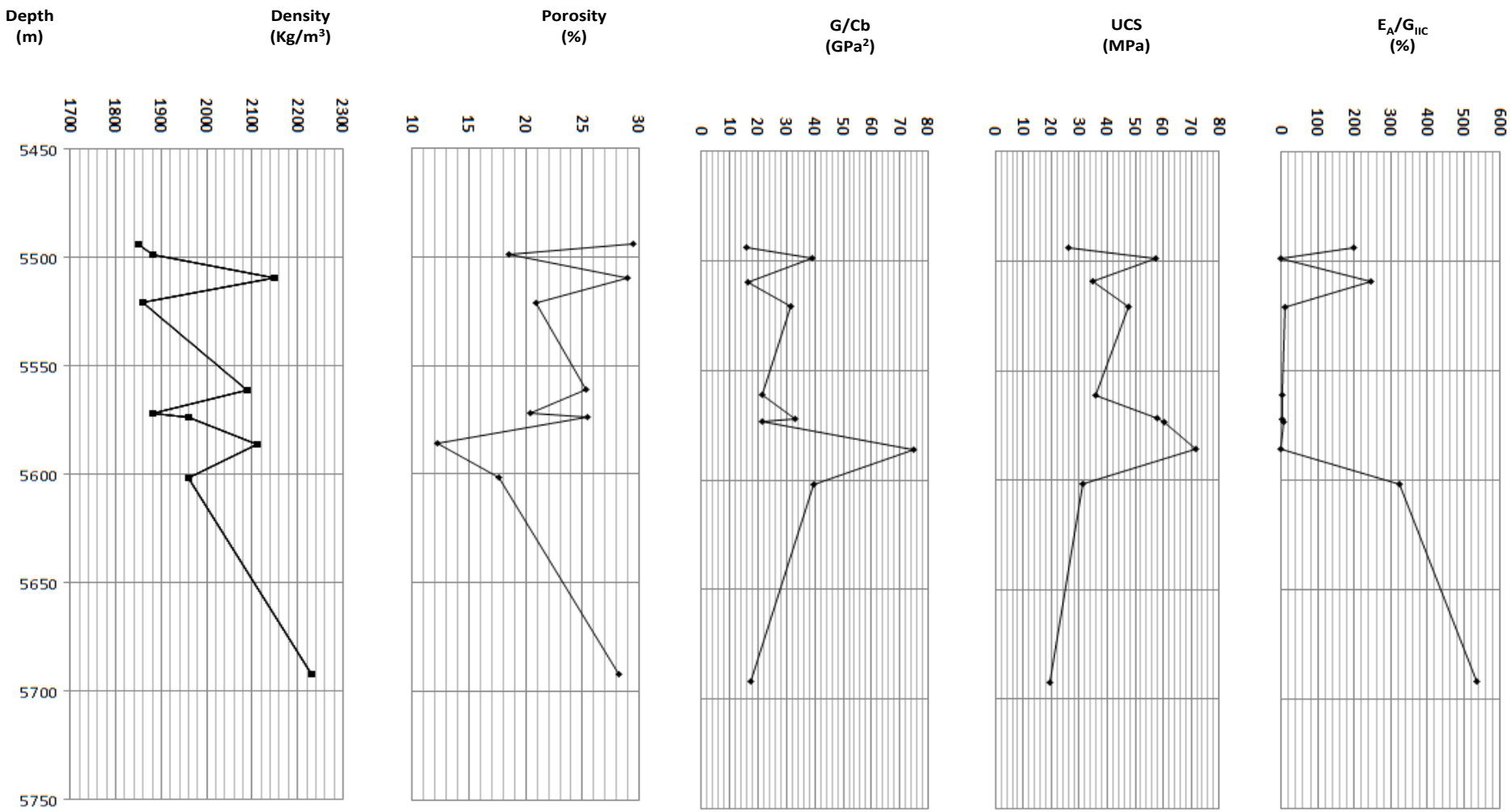

Figure 5.9: Comparison of different laboratory sand indicator for samples from well AFC in Field A.

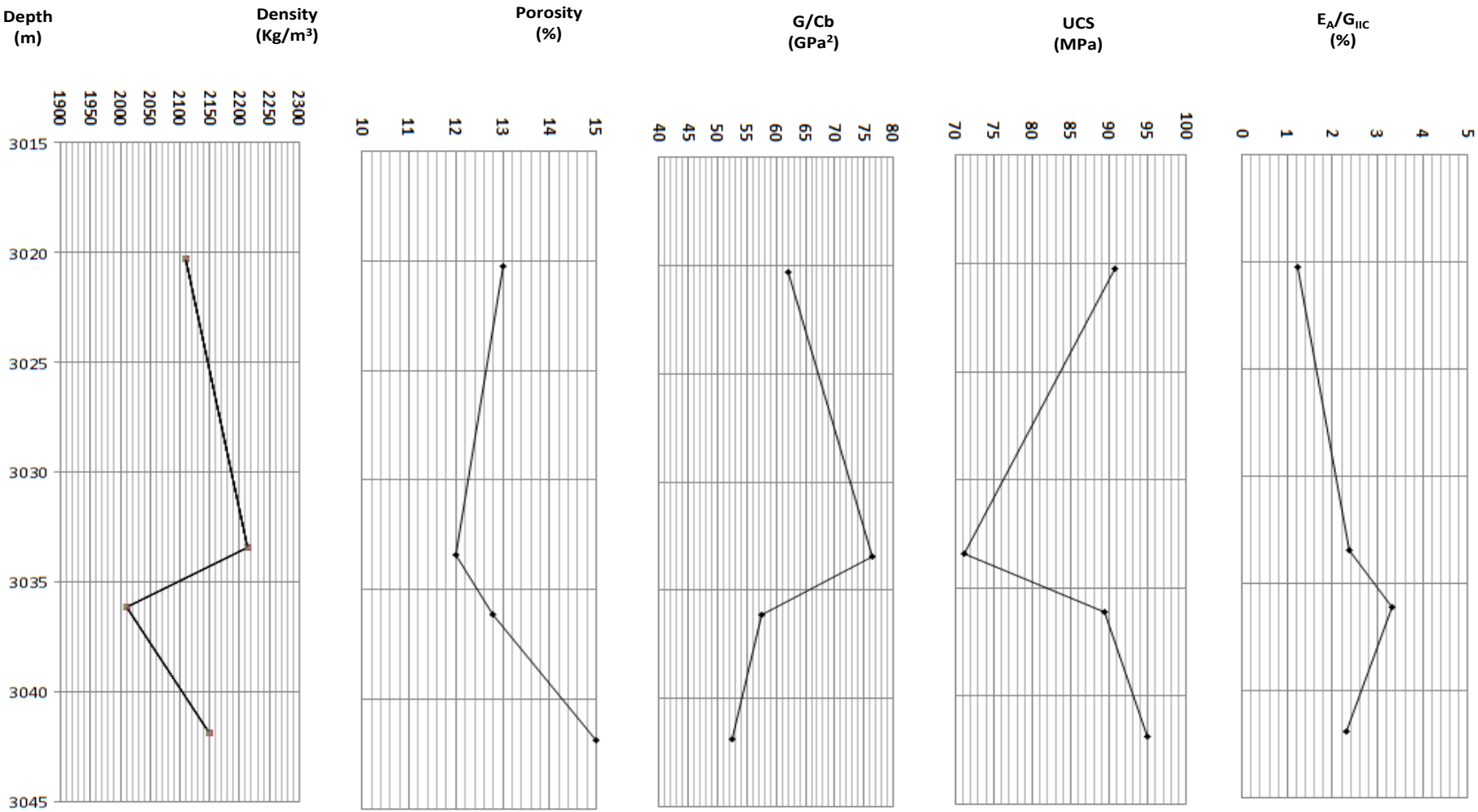

Figure 5.10: Comparison of different laboratory sand indicator for samples from well BFA in Field B.

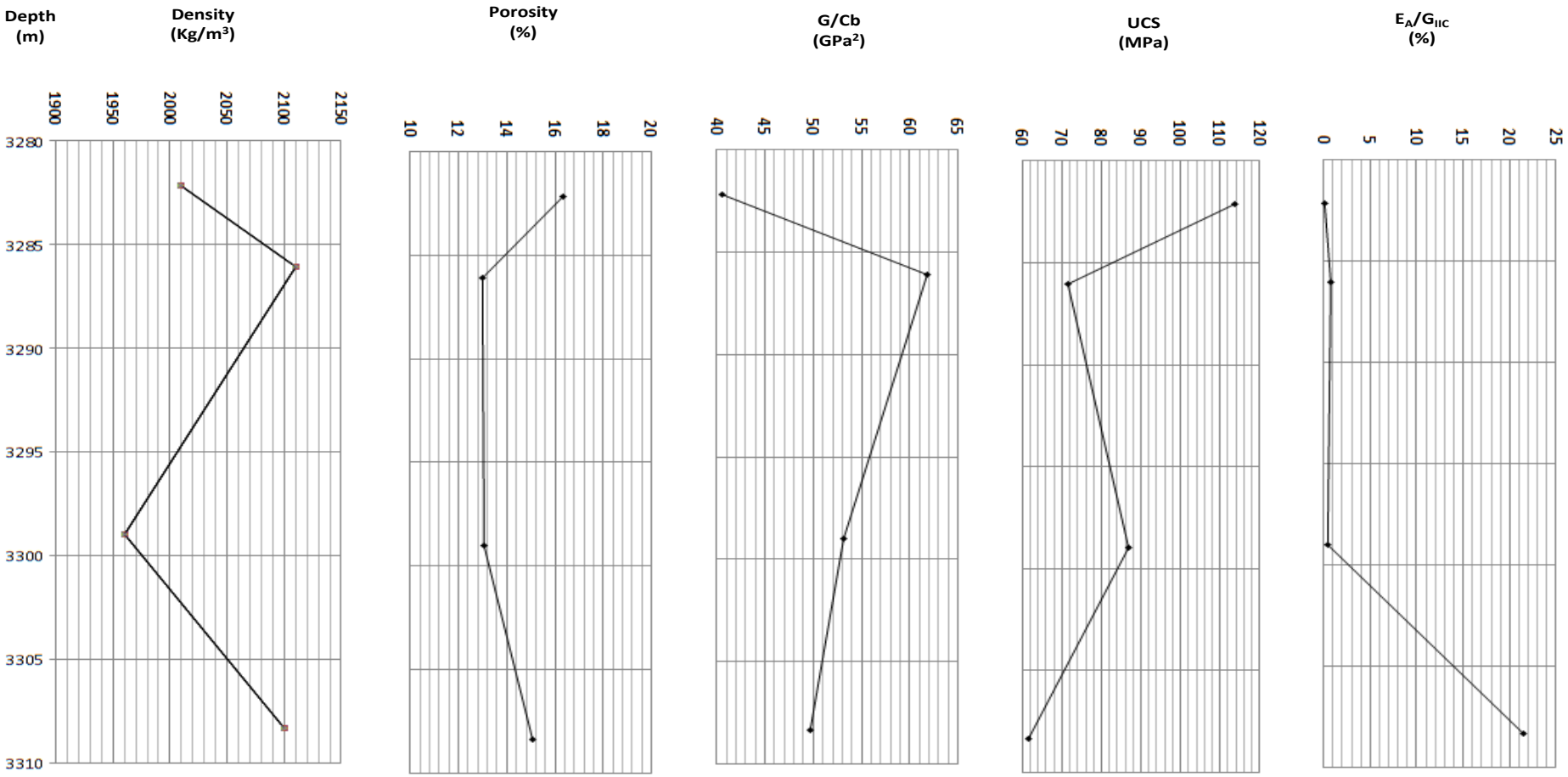

Figure 5.11: Comparison of different laboratory sand indicator for samples from well BFB in Field B.

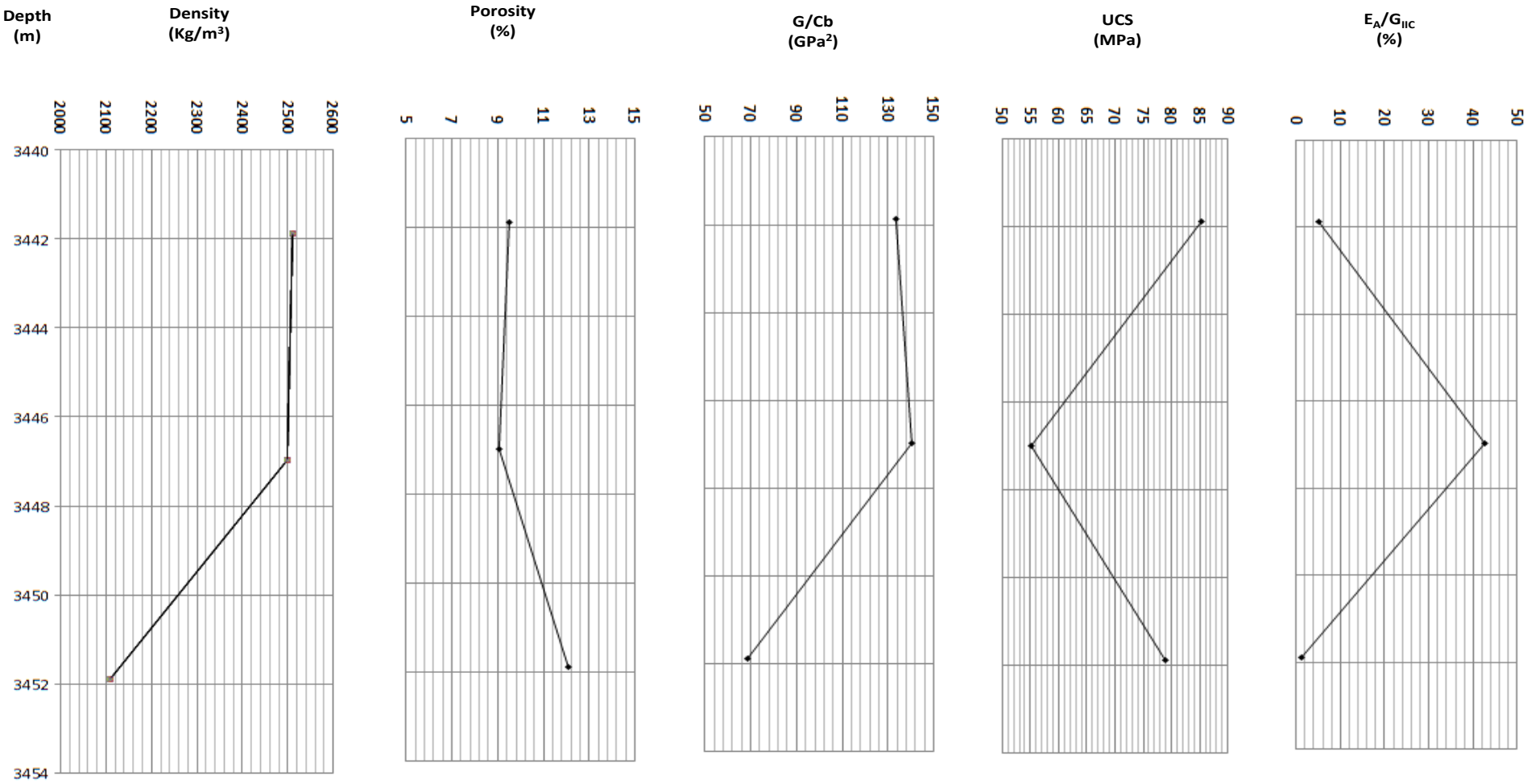

Figure 5.12: Comparison of different laboratory sand indicator for samples from well BFC in Field B.

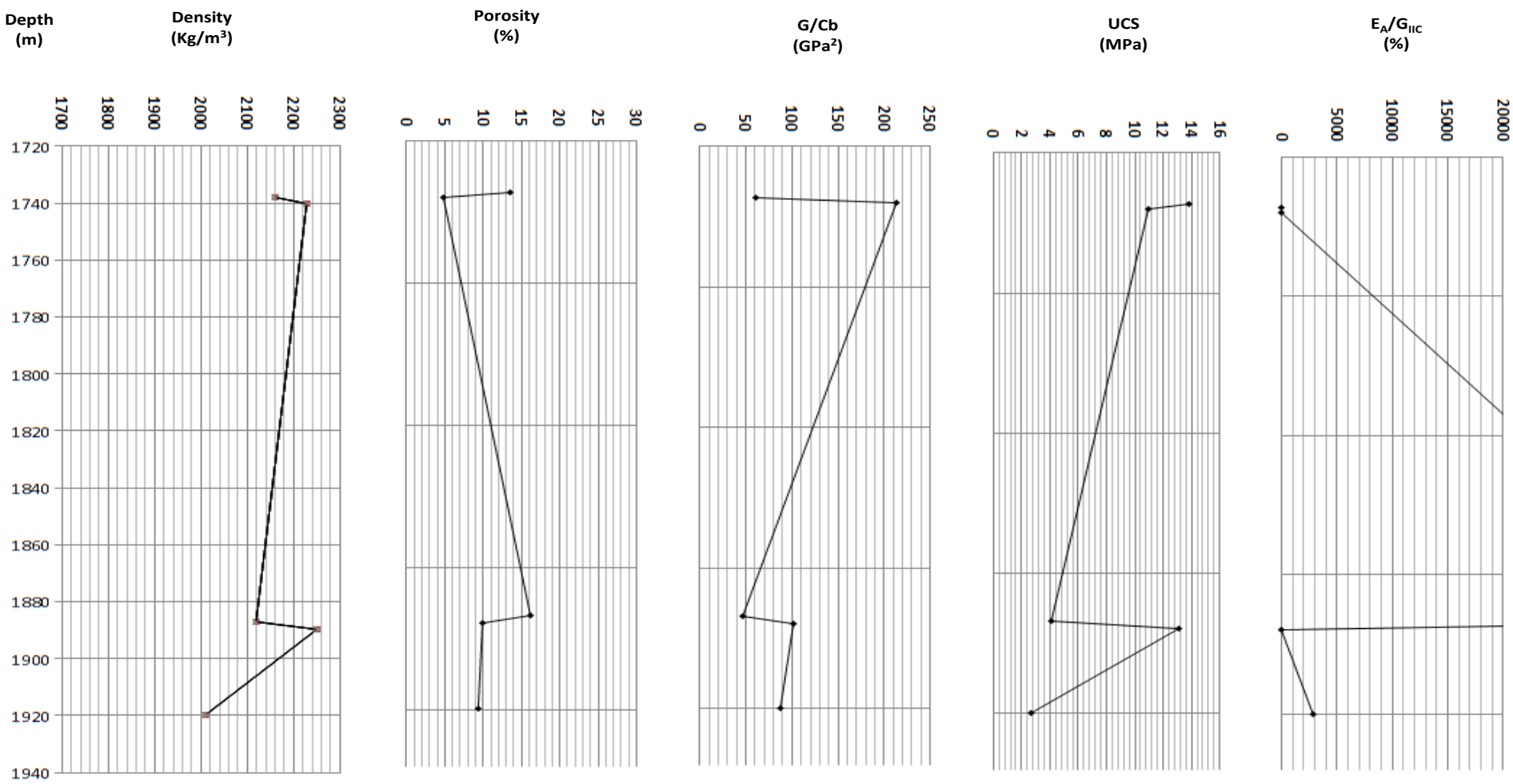

Figure 5.13: Comparison of different laboratory sand indicator for samples from CFA in Field C.

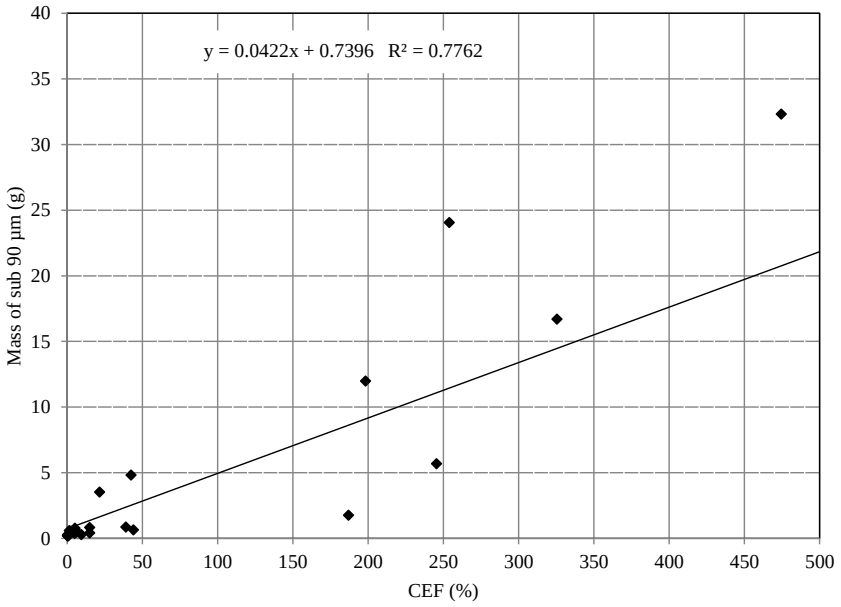

Figure 5.14: Relationship between comminution efficiency factor, CEF and the mass of sub 90 µm normalised to the mass of the sample.

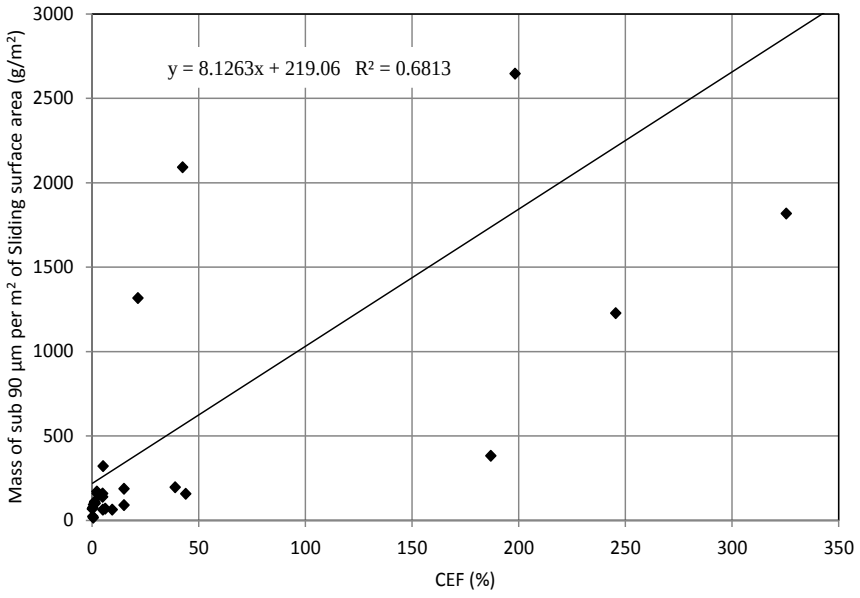

Figure 5.15: Relationship between comminution efficiency factor, CEF and the mass of sub 90 µm debris per m^2 of sliding surface.

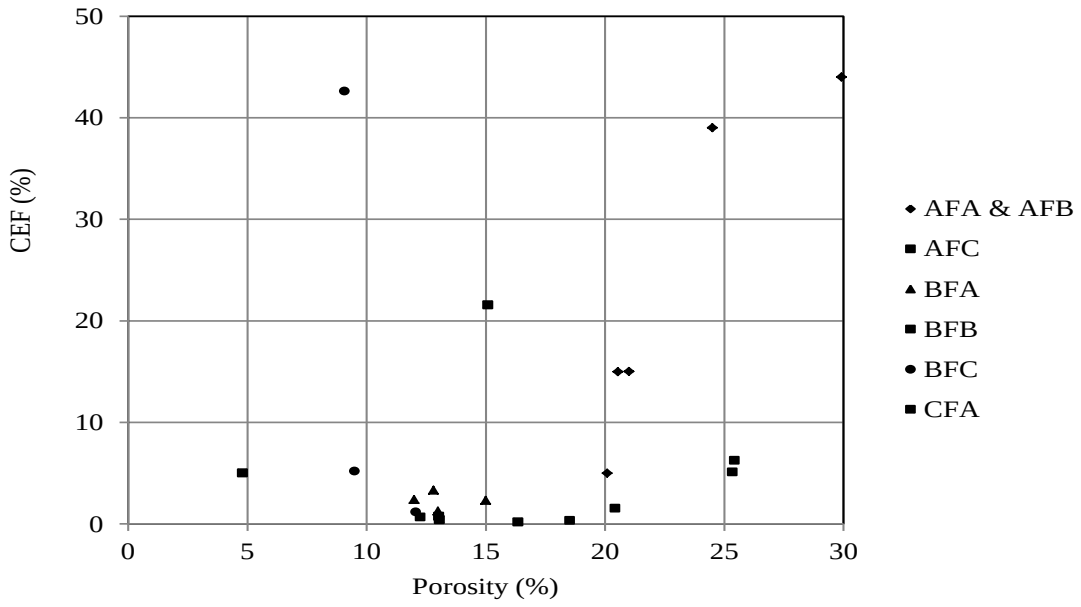

Figure 5.16: Relationship between comminution efficiency factor, CEF and porosity.

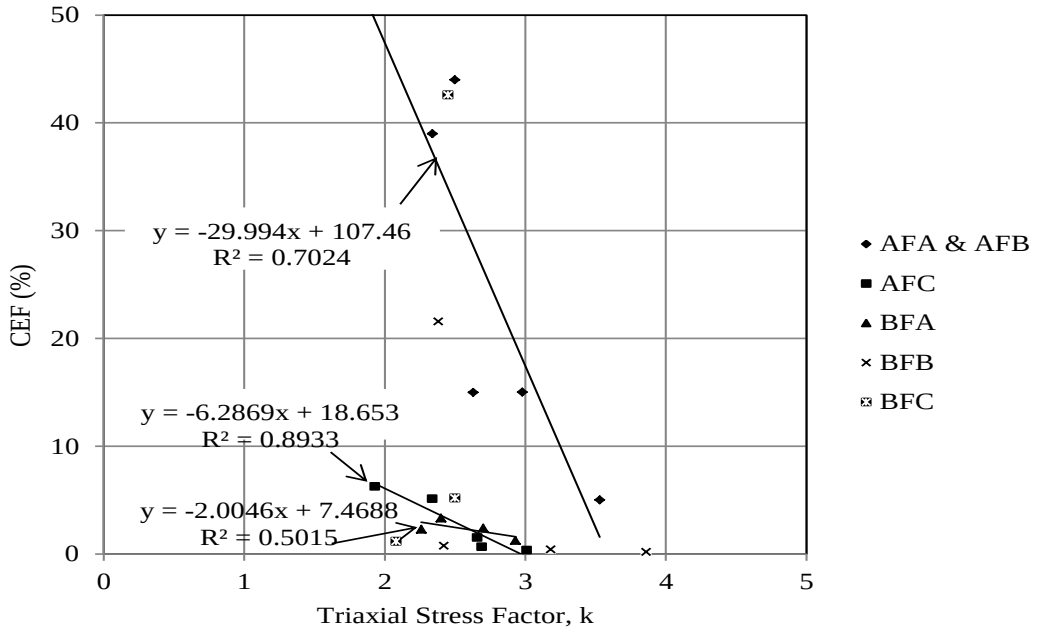

Figure 5.17: Relationship between comminution efficiency factor, CEF and triaxial stress factor, k.

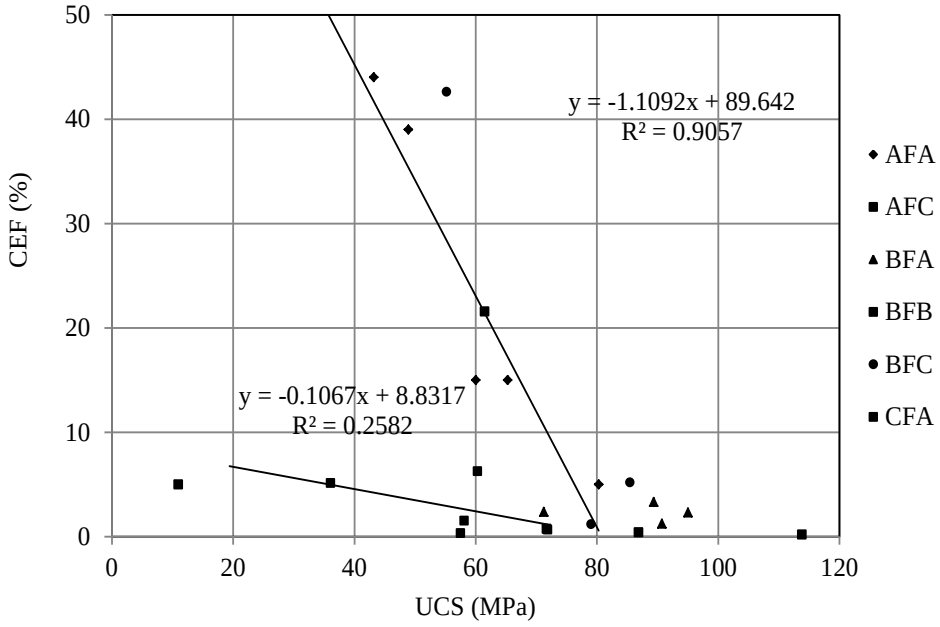

Figure 5.18: Relationship between comminution efficiency factor, CEF and UCS.

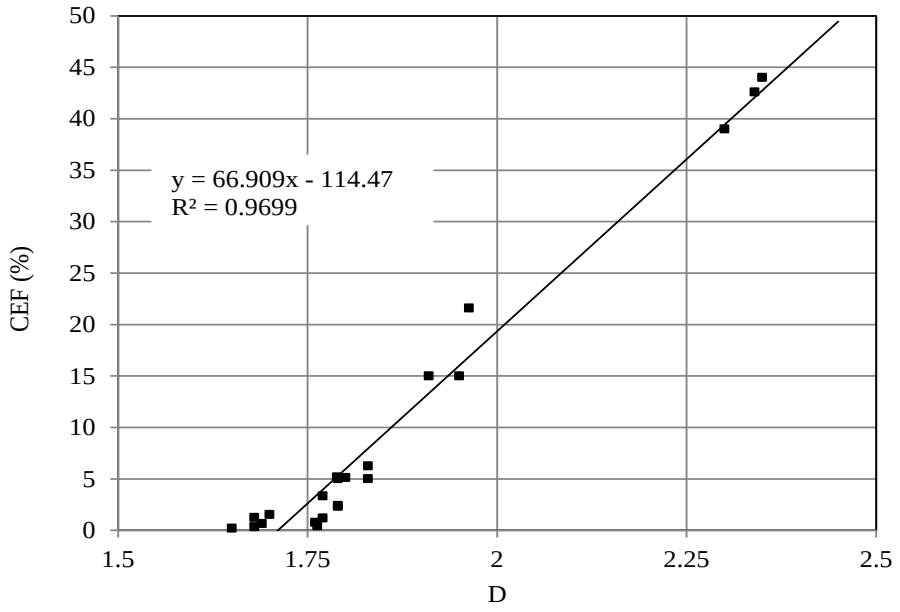

Figure 5.19: Relationship between comminution efficiency factor, CEF and fractal dimension, D.

6 Development and Application of the Yield Energy Model to Predict Wellbore Stability and Mass of Sand (Debris) Created in the Yielded Zone

6.1 Introduction

The failure of rock material around a wellbore has been investigated by numerous researchers (Pasley and J.B.Cheatham, 1963, Bradley, 1978, McLean and Addis, 1990, Russell et al., 2003, Morita, 2004, Kaarstad and Aadnoy, 2005, Al-Ajmi and Zimmerman, 2009) using the elastic solution. The elastic approach however, only predicts catastrophic rock failure and neglects the post-failure characteristic of the formation. Other investigators such as (Bratli and Risnes, 1981, Bratli et al., 1983, Detournay and Roegiers, 1986, McLean and Addis, 1990, Papamichos et al., 1994) considered elasto-plastic deformation mechanism. The elastic-plastic method assumes an annulus of material around the wellbore which deforms in a purely plastic manner and reduces the local stress concentration. An elasto-plastic interface exists further from the wellbore wall into the formation, beyond which the material deforms elastically. The plastic region may retain some strength and structural properties of the intact rock. The assumption of ideal plasticity may be valid for rocks such as salt or shale but does not describe the plastic hardening and softening behaviour associated with most sandstone.

In the field of mining engineering, the post-failure characteristics of a rock surrounding an overstressed opening are considered as a zone of broken granular material with zero cohesion surrounding the excavation. This is considered to be more representative of the failed rock *in situ*. The failure and yielding of the rock result in a decrease in the *in situ* strength and redistribution of the stresses, which in turn leads to the creation of a failed zone around the wellbore. The failed region has been referred to as a 'yield zone' (Wilson, 1977, Wilson, 1983, Somerville and Smart, 1991). The material in the yield zone does not deform plastically; but has the properties of a granular material which can be adequately described by its confining stresses.

In the preceding chapter, a new sand prediction technique based on energy concept utilising laboratory data as input parameters has been proposed. In this chapter, the strain energy approach is coupled with an existing analytical solution (yield zone) to develop a ‘hybrid’ model (yield energy) which investigates the post-failure extent of failed zone around a wellbore as a function of radial distance and also quantifies the amount of debris within the failed region.

6.2 Sand Volume Prediction

The sand production prediction models discussed in section 5.3, and the new strain energy model (section 5.4), can only predict the onset and potential of formation to produce sand but not the volume of sand that would be produced. Predicting the volume of sand particular as a function of applied stresses, drawdown and production rates once the sanding threshold is exceeded is important to ascertain if the sand produced can cause problem or be manageable. However, sand volume prediction has been historically more challenging than the prediction of sanding potential or onset. Although, onset of sanding has been investigated for more than four decades, the first attempt to predict sand volume did not appear until the late 1990s (Geilikman and Dusseault, 1997) and early 2000s (Wang and Xue, 2002, Chin and Ramos, 2002, Wang and Wan, 2004). These models were developed primarily as production enhancement mechanisms for heavy oil.

Generally, motivation for predicting sand volume in conventional reservoirs is driven by the awareness that limited amounts of sand production are often manageable and even lead to significant increase in production. In this regards several models based on laboratory experiments, field observation, theoretical and numerical analysis have been proposed to predict the rate and quantity of sand that will be produced with the fluid in a continuous and/or an episodic manner. The approaches used by these models to quantify volumetric sand production can be classified into strain-based, erosion-based and particle-based models (Adeyanju and Oyekunle, 2010). Experimental and field data are used to calibrate some of the key parameters governing these models. Vardoulakis et al. (1996) was the first to present a sand erosion based model to describe the interaction between the fluid, the solid and the fluidised solid. Mechanical deformation of the rock was not considered. Sand production as a result of volumetric plastic strain is directly related to flow rate, porosity and sand concentration. Post-failure stabilisation of wellbore is assumed to be related to local permeability increase as a result of sand production. This local permeability increase is thought to reduce the drag force on the sand and therefore stabilised the formation.

The hydrodynamic erosion model proposed by Vardoulakis et al. (1996) was subsequently coupled with the mechanical behaviour of the solid-fluid system with erosional behaviour of the solid matrix (Papamichos and Stavropoulou, 1996, Papamichos and Malmanger, 1999, Papamichos et al., 2000). The approach of Papamichos and Stavropoulou (1996) was achieved by solving momentum and continuity equations for fluid flow, solid, and fluidized solid. An elastic perfectly plastic deformation model with

Mohr–Coulomb yield criterion was then employed. In their model, cohesion, elastic modulus, permeability, and sand production coefficient are all linked to porosity via a set of calibration parameters obtained from laboratory experiment. Papamichos and Malmanger (1999) model is similar to the model of Papamichos and Stavropoulou (1996) but with the additional model coupling the product of plastic strain and fluid flow via a semi-empirical erosion criteria (van den Hoek and Geilikman, 2005). The model was validated against hollow cylinder sand experiments. They found that the observed increased in sand production rate was related to increasing stress and flow rate. Papamichos (2002) presented field data on volumetric sand production in a North Sea reservoir. The data was simulated numerically at drawdown pressures of 2, 2.5 and 3 MPa using an erosion model that coupled the near wellbore mechanical behaviour during oil production with the erosion behaviour during sand production. There is a reasonable agreement between the model results and the experimental data from sand production hollow cylinder tests with respect to time and flow rate effects.

Chin and Ramos (2002) related the amount of produced sand directly to the volume of the yielded region around the wellbore, with the assumption that all the yielded sand is removed by the hydrocarbon fluid and produced at the surface. Willson et al. (2002) focused on the parameters causing sand failure by using an empirical relationship between stress level, flow conditions and produced sand volume per perforation. The relationship was defined based on laboratory data on perforation tests and field test data. An empirical approach based on physical processes observed in sand production tests and test data from a variety of sandstones has also been used by Papamichos (2002) to predict the cumulative amount sand and sand rates during the production period. These models are based on numerical solution schemes or empirical correlations and they described sand production as a continuous process.

A sand production rate model base on the modeling concept of Geilikman and Dusseault (1997) was presented by van den Hoek and Geilikman (2005). The model captures both geomechanical impact and fluid aspects due to watercut through a reduction in strength from the loss of capillary cohesion. They assumed an elasto-viscoplastic behaviour where the amount of fluid flow and sand produced into the wellbore is directly related to flow induced change in volumetric plastic strain around the wellbore. The model was validated by comparing the amount of sand produced with field observation (e.g. van den Hoek and Geilikman, 2006). Detournay et al. (2006) proposed a model to study the onset and rate of sand using finite element model. Sand is produced if

hydrodynamic forces are higher than stress-dependant critical value that is a function of grain size.

Rijken et al. (2014) presented a finite element numerical and an empirical/analytical sand volume production models. In the numerical model, sanding parameters were first determined from laboratory and field data. The sanding parameters are changed iteratively until a good match is obtained and then upscaled in a predictive mode. The predicted sand volume from the numerical model compares well with the measured sand volume from laboratory test. The empirical/analytical model takes into account the rock strength, *in situ* stresses and drawdown pressure. A reasonable match was found when the sand volume estimated from the field case was compared with the measured sand volume from the analytical model.

The prediction of sand volume production proposed by these models adopts different strategy and assumptions (Addis et al., 2008). The analytical models usually assume a perfectly elasto-plastic constitutive behaviour and equal stresses along section of the wellbore resulting in uniform cylindrical yield zones (Chin and Ramos, 2002, van den Hoek and Geilikman, 2006). The assumption of perfect plasticity as discussed earlier may not be valid for sandstone formation. Post-failure stabilisation is accounted for by a proportional increase in the elastic formation in relation to the amount of produced sand. The model by Willson et al. (2002) is based on an empirical relationship; where as Papamichos and Malmanger (1999) and Papamichos (2002) based their sand volume prediction on hollow-cylinder laboratory tests and field data to define the appropriate input parameter for their model.

.

6.3 The Yield Zone Concept

6.3.1 Introduction

The yield zone concept is a hypothesis originally developed by Wilson (1977) to estimate passive support requirements for main roadways and to determine the behaviour of a yielded rock around a horizontal mine tunnel. The material surrounding a wellbore will yield by undergoing a reduction in its load bearing capacity if the elastic deformation is exceeded, and the excess load is redistributed further into the formation to a point far from the wellbore region where it can be accommodated. The location of this point depends on the failure criteria of the rock and the magnitude of the confining stresses. This is the radial stress acting perpendicular to the wellbore wall and the tangential stress

acting around the wellbore. The relationship between these two stresses and the failure criterion dictates the load bearing capacity of the rock. Sand particles at the edge of the wellbore wall where there is little confinement have a free surface and some of these can fail and be detached from the rock. However, failure further into the formation is restricted due to geometric effect and increase in the confinement stresses. This result in the rock accommodating the redistributed stresses, thus laws of elasticity could be applied as the rock is considered to be below its failure limit beyond this boundary (Somerville and Smart, 1991). Consequently, a yield-elastic boundary which extent depends on the confining and redistributed stresses, load deformation properties of the solid and yielded material would exist. The failed material within the boundary is considered to be a yield zone and the post-failure mechanical properties of this failed material could be considered as a zone of broken granular material with zero cohesion, or as a Coulomb material, with a residual cohesion (Wilson, 1983). The assumption of a yield zone is particularly valid in rocks where redistributed stresses are high compared with rock strength. However, it does have some limitations which are inherent in its basic assumptions:

- Existence of a circular opening with a cross-sectional area.
- The formation rock surrounding the opening is homogeneous and isotropic.
- Horizontal and vertical *in situ* stresses are equal.
- The formation rock satisfies plane strain condition.
- The formation peak and residual strength both obey the linear Mohr-Coulomb criteria.

The general distribution of the stresses around a circular wellbore with a yield zone is shown in Figure 6.1. The stress distributions are derived from relationships for the stress conditions in the yield and elastic zones (Wilson, 1983), which indicates that the stress within the yield zone is reduced in comparison with the pure elastic case. The position of the maximum tangential stress occurs at the yield/elastic boundary.

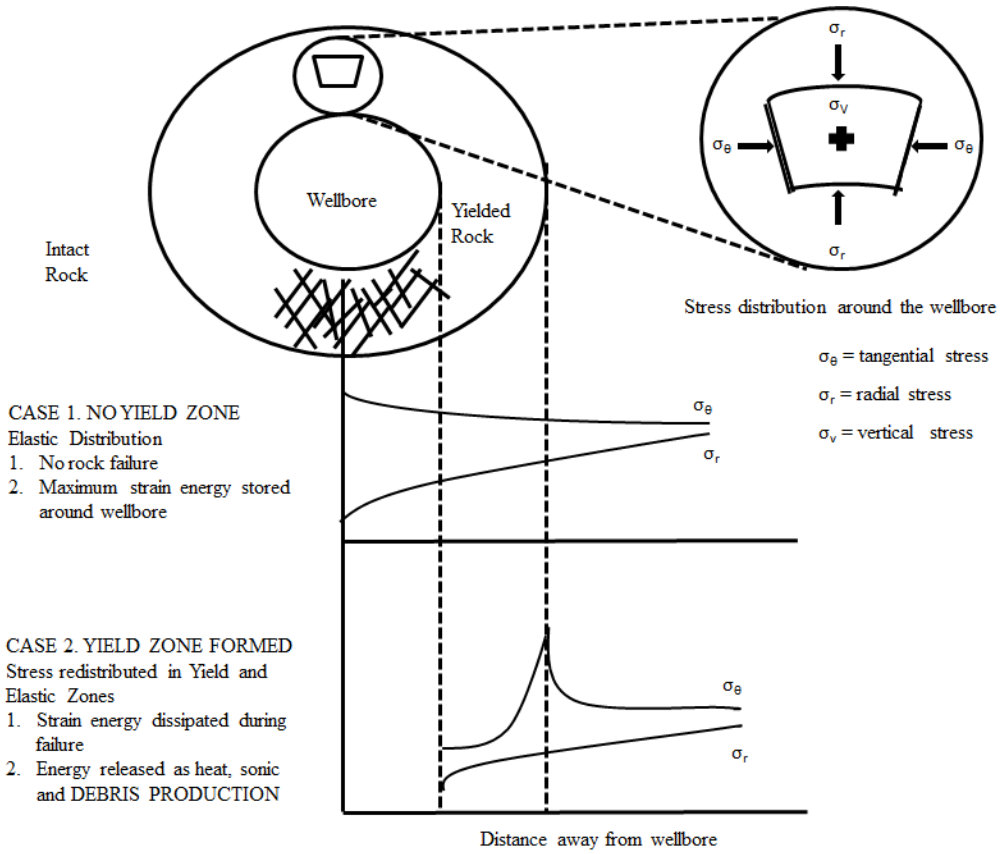

Figure 6.1: Stress distribution around a wellbore "before" and "after" initiation of yield (after Wilson, 1983).

6.3.2 Review of the Yield Zone Formulae

Generally, where the stress regime across the boundary of a wellbore opening is purely elastic, the tangential stress at the boundary will be double the virgin hydrostatic stress (Obert and Duvall, 1967). This will exceed the strength of an average rock at depth, and a "yield" zone adjacent to the boundary will form. Wilson (1977) stated that although the relationship between the stress at failure (σ_1) and the confining pressure (σ_3) is frequently curved, for a circular hole in a hydrostatic stress field, a failure criterion based on an approximate linear relationship can be assumed for the intact rock:

$$\sigma_1 = \sigma_0 + k\sigma_3 \qquad (6.1)$$

where σ_0 is the unconfined compressive strength and k is the triaxial stress factor.

Similarly a corresponding failure criterion within the yield zone is given as:

$$\sigma_1^* = \sigma_0^* + k\sigma_3 \qquad (6.2)$$

In this case σ_1^* is the stress required to cause movement in the broken material when confined by stress, σ_3 while σ_0^* is the corresponding stress at zero confinement. The resulting formulae may be transcribed as:

(a) Stress Solution within the Yield Zone

Radial stress,

$$\sigma_r = (p + p')(r/R_w)^{(k-1)} - p' \tag{6.3}$$

Tangential Stress,

$$\sigma_\theta = k(p + p')(r/R_w)^{(k-1)} - p' \tag{6.4}$$

where R_w is the radius of the wellbore and p the restraint on its boundary ($p' = \sigma'_\theta/(k-1)$.

(b) Stress Solution at the Yield/ Elastic Boundary

Radial stress,

$$\sigma_{Rye} = \frac{2q - \sigma_0}{k+1} \tag{6.5}$$

Tangential stress on the yield side boundary,

$$\sigma_{\theta y} = \frac{k(2q - \sigma_0)}{k+1} + \sigma'_0 \tag{6.6}$$

Tangential stress on the elastic side boundary,

$$\sigma_{\theta e} = \frac{k(2q - \sigma_0)}{k+1} + \sigma_0 \tag{6.7}$$

where q is opening the redistributed effective stress around the wellbore (horizontal stress-pore pressure), $\sigma_{\theta y}$ and $\sigma_{\theta e}$ are the tangential stresses acting on either side of the yield and elastic boundary.

(c) Stress Solution within the Elastic Zone

Radial stress,

$$\sigma_r = q - C(R_w/r)^2 \tag{6.8}$$

Tangential Stress,

$$\sigma_\theta = q + C(R_w/r)^2 \tag{6.9}$$

where

$$C = \left[\frac{(k-1)q + \sigma_0}{k+1}\right] \times \left[\frac{2q - \sigma_0 + p'(k+1)}{(p+p')(k+1)}\right]^{2/(k-1)} \tag{6.10}$$

The width of the yield zone at the elastic boundary ($r = R_{ye}$) can be obtained from the condition of continuity of σ_{Rye} at the yield/elastic boundary as:

$$R_{ye} = R_w \left[\frac{2q - \sigma_0 + p'(k+1)}{(p+p')(k+1)} \right]^{1/(k-1)} \qquad (6.11)$$

6.3.3 Modification of the Yield Zone Equation

In order to apply the yield zone concept to a vertical as well as an inclined oil and gas wellbore situated under non-hydrostatic conditions, Somerville and Smart (1991) modified the yield zone equation to take into account the effect of pore pressure, mud weight and wellbore inclination.

Effective stress: The consideration of effective stress concept (section 2.2.6) has been incorporated to allow the effect of pore pressure to be included in the analysis. Stress solution for the yield zone has already defined both the radial stress, σ_r and the tangential stress, σ_θ in terms of effective stress since they were derived from failure criteria taken at zero pore pressure. However, pore pressure, P_p was subtracted from the *in situ* principal stresses for the yield/elastic boundary and elastic zone solutions to account for effective stress. This is of particular relevance when examining the effect on the reservoir not immediately around the wellbore.

Mud weight: The boundary stress, p in the original equation was replaced by the mud pressure since they both provide the same function. Effective stresses are used in this modified approach, hence a zero value of p corresponds to the situation where the mud and pore pressures are equal, signifying a 'balanced' drilling process. Similarly, 'overbalanced' drilling corresponds to a positive value of p is and 'underbalanced' to a negative value of p. Therefore the lining resistance was considered to be the difference between the mud pressure and the pore pressure and was designated as P_m in the modified set of equations.

Wellbore orientation: The value of 2q in the original formulae is equal to the tangential stress acting at a point on the wall of the opening for the case of a horizontal wellbore. However, in a non-hydrostatic stress state the tangential stress will not be constant around the wellbore but would be maximum at some point depending on the relationship between the orientation of the wellbore and the initial *in situ* stresses. It is therefore required to determine the tangential stress acting around the section of an inclined wellbore. This is achieved by rotating the principal stresses to the wellbore coordinates frame using the direction cosines rule as described in section 2.6.3. The respective *in situ* rotated horizontal stresses were then inserted into equation (2.84) to obtain the tangential stress, $\sigma_{\theta i}$ which acted tangentially at the point under consideration.

The tangential stress, $\sigma_{\theta i}$ is equivalent to the value of 2q for a horizontal wellbore under hydrostatic stress regime. In terms of total stresses, the effective tangential stress is given as: $(\sigma_{\theta i} - P_p)$.

The modified stress solutions are thus given as:

(a) Yield Zone

Radial stress,

$$\hat{\sigma}_r = (P_m + p')(r/R_w)^{(k-1)} - p' - P_p \quad (6.12)$$

$$\hat{\sigma}_r = Ar^{(k-1)} - p' - P_p \quad (6.13)$$

where

$$A = \frac{(P_m + p')}{r_0{}^{k-1}} \quad (6.14)$$

Tangential Stress,

$$\sigma_\theta - P_p = k(P_m + p')(r/R_w)^{(k-1)} - p' \quad (6.15)$$

$$\hat{\sigma}_\theta = Br^{(k-1)} - p' - P_p \quad (6.16)$$

where

$$B = \frac{k(P_m + p')}{r_0{}^{k-1}} \quad (6.17)$$

(b) Yield/ Elastic Boundary

Radial stress,

$$\hat{\sigma}_{Rye} = \frac{(\sigma_{\theta i} - P_p) - \sigma_0}{k+1} \quad (6.18)$$

Tangential stress on the yield side boundary,

$$\hat{\sigma}_{\theta y} = \frac{k((\sigma_{\theta i} - P_p) - \sigma_0)}{k+1} + \sigma_0' \quad (6.19)$$

Tangential stress on the elastic side boundary,

$$\hat{\sigma}_{\theta e} = \frac{k\left((\sigma_{\theta i} - P_p) - \sigma_0\right)}{k+1} + \sigma_0' \quad (6.20)$$

Note that $\sigma_{\theta i}$ is calculated from equation (6.8).

(c) Elastic Zone

Radial stress,

$$\hat{\sigma}_r = q - {}^{D}/_{r^2} \tag{6.21}$$

Tangential Stress,

$$\hat{\sigma}_\theta = q + {}^{D}/_{r^2} \tag{6.22}$$

where

$$D = CR_w{}^2 \tag{6.23}$$

Thus the modified equation for the radius of the yield elastic boundary is:

$$R_{ye} = R_w \left[\frac{(\sigma_{\theta i} - P_p) - \sigma_0 + p'(k+1)}{(P_m + p')(k+1)} \right]^{{}^{1}/_{(k-1)}} \tag{6.24}$$

6.4 The Yield Energy Model

6.4.1 Introduction

The yield energy model is a hybrid model consisting of the yield zone (Somerville and Smart, 1991) and the strain energy model which is an associated new approach to sand prediction (see section 5.4), utilising a link between the dissipation in strain energy as the rock yields, resulting in the formation of debris. The model combines field and laboratory experimental data as input to analytical expressions to predict the stability of a formation by examining the onset of yield and volume or mass of sand (debris) in creating the yield zone, specifically with regards to mud weights, drawdown pressures and production rates.

During the drilling phase, the extent of the yield zone can be limited by the pressure applied to the side of the wellbore, and hence the mud weight required to prevent the formation of a yield zone can be determined from the yield zone equation. The potential for sand production can further be assessed in a rock specific manner by quantifying the reduction in strain energy stored in the rock as it yields around the completion on removal of the completion fluid and the imposition of drawdown during the production phase. During this process energy is dissipated, some of which is available for fragmentation of the rock along the failure surfaces. The resultant debris then becomes available as a source for sand production.

The energy dissipated during the formation of the yield zone can be determined by calculating the difference in the strain energy stored in the rock before and after creation of the yield zone. This enables a rock specific approach to be adopted by using values of the mechanical properties obtained experimentally. Inflow or deliverability expressions can be used to relate the energy dissipated during yield to production rates or drawdown. By combining the strain energy concept and the yield zone it is possible to determine the volume and mass of debris produced in creating the yield zone, which accumulates between the failure surfaces and is available for sand production.

Application of the yield energy model involves the following stages: rock mechanical testing on representative samples to obtain input parameters; initial assessment of the propensity of sand debris production (strain energy); determination of the initiation and the lateral extent of the failed rock around a wellbore (yield zone); quantifying the energy available for fracturing; applying experimentally determined comminution constants to estimate the volume and mass of debris created. Figure 6.2 shows a flow diagram of the yield energy model.

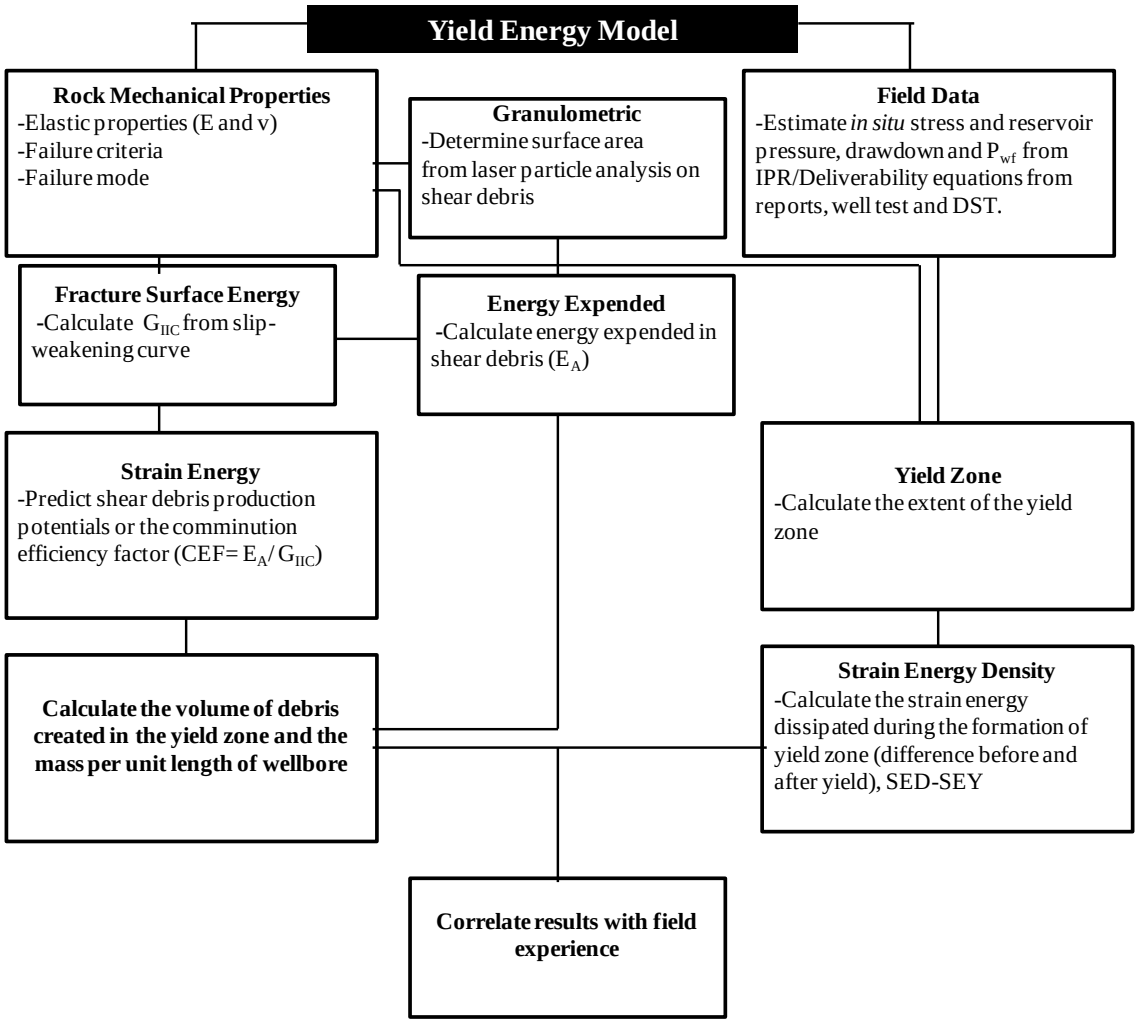

Figure 6.2: Flow diagram of stages involve in the yield energy model.

Accordingly, the yield energy model is based on the following assumptions and logic:

- During drilling and insertion of a production casing or liner, sufficient mud weight is maintained to generate enough pressure on the periphery of the well to inhibit the failure of the rock. The weight of the mud can be determined from the yield zone equation. The rock will therefore be loaded entirely within the pre-failure elastic regime, and the total strain energy stored in the rock around unit length of wellbore (SED) can be determined.
- On the initiation of production, the stabilising restraint applied to the periphery of the well is removed and rock failure is initiated. The rock will increase in volume as it fails or yields and the associated expansion will close the annulus around the liner or production casing. The liner or production casing will then generate sufficient restraint on the failed rock to inhibit further failure, creating a stable zone of failed rock, i.e. a yield zone, around the well. The yield zone

will comprise of comminuted grain-sized debris and larger fragments storing elastic strain energy. The strain energy remaining in the larger fragments for a unit of wellbore within the yield zone (SEY) can also be determined.

- The strain energy dissipated per unit length of wellbore (during rock failure) is the difference between the strain energy stored in the rock within pre-failure elastic regime (SED) and the strain energy remaining in larger fragments within the yield zone (SEY).
- The strain energy dissipated in creating grain-sized debris is then given by CEF*(SED-SEY).
- Finally, the volume or mass of grain-sized debris created per unit length of wellbore can be determined from the relation (CEF *(SED-SEY))/W_A.

6.4.2 Determination of General Strain Energy Functions

The application of a load on a surface of body produces deformation, consequently the surface on which the force acts moves as a result of the applied force. Thus a certain work is done on the body. In an elastic medium, this work is converted to potential energy of strain.

Considering a uniform bar loaded in tension as shown in Figure 6.3a. The force on the ends of the bar is $\sigma_x d_y d_z$ and the end of the bar is extended $\varepsilon_x d_x$ after application of the force. The relationship between these two quantities is shown in Figure 6.3b. The work, dW, done during the application of the load is the area of the triangle OAB, thus:

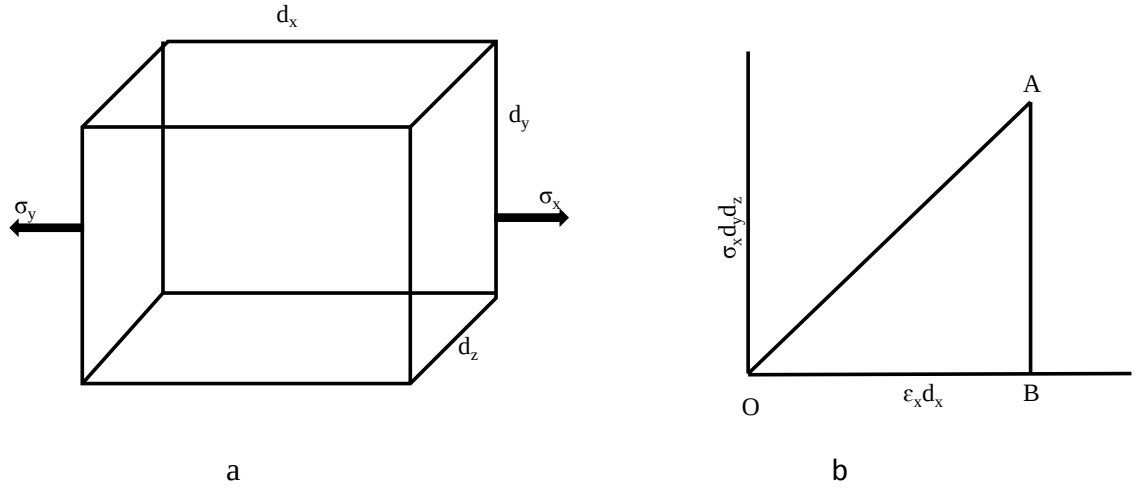

Figure 6.3: Deformation of a uniform bar under applied force (after Obert and Duvall, 1967).

$$dW = \frac{1}{2}(\text{stress} \times \text{strain}) \tag{6.25}$$

or considering a small cube of material with faces perpendicular to the principal stresses and strain, given by expression:

$$W = \frac{1}{2}\sigma_x \varepsilon_x \, dxdydx \tag{6.26}$$

A consideration of other components of stress and strain gives similar equation. Thus the total work per unit volume, W_0 resulting from simultaneous application of the six stress components σ_x , σ_y , σ_z, τ_{xy} , τ_{yz} and τ_{xz} is:

$$W_0 = \frac{1}{2}\left(\sigma_x \varepsilon_x + \sigma_y \varepsilon_y + \sigma_z \varepsilon_z + \tau_{xy}\gamma_{xy} + \tau_{yz}\gamma_{yz} + \tau_{zx}\gamma_{zx}\right) \tag{6.27}$$

The quantity W_0 is the strain energy per unit volume and can be expressed in terms of stress or strain components only by means of Hooke's law equations. Thus using equation (2.32) to equation (2.34) we get:

$$W_0 = \frac{1}{2E}\left(\sigma_x{}^2 + \sigma_y{}^2 + \sigma_z{}^2\right) - \frac{\nu}{E}\left(\sigma_x\sigma_y + \sigma_y\sigma_z + \sigma_z\sigma_x\right) + \frac{1}{2G}\left(\tau_{xy}{}^2 + yz^2 + \tau_{zx}{}^2\right) \tag{6.28}$$

The strain energy in terms of the principal stresses is then given as:

$$W_0 = \frac{1}{2E}(\sigma_1{}^2 + \sigma_2{}^2 + \sigma_3{}^2) - \frac{\nu}{E}(\sigma_1\sigma_2 + \sigma_2\sigma_3 + \sigma_3\sigma_1) \tag{6.29}$$

The strain energy per unit volume of rock, W_0 loaded elastically is given by Obert and Duvall (1967) as:

$$W_0 = \frac{1-2\nu}{6E}(\sigma_1 + \sigma_2 + \sigma_3)^2 + \frac{(\sigma_1-\sigma_2)^2 + (\sigma_2-\sigma_3)^2 + (\sigma_3-\sigma_1)^2}{12G} \tag{6.30}$$

where σ_1, σ_2 and σ_3 are principal stresses, E the Young's modulus, ν the Poison's ratio and G the shear modulus.

Changing equation (6.30) into polar stresses and retaining the plane strain condition along axis of the wellbore gives:

$$W_0 = \frac{1-2\nu}{6E}(\sigma_r + \sigma_\theta + \sigma)^2 + \frac{(\sigma_r-\sigma_\theta)^2 + (\sigma_\theta-\sigma)^2 + (\sigma-\sigma_r)^2}{12G} \tag{6.31}$$

where σ_r is the radial stress, σ_θ the tangential stress, σ is the stress along line of the wellbore.

Strain Energy within the Yield Zone (SEY)

From equation (6.12) and equation (6.16) we get:

$$\hat{\sigma}_r + \hat{\sigma}_\theta + \hat{\sigma} = Ar^{(k-1)} - p' - P_p + Br^{(k-1)} - p' - P_p + \sigma - P_p \quad (6.32)$$

$$= r^{(k-1)}(A + B) - 2p' - 3P_p + \sigma \quad (6.33)$$

and

$$\hat{\sigma}_r - \hat{\sigma}_\theta = Ar^{(k-1)} - p' - Br^{(k-1)} + p' - P_p + P_p \quad (6.34)$$

$$= r^{(k-1)}(A - B) \quad (6.35)$$

and

$$\hat{\sigma}_\theta - \hat{\sigma} = Br^{(k-1)} - p' - \sigma - P_p + P_p \quad (6.36)$$

$$= Br^{(k-1)} - p' - \sigma \quad (6.37)$$

and

$$\hat{\sigma} - \hat{\sigma}_r = \sigma - P_p - Ar^{(k-1)} + p' + P_p \quad (6.38)$$

$$= \sigma - Ar^{(k-1)} + p' \quad (6.39)$$

Therefore the total strain energy in a yielded zone can be obtained by integrating the total workdone over the radius:

$$w_0 = \int_{r_1}^{r_2} w_0 \, . \, dr \quad (6.40)$$

From equation (6.31), this becomes:

$$\int w_0 \, dr = \frac{1 - 2\nu}{6E} \int (r^{(k-1)}(A + B) - 2p' - 3P_p + \sigma)^2 dr + \frac{1}{12G} \int \left(r^{(k-1)}(A - B)\right)^2 + \left(Br^{(k-1)} - p' - \sigma\right)^2 + \left(\sigma - Ar^{(k-1)} + p'\right)^2 dr \quad (6.41)$$

Let $E = -2p' - 3P_p + \sigma$

and $F = \sigma + p'$

$$= \frac{1-2\nu}{6E}\int (r^{(k-1)}(A+B)+E)^2 dr$$

$$+\frac{1}{12G}\int \left(r^{(k-1)}(A-B)\right)^2 + \left(Br^{(k-1)} - F\right)^2 \quad (6.42)$$

$$+\left(-Ar^{(k-1)} + F\right)^2 dr$$

$$= \frac{1-2\nu}{6E}\int \left(r^{2k-2}(A+B)^2 + 2r^{k-1}(A+B) + E^2\right)dr \quad (6.43)$$

$$+\frac{1}{12G}\int r^{2k-2}(A-B)^2 + B^2 r^{2k-2}$$

$$-2Br^{k-1}.F + F^2 + A^2 r^{2k-2} - 2Ar^{k-1}.F$$

$$+ F^2.dr$$

$$= \frac{1-2\nu}{6E}\left[\frac{r^{2k-1}(A+B)^2}{2k-1} + \frac{2r^k(A+B)}{k} + E^2 r\right]_{r_1}^{r_2} \quad (6.44)$$

$$+\frac{1}{12G}\left[\frac{r^{2k-1}(A-B)^2}{2k-1}\right]_{r_1}^{r_2}$$

$$+\frac{1}{12G}\left[\frac{B^2 r^{2k-1}}{2k-1} + \frac{2BFr^k}{k} + F^2 r\right]_{r_1}^{r_2}$$

$$+\frac{1}{12G}\left[\frac{A^2 r^{2k-1}}{2k-1} + \frac{2AFr^k}{k} + F^2 r\right]_{r_1}^{r_2}$$

Strain Energy in the Elastic Zone (SED)

From equation (6.21) and equation (6.22) we get:

$$\hat{\sigma}_r + \hat{\sigma}_\theta + \hat{\sigma} = q - {}^{D}/_{r^2} - P_p + q + {}^{D}/_{r^2} - P_p + \sigma - P_p \quad (6.45)$$

$$= 2q - 3P_p + \sigma \quad (6.46)$$

and

$$\hat{\sigma}_r - \hat{\sigma}_\theta = q - {}^{D}/_{r^2} - P_p - q - {}^{D}/_{r^2} + P_p \quad (6.47)$$

$$= -{}^{2D}/_{r^2} \quad (6.48)$$

and

$$\hat{\sigma}_\theta - \hat{\sigma} = q + {}^{D}/_{r^2} - P_p - \sigma + P_p \quad (6.49)$$

$$= q + {}^{D}/_{r^2} - \sigma \quad (6.50)$$

and

$$\hat{\sigma} - \hat{\sigma}_r = \sigma - P_p - q + {}^{D}/_{r^2} + P_p \quad (6.51)$$

$$= \sigma - q + {}^{D}/_{r^2} \tag{6.52}$$

Therefore integrating the total workdone in the elastic zone from equation (6.31):

$$= \frac{1-2\nu}{6E}\int (2\,q - 3P_p + \sigma)^2 dr + \frac{1}{12G}\int \left(-{}^{2D}/_{r^2}\right)^2 + \left(q + {}^{D}/_{r^2} - \sigma\right)^2 + \left(\sigma - q + {}^{D}/_{r^2}\right)^2 dr \tag{6.53}$$

Let $G = -\sigma + q$

and $M = 2\,q - 3P_p + \sigma$

$$= \frac{1-2\nu}{6E}\int M^2 dr + \frac{1}{12G}\int \left(-{}^{2D}/_{r^2}\right)^2 + \left({}^{D}/_{r^2} + G\right)^2 + \left({}^{D}/_{r^2} - G\right)^2 dr \tag{6.54}$$

$$= \frac{1-2\nu}{6E}\int M^2 dr + \frac{1}{12G}\int 4{}^{D^2}/_{r^4} + {}^{D^2}/_{r^4} + 2{}^{GD}/_{r^2} + G^2 + {}^{D^2}/_{r^4} - 2{}^{GD}/_{r^2} + G^2 . dr \tag{6.55}$$

$$= \frac{1-2\nu}{6E}[M^2 r]_{r_1}^{r_2} + \frac{1}{12G}\left[-4{}^{D^2}/_{3r^3} - {}^{D^2}/_{3r^3} - 2{}^{GD}/_{r} + G^2 r - {}^{D^2}/_{3r^3} + 2{}^{GD}/_{r} + G^2 r\right]_{r_1}^{r_2} \tag{6.56}$$

$$= \frac{1-2\nu}{6E}[M^2 r]_{r_1}^{r_2} + \frac{1}{12G}\left[-6{}^{D^2}/_{3r^3} + 2G^2 r\right]_{r_1}^{r_2} \tag{6.57}$$

The final closure equation is given as (Wilson, 1977):

$$C_L = R_w \frac{1+\nu}{E}\left[\frac{(k-1)(\sigma_{\theta i} - P_p) + \sigma_0}{k+1}\right] \left[\frac{2(\sigma_{\theta i} - P_p) - \sigma_0 + p'(k+1)}{(p+p')(k+1)}\right]^{2.2/(k-1)} \tag{6.76}$$

6.5 Field Data Requirement

In addition to the parameters which are determined from laboratory tests, the yield energy model also requires input parameters that can only be acquired from the field. Knowledge of both the initial stress state and its subsequent changes with progressive

reservoir depletion and varying drawdown are necessary for the yield energy model. These data include *in situ* stresses, formation fluid pressure and deliverability relationship. The deliverability relationship describing the relationship between production rate and fluid pressure provides the means of studying changes to the *in situ* stress magnitude due to hydrocarbon production.

6.5.1.1 *In Situ Stress State*

Conventionally in the North Sea, particularly the Central North Sea, the overburden stress is assumed to be the maximum principal stress and the maximum and the minimum horizontal stress gradients are assumed to be the same ($\sigma_v > \sigma_H \sim \sigma_h$) (Hillis and Nelson, 2005). In this thesis, the vertical overburden stress, σ_v, has been calculated by assuming a stress gradient of 21.02 kPa/m depth and the variation of this stress with the maximum horizontal stress, σ_H is taken as 0.8. This simplified stress model could be improved by applying casing leak off test or minifrac data to estimate the *in situ* minimum principal horizontal stress.

6.5.1.2 *Wellbore Inclination*

Both the wellbore inclination with respect to vertical and the wellbore orientation with respect to the unequal *in situ* horizontal stresses are required in order to transform the principal stresses into the wellbore coordinate frame. Deviation and survey data were obtained to define the wellbore orientation.

6.5.1.3 *Formation Fluid Pressure*

Two measures of the reservoir fluid pressure are required for the analysis. The first is the far-field pressure which is equivalent to the static reservoir pressure, P_r. The second is the flowing bottomhole pressure, P_{wf} which is calculated using deliverability expression to determine the pressure drawdown, ΔP at the wellbore as a function of production rate (see 6.5.1.4). The static reservoir pressure is determined using pressure build-up data from well testing and Repeat Formation Test (RFT) data. The values of P_r are usually reported as relative to some particular datum level in the reservoir. Thus it is necessary to calculate the actual reservoir static pressure, P'' at a particular depth for any given sample. This is achieved by using the fluid gradient in this case the gas gradient, ρ_g and the difference in depth between the datum and the depth of the sample, Δh according to the following expressions:

$$P'' = \Delta P + P_{datum} \tag{6.58}$$

where ΔP is the pressure difference due to the column of gas between the datum and the depth of the sample:

$$\Delta P = \Delta h \times \rho_g \tag{6.59}$$

6.5.1.4 *Inflow Performance Relation (IPR)/Deliverability Relationship*

The relationship between pressure drawdown, Δp (the difference between the average reservoir pressure, $\bar{p}$ and the bottomhole pressure, p_{wf}) and the hydrocarbon production rate can be described using either IPR or deliverability curves for oil and gas wells respectively. Average pressure is normally used to define the productivity of a well in a bounded drainage since this quantity is observable from a well test. Thus for an oil well in a semi-steady state, the pressure drawdown can be related to the production via:

$$\bar{p} - p_{wf} = \frac{q\mu}{2\pi kh}\left[\ln\frac{r_e}{r_w} - \frac{3}{4} + S\right] \tag{6.60}$$

and for a gas field we have:

$$\bar{p}^2 - p_{wf}^2 = \frac{111.7Q\mu ZT}{kh}\left[\ln\frac{r_e}{r_w} - \frac{3}{4} + S\right] \tag{6.61}$$

Such relationship can be derived directly by observing production rate-pressure changes during multi-rate well test (Dake, 1986) or by substituting permeability and skin factor values derived from well test analysis into a suitable inflow equation. Permeability values may also be estimated from core data if well test data are not available. The deliverability curves used by the analytical model in this thesis are based on pseudo-pressure to accounts for the variability of compressibility and viscosity of gas with respect to pressure. In terms of real gas pseudo-pressures, the gas inflow equation becomes:

$$m(P_s) - m(P_{wf}) = \frac{111.7QT}{kh}\left[\ln\frac{r_e}{r_w} - \frac{3}{4} + S\right] \tag{6.62}$$

where $m(P_s)$ and $m(P_{wf})$ are static and flowing bottomhole gas pseudo pressures, T is the temperature (K), k is the permeability (m^2), r_e is the drainage radius (m), r_w is the wellbore radius (m) and S is the total skin factor. The total skin factor is composed of the mechanical skin factor, S', which is determined from buildup test and the rate dependent skin factor, D which is calculated from multiple-rate test. D is a function of permeability, being larger in low permeability reservoirs.

This can be written in the general form:

$$m(P_s) - m(P_{wf}) = BQ + FQ^2 \tag{6.63}$$

where Q is the production rate and B and F are constants.

From equation (6.62) the coefficient B and F in equation (6.63) can be expressed as:

$$B = \frac{111.7T}{kh}\left[\ln\frac{r_e}{r_w} - \frac{3}{4} + S'\right] \quad (6.64)$$

$$F = \frac{111.7TD}{kh} \quad (6.65)$$

The real gas pseudo-pressure as a function of the actual pressure was determined from PVT data using a simple graphical method of numerical integration base on trapezoidal rule (e.g. Dake, 1986), in which a linear function was satisfactory used for the range of values encountered. The relationship is then determined by applying well test, Rm and core data to determine the coefficient in equation (6.63). Well test data is considered to yield a more representative relationship since the portion of the formation which actually contribute to production is tested and the influence of skin effect and perforation location are automatically included.

Although the coefficient B and F in equation (6.63) can be determined using a suitable inflow equation, a simpler method is to use actual observation of pressure and flowrate data (Dake, 1986). Plotting the function $\left(m(P_s) - m(P_{wf})\right)/Q$ versus Q would produce a linear graph with slope F and intercepts B when $Q = 0$.

However, not all the samples tested in the laboratory have corresponding well test data. In such cases, deliverability expressions were generated using core analysis data for the permeability estimate. The mechanical and rate dependent skin factors were assumed to be the same across the horizon since in most cases the geometric mean permeability determined from core are close to the permeability determined from DST data.

The deliverability expressions used in this study are presented below.

Well AFA

1. Famgee horizon: 2787 – 2818 m

$$m(P_s) - m(P_{wf}) = 2052.5 \times Q + (3.4 \times 10^{-2}) \times Q^2 \quad (6.66)$$

2. Deekay horizon: 3709 – 3727 m

$$m(P_s) - m(P_{wf}) = 5423.6 \times Q + (2.6 \times 10^{-2}) \times Q^2 \quad (6.67)$$

Well AFB

1. Famgee horizon: 2750 – 3304 m

$$m(P_s) - m(P_{wf}) = 466.4 \times Q + (2.4 \times 10^{-3}) \times Q^2 \quad (6.68)$$

2. Deekay horizon: 3407 – 3427 m!**

$$m(P_s) - m(P_{wf}) = 5083.0 \times Q + (7.6 \times 10^{-2}) \times Q^2 \quad (6.69)$$

!**determine from equation (6.64) and equation (6.65) using k = core geometric mean permeability, S' and D as skin factor data from Deekay in well AFA, h = cored interval, T = RFT data, r_e assumed 3.05×10^2 m.

6.6 Application of the Yield Energy Model to Predict Wellbore Stability and Mass of Sand (Debris) Created in the Yielded Zone

The yield energy model has been applied to determine the extent of growth of damage zone around a wellbore and also estimate the mass of sand in the yielded zone. A field specific approach has been pursued by utilising results from the laboratory tests on representative samples (section 4.2) and field data as input parameters. Accordingly, the analysis was conducted on samples from Wells AFA, AFB, BFA, BFB and BFC which have available well test data. However, since the yield energy model is based on the assumption of a brittle failure mode, it is therefore not applicable to samples displaying ductile or transitional failure modes. Consequently, the model was only applied to samples displaying brittle failure mode from these wells.

The stability of a wellbore during drilling operation, with particular reference to the role of the drilling fluid in supporting the wellbore is first analysed by determining the appropriate weight of the drilling fluid required to prevent failure at the depth considered. The growth of the yielded zone during hydrocarbon production as a function of drawdown pressures and production rates for the individual wells and the associated mass of debris in the yield zone is then analysed. The mass of debris created during failure which is available for production as sand is calculated following the procedure and utilising the analytical equations detailed in section 6.4.

6.6.1 Wellbore Stability during Drilling Phase

Mechanical damage of the formation in all cases is an irreversible process, responsible for alteration of the stress distribution capacity of the rock surrounding a wellbore. Thus, prior to assessing the risk associated with wellbore stability and prediction the volume or mass of sand produced due to effect of hydrocarbon production, it is crucial to evaluate the extent of any related drilling damages. This is useful in evaluating any existing formation damage prior to production and also enables future drilling programs to be planned in order to minimise wellbore stability problems.

The mechanical properties derived for each sample were used in conjunction with the estimated stresses at each particular sample depth, and an estimate from well data of the pore pressure and mud weight in the yield zone equation, to generate the diameter of the yield zone around the wellbore for different mud weights. In the analysis, the extent of the yield zone is expressed as the ratio of the yield zone radius to the original wellbore radius. Thus, formation failure is indicated where this value is greater than 1 and stable conditions indicated by any value lower than 1.

Field A: The influence of range of drilling mud weights on stability of the wellbore for the reservoir samples from the three wells in Field A are plotted in Figure 6.4a and expressed in terms of the calculated normalised yield zone ratio. A thick broken line indicates the condition of incipient wellbore failure where this value is 1. It can be seen from Figure 6.4a that mud weight in excess of 1078.43 Kg/m^3 is required to prevent the development of yield zone during drilling of the Famgee horizon in wells AFA and AFB. The Deekay horizon on the other which is deeper require a higher mud weight of around 1198.26 Kg/m^3 to prevent development of a yield zone. It is evident that wellbore failure is unlikely to have occurred during drilling as the range of mud weight used in these wells as reported in the final well report is above the minimum calculated values to prevent yield. This analysis is supported by examination of calliper logs from these wells which do not show any sign of borehole enlargement. As a further check the critical wellbore pressure required to initiate tensile failure of the formation was also calculated. Mud weight in excess of 2995.66 Kg/m^3 would be required for the onset of such failure.

Field B: The relationship between mud weight and yield zone development for wells BFA and BFB and BFC are shown in Figure 6.4b. Based on this analysis, it was found that mud weight slightly greater than 1018.52 Kg/m^3 is required to ensure complete inhibition of yield even in the weakest samples tested in wells BFA and BFB and BFC.

Generally, a comparison of the calculated yield zone with the calliper logs and drilling observation indicate very good agreement. This validates the yield zone model and provides the confidence to carry on with further analysis.

6.6.2 Effect of Pressure Drawdown on Wellbore Stability and Mass of Sand (Debris) Created in the Yielded Zone

During production, the mud weight no longer reinforces the side of the wellbore, and the extent of the yield zone will increase. Since the effective stress depends on the pore pressure, the drawdown will also affect the extent of the yield zone. Therefore, the yield

zone dimension is calculated and plotted for a series of drawdown pressures and depletion conditions.

Field A: The effect of pressure drawdown arising from hydrocarbon production on wellbore stability for samples from wells AFA and AFB can be directly observe in Figure 6.5a. The analysis was conducted for an 8.5" diameter wellbore. It is unlikely that the formation will yield if production is maintained below drawdown pressure of 12 MPa for the brittle failed samples. The figure also indicates that brittle behaviour the Deekay horizon tends to require greater pressure drawdown than the Famgee horizon before failure occurs. This is generally consistent with the geomechanical appraisals that the Deekay horizon tends to be stiffer and slightly stronger than the Famgee horizon (see section 4.2). The apparent difference in the trends of the Deekay and the Famgee horizon also serves to show that mechanical responses are somewhat different between sandstones of different stratigraphic age; the Famgee horizon is Paleocene while the Deekay horizon is Jurassic. This implies that both horizons should be considered independently with respect to formation stability analysis. The influence of drawdown pressure and production rate on the extent of a yield zone around a wellbore and the associated mass of sand produced has been assessed.

Figure 6.5b shows the mass debris associated with yield zone as a function of drawdown pressure for the brittle failed samples. Debris created by comminution along shear failure surfaces will not be a problem until high drawdown of over 12 MPa are imposed. The analysis predicts that sample AFA-2 will produce the most amount of shear debris and that debris production will increase rapidly once the threshold drawdown pressure is attained. However, this is has been identified to be artefact arising because the sample is close to the brittle-ductile transition resulting in abnormally low critical energy release rate.

Field B: The effect of drawdown pressure on yield zone development for samples from Field B can be directly observed from Figure 6.6a. The first point to note from this figure is that even at zero drawdown, majority of the samples examined are in a state of yield particularly two of the three samples from well BFC. This implies that throughout the well testing period of Field B, yield has been ongoing. However, the growth of the yield zone is fairly stable below drawdown pressure of 6.9 MPa but rapidly increases as the drawdown pressure is increased beyond this point. The yield zone radius undergoes fairly similar changes for most of the samples with increasing drawdown. Well BFC displays the largest growth in the yield zone while well BFA shows the most limited

range of behaviour. This relationship is a reflection of the geomechanical characteristics of the samples, where samples from well BFC are the weakest and samples from well BFA the strongest in this field. The extension of the yield zone indicates the formation of an unstable region which is susceptible to be removed from the wellbore or perforation wall by fluid flow forces. This would consequently enlarge the wellbore and further increase the yield zone.

Figure 6.6b shows the mass of debris associated with the yield zone for the wells in Field B. This figure illustrates that samples from well BFC are prone to produce greater mass of debris and thus reiterating the fact that greater debris production has been reported in the well test report. Several samples from well BFB are also found to produce fairly high quantities of debris although the samples which produce the least is from this well. It is also quite interesting to note that samples from well BFA are closely bunched together and do not share the variability observed in samples from wells BFB and BFC.

6.6.3 Effect of Production Rate on Wellbore Stability and Mass of Sand (Debris) Created in the Yielded Zone

Production engineers tend to work with production rates rather than the actual drawdown pressures when determining the required hydrocarbon output from a well. The drawdown for a particular production rate is governed by the deliverability relationship and thus is an appropriate parameter to be used for comparing formation stability between different wells or the same well penetrating different reservoir horizons. Formation stability has been analysed as a function of production rates as related to the drawdown pressures using the deliverability relationship presented in section 6.5.1.4.

Field A: The effect of different production rates on yield zone development for the brittle sandstones is shown in Figure 6.7a. It can be observed that any increase in production rate above 2.1 x 10^6 sm^3/d for most of the Deekay samples would result in a drastic growth of the yield zone and the accompanying debris created increase at a much sharper rate with increase production rate. Production rate has a relatively subtle influence on the Famgee samples where most of the sample did not show any yield development even at 4.2 x 10^6 sm^3/d. This is quite contrary to the result from only considering the pressure drawdown. It can be clearly seen that the Deekay samples are predicted to fail before the 'weaker' Famgee samples. The main reason for this lies in the difference in deliverability expressions that are determined from well test data. Both Deekay horizons in wells AFA and AFB are characterised by high pressure drawdown at lower production rate compared to the Famgee horizon. Average permeabilities as obtained from the well

test data shows that the Deekay horizons are between 45 to 55 mD whereas the average permeability across the perforated interval in the Famgee horizon is 250 mD. The single Famgee sample from well AFB is also associated with a horizon with a low average permeability. This result highlights the importance of considering each horizon as an individual entity. The influence of production rate and indeed previous production history has an important implication regarding the completion and production strategy of a well intercepting more than on producing horizon. Whilst the Famgee horizon can sustain high production rates in excess of 4.2 x 10^6 sm^3/d, due to high deliverability at low drawdown, the Deekay horizon will have yielded at approximately half of this production rates. Thus if both horizons were to be produced together, the Deekay horizon would limit the production rates for the Famgee horizon. It would be desirable to develop or produce each horizon independently.

The mass of potential shear debris created for the samples predicted to fail in a brittle mode below the production rate of 4.2 x 10^6 sm^3/d is presented in Figure 6.7b. The analysis is conducted on the two samples predicted to fail in brittle manner (samples AFA-8 and AFB-2) which resulted in formation of yield zone up to maximum production rate of 4.2 x 10^6 sm^3/d. While sample AFB-2 produced relative amount of debris from around production rate of 3.6 x 10^6 sm^3/d, sample AFA-8 appears to produce excessive quantities of debris at a much lower rate, however, this has already been identified to be an artefact arising because the sample is close to the brittle-ductile transition resulting in abnormally low critical energy release rate.

Field B: The effect of production rate on yield zone development for samples from Field B can be seen in Figure 6.8. Increasing production rate from wells BFB and BFC is unlikely to create significant additional debris unless high flow rates are employed. The extent of the yield zone and mass of debris produced increases gradually at quite a low rate until production is increased to 2.8 x 10^6 sm^3/d. Production rate has relatively subtle influence for these wells particularly at lower production rates. However, due to the radically different IPR expression for well BFA, any increase in production rate above 2.1 x 10^6 sm^3/d would result in a drastic increase in the growth of the yield zone and the accompanying debris created as shown in Figure 6.8. This is of course due to the very different IPR expression for well BFA compared to the other two wells. These plots further highlight the potential error that could arise by assuming similar responses from all wells in the same formation. The form of the deliverability relationship is a significant

factor in determining the yield behaviour as production rates and reservoir pressures changes.

6.7 General Discussion

The yield energy model has been applied to predict the diameter of a yield zone, causing rock fragmentation and also quantify the mass of the sand produced. The quantification of the produced sand has been achieved by the subsequent application of a new approach (strain energy) to sand prediction, utilising a link between dissipation in strain energy as the rock yields and the resulting sand production. The onset of yield, sand production potential and the mass of sand produced depends on the effective stresses surrounding the wellbore and the failure criteria of rock material. Yield and fragmentation of the rock occur when the rock is exposed to stresses which exceed its failure criteria. This creates a yield zone and hence the potential for well instability and sand production. The greater the extent of the yield zone, i.e. the more damaged the rock is, the easier it will be to remove the material. The variation in wellbore diameter reflects the relative potential for the various rock types to create a yield zone. During the drilling phase, the extent of the yield zone can be limited by the pressure applied to the side of the wellbore. Hence the mud weight required to inhibit the formation of the yield can be determined from the modified yield zone equation. However, drawdown during production will reduce the pore pressure in the reservoir section, increasing the effective stress and hence also the size of the yield zone and the mass of failed sand. The ultimate extent of the yield zone and the mass of debris created for a given drawdown or production rate in a particular rock is therefore an indication of a potential for rock to produced sand.

Application of the yield energy model to reservoir sandstones predicts a substantial increase in the diameter of yield zone as drawdown pressure and production rate are increased, causing rock fragmentation and created sand debris. Consequently the mass of sand created is also increased since further creation of yield zone is accompanied by rock fragmentation. The magnitude of the drawdown pressure and the production rate on the extent of a yield zone around a wellbore and the associated mass of sand produced are related to the reservoir permeability and the completion height will result not only in different stability characteristics between wells but also different producing horizons within a single well. Drawdown at a particular production rate can also increase if the total skin (inertial, formation damage and other) effects increases. The rate of increase in drawdown with increasing production rate is much greater in low permeability horizons.

The effect of reservoir pressure on the yield zone and mass of sand debris is shown in Figure 6.9. As the reservoir pressure decreases yield and sand debris development are initiated at lower pressures because the effective stresses acting on the rock *in situ* are increased. The production rate is expected to be more important in determining the transport of the debris to the wellbore or surface since it will directly influence the viscous forces involved. It is evident from this study and other work that various other factors may also contribute significantly to the onset of formation failure and hence sand production. Some of these factors can be managed e.g. using production rate/drawdown, reservoir pressure to control the effective stress state. Others such as rock strength and cannot be easily controlled but an understanding of their influence on formation stability will aid in predicting the mass of failed sand using the yield energy model. The efficiency of a particular rock to produced debris during failure has been found to correlate with several rock properties such as porosity, uniaxial compressive strength and triaxial stress factor.

The above discussion has been conducted based on an analysis using values of rock strength determined in the laboratory on dry rocks. It is known, however, that the compressive strength of a water saturated samples may be reduced by up to one third (Colback and Wiid, 1975). It is strongly recommended that further research to determine the effect of fluid saturation on rock strength to be conducted.

The effect of quality of the core material cannot be discounted as an influence on the results. The eight pre-plugged samples supplied were of poor quality. It is possible that the extended cleaning required to remove the salt crystals, which had formed in the pore, spaces could have detrimental effect on the mechanical strength but it was not possible to qualify this assertion. The two samples plugged were of much better quality, however, the results do not appear to be anomalous when compared with the other eight samples.

The yield energy approach can only predict the volume of sand debris generated by shear failure of formation and assumes that all of the failed sand is produced. The actual volume of sand which is produced at the wellbore is determined by the flow of fluid through the damaged zone, particularly the effect of increase in viscous forces. Viscous forces induce tensile stresses in the zone of debris causing it to dilate (Perkins and Weingarten, 1988). At some stage this tensile stresses will be sufficient to overcome the cohesion due to the mechanical interaction of the sand particles and the debris will become fluidised, resulting in sand production in the wellbore. In the analysis above, it is assumed that all the sand in the yielded zone would be produced at the surface, however,

much work remains to be done to identify the parameters controlling such behaviour, particularly the dependence of the actual volume of debris produced in relation to fluid flow rate and whether there is a relationship with the extent of yield zone, volume of debris created and the volume of debris actually produced. In the case of multiple fractures, the development of a technique to determine and distribute the fracture surface energy is also necessary. If the effect of viscous force can be accounted for and combined with field observations, a mechanism would then exist to predict the mass or volume of sand produced and stability of the formation at a given production rate or drawdown.

The identification of the range of failure mode in different sandstones from laboratory tests and the requirement for input parameters indicates the importance of conducting a geomechanical appraisal as a first stage of any sand production prediction and wellbore stability study. It has been shown that both the failure mode and strength parameters of the sandstones are important factors in determining yield extent and consequently the mass of the sand in the yielded zone. In the laboratory tests, the effective stress on the rock sample governs failure; however, sample size, shape, saturation and initial defect may also influence failure. Loading conditions and lithology affect the processes of gouge grain breakage (Marone and Scholz, 1989).

Particle size distribution analysis of comminution debris has shown a relationship between failure mode and the weight percentage of comminution product of the various sandstones tested. It has been observed that a lesser weight of debris relative to the weight of the original sample is associated with brittle failure and the development of a through-going shear fractures compared to ductile and transitional failure modes. This result is probably related to the fact that grain fracture and comminution is localised to the shear fracture surfaces in the case of brittle failure whereas comminution is distributed throughout the sample in the case of ductile failure. This observation is consistent with the strain energy approach which predicted plastically failed samples to produce substantial amount of debris relative to brittle failed samples. Sand production resulting from brittle failure would come from localised shear failure surface rather than all the rock deforming plastically and been produced as sand. However, brittle failed samples have more concentration of finer particles probably due to frictional sliding. Grain comminution can have a first order control on frictional behaviour during granular shear, primarily due to changes in grain shape, size and size distribution (Marone and Scholz, 1989). A relationship also exists between stratigraphic age and debris production, particularly for the samples from wells AFA and AFB. The size distribution of the Famgee (Paleocene)

samples in the sub 90 μm comminuted fraction being monomodal whilst that for the Deekay (Jurassic) sandstones appears to be bimodal. These results could also be important in determining the optimum screen size for gravel packing. The particle size of comminuted sand has been found to reduce with increasing confining pressure. These results are consistent with earlier studies examining the relationship between confining stresses and particle size distribution (Engelder 1974, Anderson et al. 1980, 1983, Olgaard & Brace 1983, Sammis et al. 1986, 1987).

(a) Effect of mud weight on wellbore stability for brittle samples from wells AFA and AFB.

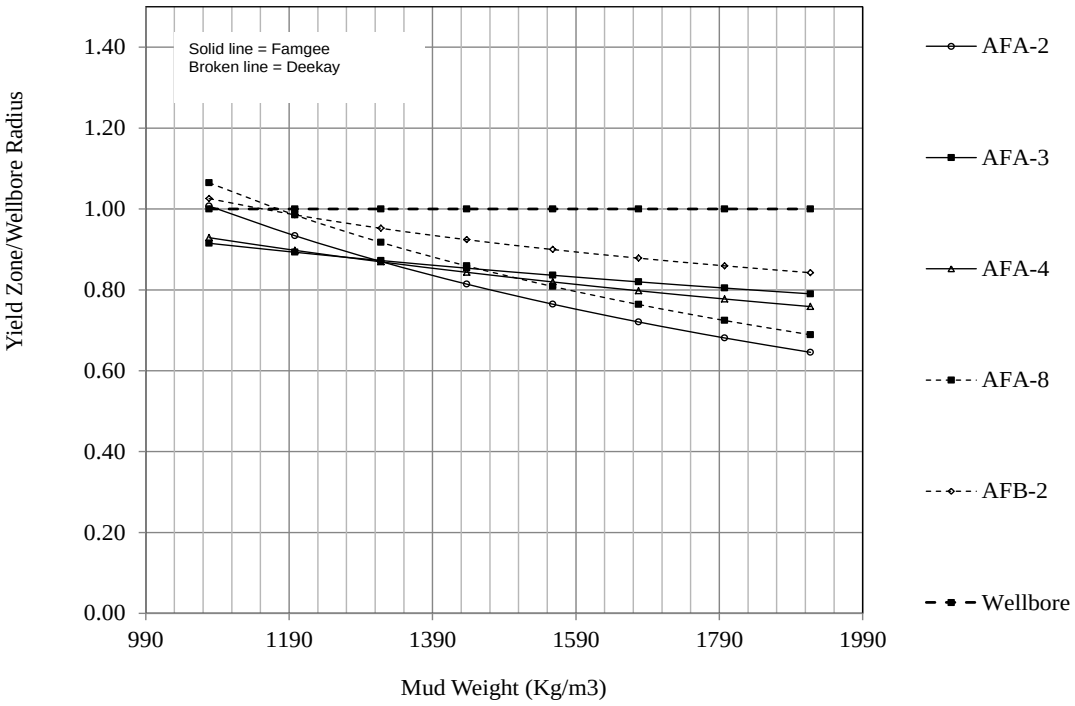

(b) Effect of mud weight on wellbore stability for brittle samples from wells BFA, BFB and BFC.

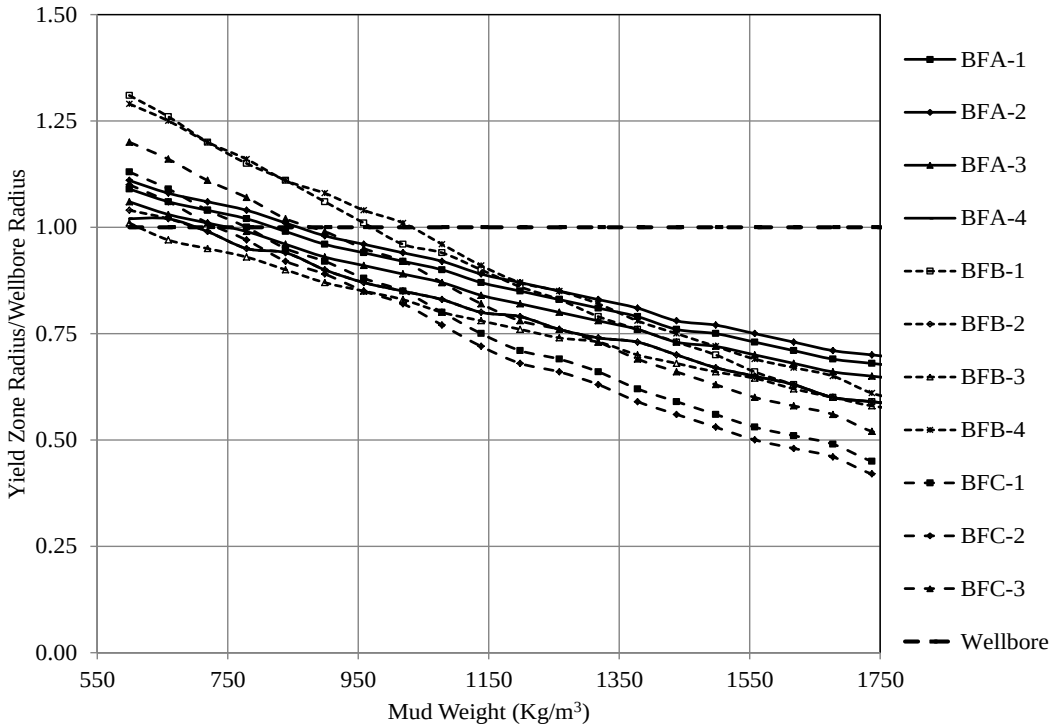

Figure 6.4: Effect of mud weight on development of yield zone.

(a) Effect of pressure drawdown on yield development for brittle sandstones from wells AFA and AFB.

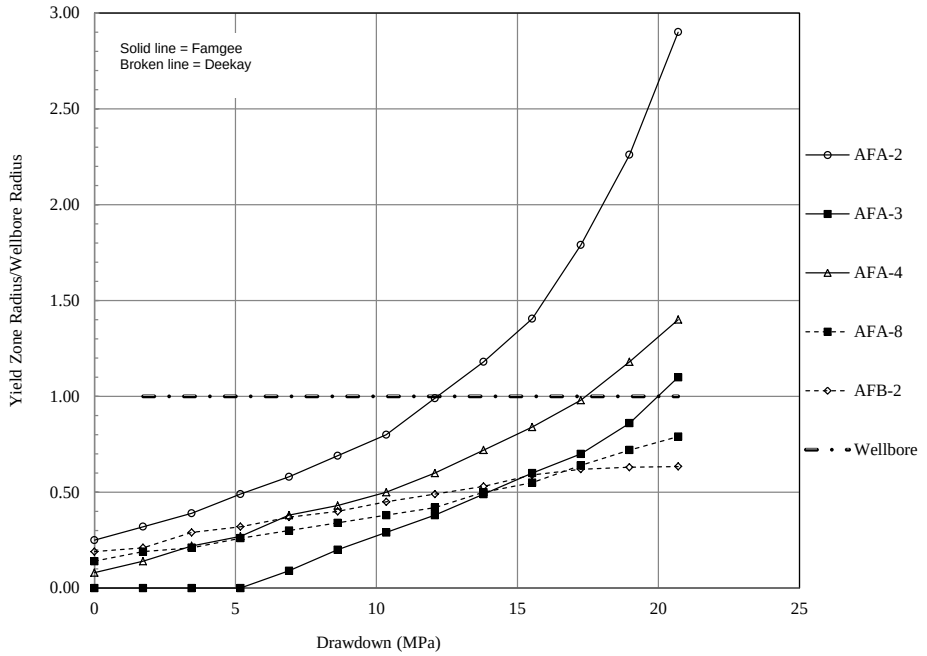

(b) Effect of pressure drawdown on mass of debris per foot depth associated with brittle/shear failure from wells AFA and AFB.

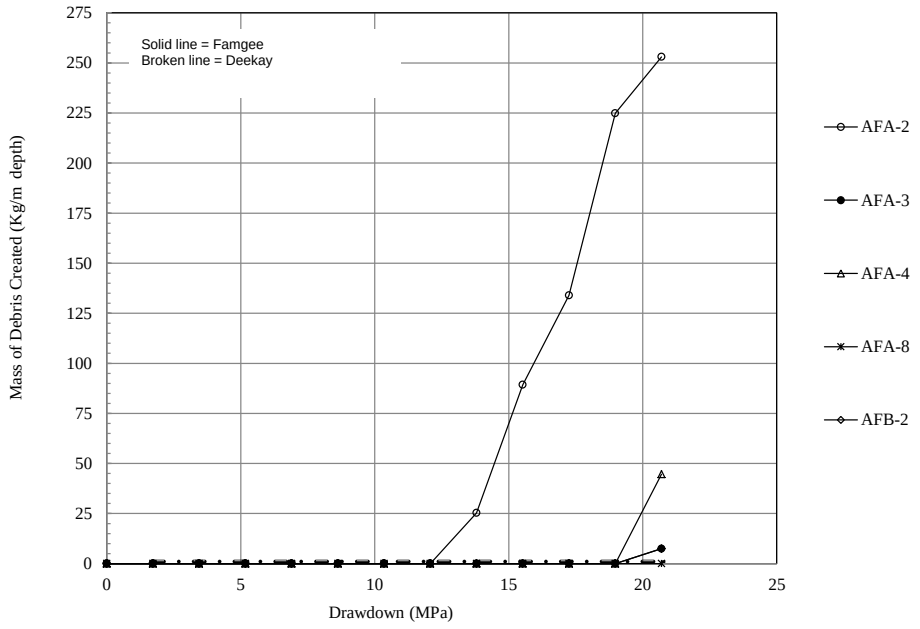

Figure 6.5: Effect of pressure drawdown on wellbore stability and mass of debris produced for samples from Field A.

(a) Effect of pressure drawdown on yield development for brittle sandstones from wells BFA, BFB and BFC.

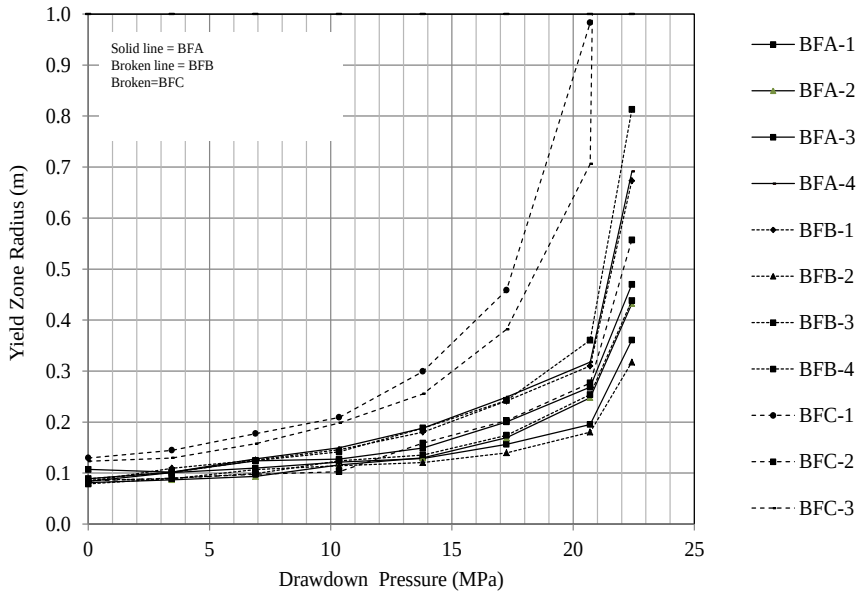

(b) Mass of debris per foot depth associated with brittle/shear failure as a function of drawdown from wells BFA, BFB and BFC.

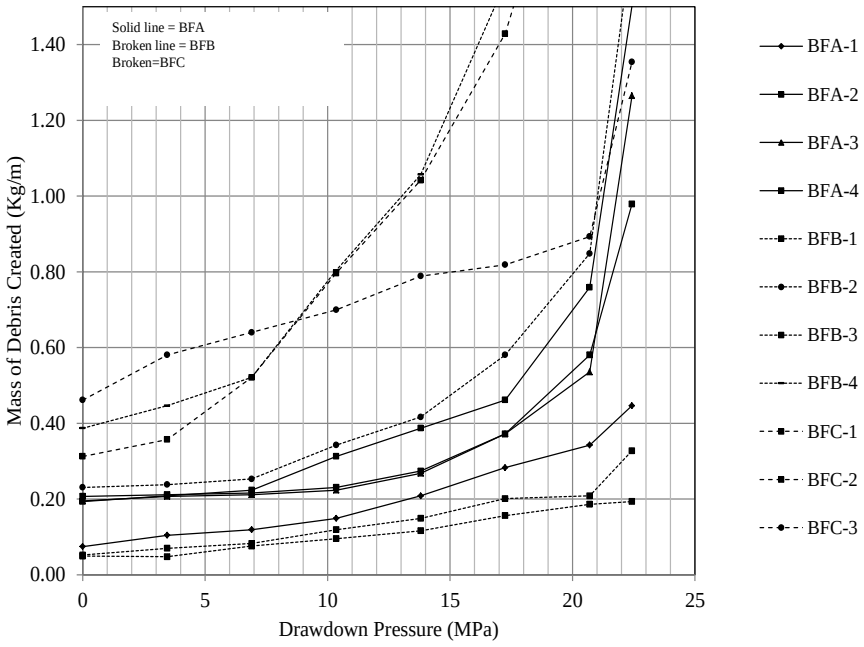

Figure 6.6: Effect of pressure drawdown on wellbore stability and mass of debris produced for samples from Field B.

(a) Effect of production rate on yield zone development failure on samples from wells AFA and AFB.

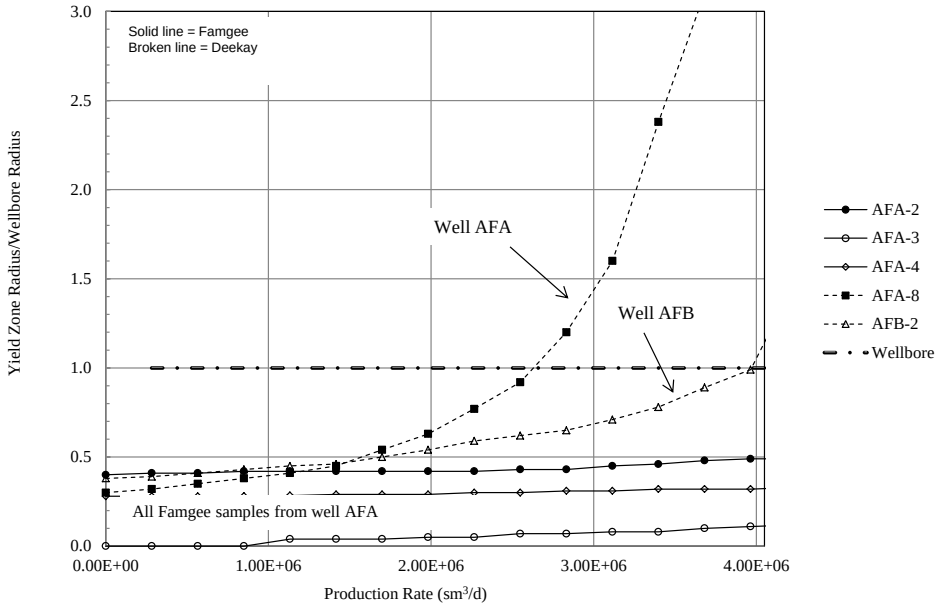

(b) Effect of production rate on mass of debris per foot depth associated with brittle/shear failure on samples from wells AFA and AFB.

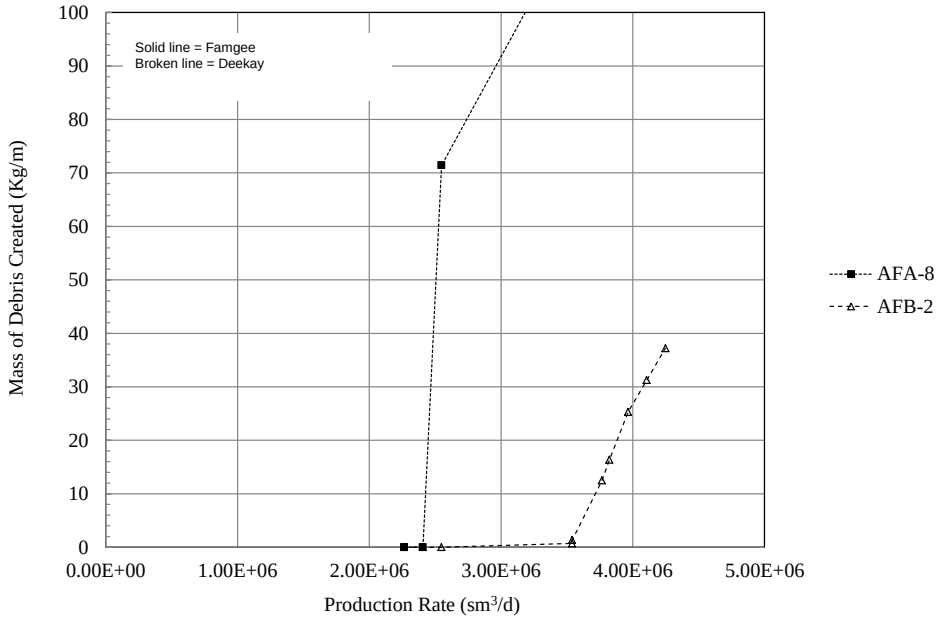

Figure 6.7: Effect of production rate on wellbore stability and mass of debris produced for samples from Field A.

(a) Effect of production rate on yield zone development failure on samples from wells BFA, BFB and BFC.

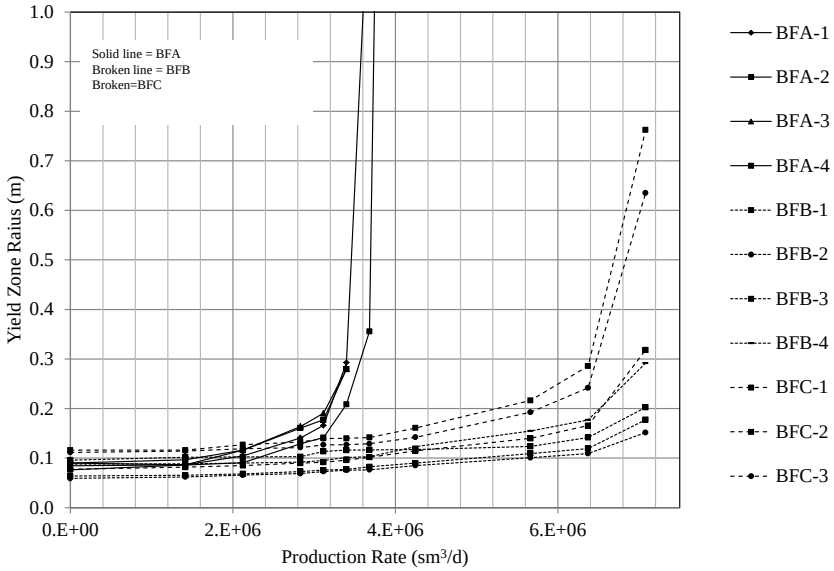

(b) Effect of production rate on mass of debris per foot depth associated with brittle/shear failure on samples from wells BFA, BFB and BFC.

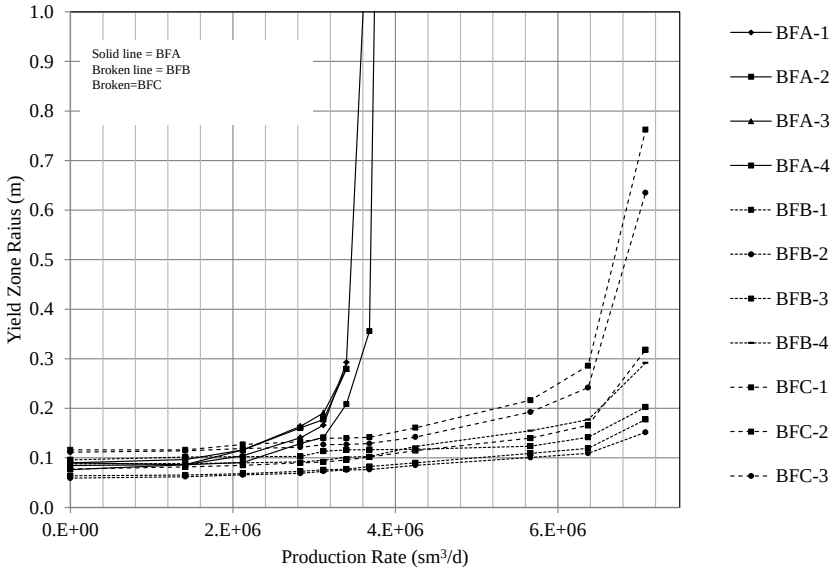

Figure 6.8: Effect of production rate on wellbore stability and mass of debris produced for samples from Field B.

(a) Effect of reservoir pressure at 3.45 MPa drawdown pressure on yield zone development failure on samples from wells BFA, BFB and BFC.

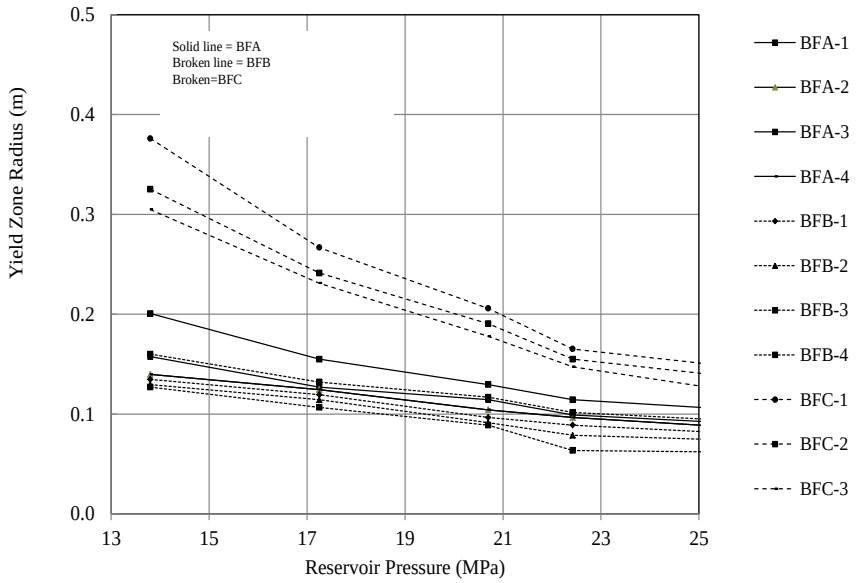

(b) Effect of reservoir pressure at 3.45 MPa drawdown pressure on mass of debris per foot depth associated with brittle/shear failure on samples from wells BFA, BFB and BFC.

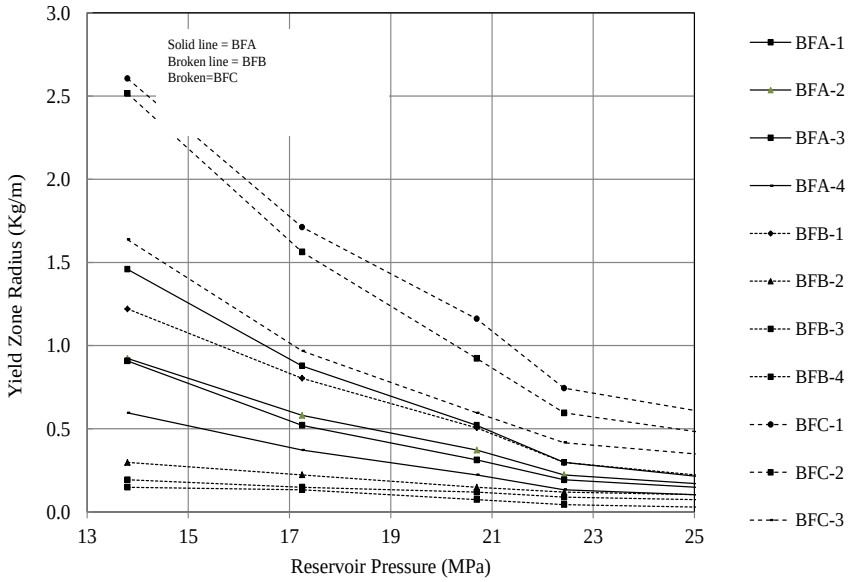

Figure 6.9: Effect of reservoir pressure on wellbore stability and mass of debris produced

7 Conclusions and Recommendations

7.1 Conclusions

The main objective of this research is to develop a new approach that would be able to predict the propensity of a formation to produce sand and also the mass of sand produced. As such laboratory tests were conducted on both reservoir and a range of analogue sandstones to derive input parameters in conducting the analysis. The key conclusions from this research are:

I. A new approach (yield energy model) for predicting the potential of sand production in a yielded zone by coupling the yield zone concept and the strain energy approach has been presented and applied to reservoir samples. The model uses an estimate of the strain energy dissipated in shear debris production as a means of assessing the sand production associated with broken rock inside the yield zone surround a wellbore. It is argued that the major source of sand production in competent rock is associated by the debris created by slippage along shear fractures in the yielded zone along perforation wall. Therefore, the model is only applicable to competent rock types that fail in brittle mode.

II. The development has also been employed to estimate the mass of sand generated between shear planes due to induced drawdown and production rate.

III. Both yield and sand volume development have been observed to be strongly dependent on rock strength, pressure drawdown and hydrocarbon production rates.

IV. An estimate of the critical drawdown or production rate that would result in yield development and the associated mass of sand produced can be determined using the model.

V. Inflow performance behaviour of not only individual wells but also each producing horizon is critical controls on sand production potential of a formation.

VI. The identification of a range of failure modes in the reservoir sandstones has emphasised the importance of conducting a geomechanical appraisal as a first stage of any formation stability and sand production prediction study.

VII. The particle size distribution of comminuted debris is influenced by initial mineralogical properties, particle size, sorting, confining pressure, and dominant failure mode. A lesser weight of fine relative to the weight of the original sample is associated with brittle failure and the development of through-going shear fractures compared to ductile and transitional failure modes. There is a systematic

change towards a greater volume of fraction of smaller particles with increasing confining pressure.

VIII. Fractal fragmentation theory has been used to quantify comminution shear debris from triaxial tests. The particle size distribution of comminution shear debris from the triaxial tests exhibit fractal behaviour. The derived empirical fractal dimension lies within the values of 2.15–2.63, consistent with previously published literature data.

7.2 Recommendations for Future Research

The following areas are recommended for further research:

I. Sand debris prediction based on the strain energy in this thesis focuses on a brittle failed sample with a single through-going fracture. The development of a technique to determine and distribute the fracture surface energy in the case of multiple fractures is recommended to extent the application of the model.

II. The yield energy approach can only predict the volume of debris generated by shear failure of formation. The actual volume of sand which is produced at the wellbore is determined by the flow of fluid through the damaged zone. Viscous forces induce tensile stresses in the zone of debris causing it to dilate (Perkins and Weingarten, 1988). At some stage this tensile stresses will be sufficient to overcome the cohesion due to the mechanical interaction of the sand particles and the debris will become fluidised, resulting in sand production in the wellbore. It is recommended that further work should be done to identify the parameters controlling such behaviour, the dependence of the actual volume of debris produced in relation to fluid flow rate and whether there is a relationship with the extent of yield zone, volume of debris created and the volume of debris actually produced.

III. The development of numerical code to produce continuous slip-weakening curve used in determination of the fracture surface energy should be developed. This would reduce an inherent error which exists in the determination of the area under the slip-weakening curve.

IV. Rock mechanical properties were determined from dry rock. However, it is known that fluid saturation can alter the strength of formation. Therefore, it is recommended that further research be conducted to determine the influenced of fluid saturation on yield zone development and associate mass of sand.

8 References

AADNØY, B. S. 1987. A complete elastic model for fluid-induced and in-situ generated stresses with the presence of a borehole. *Energy Sources,* 9**,** 239-259.

ABERCROMBIE, R. E. & RICE, J. R. 2005. Can observations of earthquake scaling constrain slip weakening? *Geophysical Journal International,* 162**,** 406-424.

ADDIS, M. A., GUNNINGHAM, M. C., BRASSART, P. C., WEBERS, J., SUBHI, H. & HOTHER, J. A. Sand Quantification: The Impact on Completion Design, Facilities Design, and Risk Evaluation. SPE Annual Technical Conference and Exhibition, 2008. Society of Petroleum Engineers.

ADEYANJU, O. A. & OYEKUNLE, L. O. 2011. Experimental Studies of Sand Production from Unconsolidated Sandstone Niger-Delta Petroleum Reservoir. *Nigeria Annual International Conference and Exhibition.* Abuja, Nigeria: Society of Petroleum Engineers.

AHMED, H. A. & DRZYMAŁA, J. 2005. Two-dimensional fractal linearization of distribution curves. *Physicochemical Problems of Mineral Processing,* 39**,** 129-139.

AKI, K. & RICHARDS, P. G. 1980. *Quantitative seismology,* San Francisco, W. H. Freeman & co.

AL-AJMI, A. M. & ZIMMERMAN, R. W. 2009. A new well path optimization model for increased mechanical borehole stability. *Journal of Petroleum Science and Engineering,* 69**,** 53-62.

AL-AWAD, M. N. & DESOUKY, S. E. M. 1997. Prediction of Sand Production from a Saudi Sandstone Reservoir. *Oil & Gas Science and Technology - Rev. IFP,* 52**,** 407-414.

AL-HINAI, S., FISHER, Q. J., AL-BUSAFI, B., GUISE, P. & GRATTONI, C. A. 2008. Laboratory measurements of the relative permeability of cataclastic fault rocks: An important consideration for production simulation modelling. *Marine and Petroleum Geology,* 25**,** 473-485.

ALLEN, T. 1975. *Particle size measurement,* London, Chapman and Hall.

AMEEN, M. S., SMART, B. G. D., SOMERVILLE, J. M., HAMMILTON, S. & NAJI, N. A. 2009. Predicting rock mechanical properties of carbonates from wireline logs (A case study: Arab-D reservoir, Ghawar field, Saudi Arabia). *Marine and Petroleum Geology,* 26**,** 430-444.

ANDERSON, J., L., OSBORNE, R. H. & PALMER, D. F. 1980. Petrogenesis of cataclastic rocks within the San Andreas fault zone of Southern California U.S.A. *Tectonophysics,* 67**,** 221-249.

ANDERSON, M. A. & JONES JR, F. O. 1985. A comparison of hydrostatic-stress and uniaxial-strain pore-volume compressibilities using nonlinear elastic theory. The 26th US Symposium on Rock Mechanics (USRMS). American Rock Mechanics Association.

ANDREWS, J. S., KJORHOLT, H. & JORANSON, H. Production enhancement from sand management philosophy. A Case Study from Statfjord and Gullfaks. SPE European Formation Damage Conference, 2005. Society of Petroleum Engineers.

ANTHEUNIS, D., VRIEZEN, P. B., SCHIPPER, B. A. & VAN DER VLIS, A. C. 1976a. Perforation Collapse: Failure of Perforated Friable Sandstones.

ANTHEUNIS, D., VRIEZEN, P. B., SCHIPPER, B. A. & VAN DER VLIS, A. C. 1976b. Perforation Collapse: Failure of Perforated Friable Sandstones. *SPE European Spring Meeting.* Amsterdam, Netherlands: 1976 Copyright 1976.

ANTONELLINI, M. A., AYDIN, A. & POLLARD, D. D. 1994. Microstructure of deformation bands in porous sandstones at Arches National Park, Utah. *Journal of Structural Geology,* 16**,** 941-959.

ARII, H., MORITA, N., ITO, Y. & TAKANO, E. 2005. Sand-Arch Strength Under Fluid Flow With and Without Capillary Pressure. *SPE Annual Technical Conference and Exhibition.* Dallas, Texas: Society of Petroleum Engineers.

ATKINSON, B. K. 1987. *Fracture Mechanics of Rock,* Academic Press, NY, 534p.

AYDIN, A. 1978. Small faults formed as deformation bands in sandstone. *pure and applied geophysics,* 116**,** 913-930.

AYDIN, A. & JOHNSON, A. 1978. Development of Faults as Zones of Deformation Bands and as Slip Surfaces in Sandstone. *In:* BYERLEE, J. & WYSS, M. (eds.) *Rock Friction and Earthquake Prediction.* Birkhäuser Basel.

BEELER, N. M., TULLIS, T. E., BLANPIED, M. L. & WEEKS, J. D. 1996. Frictional behavior of large displacement experimental faults. *Journal of Geophysical Research: Solid Earth,* 101**,** 8697-8715.

BEHRMANN, L. A., WILLSON, S. M., DE BREE, P. & PRESLES, C. 1993. Field Implications from Full-Scale Sand Production Experiments. *SPE Annual Technical Conference and Exhibition.* San Antonio, Texas.

BERG, R. R. 1986. *Reservoir Sandstones,* Prentice-Hall.

BÉSUELLE, P., BAUD, P. & WONG, T. 2003. Failure Mode and Spatial Distribution of Damage in Rothbach Sandstone in the Brittle-ductile Transition. *pure and applied geophysics,* 160**,** 851-868.

BÉSUELLE, P., DESRUES, J. & RAYNAUD, S. 2000. Experimental characterisation of the localisation phenomenon inside a Vosges sandstone in a triaxial cell. *International Journal of Rock Mechanics and Mining Sciences,* 37**,** 1223-1237.

BIEGEL, R. L., SAMMIS, C. G. & DIETERICH, J. H. 1989. The frictional properties of a simulated gouge having a fractal particle distribution. *Journal of Structural Geology,* 11**,** 827-846.

BIOT, M. A. 1941. General Theory of Three Dimensional Consolidation *J. Appl. Phys.,* 12**,** 155-164.

BIOT, M. A. 1956. Theory of propagation of elastic waves in a fluid-saturated porous solid. I. Low-frequency range. *The Journal of the Acoustical Society of America,* 28**,** 168-178.

BOS, B. & SPIERS, C. 2001. Experimental investigation into the microstructural and mechanical evolution of phyllosilicate-bearing fault rock under conditions favouring pressure solution. *Journal of Structural Geology,* 23**,** 1187-1202.

BRADLEY, W. B. 1978. *Failure of Inclined Boreholes.*

BRADY, B. H. G. & BROWN, E. T. 1985. *Rock mechanics: for underground mining,* London, George Allen & Unwin.

BRATLI, R. F., HORSRUD, P. & RISNES, R. 1983. ROCK MECHANICS APPLIED TO THE REGION NEAR A WELLBORE. Australian Geomechanical Society, Permission to Distribute - International Society for Rock Mechanics.

BRATLI, R. K. & RISNES, R. 1981. Stability and Failure of Sand Arches. *Society of Petroleum Engineers Journal,* 21**,** 236-248.

BROWN, E., BRAY, J. & SANTARELLI, F. 1989. Influence of stress-dependent elastic moduli on stresses and strains around axisymmetric boreholes. *Rock mechanics and rock engineering,* 22**,** 189-203.

BYERLEE, J. D. 1968. Brittle-ductile transition in rocks. *Journal of Geophysical Research,* 73**,** 4741-4750.

CARPINTERI, A., CHIAIA, B. & CORNETTI, P. 2003. On the mechanics of quasi-brittle materials with a fractal microstructure. *Engineering Fracture Mechanics,* 70**,** 2321-2349.

CARPINTERI, A. & PUGNO, N. 2002. A fractal comminution approach to evaluate the drilling energy dissipation. *International journal for numerical and analytical methods in geomechanics,* 26**,** 499-513.

CHARLEZ, P. A. 1991. *Rock Mechanics: Theoretical Fundamentals,* Atlasbooks Dist Serv.

CHENG, C., PENNINGTON, W. & PAILLET, F. 1992. Acoustic Waveform Logging-Advances in Theory and Application. Massachusetts Institute of Technology. Earth Resources Laboratory.

CHESTER, F. M. & LOGAN, J. M. 1987. Composite planar fabric of gouge from the Punchbowl Fault, California. *Journal of Structural Geology,* 9**,** 621-IN6.

CHIN, L. Y. & RAMOS, G. G. 2002. Predicting Volumetric Sand Production in Weak Reservoirs. *SPE/ISRM Rock Mechanics Conference*. Irving, Texas: Copyright 2002, Society of Petroleum Engineers Inc.

CLEARLY, M. P., MELVAN, J. J. & KOHLHAAS, C. A. 1979. The Effect of Confining Stress and Fluid Properties on Arch Stability in Unconsolidated Sand. *SPE Annual Technical Conference and Exhibition.* Las Vegas, Nevada: 1979 Copyright 1979 American institute of Mining, Metallurgical, and Petroleum Engineers Inc.

CLEARY, J. M. 1959. *Hydraulic Fracture Theory; Part III.-Elastic Properties of Sandstone*.

COATES, G. R. & DENOO, S. A. 1981. Mechanical Properties Program Using Borehole Analysis And Mohr's Circle.

COLBACK, P. & WIID, B. 1975. The influence of moisture content on the compressive strength of rocks. *Geophysics*.

COLLINS, P. M. Geomechanics And Wellbore Stability Design Of An Offshore Horizontal Well North Sea. SPE International Thermal Operations and Heavy Oil Symposium and International Horizontal Well Technology Conference, 2002. Society of Petroleum Engineers.

COOK, J. M., BRADFORD, I. D. R. & PLUMB, R. A. 1994. A Study of the Physical Mechanisms of Sanding and Application to Sand Production Prediction. *SPE European Petroleum Conference.* London, UK.

CRAWFORD, B. R. 1998. Experimental fault sealing: shear band permeability dependency on cataclastic fault gouge characteristics. *Geological Society, London, Special Publications,* 127**,** 27-47.

CRAWFORD, B. R., GOOCH, M. J. & WEBB, D. W. 2004. Textural Controls On Constitutive Behavior In Unconsolidated Sands: Micromechanics And Cap Plasticity. American Rock Mechanics Association.

CUI, L., AN, L. & GONG, W. 2006. Effects of process parameters on the comminution capability of high pressure water jet mill. *International Journal of Mineral Processing,* 81**,** 113-121.

DAKE, L. P. 1986. *Fundamentals of Reservoir Engineering,* Amsterdam, Elsevier.

DAVID, C., MENENDEZ, B., ZHU, W. & WONG, T. F. 2001. Mechanical compaction, microstructures and permeability evolution in sandstones. *Physics and Chemistry of the Earth, Part A: Solid Earth and Geodesy,* 26**,** 45-51.

DEERE, D. U. & MILLER, R. 1966. Engineering classification and index properties for intact rock. DTIC Document.

DETOURNAY, E. & ROEGIERS, J. C. 1986. Comment on "wellbore breakouts and in situ stress". *J. Geoghys, Res***,** 14161-1416.

DJAMARANI, K. M. & CLARK, I. M. 1997. Characterization of particle size based on fine and coarse fractions. *Powder Technology,* 93**,** 101-108.

DOEBELIN, E. O. 1990. *Measurement Systems: Application and Design*, McGraw-Hill.

DRUCKER, D. C., PRAGER, W., MATHEMATICS, B. U. D. O. A. & RESEARCH, U. S. O. O. N. 1951. *Soil Mechanics and Plastic Analysis Or Limit Design*, Division of Applied Mathematics, Brown University.

DUNN, D. E., LAFOUNTAIN, L. J. & JACKSON, R. E. 1973. Porosity dependence and mechanism of brittle fracture in sandstones. *Journal of Geophysical Research,* 78**,** 2403-2417.

DURRETT, J. L., GOLBIN, W. T., MURRAY, J. W. & TIGHE, R. E. 1977. Seeking a Solution to Sand Control.

DUSSEAULT, M. B. & SANTARELLI, F. J. 1989. A Conceptual Model For Massive Solids Production In Poorly-consolidated Sandstones. A.A. Balkema. Permission to Distribute - International Society for Rock Mechanics.

DYKE, C. & DOBEREINER, L. 1991. Evaluating the strength and deformability of sandstones. *Quarterly Journal of Engineering Geology and Hydrogeology,* 24**,** 123-134.

EDWARDS, D. P., SHARMA, Y. & CHARRON, A. Zones of Sand Production Identified by Log Derived Mechanical Properties: a Case Study. Proceedings SPWLA 8th European Formation Evaluation Symposium, 1983 London.

ENGELDER, J., LOGAN, J. & HANDIN, J. 1975. The sliding characteristics of sandstone on quartz fault-gouge. *pure and applied geophysics,* 113**,** 69-86.

ENGELDER, J. T. 1974. Cataclasis and the generation of fault gouge. *Geological Society of America Bulletin,* 85**,** 1515-1522.

EVANS, W. M. 1973. *A System for Combined Determination of Dynamic and Static Elastic Properties.* PhD, Univesrsity of Texas at Austin.

FAIRHURST, C. 1968. Methods of determining in-situ rock stresses at great depth. Missouri River Division, U.S. Army Corps of Engineers, School of Mineral and Matallurgical Engineering, University of Minnesota, Minneapolis.

FARQUHAR, R., SMART, B., TODD, A., TOMPKINS, D. & TWEEDIE, A. Stress sensitivity of low-permeability sandstones from the Rotliegendes sandstone. SPE Annual Technical Conference and Exhibition, 1993. Society of Petroleum Engineers.

FARQUHAR, R., SOMERVILLE, J. & SMART, B. Porosity as a geomechanical indicator: an application of core and log data and rock mechanics. European Petroleum Conference, 1994. Society of Petroleum Engineers.

FARQUHAR, R. A. 1993. *The Petro-mechanical Characterisation of the Rotliegendes Sandstones.* PhD, Heriot-Watt University.

FISHER, Q. J., CASEY, M., CLENNELL, M. B. & KNIPE, R. J. 1999. Mechanical compaction of deeply buried sandstones of the North Sea. *Marine and Petroleum Geology,* 16**,** 605-618.

FJÆR, E., HOLT, R. M., HORSRUD, P., RAAEN, A. M. & RISNES, R. 2008. Petroleum Related Rock Mechanics, 2nd Edition *In:* E. FJÆR, R. M. H. P. H. A. M. R. & RISNES, R. (eds.) *Developments in Petroleum Science.* Elsevier.

FJAER, E., HOLT, R. M., HORSRUD, P., RAAEN, A. M. & RISNES, R. 2008. *Petroleum Related Rock Mechanics, Amsterdam ; Boston, Elsevier.*

FOLK, R. L. & WARD, W. C. 1957. Brazos River bar: a study in the significance of grain size parameters. *Journal of Sedimentary Research,* 27.

FORTIN, J., STANCHITS, S., DRESEN, G. & GUÉGUEN, Y. 2006. Acoustic emission and velocities associated with the formation of compaction bands in sandstone. *Journal of Geophysical Research: Solid Earth, 111, B10203.*

FRANQUET, J. A. & ECONOMIDES, M. J. Effect of stress and stress path on Young's modulus and Poisson ratio of unconsolidated rocks: a new idea for hydraulic fracturing. Latin American and Caribbean Petroleum Engineering Conference, 1999. Society of Petroleum Engineers.

GEERTSMA, J. 1985. Some Rock-Mechanical Aspects of Oil and Gas Well Completions. Society of Petroleum Engineers Journal, 25, 848-856.

GEILIKMAN, M. & DUSSEAULT, M. 1997. Fluid rate enhancement from massive sand production in heavy-oil reservoirs. *Journal of Petroleum Science and Engineering, 17, 5-18.*

GHALAMBOR, A., HAYATDAVOUDI, A., ALCOCER, C. F. & KOLIBA, R. J. 1989. Predicting Sand Production in U.S. Gulf Coast Gas Wells Producing Free Water.

GRATON, L. C. & FRASER, H. 1935. Systematic packing of spheres: with particular relation to porosity and permeability. *The Journal of Geology***,** 785-909.

GRIFFITH, A. A. 1921. The Phenomena of Rupture and Flow in Solids. *Philosophical Transactions of the Royal Society of London. Series A, Containing Papers of a Mathematical or Physical Character,* 221**,** 163-198.

GRIFFITH, A. A. The theory of rupture. *In:* BIEZENO C. B., B. J. M. T. B. E. D., DELFT, NETHERLANDS), ed. Proceedings of First International Congress on Applied Mechanics, 1924 Delft, Netherlands. 55-63.

ROCK MECHANIC RESEARCH GROUP, 2005. The Determination of the Poro-Elastic Constnat for an Overpressured North Sea Sandstone.

GUATTERI, M., SPUDICH, P. & BEROZA, G. C. 2001. Inferring rate and state friction parameters from a rupture model of the 1995 Hyogo-ken Nanbu (Kobe) Japan earthquake. *Journal of Geophysical Research: Solid Earth,* 106**,** 26511-26521.

GUEGUEN, Y. & PALCIAUSKAS , V. 1994. *Introduction to the Physics of Rocks,* New Jersey, Princeton University Press.

GUPTA, A. & YAN, D. 2006. *Mineral Processing Design and Operation: An Introduction*, Elsevier Science.

HAIMSON, B. & CHANG, C. 2000. A new true triaxial cell for testing mechanical properties of rock, and its use to determine rock strength and deformability of Westerly granite. *International Journal of Rock Mechanics and Mining Sciences,* 37**,** 285-296.

HAIMSON, B. & RUDNICKI, J. W. 2010. The effect of the intermediate principal stress on fault formation and fault angle in siltstone. *Journal of Structural Geology,* 32**,** 1701-1711.

HALL, C. D. J. & HARRISBERGER, W. H. 1970. Stability of Sand Arches: A Key to Sand Control. *Society of Petroleum Engineers Journal,* 22**,** 821-829.

HANDIN, J., HAGER JR, R. V., FRIEDMAN, M. & FEATHER, J. N. 1963a. Experimental deformation of sedimentary rocks under confining pressure: pore pressure tests. *Aapg Bulletin,* 47**,** 717-755.

HANDIN, J., HAGER, R. V., FRIEDMAN, M. & FEATHER, J. N. 1963b. Experimental deformation of sedimentary rocks under confining pressure; pore pressure tests. *AAPG Bulletin,* 47**,** 717-755.

HAROUAKA, A., MTAWAA, B., AL-MAJED, A., ABDULRAHEEM, A. & KLIMENTOS, T. 1995. Multistage triaxial testing of actual reservoir cores under simulated reservoir conditions. *Soc. Of Core Analysts***,** 1-9.

HARRISON, J. P. & HUDSON, J. A. 2000. Engineering Rock Mechanics – An Introduction to the Principles, Elsevier Science.
HAWKES, I. & MELLOR, M. 1970. Uniaxial testing in rock mechanics laboratories. *Engineering Geology,* 4**,** 179-285.
HERDAN, G. 1960. *Small Particle Statistics,* London, Butterworths.
HILLIS, R. R. & NELSON, E. J. In situ stresses in the North Sea and their applications: Petroleum geomechanics from exploration to development. Geological Society, London, Petroleum Geology Conference series, 2005. Geological Society of London, 551-564.
HIRTH, G. & TULLIS, J. 1989. The effects of pressure and porosity on the micromechanics of the brittle-ductile transition in quartzite. *Journal of Geophysical Research: Solid Earth,* 94**,** 17825-17838.
HOEK, E. & BROWN, E. T. 1980. *Underground Excavations in Rock,* Institution of Mining and Metallurgy.
HOLT, R. M. 1990. Permeability reduction induced by a nonhydrostatic stress field. *SPE Formation Evaluation,* 5**,** 444-448.
HOLT, R. M., BRIGNOLI, M. & KENTER, C. J. 2000. Core quality: quantification of coring-induced rock alteration. International Journal of Rock Mechanics and Mining Sciences, 37, 889-907.
HOLT, R. M. & KENTER, C. J. Laboratory simulation of core damage induced by stress release. The 33th US Symposium on Rock Mechanics (USRMS), 1992. American Rock Mechanics Association.
HOLT, R. M. & FJAER, E. 1991. Validity of Multiple Failure State Triaxial Tests In Sandstones. A.A. Balkema. Permission to Distribute - International Society for Rock Mechanics.
HOLT, R. M., INGSOY, P. & MIKKELSON, M. 1989. Rock Mechanical Analysis of North Sea Reservoir Formations. *SPE Formation Evaluation,* 4**,** 33-37.
HOSHINO, K. & CHOSAJO, N. C. 1972. *Mechanical Properties of Japanese Tertiary Sedimentary Rocks Under High Confining Pressures,* Geological Survey of Japan.
HUDSON, J. A. & COOLING, C. M. 1988. In Situ rock stresses and their measurement in the U.K.—Part I. The current state of knowledge. *International Journal of Rock Mechanics and Mining Sciences & Geomechanics Abstracts,* 25**,** 363-370.
HUTCHEON, R., SOMERVILLE, J. & SMART, B. 2001. Influence of driving stress on cataclastic deformation and permeability in well cemented sandstones. *Physics and Chemistry of the Earth, Part A: Solid Earth and Geodesy,* 26**,** 39-43.
IRWIN, G. R. 1958. Fracture. *In:* FLUGGE, S. (ed.) *Encyclopedia of Physics.* Berlin: Springer- Verlag.
JAEGER, J. C., COOK, N. G. W. & ZIMMERMAN, R. 2007. *Fundamentals of Rock Mechanics,* Wiley.
JAMISON, W. R. & STEARNS, D. W. 1982. Tectonic deformation of Wingate Sandstone, Colorado National Monument. *AAPG Bulletin,* 66**,** 2584-2608.
JONES, M. E. 1987. *Reservoir compaction and surface subsidence due to hydrocarbon extraction,* H.M.S.O., London.
KAARSTAD, E. & AADNOY, B. S. Optimization of borehole stability using 3-D stress optimization. SPE Annual Technical Conference and Exhibition, 2005. Society of Petroleum Engineers.
KESSLER, N., WANG, Y. & SANTARELLI, F. J. 1993. A Simplified Pseudo 3D Model To Evaluate Sand Production Risk in Deviated Cased Holes. *SPE Annual*

Technical Conference and Exhibition. Houston, Texas: 1993 Copyright 1993, Society of Petroleum Engineers, Inc.

KHAKSAR, A., RAHMAN, K., GHANI, J. & MANGOR, H. 2008. Integrated Geomechanical Study for Hole Stability, Sanding Potential and Completion Selection: A Case Study from South East Asia. *SPE Annual Technical Conference and Exhibition.* Denver, Colorado, USA: Society of Petroleum Engineers.

KOOIJMAN, A., VAN DEN ELZEN, M. & VEEKEN, C. Hollow-Cylinder Collapse: Measurement of Deformation And Failure In an X-Ray CT Scanner Observation of Size Effect. The 32nd US Symposium on Rock Mechanics (USRMS), 1991 Norman, Oklahoma. American Rock Mechanics Association.

KOOIJMAN, A. P., HALLECK, P. M., DE BREE, P., VEEKEN, C. A. M. & KENTER, C. J. 1992. Large-Scale Laboratory Sand Production Test. *SPE Annual Technical Conference and Exhibition.* Washington, D.C.: 1992 Copyright 1992, Society of Petroleum Engineers Inc.

KOVARI, K. & TISA, A. 1975. Multiple failure state and strain controlled triaxial tests. *Rock mechanics,* 7**,** 17-33.

LAMBE, T. W. & WHITMAN, R. V. 1969. *Soil Mechanics,* Wiley.

LAWN, B. R. 1993. *Fracture of brittle solids,* Cambridge university press.

LOVELL, J. P. B. 1983. Permian and Triassic. *In:* CRAIG, G. Y. (ed.) *Geology of Scotland.* 2nd ed. Edinburgh: Scottish Academic Press.

LOWDEN, B., BRALEY, S., HURST, A. & LEWIS, J. 1992. Sedimentological studies of the Cretaceous Lochaline Sandstone, NW Scotland. *Geological Society, London, Special Publications,* 62**,** 159-162.

LU, P., JEFFERSON, I., ROSENBAUM, M. & SMALLEY, I. 2003. Fractal characteristics of loess formation: evidence from laboratory experiments. *Engineering geology,* 69**,** 287-293.

MAIR, K., MAIN, I. & ELPHICK, S. 2000. Sequential growth of deformation bands in the laboratory. *Journal of Structural Geology,* 22**,** 25-42.

MAIR, K. & MARONE, C. 1999. Friction of simulated fault gouge for a wide range of velocities and normal stresses. *Journal of Geophysical Research: Solid Earth (1978–2012),* 104**,** 28899-28914.

MAIR K., ELPHICK S.C. & I.G., M. 2002. Influence of confining pressure on the mechanical and structural evolution of laboratory deformation band. *Geophysical Research Letters,* 29:10.1029/2001GL013964.

MANDELBROT, B. B. 1983. The fractal geometry of nature/Revised and enlarged edition. *New York, WH Freeman and Co., 1983, 495 p.,* 1.

MARONE, C. 1991. A note on the stress-dilatancy relation for simulated fault gouge. *pure and applied geophysics,* 137**,** 409-419.

MARONE, C., RALEIGH, C. B. & SCHOLZ, C. 1990. Frictional behavior and constitutive modeling of simulated fault gouge. *Journal of Geophysical Research: Solid Earth (1978–2012),* 95**,** 7007-7025.

MARONE, C. & SCHOLZ, C. 1989. Particle-size distribution and microstructures within simulated fault gouge. *Journal of Structural Geology,* 11**,** 799-814.

MCLEAN, M. R. & ADDIS, M. A. 1990. Wellbore Stability Analysis: A Review of Current Methods of Analysis and Their Field Application. *SPE/IADC Drilling Conference.* Houston, Texas: 1990 Copyright 1990, IADC/SPE Drilling Conference.

MECHANICS, I. S. O. R. 1983. Suggested methods for determining the strength of rock materials in triaxial compression: Revised version. *International Journal of Rock Mechanics and Mining Sciences & Geomechanics Abstracts.*

MOGI, K. 1971. Effect of the triaxial stress system on the failure of dolomite and limestone. *Tectonophysics,* 11**,** 111-127.

MORITA, N. 2004. Well Orientation Effect on Borehole Stability. *SPE Annual Technical Conference and Exhibition.* Houston, Texas: Society of Petroleum Engineers.

MORITA, N. & FUH, G. F. 1998. Prediction of Sand Problems of a Horizontal Well from Sand Production Histories of Perforated Cased Wells. *SPE annual Technical Conference and Exhibition.* New Orleans, Louisiana.

MORITA, N., GRAY, K., SROUJI, F. A. & JOGI, P. 1992. Rock-property changes during reservoir compaction. *SPE formation evaluation,* 7**,** 197-205.

MORITA, N., WHITFILL, D. L., FEDDE, O. P. & LEVIK, T. H. 1989a. Parametric Study of Sand-Production Prediction: Analytical Approach. *SPE Production Engineering,* 4**,** 25-33.

MORITA, N., WHITFILL, D. L., MASSIE, I. & KNUDSEN, T. W. 1989b. Realistic Sand-Production Prediction: Numerical Approach. *SPE Production Engineering,* 4**,** 15-24.

MORROW, C. A. & BYERLEE, J. D. 1989. Experimental studies of compaction and dilatancy during frictional sliding on faults containing gouge. *Journal of Structural Geology,* 11**,** 815-825.

MURRELL, S. A. F. 1958. *The strength of coal under triaxial compression,* London, Buterworths.

NGWENYA, B. T., KWON, O., ELPHICK, S. C. & MAIN, I. G. 2003. Permeability evolution during progressive development of deformation bands in porous sandstones. *Journal of Geophysical Research: Solid Earth,* 108**,** 2343.

NGWENYA, B. T., SHIMMIELD, G. B. & ELPHICK, S. C. 1993. Novel Approach to Testing Core Samples at Reservoir Conditions. *PROCEEDINGS- SOCIETY OF CORE ANALYSTS; SCA-9325 Annual technical conference*

NORDGREN, R. P. 1977. Strength Of Well Completions. Colorado School of Mines Press. Permission to Distribute - American Rock Mechanics Association.

NOURI, A., KURU, E. & VAZIRI, H. 2009. Elastoplastic Modelling of Sand Production Using Fracture Energy Regularization Method. *Journal of Canadian Petroleum Technology,* 48**,** 64-71.

NOURI, A., VAZIRI, H., KURU, E. & ISLAM, R. 2006a. A comparison of two sanding criteria in physical and numerical modeling of sand production. *Journal of Petroleum Science and Engineering,* 50**,** 55-70.

NOURI, A., VAZIRI, H. H., BELHAJ, H. A. & ISLAM, M. R. 2006b. Sand-Production Prediction: A New Set of Criteria for Modeling Based on Large-Scale Transient Experiments and Numerical Investigation. *SPE Journal,* 11**,** pp. 227-237.

NUR, A. & BYERLEE, J. D. 1971. An exact effective stress law for elastic deformation of rock with fluids. *J. Geophys. Res.,* 76**,** 6414-6419.

OBERT, L. & DUVALL, W. I. 1967. *Rock mechanics and the design of structures in rock,* Wiley.

OJALA, I. O., NGWENYA, B. T. & MAIN, I. G. 2004. Loading rate dependence of permeability evolution in porous aeolian sandstones. *Journal of Geophysical Research: Solid Earth (1978–2012),* 109.

OKUBO, P. G. & DIETERICH, J. H. 1984. Effects of physical fault properties on frictional instabilities produced on simulated faults. *Journal of Geophysical Research: Solid Earth,* 89**,** 5817-5827.

OLGAARD, D. L. & BRACE, W. F. 1983. The microstructure of gouge from a mining-induced seismic shear zone. *International Journal of Rock Mechanics and Mining Sciences & Geomechanics Abstracts,* 20**,** 11-19.

PALMER, I. D., HIGGS, N., ISPAS, I., BAKSH, K. & KRIEGER, K. D. 2006. Prediction of Sanding Using Oriented Perforations in a Deviated Well, and Validation in the Field. *International Symposium and Exhibition on Formation Damage Control.* Lafayette, Louisiana U.S.A.: Society of Petroleum Engineers.

PALMER, I. D., HIGGS, N. G., MATHERS, R. M. & HERMAN, S. R. 2008. Sanding Study for Deepwater Indonesia Development Wells: A Case History of Prediction and Production. *SPE International Symposium and Exhibition on Formation Damage Control.* Lafayette, Louisiana, USA: Society of Petroleum Engineers.

PAPAMICHOS, E. 2002. Sand Mass Prediction in a North Sea Reservoir. *SPE/ISRM Rock Mechanics Conference.* Irving, Texas: 2002,. Society of Petroleum Engineers Inc.

PAPAMICHOS, E. & MALMANGER, E. M. 1998. A Sand Erosion Model for Volumetric Sand Predictions in a North Sea Reservoir. *Latin American and Caribbean Petroleum Engineering Conference.* Caracas, Venezuela: Society of Petroleum Engineers.

PAPAMICHOS, E., SKJÆRSTEIN, A. & TRONVOLL, J. A volumetric sand production experiment. 4th North American Rock Mechanics Symposium, 2000. American Rock Mechanics Association.

PAPAMICHOS, E. & STAVROPOULOU, M. An erosion-mechanical model for sand production rate prediction. International Journal of Rock Mechanics and Mining Science & Geomechanics Abstracts, 1996. 531-532.

PAPAMICHOS, E., STENEBRÅTEN, J., & CASTRO, G. C. D. 2008. Rock type and hole failure pattern effects on sand production. American Rock Mechanics Association.

PAPAMICHOS, E., VARDOULAKIS, I. & SULEM, J. 1994. Generalized continuum models for borehole stability analysis.

PASLEY, P. R. & J.B.CHEATHAM 1963. Rock Stresses Induced by Flow of Fluids into Boreholes. *Soc. Pet. Eng.* , 1**,** 85.89.

PATERSON, M. & WONG, T.-F. 2005. *Experimental Rock Deformation – The Brittle Field, 2nd edition*, Springer-Verlag.

PEDEN, J. M. & YASSIN, A. A. M. 1986. The Determination of Optimum Completion and Production Conditions for Sand-Free Oil Production. *SPE Annual Technical Conference and Exhibition.* New Orleans, Louisiana: 1986 Copyright 1986, Society of Petroleum Engineers, Inc. This paper was prepared for presentation at the 61st Annual Technical Conference and Exhibition of the Society of Petroleum Engineers held in New Orleans, Louisiana, U.S.A., October 5-8.

PERKINS, T. K. & WEINGARTEN, J. S. 1988. Stability and Failure of Spherical Cavities in Unconsolidated Sand and Weakly Consolidated Rock. *SPE Annual Technical Conference and Exhibition.* Houston, Texas: 1988 Copyright 1988, Society of Petroleum Engineers.

PETTIJOHN, F. J. 1987. *Sand and sandstone*, Springer.

PLUMB, R. A. 1994. Influence of composition and texture on the failure properties of clastic rocks. *Rock Mechanics in Petroleum Engineering.* Delft, Netherlands: Society of Petroleum Engineers.

PRESLES, C. & CREUSOT, M. 1997. A Sand Failure Test Can Cut Both Completion Costs And The Number Of Developement Wells. *SPE European Formation Damage Conference.* The Haque, The Netherlands.

RANJITH, P. G., PERERA, M. S. A., PERERA, W. K. G., WU, B. & CHOI, S. K. 2013. Effective parameters for sand production in unconsolidated formations:

An experimental study. *Journal of Petroleum Science and Engineering,* 105**,** 34-42.

RAWLING, G. C. & GOODWIN, L. B. 2003. Cataclasis and particulate flow in faulted, poorly lithified sediments. *Journal of Structural Geology,* 25**,** 317-331.

READ, R. S. 2004. 20 years of excavation response studies at AECL's Underground Research Laboratory. *International Journal of Rock Mechanics and Mining Sciences,* 41**,** 1251-1275.

RICE, J. R. 1968. A Path Independent Integral and the Approximate Analysis of Strain Concentration by Notches and Cracks. *Journal of Applied Mechanics,* 35**,** 379-386.

RICE, J. R. The mechanics of earthquake rupture. *In:* DZIEWONSKI, A. M. & BOSCHI, E., eds. Physics of the Earth's Interior, 1980. 555-649.

RICE, J. R. Shear instability in relation to the constitutive description of fault slip. *In:* GAY, N. C. & WAINWRIGHT, E. H., eds. Rockburst and Seismicity in Mines, 1984 S. African Institute of Mining and Metallurgy, Johannesburgh. 57-62.

RICE, J. R., SAMMIS, C. G. & PARSONS, R. 2005. Off-Fault Secondary Failure Induced by a Dynamic Slip Pulse. *Bulletin of the Seismological Society of America,* 95**,** 109-134.

RIJKEN, M. C. M., CAMERON, J. A., JONES, C., EL-FAYOUMI, A. M. & RAY, P. Estimating Sand Production Volume in Oil and Gas Reservoir. SPE Annual Technical Conference and Exhibition, 2014. Society of Petroleum Engineers.

RISNES, R., BRATLI, R. & HORSRUD, P. 1982a. Sand Arching - A Case Study. *European Petroleum Conference.* London, United Kingdom: 1982.

RISNES, R., BRATLI, R. K. & HORSRUD, P. 1982b. Sand Stresses Around a Wellbore. *Society of Petroleum Engineers Journal,* 22**,** 883-898.

ROSIN, P. & RAMMLER, E. 1933. The laws governing the fineness of powdered coal. *Journal of the Institute of Fuel,* 7**,** 29-36.

RUDNICKI, J. W. 1980. Fracture Mechanics Applied to the Earth's Crust. *Annual Review of Earth and Planetary Sciences,* 8**,** 489-525.

RUSSELL, K., AYAN, C., HART, N., RODRIGUEZ, J., SCHOLEY, H., SUGDEN, C. & DAVIDSON, J. Predicting and preventing wellbore instability using the latest drilling and logging technologies: Tullich Field Development, North Sea. SPE annual technical conference and exhibition, 2003. Society of Petroleum Engineers.

RUSSELL, K. A., AYAN, C., HART, N., RODRIGUEZ, J., SCHOLEY, H., SUGDEN, C. E. & DAVIDSON, J. K. 2006. Predicting and Preventing Wellbore Instability: Tullich Field Development North Sea. *SPE Drilling & Completion,* 21**,** 12-22.

SAMMIS, C., KING, G. & BIEGEL, R. 1987. The kinematics of gouge deformation. *pure and applied geophysics,* 125**,** 777-812.

SAMMIS, C. G. & ASHBY, M. F. 1986. The failure of brittle porous solids under compressive stress states. *Acta Metallurgica,* 34**,** 511-526.

SAMMIS, C. G. & OSBORNE, R. H. 1982. Textural and petrographic modal analysis of gouge from a depth of 165 m in the San Andreas fault zone. *EOS,* 63.

SAMMIS, C. G., OSBORNE, R. H., ANDERSON, J. L., BANERDT, M. & WHITE, P. 1986. Self-similar cataclasis in the formation of fault gouge. *pure and applied geophysics,* 124**,** 53-78.

SANFILIPPO, F., BRIGNOLI, M., GIACCA, D. & SANTARELLI, F. J. 1997. Sand Production: From Prediction to Management. *SPE European Formation Damage Conference.* The Hague, Netherlands: 1997 Copyright 1997, Society of Petroleum Engineers, Inc.

SANFILIPPO, F., RIPA, G., BRIGNOLI, M. & SANTARELLI, F. J. 1995. Economical Management of Sand Production by a Methodology Validated on an Extensive Database of Field Data. *SPE Annual Technical Conference and Exhibition.* Dallas, Texas: 1995 Copyright 1995, Society of Petroleum Engineers, Inc.

SANTARELLI, F. J. & BROWN, E. T. 1989. Failure of three sedimentary rocks in triaxial and hollow cylinder compression tests. *International Journal of Rock Mechanics and Mining Sciences & Geomechanics Abstracts,* 26**,** 401-413.

SANTARELLI, F. J., BROWN, E. T. & MAURY, V. 1986. Analysis of Borehole stresses using pressure-dependent, linear elasticity. *International Journal of Rock Mechanics and Mining Sciences & Geomechanics Abstracts,* 23**,** 445-449.

SANTARELLI, F. & DUSSEAULT, M. Core quality control in petroleum engineering. The 32nd US Symposium on Rock Mechanics (USRMS), 1991. American Rock Mechanics Association.

SATTLER, A. R. 1989. Core analysis in a low permeability sandstone reservoir: Results from the Multiwell Experiment. *a report by Sandia National Laboratories for The Department of Energy*.

SCHUHMANN, R., JR 1940. Principles of Comminution, 1 — size distribution and surface calculation. *Tech. Pub. AIME No. 1189*

SCOTT, T. E. & NIELSEN, K. C. 1991. The effects of porosity on the brittle-ductile transition in sandstones. *Journal of Geophysical Research: Solid Earth,* 96**,** 405-414.

SENSENY, P. Laboratory measurements of mechanical properties of sandstones and shales. SPE/DOE Low Permeability Gas Reservoirs Symposium, 1983a. Society of Petroleum Engineers.

SENSENY, P. E. 1983b. Laboratory Measurements of Mechanical Properties of Sandstones and Shales. *SPE/DOE Low Permeability Gas Reservoirs Symposium.* Denver, Colorado: 1983.

SHELL 1993. Rock Mechanics Manual. Shell Research B.V.

SHIMAMOTO, T. & LOGAN, J. M. 1981. Effects of simulated clay gouges on the sliding behavior of Tennessee sandston. *Tectonophysics,* 75**,** 243-255.

SKEMPTON, A. W. Effective stress in Soils, Concrete and Rocks. Conference on Pore Pressure and Suction in Soils, 30-31 March 1961 London. Butterworths.

SKOPEC, R. In-Situ Stress Evaluation in Core Analysis. paper SCA-9103 presented at the 1991 SCA Technical Conference, Houston, 1991. 21-22.

SMART, B. G. D. & CRAWFORD, B. R. 1990. An Investigation of Shear Debris Comminution As a Mechanism of Strain Energy Release For Frictional Sliding On Dominant Parting Planes. A.A. Balkema. Permission to Distribute - International Society for Rock Mechanics.

SOMERVILLE, J. M. & SMART, B. G. D. 1991. The Prediction of Well Stability Using the Yield Zone Concept. *Offshore Europe.* Aberdeen, United Kingdom: 1991 Copyright 1991, Society of Petroleum Engineers, Inc.

STEIN, N. 1976. Mechanical Properties of Friable Sands From Conventional Log Data (includes associated papers 6426 and 6427). *SPE Journal of Petroleum Technology,* 28**,** 757-763.

STEIN, N. & HILCHIE, D. W. 1972. Estimating the Maximum Production Rate Possible from Friable Sandstones Without Using Sand Control. *SPE Journal of Petroleum Technology,* 24**,** 1157-1160.

STEIN, N., ODEH, A. S. & JONES, L. G. 1974. Estimating Maximum Sand-Free Production Rates From Friable Sands for Different Well Completion Geometries. *SPE Journal of Petroleum Technology,* 26**,** 1156-1158.

TAŞDEMIR, A. 2009. Fractal evaluation of particle size distributions of chromites in different comminution environments. *Minerals Engineering,* 22**,** 156-167.
TAŞDEMIR, A. & TAŞDEMIR, T. 2009. A Comparative Study on PSD Models for Chromite Ores Comminuted by Different Devices. *Particle & Particle Systems Characterization,* 26**,** 69-79.
TAYLOR, B. J., EASTWOOD, T. & INSTITUTE OF GEOLOGICAL, S. 1971. *British regional geology: Northern England,* London, H.M. Stationery Off.
TEEUW, D. 1971. Prediction of Formation Compaction from Laboratory Compressibility Data.
TEMMERMAN, M., JENSEN, P. D. & HÉBERT, J. 2013. Von Rittinger theory adapted to wood chip and pellet milling, in a laboratory scale hammermill. *Biomass and Bioenergy,* 56**,** 70-81.
TERZAGHI, K. 1923. Die berechnung der durchlassigkeitsziffer des tones aus dem verlauf der hydrodynamischen spannungserscheinungen. *Sitznugshrichte Akad. Wissen. Wien of Mathem. Naturw,* 132**,** 125-138.
TERZAGHI , K. The shearing resistance of saturated soils and the angle between planes of shear. International Conference of Soil Mechanics and Foundation Engineering, 1936 Cambridge. 54-56.
TIPPIE, D. B. & KOHLHAAS, C. A. 1973. Effect of Flow Rate on Stability of Unconsolidated Producing Sands. *Fall Meeting of the Society of Petroleum Engineers of AIME.* Las Vegas, Nevada: 1973 Copyright 1973, American Institute of Mining, Metallurgical, and Petroleum Engineers, Inc.
TIXIER, M. P., LOVELESS, G. W. & ANDERSON, R. A. 1975. Estimation of Formation Strength From the Mechanical-Properties Log
TRONVOLL, J. & FJAER, E. Experimental study of sand production from perforation cavities. International journal of rock mechanics and mining sciences & geomechanics abstracts, 1994. Elsevier, 393-410.
TRONVOLL, J. & HALLECK, P. M. 1994. Observations of sand production and perforation cleanup in a weak sandstone. *Rock Mechanics in Petroleum Engineering.* Delft, Netherlands: 1994 Copyright 1994, Society of Petroleum Engineers, Inc.
TRONVOLL, J., MORITA, N. & SANTARELLI, F. J. 1992. Perforation Cavity Stability: Comprehensive Laboratory Experiments and Numerical Analysis. *SPE Annual Technical Conference and Exhibition.* Washington, D.C.: 1992 Copyright 1992, Society of Petroleum Engineers Inc.
TRONVOLL, J., PAPAMICHOS, E., SKJAERSTEIN, A. & SANFILIPPO, F. 1997. Sand Production in Ultra-Weak Sandstones: Is Sand Control Absolutely Necessary? *Latin American and Caribbean Petroleum Engineering Conference.* Rio de Janeiro, Brazil: 1997 Copyright 1997, Society of Petroleum Engineers, Inc.
TRONVOLL, J. R. Experimental investigation of perforation cavity stability. The 33th US Symposium on Rock Mechanics (USRMS), 1992. American Rock Mechanics Association.
TUCKER, M. E. 2009. *Sedimentary petrology: an introduction to the origin of sedimentary rocks,* John Wiley & Sons.
TURCOTTE, D. L. 1986. Fractals and fragmentation. *Journal of Geophysical Research: Solid Earth,* 91**,** 1921-1926.
TURCOTTE, D. L. 1992. *Fractals and Chaos in Geology and Geophysics,* Cambridge University Press.

TYLER, S. W. & WHEATCRAFT, S. W. 1992. Fractal scaling of soil particle-size distributions: analysis and limitations. *Soil Science Society of America Journal,* 56**,** 362-369.

VARDOULAKIS, I., STAVROPOULOU, M. & PAPANASTASIOU, P. 1996. Hydro-mechanical aspects of the sand production problem. *Transport in Porous media,* 22, 225-244.

VAJDOVA, V., BAUD, P. & WONG, T.-F. 2004. Permeability evolution during localized deformation in Bentheim sandstone. *Journal of Geophysical Research: Solid Earth,* 109**,** B10406.

VAN DEN HOEK, P. J. & GEILIKMAN, M. B. Prediction of sand production rate in oil and gas reservoirs: field validation and practical use. SPE Annual Technical Conference and Exhibition, 2005. Society of Petroleum Engineers.

VAN DEN HOEK, P. J. & GEILIKMAN, M. B. Prediction of Sand Production Rate in Oil and Gas Reservoirs: Importance of Bean-Up Guidelines SPE Russian Oil and Gas Technical Conference and Exhibition, 2006. Society of Petroleum Engineers.

VAN DEN HOEK, P. J., HERTOGH, G. M. M., KOOIJMAN, A. P., DE BREE, P., KENTER, C. J. & PAPAMICHOS, E. 1996. A New Concept of Sand Production Prediction: Theory and Laboratory Experiments. *SPE Annual Technical Conference and Exhibition.* Denver, Colorado: 1996 Copyright 1996, Society of Petroleum Engineers, Inc.

VAZIRI, H., WANG, X. & PALMER, I. 1997. Well-bore completion technique and geotechnical parameters influencing gas production. *Canadian geotechnical journal,* 34**,** 87-101.

VAZIRI, H., XIAO, Y. & PALMER, I. 2002. Assessment of several sand prediction models with particular reference to HPHT wells. *SPE/ISRM Rock Mechanics Conference.* Irving, Texas: Copyright 2002, Society of Petroleum Engineers Inc.

VAZIRI, H. H. 1988. Theoretical Analysis Of Stress, Pressure, And Formation Damage During Production. *Journal of Canadian Petroleum Technology,* 27.

VAZIRI, H. H. 2004. Integrated Soil And Rock Mechanics: A Major Step Towards Consistent And Improved Sand Production Prediction And Management. American Rock Mechanics Association.

VEEKEN, C. A. M., DAVIES, D. R., KENTER, C. J. & KOOIJMAN, A. P. 1991. Sand Production Prediction Review: Developing an Integrated Approach. *SPE Annual Technical Conference and Exhibition.* Dallas, Texas: 1991 Copyright 1991, Society of Petroleum Engineers, Inc.

VOLONTE, G., SCARFATO, F. & BRIGNOLI, M. 2013. Sand Prediction: A Practical Finite-Element 3D Approach for Real Field Applications. *SPE Production & Operations,* 28**,** 95-108.

VON RITTENGER, P. R. 1867. *Lehrbuch der Aufbereitungskonde,*.

VRIEZEN, P. B., SPIJKER, A. & VAN DER VLIS, A. C. 1975. Erosion of Perforation Tunnels in Gas Wells. *Fall Meeting of the Society of Petroleum Engineers of AIME.* Dallas, Texas: 1975 Copyright 1975.

WALTON, I. C., ATWOOD, D. D., HALLECK, P. M. & BIANCO, L. C. B. 2002. Perforating Unconsolidated Sands: An Experimental and Theoretical Investigation. *SPE Drilling & Completion,* 17**,** 141-150.

WANG, Y. & PAPAMICHOS, E. 2012a. Sand Prediction by Different Criteria and a Validation by a Perforated Test in a Sandstone. *SPE Heavy Oil Conference Canada.* Calgary, Alberta, Canada: Society of Petroleum Engineers.

WANG, Y. & PAPAMICHOS, E. 2012b. Sand Prediction By Different Criteria And Validation Through a Hollow Cylinder Test. American Rock Mechanics Association.
WANG, J. & WAN, R. 2004. Computation of sand fluidization phenomena using stabilized finite elements. *Finite elements in analysis and design, 40, 1681-1699.*
WANG, Y. & XUE, S. Coupled reservoir-geomechanics model with sand erosion for sand rate and enhanced production prediction. International Symposium and Exhibition on Formation Damage Control, 2002. Society of Petroleum Engineers.
WARPINSKI, N. R. & SMITH, M. B. 1989. Rock mechanics and fracture geometry. *Chapter 3 ,in: J.L. Gidley (Ed.), et al., Recent Advances in Hydraulic Fracturing, SPE Monograph, Vol. 12 (1989).*
WEINGARTEN, J. S. & PERKINS, T. K. 1995. Prediction of Sand Production in Gas Wells: Methods and Gulf of Mexico Case Studies. *SPE Journal of Petroleum Technology,* 47**,** 596-600.
WEISSENBURGER, K. W., MORITA, N., MARTIN, A. J. & WHITFILL, D. L. 1987. The Engineering Approach to Sand Production Prediction. *SPE Annual Technical Conference and Exhibition.* Dallas, Texas: 1987 Copyright 1987, Society of Petroleum Engineers.
Well Test Report. 2007. Field A.
Well Test Report. 2009. Field B.
WHITE, J. E. 1983. *Underground Sound: Application of Seismic Waves,* Elsevier.
WILLIS, J. R. 1967. A Comparison of the Fracture Criteria of Barenblatt and Griffith. *J. Mech. Phys. Solids 15 (l967) 151-162.*
WILSON, A. H. 1977. The Stability of tunnels in soft rock at depth. *in Conference on Rock Engineering.* Newcastle on Tyne.
WILSON, A. H. 1983. The stability of underground workings in the soft rocks of the Coal Measures. *International Journal of Mining Engineering,* 1**,** 91-187.
WILLSON, S. M., MOSCHOVIDIS, Z. A., CAMERON, J. R. & PALMER, I. D. 2002. New Model for Predicting the Rate of Sand Production. *SPE/ISRM Rock Mechanics Conference*. Irving, Texas: Copyright 2002, Society of Petroleum Engineers Inc.
WONG, S.W., VEEKEN, C. A. M. & KENTER, C. J. 1994. The Rock-Mechanical Aspects of Drilling a North Sea Horizontal Well. *SPE Drilling & Completion,* 9**,** 47-52.
WONG, T.-F. 1982. Shear fracture energy of Westerly granite from post-failure behavior. *Journal of Geophysical Research: Solid Earth,* 87**,** 990-1000.
WONG, T.-F. 1990. Mechanical compaction and the brittle—ductile transition in porous sandstones. *Geological Society, London, Special Publications,* 54**,** 111-122.
WONG, T.-F. & BAUD, P. 2012. The brittle-ductile transition in porous rock: A review. *Journal of Structural Geology,* 44**,** 25-53.
WONG, T.-F., DAVID, C. & ZHU, W. 1997. The transition from brittle faulting to cataclastic flow in porous sandstones: Mechanical deformation. *Journal of Geophysical Research: Solid Earth,* 102**,** 3009-3025.
WONG, T. 1986. On the normal stress dependence of the shear fracture energy. *Earthquake Source Mechanics.* Washington, DC: AGU.
WOOD, D. C. 1979. *The effect of sand size on arch stability in unconsolidated sands.*
WU, B. & TAN, C. P. 2002. Sand Production Prediction of Gas Field - Methodology and Field Application. *SPE/ISRM Rock Mechanics Conference.* Irving, Texas: Copyright 2002, Society of Petroleum Engineers Inc.

WU, B., YAAKUB, M. A., TAN, C. P., YEOW, L. M. & JOHAR, Z. 2004. Sand Production Prediction Study for a Multi-Field Gas Development. American Rock Mechanics Association.

YALE, D., NIETO, J. A. & AUSTIN, S. The effect of cementation on the static and dynamic mechanical properties of the Rotliegendes sandstone. Proc, 1995. 169-175.

YALE, D. P. 1984. *Network Modelling of Flow, Storage and Deformation in Porous Rocks.* Stanford University.

YALE, D. P. & CRAWFORD, B. Plasticity and permeability in carbonates: dependence on stress path and porosity. EUROCK 98. Symposium, 1998.

YI, X., ONG, S. & RUSSELL, J. Characterizing Pore Compressibility Reservoir Compaction and Stress Path under Uniaxial Strain Condition for Nonlinear Elastic Rock. Alaska Rocks 2005 The 40th US Symposium on Rock Mechanics (USRMS), 2005. American Rock Mechanics Association.

ZHANG, J. 2013. Borehole stability analysis accounting for anisotropies in drilling to weak bedding planes. International Journal of Rock Mechanics and Mining Sciences, 60, 160-170.